

UNIVERSITY OF CALIFORNIA  
SANTA CRUZ

**SEARCH FOR WW AND WZ RESONANCES IN  $\ell\nu qq$  FINAL  
STATES IN  $pp$  COLLISIONS AT  $\sqrt{s} = 13$  TEV WITH THE ATLAS  
DETECTOR**

A dissertation submitted in partial satisfaction of the  
requirements for the degree of

DOCTOR OF PHILOSOPHY

in

PHYSICS

by

**Natasha Woods**

December 2019

The Dissertation of Natasha Woods  
is approved:

---

Abraham Seiden, Chair

---

Mike Hance

---

Bruce Schumm

---

Quentin Williams  
Vice Provost and Dean of Graduate Studies

Copyright © by

Natasha Woods

2019

# Table of Contents

List of Figures	vi
List of Tables	xv
Abstract	xvii
Dedication	xviii
Acknowledgments	xix
<b>I Introduction</b>	<b>1</b>
<b>1 Introduction</b>	<b>2</b>
<b>II Theoretical Motivation</b>	<b>6</b>
<b>2 The Standard Model of Particle Physics</b>	<b>7</b>
2.1 Introduction . . . . .	7
2.2 Quantum Field Theory . . . . .	7
2.3 $U(1)_{EM}$ Local Gauge Invariance . . . . .	8
2.4 Yang-Mills Gauge Theories . . . . .	11
2.5 Particles in the Standard Model . . . . .	12
2.6 Higgs Mechanism . . . . .	17
2.7 Electroweak Theory . . . . .	18
2.8 Quantum ChromoDynamics . . . . .	19
<b>3 Standard Model Successes and Limitations</b>	<b>24</b>
<b>4 New Physics Models with Diboson Resonances</b>	<b>27</b>
4.1 Randall Sundrum Bulk Model . . . . .	27
4.2 Extended Scalar Sector . . . . .	29

4.3	Simple Standard Model Extensions . . . . .	30
<b>III</b>	<b>Experimental Setup</b>	<b>33</b>
<b>5</b>	<b>LHC</b>	<b>34</b>
5.1	LHC Layout and Design . . . . .	36
<b>6</b>	<b>The ATLAS Detector</b>	<b>41</b>
6.1	Coordinate System . . . . .	43
6.2	Inner Detector . . . . .	44
6.2.1	Pixel Detector . . . . .	47
6.2.2	Semiconductor Tracker . . . . .	47
6.2.3	Transition Radiation Tracker . . . . .	47
6.3	Calorimeters . . . . .	49
6.4	Muon Spectrometer . . . . .	53
6.5	Magnet System . . . . .	57
6.6	Trigger System . . . . .	58
<b>IV</b>	<b>Method</b>	<b>60</b>
<b>7</b>	<b>Dataset and Simulated Samples</b>	<b>61</b>
7.1	Dataset . . . . .	61
7.2	Simulated Samples . . . . .	64
<b>8</b>	<b>Objects</b>	<b>65</b>
8.1	Electrons . . . . .	65
8.2	Muons . . . . .	66
8.3	Jets . . . . .	67
8.3.1	Small-R jets . . . . .	70
8.3.2	Large-R jets . . . . .	70
8.3.3	Variable Radius jets . . . . .	73
8.3.4	Jet Flavor Tagging . . . . .	74
8.4	MET/Neutrinos . . . . .	74
8.5	Overlap Removal . . . . .	74
<b>9</b>	<b>Event Selection and Categorization</b>	<b>76</b>
9.1	Pre-selection . . . . .	76
9.2	Trigger . . . . .	76
9.3	non-VBF/VBF RNN . . . . .	78
9.4	Topological Cuts . . . . .	85
9.5	Selection Acceptance times efficiency for Signal Events . . . . .	95

9.6	Background Estimate . . . . .	96
9.6.1	Control Regions . . . . .	96
9.6.2	Fake Lepton Backgrounds . . . . .	96
<b>10</b>	<b>Systematic Uncertainties</b>	<b>110</b>
10.1	Experimental Systematics . . . . .	110
10.2	Theory Systematics . . . . .	112
<b>11</b>	<b>Statistical Analysis</b>	<b>120</b>
11.1	Likelihood Function Definition . . . . .	120
11.2	Fit Configuration . . . . .	121
11.3	Best Fit $\mu$ . . . . .	123
11.4	Discovery Test . . . . .	124
11.5	Exclusion Limits . . . . .	125
<b>V</b>	<b>Results</b>	<b>127</b>
<b>12</b>	<b>Statistical Interpretation</b>	<b>128</b>
12.1	Discovery Tests . . . . .	128
12.2	Systematic Profiling and Correlations . . . . .	134
12.3	Expected and Measured Yields . . . . .	135
12.4	Limits . . . . .	149
<b>VI</b>	<b>Quark and Gluon Tagging</b>	<b>151</b>
<b>13</b>	<b>Prospects</b>	<b>152</b>
<b>14</b>	<b><math>n_{trk}</math> Calibration</b>	<b>159</b>
<b>15</b>	<b>Application</b>	<b>165</b>
<b>VII</b>	<b>Conclusion</b>	<b>170</b>
<b>16</b>	<b>Conclusions</b>	<b>171</b>
	<b>Bibliography</b>	<b>172</b>

# List of Figures

2.1	The particles of the Standard Model. . . . .	14
2.2	Summary of how Standard Model particles interact with other Standard Model particles. . . . .	15
2.3	This figure shows the three dominant QCD interactions. From Ref. [17] . . . . .	21
2.4	Strength of the U(1), SU(2), and SU(3) gauge couplings as a function of the energy scale of the interaction ( $Q$ ). From Ref. [11] . . . . .	22
3.1	A comparison of cross section measurements at $\sqrt{s} = 7, 8, 13$ TeV from ATLAS compared to theoretical measurements. From Ref. [5]	26
4.1	Cartoon of RS Bulk Model . . . . .	28
5.1	Scaling of cross sections with $\sqrt{s}$ . Natasha: write more here . . . . .	35
5.2	LHC Layout. Natasha write more . . . . .	37
5.3	LHC Accelerator. Natasha write more . . . . .	39
6.1	Big picture layout of ATLAS detector. Natasha: write more . . . . .	42
6.2	Big picture layout of ATLAS detector. Natasha: write more . . . . .	42
6.3	A simplified schematic of how different particles interact and are detected within ATLAS. . . . .	43
6.4	Layout of ATLAS Inner Detector . . . . .	45
6.5	Layout of ATLAS ID Barrel System. . . . .	46
6.6	Overview of ATLAS electromagnetic and hadronic calorimeters. . . . .	50

6.7	Schematic of ECAL . . . . .	51
6.8	Schematic of HCAL . . . . .	52
6.9	Schematic of Muon Spectrometer [cite G35] . . . . .	55
6.10	Schematic of MDT chamber. [cite G35] . . . . .	56
6.11	Schematic of RPC chamber, which is used for triggering in the central region of the detector [cite G35]. . . . .	56
6.12	Schematic of TGC chamber, which is used for triggering in the muon end-cap region. [cite G35] . . . . .	57
6.13	Layout of ATLAS magnet systems. . . . .	58
7.1	Integrated luminosity for data collected from ATLAS from 2011 - 2018 . . . . .	62
7.2	Mean number of interactions per crossing for data collected from ATLAS from 2011 - 2018 . . . . .	63
8.1	This figure shows the breakdown of the muon reconstruction efficiency scale factor measured in $Z \rightarrow \mu\mu$ as a function of $p_T$ [4]. . . . .	67
8.2	[7] This diagram shows the calibration stages for EM jets. . . . .	69
8.3	The upper cut on $D_2$ (a) and jet mass window cut i.e. the upper and lower boundary of the mass (b) of the $W$ -tagger as a function of jet $p_T$ . Corresponding values for $Z$ -tagger are shown in (c) and (d). The optimal cut values for maximum significance are shown as solid markers and the fitted function as solid lines. Working points from $VV \rightarrow JJ$ [ATLAS-HDBS-2018-31-002] is also shown as dashed lines as a reference. Natasha reword? . . . . .	72
8.4	Natasha write caption . . . . .	73
9.1	RNN architecture. Natasha add caption . . . . .	80
9.2	This figure shows the embedded logic in LSTM cells. This image was taken from [22]. . . . .	81
9.3	RNN Score distribution for ggF and VBF signals and backgrounds.	82

9.4	ROC curve using k-fold validation for RNN. . . . .	83
9.5	Comparison of GGF Z' limits for different RNN score selections. The bottom panel shows the ratio of the upper limits set for different RNN cuts to the cut-based analysis. In this panel smaller numbers, indicate that the expected upper limit is smaller than the cut-based analysis, which is desired. . . . .	84
9.6	Event Categorization. Natasha write more. . . . .	87
9.7	Data MC comparison for the merged WW HP TCR. The bottom panel shows the ratio of the difference between data and simulation to simulation. The red bands include the all systematic and statistical uncertainties on the background. . . . .	89
9.8	Data MC comparison for the merged WW LP TCR. The bottom panel shows the ratio of the difference between data and simulation to simulation. The red bands include the all systematic and statistical uncertainties on the background. . . . .	90
9.9	Data MC comparison for the merged WZ HP TCR. The bottom panel shows the ratio of the difference between data and simulation to simulation. The red bands include the all systematic and statistical uncertainties on the background. . . . .	91
9.10	Data MC comparison for the merged WZ LP TCR. The bottom panel shows the ratio of the difference between data and simulation to simulation. The red bands include the all systematic and statistical uncertainties on the background. . . . .	92
9.11	Data MC comparison for the resolved WW TCR. The bottom panel shows the ratio of the difference between data and simulation to simulation. The red bands include the all systematic and statistical uncertainties on the background. . . . .	93
9.12	Data MC comparison for the resolved WZ TCR. The bottom panel shows the ratio of the difference between data and simulation to simulation. The red bands include the all systematic and statistical uncertainties on the background. . . . .	94

9.13 Selection acceptance times efficiency for the $W' \rightarrow WZ \rightarrow \ell\nu qq$ events from MC simulations as a function of the $W'$ mass for (a) Drell-Yan and (b) VBF production, combining the merged HP and LP signal regions of the $WW \rightarrow \ell\nu J$ selection and the resolved regions of the $WW \rightarrow \ell\nu jj$ selection. . . . .	95
9.14 Selection acceptance times efficiency for the $G \rightarrow WW \rightarrow \ell\nu qq$ events from MC simulations as a function of the $G$ mass for (a) Drell-Yan and (b) VBF production, combining the merged HP and LP signal regions of the $WW \rightarrow \ell\nu J$ selection and the resolved regions of the $WW \rightarrow \ell\nu jj$ selection. . . . .	96
9.15 The $E_T^{miss}$ distribution in MJCR for 2017 data in the electron channel(left), muon channel with W-boson pT < 150 GeV (center) and > 150 GeV (right). Multi-jet templates are calculated as remaining data components after excluding known MC . . . . .	98
9.16 Postfit Data/MC comparison of distributions of $E_T^{miss}$ , $m_T^W$ , lepton and neutrino $p_T$ , $m_{\ell\nu jj}$ , lepton- $\nu$ angular distance in the $WW$ electron channel. The MJ template is obtained from the pre-MJ-fit. . . . .	99
9.17 Postfit Data/MC comparison of distributions of $E_T^{miss}$ , $m_T^W$ , lepton and neutrino $p_T$ , $m_{\ell\nu jj}$ , lepton- $\nu$ angular distance in the $WW$ muon channel. The MJ template is obtained from the pre-MJ-fit. . . . .	100
9.18 Postfit Data/MC comparison of distributions of $E_T^{miss}$ , $m_T^W$ , lepton and neutrino $p_T$ , $m_{\ell\nu jj}$ , lepton- $\nu$ angular distance in the $WZ$ untag electron channel. The MJ template is obtained from the pre-MJ-fit. . . . .	101
9.19 Postfit Data/MC comparison of distributions of $E_T^{miss}$ , $m_T^W$ , lepton and neutrino $p_T$ , $m_{\ell\nu jj}$ , lepton- $\nu$ angular distance in the $WZ$ untag muon channel. The MJ template is obtained from the pre-MJ-fit. . . . .	102
9.20 Postfit Data/MC comparison of distributions of $E_T^{miss}$ , $m_T^W$ , lepton and neutrino $p_T$ , $m_{\ell\nu jj}$ , lepton- $\nu$ angular distance in the $WZ$ untag electron channel. The MJ template is obtained from the pre-MJ-fit. . . . .	103

9.21 Postfit Data/MC comparison of distributions of $E_T^{miss}$ , $m_T^W$ , lepton and neutrino $p_T$ , $m_{\ell\nu jj}$ , lepton- $\nu$ angular distance in the $WZ$ untag muon channel. The MJ template is obtained from the pre-MJ-fit.	104
9.22 Postfit Data/MC comparison of distributions of $E_T^{miss}$ , $m_T^W$ , lepton and neutrino $p_T$ , $m_{\ell\nu jj}$ , lepton- $\nu$ angular distance in the VBF $WW$ electron channel. The MJ template is obtained from the pre-MJ-fit.	105
9.23 Postfit Data/MC comparison of distributions of $E_T^{miss}$ , $m_T^W$ , lepton and neutrino $p_T$ , $m_{\ell\nu jj}$ , lepton- $\nu$ angular distance in the VBF $WW$ muon channel. The MJ template is obtained from the pre-MJ-fit.	106
9.24 Postfit Data/MC comparison of distributions of $E_T^{miss}$ , $m_T^W$ , lepton and neutrino $p_T$ , $m_{\ell\nu jj}$ , lepton- $\nu$ angular distance in the VBF $WZ$ electron channel. The MJ template is obtained from the pre-MJ-fit.	107
9.25 Postfit Data/MC comparison of distributions of $E_T^{miss}$ , $m_T^W$ , lepton and neutrino $p_T$ , $m_{\ell\nu jj}$ , lepton- $\nu$ angular distance in the VBF $WZ$ muon channel. The MJ template is obtained from the pre-MJ-fit.	108
10.1 The W/Z+jet systematics for the a) Merged ggF, b) Resolved ggF, c) Merged VBF, and d) Resolved VBF regions. The top subplot shows the nominal and variation distributions/bands, the middle shows the ratio of the two, and the final shows just the shape of the envelope (the final uncertainty).	114
10.2 The two-point generator comparison between Sherpa and MadGraph for the W/Z+jet samples in the a) Merged ggF, b) Resolved ggF, c) Merged VBF, and d) Resolved VBF regions. The normalization of the Madgraph sample is set to the Sherpa value to consider only shape effects. The bottom inlet shows the ratio of the two.	115
10.3 Ratio between the variations of generator (red) and hadronization (blue) variations for the Merged regime for $t\bar{t}$ sample.	116
10.4 Ratio between the variations of generator (red) and hadronization (blue) variations for the Resolved regime for $t\bar{t}$ sample.	116

10.5	Ratio between the variations of ISR up (red) and down (blue) variations for the Merged regime for $t\bar{t}$ sample. . . . .	117
10.6	Ratio between the variations of ISR up (red) and down (blue) variations for the Resolved regime for $t\bar{t}$ sample. . . . .	118
10.7	Ratio between the variations of FSR up (red) and down (blue) variations for the Merged regime for $t\bar{t}$ sample. . . . .	119
10.8	Ratio between the variations of FSR up (red) and down (blue) variations for the Resolved regime for $t\bar{t}$ sample. . . . .	119
11.1	The HVT signal mass resolution as a function of mass fit with a straight line in the Resolved ggF region (left) and VBF (right) region. . . . .	123
11.2	The HVT signal mass resolution as a function of mass fit with a straight line in the Merged ggF region (left) and VBF (right) region. . . . .	123
12.1	These plots show the measured $p_0$ value as a function of resonance mass for HVT Z' DY production. . . . .	129
12.2	These plots show the measured $p_0$ value as a function of resonance mass for HVT Z' VBF production. . . . .	130
12.3	These plots show the measured $p_0$ value as a function of resonance mass for HVT W' DY production. . . . .	131
12.4	These plots show the measured $p_0$ value as a function of resonance mass for HVT W' VBF production. . . . .	132
12.5	These plots show the measured $p_0$ value as a function of resonance mass for the RS Graviton DY production. . . . .	133
12.6	Ranked systematics and their fitted values for WW DY (right) and VBF (left) selections. . . . .	134
12.7	Ranked systematics and their fitted values for WZ DY (right) and VBF (left) selections. . . . .	135
12.8	Correlations between systematics for WW DY (right) and VBF (left) selections. . . . .	135

12.9 This figure shows the distribution of $m_{\ell\nu qq}$ in the DY WW control regions. . . . .	143
12.10 This figure shows the distribution of $m_{\ell\nu qq}$ in the DY WZ control regions. . . . .	144
12.11 This figure shows the distribution of $m_{\ell\nu qq}$ in the VBF WW control regions. . . . .	145
12.12 This figure shows the distribution of $m_{\ell\nu qq}$ in the VBF WZ control regions. . . . .	146
12.13 This figure shows the distribution of $m_{\ell\nu qq}$ in the GGF WW signal regions. . . . .	147
12.14 This figure shows the distribution of $m_{\ell\nu qq}$ in the GGF WZ Untag signal regions. . . . .	147
12.15 This figure shows the distribution of $m_{\ell\nu qq}$ in the GGF WZ Tag signal regions. . . . .	148
12.16 This figure shows the distribution of $m_{\ell\nu qq}$ in the VBF WZ Tag signal regions. . . . .	148
12.17 This figure shows the distribution of $m_{\ell\nu qq}$ in the VBF WZ Tag signal regions. . . . .	149
12.18 This figure shows theory, expected and observed limits for HVT $W'$ DY (left) and VBF (right) production. . . . .	149
12.19 This figure shows theory, expected and observed limits for HVT $Z'$ DY (left) and VBF (right) production. . . . .	150
12.20 This figure shows theory, expected and observed limits for RS Gravitons via DY production. . . . .	150
13.1 PDGID of the truth-level parton matched to the small-R jets passing the Resolved GGF WW Signal Region selections for the (a) Leading (b) Sub-Leading jets . These distributions are shown for 300, 500, and 700GeV Z' signals and the background. . . . .	154

13.2 The number of tracks in small-R jets in events passing the Resolved GGF WW Signal Region selections for the (a) Leading (b) Sub-Leading jets. These distributions are shown for 300, 500, and 700GeV Z' signals and the background. . . . .	154
13.3 The number of tracks in background small-R jets in events passing the Resolved GGF WW Signal region selection vs. $\ln(p_T)$ for (a)Leading (b) Sub-Leading jets. The best fit line for the distribution is also shown, as well as the percentage of jets that pass a cut of number of tracks $< 4 \times \ln(p_T) - 5$ . Note the number of total entries in these plots has been normalized to one. . . . .	155
13.4 The number of tracks in small-R jets in 300GeV Z' events passing the Resolved GGF WW Signal region selection vs. $\ln(p_T)$ for (a)Leading (b) Sub-Leading jets. The best fit line for the distribution is also shown, as well as the percentage of jets that pass a cut of number of tracks $< 4 \times \ln(p_T) - 5$ .Note the number of total entries in these plots has been normalized to one. . . . .	155
13.5 The number of tracks in small-R jets in 500GeV Z' events passing the Resolved GGF WW Signal region selection vs. $\ln(p_T)$ for (a)Leading (b) Sub-Leading jets. The best fit line for the distribution is also shown, as well as the percentage of jets that pass a cut of number of tracks $< 4 \times \ln(p_T) - 5$ .Note the number of total entries in these plots has been normalized to one. . . . .	156
13.6 The number of tracks in small-R jets in 700GeV Z' events passing the Resolved GGF WW Signal region selection vs. $\ln(p_T)$ for (a)Leading (b) Sub-Leading jets. The best fit line for the distribution is also shown, as well as the percentage of jets that pass a cut of number of tracks $< 4 \times \ln(p_T) - 5$ .Note the number of total entries in these plots has been normalized to one. . . . .	156

13.7 The number of tracks in leading small-R jets in background events passing the Resolved GGF WW Signal region selection vs. $\ln(p_T)$ for (a)Gluons (b) Quarks jets. The best fit line for the distribution is also shown, as well as the percentage of jets that pass a cut of number of tracks $< 4 \times \ln(p_T) - 5$ .Note the number of total entries in these plots has been normalized to one. . . . .	157
13.8 ROC Curve for Quark and Gluon Tagging with a cut on the number of tracks that depends on the $\ln(p_T)$ . . . . .	157
13.9 The top panel shows the distribution of $m_{lvqq}$ with and without quark gluon tagging. The middle panel shows the ratio of the signals and backgrounds with and without quark gluon tagging. The bottom panel shows the change in $S/\sqrt{B}$ with quark gluon tagging. . . . .	158
15.1 The top panel shows the distribution of $m_{lvqq}$ with and without requiring jets to be true quarks. The middle panel shows the ratio of the signals and backgrounds with and without requiring jets to be true quarks. The bottom panel shows the change in $S/\sqrt{B}$ when requiring jets to be true quarks. . . . .	166
15.2 Unfolded and extracted $n_C$ qg dstbs. . . . .	167
15.3 PDGID of the truth-level parton matched to the small-R jets passing the Resolved GGF WW Signal Region selections for the (a) Leading (b) Sub-Leading jets . These distributions are shown for 300, 500, and 700GeV Z' signals and the background. . . . .	168
15.4 These figures show the impact of the uncertainties on the number of tracks in the leading jet in the sum of the background sample in the Resolved GGF WW SR (a) tracking efficiency (b) fake (c) PDF (d) ME (e) unfolding uncertainties. . . . .	169

# List of Tables

2.1	Representations of the SM fermions under $SU(3)_C \times SU(2)_L \times U(1)_Y$ gauge symmetry group. $SU(2)_L$ gauge transformations allow one to go between rows and $SU(3)_C$ transformations allow one to go between columns in these fermion representations. [REWORD]	13
9.1	The list of triggers used in the analysis. . . . .	77
9.2	Summary of selection criteria used to define the signal region (SR), $W$ +jets control region ( $W$ CR) and $t\bar{t}$ control region ( $t\bar{t}$ CR) for merged 1-lepton channel. . . . .	87
9.3	The list of selection cuts in the resolved analysis for the $WW$ and $WZ$ signal regions (SR), $W$ +jets control region (WR) and $t\bar{t}$ control region (TR). . . . .	88
9.4	Definitions of “inverted” leptons used in multijet control region . .	98
9.5	Fit validation result in WCRs for 2015+16 data. The fit is done in various WCRs, in order to obtain the corresponding scale factors for MJ templates: ggF resolved WCR for the $WW \rightarrow lvqq$ selection, ggF resolved untagged WCR for the $WZ \rightarrow lvqq$ selection, ggF resolved tagged WCR for the $WZ \rightarrow lvqq$ selection, VBF resolved WCR for the $WW \rightarrow lvqq$ selection, and VBF resolved WCR for the $WZ \rightarrow lvqq$ selection. Post-fit event yields for electroweak processes and MJ contributions are shown. The SF column shows the corresponding normalization scale factors for electroweak processes from the fit. R.U. stands for relative uncertainty. . . . .	109

12.1	Expected and Measured for DY $WW$ $W+\text{jets}$ , $t\bar{t}$ control regions and signal regions. . . . .	136
12.2	Expected and Measured for DY $WZ$ $W+\text{jets}$ , $t\bar{t}$ tag and untag control regions. . . . .	137
12.3	Expected and Measured for DY $WZ$ $W+\text{jets}$ , $t\bar{t}$ tag and untag signal regions. . . . .	138
12.4	Expected and Measured for VBF $WW$ $W+\text{jets}$ , $t\bar{t}$ control regions and signal regions. . . . .	139
12.5	Expected and Measured for VBF $WZ$ $W+\text{jets}$ , $t\bar{t}$ control regions and signal regions. . . . .	140
12.6	Fitted background normalizations for $t\bar{t}$ and $W+\text{jets}$ backgrounds for the DY $WW$ analysis region. . . . .	141
12.7	Fitted background normalizations for $t\bar{t}$ and $W+\text{jets}$ backgrounds for the DY $WZ$ analysis region. . . . .	141
12.8	Fitted background normalizations for $t\bar{t}$ and $W+\text{jets}$ backgrounds for the VBF $WW$ analysis region. . . . .	141
12.9	Fitted background normalizations for $t\bar{t}$ and $W+\text{jets}$ backgrounds for the VBF $WZ$ analysis region. . . . .	142

## Abstract

Search for  $WW$  and  $WZ$  Resonances in  $\ell\nu qq$  final states in  $pp$  collisions at

$\sqrt{s} = 13$  TeV with the ATLAS detector

by

Natasha Woods

This thesis presents a search for  $WW$  and  $WZ$  resonances using data from  $pp$  collisions at  $\sqrt{s} = 13$  TeV using the ATLAS detector, corresponding to an integrated luminosity of  $139 \text{ fb}^{-1}$ . Diboson resonances are predicted in a number of Standard Model (SM) extensions, such as Extended Gauge Models, and Extra dimensional models. This search looks for resonances where one  $W$  boson decays leptonically and the other  $W$  or  $Z$  boson decays hadronically. This search is sensitive to diboson resonance production via vector-boson fusion as well as quark-antiquark annihilation and gluon-gluon fusion mechanisms. No significant excess of events is observed with respect to the Standard Model backgrounds, and constraints on the masses of new  $W'$ ,  $Z'$ , and bulk-RS Gravitons are extended to up to 3.3 TeV, depending on the model. As the dominant backgrounds in this search contain gluons, classifying jets as quark-initiated or gluon-initiated would make this analysis more sensitive to new physics. Towards this end, this thesis provides a calibrated quark-gluon tagger based on the multiplicity of charged particles within a jet.

Loving Dedication

å

xviii

## **Acknowledgments**

Proper acknowledgments of everyone else who helped you graduate. Write later.

# **Part I**

## **Introduction**

# <sup>3</sup> Chapter 1

## <sup>4</sup> Introduction

<sup>5</sup> In general, humanity has continually strived to understand the structure and  
<sup>6</sup> dynamics of reality for widely varying reasons. Each academic field uses a spe-  
<sup>7</sup> cific set of concepts and models to describe nature. Physics is one such field,  
<sup>8</sup> that uses mathematical objects to systematically develop testable models about  
<sup>9</sup> the universe. Currently, the most fundamental types particles are fermions and  
<sup>10</sup> bosons. Fermions are the particles that make up the "ordinary" matter of the  
<sup>11</sup> universe, while bosons are the quanta of the fundamental forces. The Standard  
<sup>12</sup> Model (SM) of particle physics describes the quantum behavior of three of the  
<sup>13</sup> four fundamental forces: electromagnetic, strong, and weak forces.

<sup>14</sup> The Standard Model has consistently described much of reality to an extreme  
<sup>15</sup> degree of accuracy. It has predicted cross sections for strong and electroweak  
<sup>16</sup> processes that span over ten orders of magnitude [see Fig. 3.1] and contains no  
<sup>17</sup> known logical inconsistencies. Despite the reality of the Standard Model, it still  
<sup>18</sup> fails to describe aspects of reality and suffers from aesthetic issues. The SM fails  
<sup>19</sup> to account for dark matter, dark energy, neutrino masses, the hierarchy of the  
<sup>20</sup> fundamental force strengths, and other issues that may have not been noticed  
<sup>21</sup> yet! This incompleteness may indicate that a more fundamental theory exists. It

22 is hoped that such a theory would address the aforementioned phenomena and  
23 the ad-hoc structure and parameter values of the SM. In particular the relative  
24 scales of the fundamental forces impose oddly fine-tuned SM parameters, unless  
25 there is additional structure at higher energies (e.g. between the electroweak and  
26 Planck scales). This and other theoretical arguments motivate the search for new  
27 physics at the TeV scale. The set of theories that hope to explain more of reality  
28 are known as Beyond the Standard Model theories (BSM). Many of these theories,  
29 if true, would revolutionize concepts of symmetry and space-time, which would  
30 be intrinsically meaningful.

31 To probe the physics at this high energy frontier, physicists often collide ener-  
32 getic particles that combine to produce massive particles, such as the Higgs boson  
33 and top quark. The more energetic the colliding particles are the more massive  
34 produced particles can be. Currently, the world's highest energy particle collider  
35 is the Large Hadron Collider (LHC) at the European Organization for Nuclear  
36 Research (CERN).

37 This thesis presents a search for  $WW$  and  $WZ$  resonances using data from  $pp$   
38 collisions at  $\sqrt{s} = 13$  TeV using the ATLAS detector at CERN, corresponding  
39 to an integrated luminosity of  $139 \text{ fb}^{-1}$ . Diboson resonances are predicted in a  
40 number of BSM theories, such as Extended Gauge Models and Extra dimensional  
41 models. This search looks for resonances where one  $W$  boson decays leptonically  
42 and the other  $W$  or  $Z$  boson decays hadronically. This search is sensitive to  
43 diboson resonance production via vector-boson fusion as well as quark-antiquark  
44 annihilation and gluon-gluon fusion mechanisms (which will be collectively called  
45 non-VBF modes).

46 To search for these new resonances, Monte-Carlo simulations are used to model  
47 SM backgrounds and BSM signals. In these simulations, a series of optimized cuts

48 are used to create signal regions (SR) to identify the leptonic and hadronic decay  
49 products of the resonance, maximize signal acceptance, and minimize background  
50 contamination. In these regions, the resonance mass is calculated as the combined  
51 system mass of the leptonic and hadronic system. The expected resonance mass  
52 distribution from the simulated backgrounds and anticipated signal are compared  
53 to data to search for the existence of these BSM signals (also known as a "bump  
54 hunt"). Control regions enriched in the dominant backgrounds,  $t\bar{t}$  and  $W+\text{jets}$   
55 (TCR and WCR, respectively) are constructed to be orthogonal to SRs and used  
56 to determine the normalization of the  $t\bar{t}$  and  $W+\text{jets}$  backgrounds in SRs.

57 The VBF  $W'$  and  $Z'$  and ggF  $W'$  and  $Z'$  resonances studied have unique  
58 SR and CR selections to maximize analysis sensitivity. RS Graviton signals are  
59 probed using the same selections as the ggF  $Z'$  signal. Additionally, more mas-  
60 sive resonances are more likely to have boosted  $W/Z$  bosons. As the boost of  
61 the hadronically decaying boson increases the separation of its hadronic decay  
62 products decreases. When the hadronically decaying boson has sufficient boost,  
63 the two quarks will overlap and not be identified separately. For this reason, a  
64 set of "resolved" selections are used when the hadronic decay products are recon-  
65 structed separately, and "merged" selections when the decay products overlap and  
66 identified as a single object in the event.

67 The aforementioned SR definitions veto events with  $b$ -jets to minimize  $t\bar{t}$  con-  
68 tamination. However,  $b$ -jets are anticipated from  $W'$  resonances from the hadron-  
69 ically decaying  $Z$  boson. To increase the signal acceptance of these resonances,  
70 a  $Z \rightarrow bb$  tagger is used to construct additional SR and CRs called the "tagged"  
71 regions (and "untagged" if the event fails the  $Z \rightarrow bb$  tagger).

72 For each signal model, the simulated and measured resonance mass distribu-  
73 tions in the relevant SR and CRs are combined to construct a likelihood. This

74 likelihood is parameterized by the signal strength parameter,  $\mu$  and systematic  
75 uncertainties of the resonance mass distribution. This likelihood is used to quan-  
76 tify the likelihood of a certain signal model given the anticipated backgrounds and  
77 measured data.

78 No significant excess of events is observed with respect to the Standard Model  
79 backgrounds, and constraints on the masses of new  $W'$ ,  $Z'$ , and bulk-RS Gravi-  
80 tons are extended to up to 3.3 TeV, depending on the model. As the dominant  
81 backgrounds in this search contain gluons, classifying jets as quark-initiated or  
82 gluon-initiated would improve the sensitivity of this analysis to new physics. To-  
83 wards this end, this thesis provides a calibrated quark-gluon tagger based on the  
84 multiplicity of charged particles within a jet.

## Part II

85

## Theoretical Motivation

86

<sup>87</sup> **Chapter 2**

<sup>88</sup> **The Standard Model of Particle**

<sup>89</sup> **Physics**

<sup>90</sup> **2.1 Introduction**

<sup>91</sup> By determining the dynamics of the most elementary degrees of freedom, par-  
<sup>92</sup> ticle physics hopes to uncover the fundamental laws of the universe. The definition  
<sup>93</sup> of elementary has evolved through time and currently refers to matter and force  
<sup>94</sup> mediating particles: fermions and bosons, respectively. The Standard Model of  
<sup>95</sup> Particle Physics (SM) describes the quantum behavior of three of the four funda-  
<sup>96</sup> mental forces: weak, strong, and electromagnetic, via boson and fermion interac-  
<sup>97</sup> tions. Gravity is not included in the SM and still under investigation.

<sup>98</sup> **2.2 Quantum Field Theory**

<sup>99</sup> In the SM, forces (and particles) are represented as fields. In this context,  
<sup>100</sup> fields are mathematical objects that define a tensor (e.g. scalar, vector, etc) at  
<sup>101</sup> every point on a manifold, here the manifold is space-time. These fields obey laws

102 dictated by Quantum Field Theory (QFT). Particles arise naturally in QFT as  
103 quantized field excitations localized in spacetime.

104 According to Noether's theorem, symmetries of a field give rise to conserved  
105 quantities (e.g. time-translation invariance leads to energy conservation). Often  
106 in the history of physics, a conserved quantity of a field is found and then the  
107 underlying symmetry of the field is inferred. Gauge symmetries are symmetries  
108 among the internal degrees of freedom of the field (components of the tensor),  
109 which give rise to quantities associated with fields. By specifying the symmetries  
110 of a system the dynamics and conserved quantities of the system may be succinctly  
111 defined.

## 112 **2.3 $U(1)_{EM}$ Local Gauge Invariance**

113 The Lagrangian of Quantum Electrodynamics (QED) describes the electro-  
114 magnetic force. QED may be derived by requiring local  $U(1)_{EM}$  gauge invariance  
115 of the free dirac fermion Lagrangian,  $\psi$ :

$$\mathcal{L} = i\bar{\psi}\gamma^\mu\partial_\mu\psi - m\bar{\psi}\psi \quad (2.1)$$

116 This symmetry may be represented as a complex number with unit modulus,  
117  $e^{i\theta}$ .  $U(1)$  gauge invariance requires this gauge transformation of  $\psi$  will leave the  
118 Lagrangian unchanged.

$$\psi(x) \rightarrow \psi'(x) = e^{i\theta(x)}\psi(x) \quad (2.2)$$

119 NB: This transformation is a local gauge transformation as  $\theta$  depends on the  
120 spacetime coordinate.

121 By requiring this symmetry of the free Dirac fermion Lagrangian:

$$\mathcal{L} = i\bar{\psi}\gamma^\mu\partial_\mu\psi - m\bar{\psi}\psi \quad (2.3)$$

<sub>122</sub> The mass term is unaffected, but the kinetic term is modified due to  $\theta(x)$ .

$$\mathcal{L} \rightarrow \mathcal{L}' = i\bar{\psi}e^{-i\theta(x)}\gamma^\mu\partial_\mu\psi e^{i\theta(x)} - m\bar{\psi}e^{-i\theta(x)}\psi e^{i\theta(x)} \quad (2.4)$$

<sub>123</sub>

$$= i\bar{\psi}\gamma^\mu(\partial_\mu\psi + i\psi\partial_\mu\theta) - m\bar{\psi}\psi \quad (2.5)$$

<sub>124</sub> The  $\partial_\mu\theta$  terms breaks the gauge invariance of the Lagrangian. By introducing a  
<sub>125</sub> new field,  $A_\mu$  we can recover the gauge invariance of the derivative. Now redefining  
<sub>126</sub> the derivative as the covariant derivative:

$$D_\mu\psi \equiv (\partial_\mu - iqA_\mu)\psi \quad (2.6)$$

<sub>127</sub> And letting  $A_\mu$  transform under  $U(1)$  as:

$$A_\mu \rightarrow A_\mu + \delta A_\mu \quad (2.7)$$

<sub>128</sub> The transformed covariant derivative becomes:

$$D_\mu\psi \rightarrow D_\mu\psi' = (\partial_\mu - iqA_\mu)\psi' \quad (2.8)$$

<sub>129</sub>

$$= (\partial_\mu - iq(A_\mu + \delta A_\mu))\psi e^{i\theta} \quad (2.9)$$

<sub>130</sub>

$$= e^{i\theta}D_\mu + ie^{i\theta}\psi(\partial_\mu\theta - q\delta A_\mu) \quad (2.10)$$

<sub>131</sub> The covariant derivative can be made gauage invariant by setting the last term  
<sub>132</sub> to zero.

$$\delta A_\mu = \frac{1}{q} \partial_\mu \theta \quad (2.11)$$

<sub>133</sub> So now  $A_\mu$  transforms as:

$$A_\mu \rightarrow A_\mu + \frac{1}{q} \partial_\mu \theta \quad (2.12)$$

<sub>134</sub> Finally, replacing the derivative with the covariant derivative the Dirac La-  
<sub>135</sub> grangian we have:

$$\mathcal{L} = i\bar{\psi}\gamma^\mu D_\mu \psi - m\bar{\psi}\psi - \frac{1}{4}F_{\mu\nu}F^{\mu\nu} \quad (2.13)$$

<sub>136</sub>

$$= \mathcal{L}_{QED} \quad (2.14)$$

<sub>137</sub> Here  $F_{\mu\nu} \equiv \partial_\mu A_\nu - \partial_\nu A_\mu$ . This last term in the Lagrangian is the kinetic  
<sub>138</sub> energy of the gauge boson field.

<sub>139</sub> So we have derived the QED Lagrangian. By requiring the free Dirac La-  
<sub>140</sub> grangian to be invariant under U(1) transformations we have generated a new  
<sub>141</sub> gauge boson field,  $A_\mu$ , which describes the photon. As expected the photon inter-  
<sub>142</sub> acts with fermions.

<sub>143</sub> Stepping back, a global U(1) gauge symmetry of the free Dirac Lagrangian  
<sub>144</sub> implies we cannot measure the absolute phase of a charged particle. A local U(1)  
<sub>145</sub> gauge symmetry changes the phase of fields differently across space time. For this  
<sub>146</sub> type of transformation to leave the Lagrangian invariant, we had to introduce an  
<sub>147</sub> additional field,  $A_\mu$ , which "communicates" these phase changes across space-time.  
<sub>148</sub> In less formal language this effectively means: if the field at one location changes,  
<sub>149</sub> this change is conferred to other particles via  $A_\mu$ .

## 150 2.4 Yang-Mills Gauge Theories

151 Requiring  $U(1)_{EM}$  gauge invariance of the free Dirac Lagrangian gave us QED.

152 Requiring different gauge symmetries we can derive the structure of other inter-

153 actions. Any gauge symmetry may be written as:

$$\psi_i \rightarrow \exp(i\theta^a T_{ij}^a) \psi_j \quad (2.15)$$

154 Here  $\theta$  is a dimensionless real parameter and  $T$  is the generator of the gauge

155 symmetry group. With this the covariant derivative can be written as:

$$D_\mu \psi_i \equiv \partial_\mu \psi_i + ig A_\mu^a T_{ij}^a \psi_j \quad (2.16)$$

156 Then the gauge field must transform as:

$$A_\mu^a \rightarrow A_\mu^a - \frac{1}{g} \partial_\mu \theta^a - f^{abc} \theta^b A_\mu^c \quad (2.17)$$

157 Here  $f$  is the structure constant of the gauge group. The field strength tensor

158 is given by:

$$F_{\mu\nu}^a \equiv \partial_\mu A_\nu^a - \partial_\nu A_\mu^a - g f^{abc} A_\mu^b A_\nu^c \quad (2.18)$$

159

$$F_{\mu\nu}^a \rightarrow F_{\mu\nu}^a - f^{abc} \theta^b F_{\mu\nu}^c \quad (2.19)$$

160 This gives the Yang-Mills Lagrangian:

$$\mathcal{L}_{YM} = -\frac{1}{4} F_{\mu\nu}^{a\mu\nu} F_{\mu\nu}^a + i \bar{\psi}_i \gamma^\mu D_\mu \psi_i + m \bar{\psi}_i \psi_i \quad (2.20)$$

## 161 2.5 Particles in the Standard Model

162 The SM consists of fermions (half-integer spin matter constituents) and bosons  
163 (integer spin force mediators). Fermions are spinor representations of the Poincare  
164 group and can be further separated into leptons and quarks. Bosons are the result  
165 of requiring a particular symmetry among the spinor fields:

$$SU(3)_C \times SU(2)_L \times U(1)_Y \quad (2.21)$$

166  $SU(3)_C$  is the symmetry group of the strong force and generates eight gluon  
167 fields,  $G_\mu$ .  $SU(2)_L$  is the symmetry group of the Electroweak force and generates  
168 three electroweak boson fields. The mixing of this  $SU(2)_L$  and  $U(1)_Y$  gives rise  
169 to the photon field, where Y is the weak-hypercharge:

$$Y = 2(Q - T_3) \quad (2.22)$$

170 Q is the electromagnetic charge, and  $T_3$  is the z-component of the weak isospin.  
171 Weak isospin is the charge associated with the  $SU(2)_L$  symmetry. The correspond-  
172 ing covariant derivative is then:

$$D_\mu \phi \equiv (\partial_\mu + ig_1 B_\mu Y_{L/R} + [ig_2 W_\mu^\alpha T^\alpha]_L + [ig_3 G_\mu^\alpha \tau^\alpha]_C) \psi \quad (2.23)$$

173 It is important to note that the gauge symmetry of the SM yields a particular  
174 structure of the fermion representations. So for a given fermion to interact with  
175 a given gauge field it must have a non-zero corresponding Noether charge for  
176 that gauge symmetry. If the corresponding Noether charge is zero, that fermion  
177 transforms as a singlet and does not participate in that gauge interaction.

178 Fermions are divided into quarks and leptons based on their transformations  
179 under  $SU(3)_C$ . Quarks transform as color triplets. Leptons transform as color

singlets and consequently do not interact with gluons. Fermions may be further  
 classified by their  $SU(2)_L$  interactions. Only the left-chiral part of fermions (denoted by L here) transform as  $SU(2)_L$  doublets, the right-chiral part forms singlets under this gauge. Lastly, all these groups of particles come in three generations, each a heavier copy of the previous, but with differing flavor quantum numbers.  
 This is summarized in Table 2.1 and shown in Figures 2.1 and 2.2.

SM Fermion Gauge Group	First Generation	Second Generation	Third Generation	$(SU(3)_C, SU(2)_L, U(1)_Y)$ Representations
Left-handed quarks	$\begin{pmatrix} u_L^r & u_L^g & u_L^b \\ d_L^r & d_L^g & d_L^b \end{pmatrix}$	$\begin{pmatrix} c_L^r & c_L^g & c_L^b \\ s_L^r & s_L^g & s_L^b \end{pmatrix}$	$\begin{pmatrix} t_L^r & t_L^g & t_L^b \\ b_L^r & b_L^g & b_L^b \end{pmatrix}$	$(3, 2, \frac{1}{6})$
Right-handed quarks	$(u_R^r, u_R^g, u_R^b)$ $(d_R^r, d_R^g, d_R^b)$	$(c_R^r, c_R^g, c_R^b)$ $(s_R^r, s_R^g, s_R^b)$	$(t_R^r, t_R^g, t_R^b)$ $(b_R^r, b_R^g, b_R^b)$	$(3, 1, \frac{2}{3})$ $(3, 1, -\frac{1}{3})$
Left-handed leptons	$\begin{pmatrix} \nu_e^L \\ e_L \end{pmatrix}$	$\begin{pmatrix} \mu_e^L \\ \mu_L \end{pmatrix}$	$\begin{pmatrix} \tau_e^L \\ \tau_L \end{pmatrix}$	$(1, 2, -\frac{1}{2})$
Right-handed leptons	$e_R$	$\mu_R$	$\tau_R$	$(1, 1, -1)$

**Table 2.1:** Representations of the SM fermions under  $SU(3)_C \times SU(2)_L \times U(1)_Y$  gauge symmetry group.  $SU(2)_L$  gauge transformations allow one to go between rows and  $SU(3)_C$  transformations allow one to go between columns in these fermion representations. [REWORD]

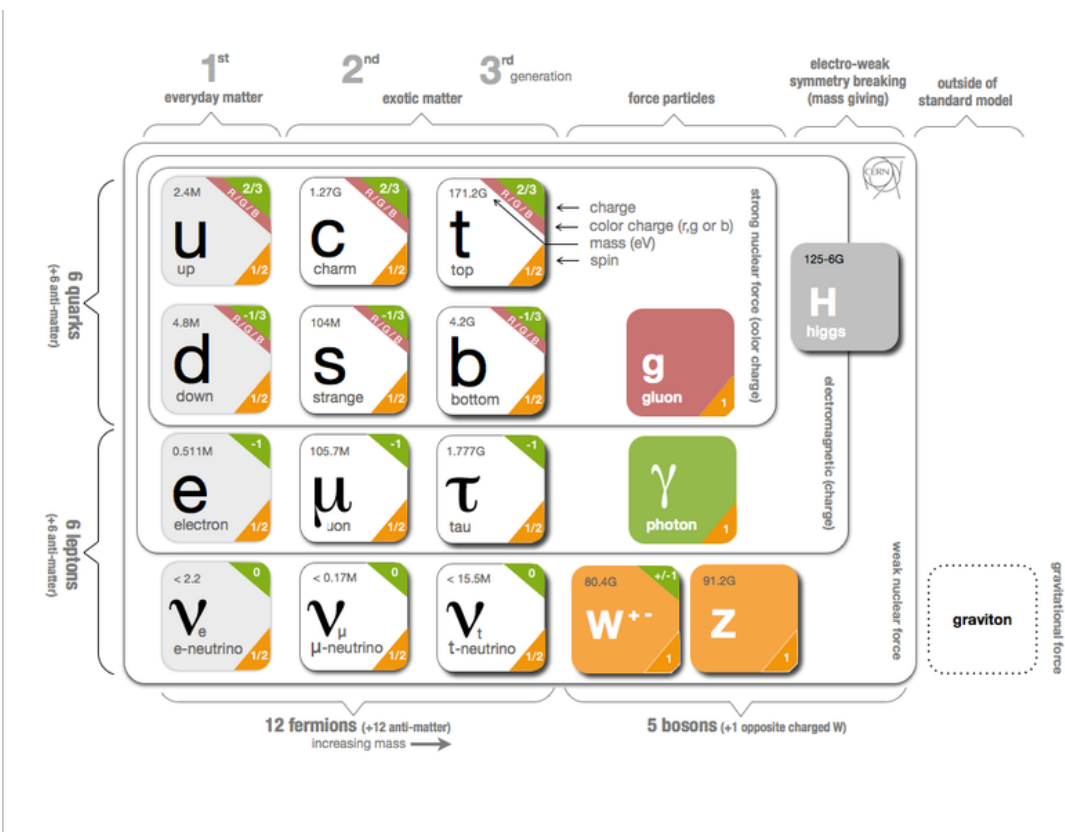


**Figure 2.1:** The particles of the Standard Model.

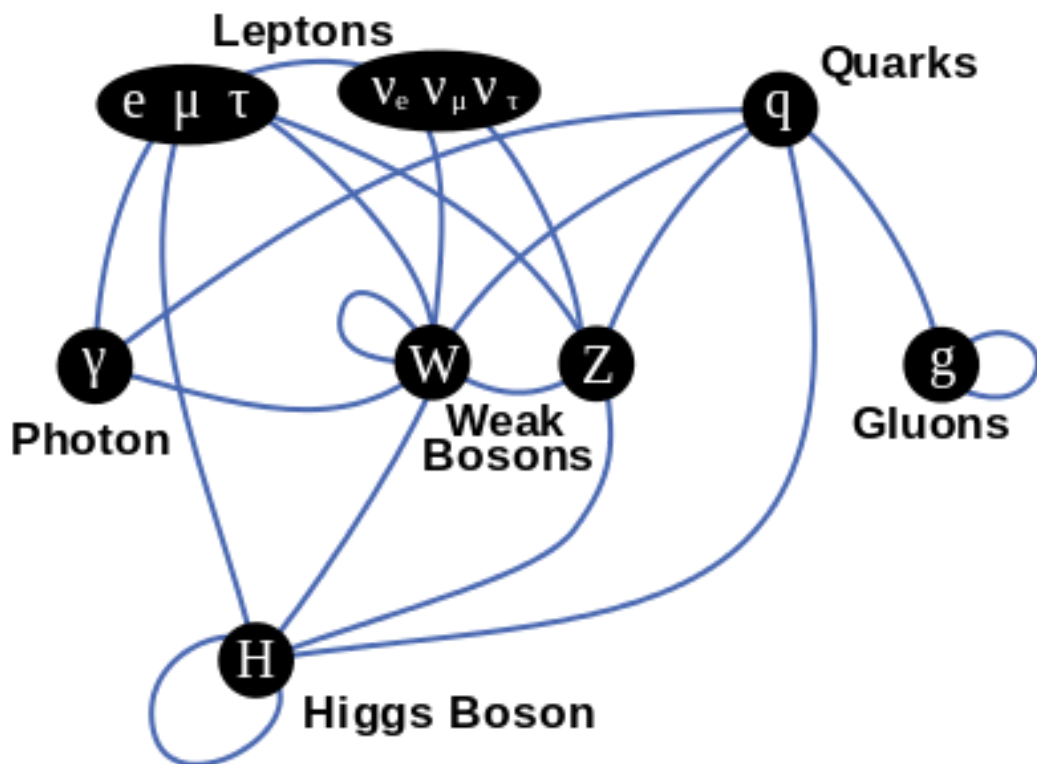


**Figure 2.2:** Summary of how Standard Model particles interact with other Standard Model particles.

<sup>186</sup> Now we can understand the SM Lagrangian density as a Yang-Mills theory  
<sup>187</sup> with the gauge group:  $SU(3)_C \times SU(2)_L \times U(1)_Y$  with an additional  $SU(2)$  complex  
<sup>188</sup> scalar Higgs field doublet that will be discussed later.

$$\begin{aligned} \mathcal{L}_{SM} = & \underbrace{-\frac{1}{4}B_{\mu\nu}B^{\mu\nu} - \frac{1}{4}W_{\mu\nu}^aW^{a\mu\nu} - \frac{1}{4}G_{\mu\nu}^\alpha G^{\alpha\mu\nu}}_{\text{Kinetic Energies and Self-Interactions of Gauge Bosons}} \\ & + \underbrace{\bar{L}_i \gamma^\mu (i\partial_\mu - \frac{1}{2}g_1 Y_{iL} B_\mu - \frac{1}{2}g_2 \sigma^a W_\mu^a) L_i}_{\text{Kinetic Energies and EW Interactions of Left-handed Fermions}} \\ & + \underbrace{\bar{R}_i \gamma^\mu (i\partial_\mu - \frac{1}{2}g_1 Y_{iR} B_\mu) R_i}_{\text{Kinetic Energies and EW Interactions of Right-Handed Fermions}} \\ & + \underbrace{\frac{ig_3}{2} \bar{Q}_j \gamma^\mu \lambda^\alpha G_\mu^\alpha Q_j}_{\text{Strong Interactions between Quarks and Gluons}} \\ & + \underbrace{\frac{1}{2} |(i\partial_\mu - \frac{1}{2}g_1 B_\mu - \frac{1}{2}g_2 \sigma^a W_\mu^a)\Phi|^2 - V(\Phi)}_{\text{Electroweak Boson Masses and Higgs Couplings}} \\ & - (\underbrace{y_{kl}^d \bar{L}_k \Phi R_l + y_{kl}^u \bar{R}_k \tilde{\Phi} L_l + h.c.}_{\text{Fermion Mass terms and Higgs Couplings}}) \end{aligned}$$

<sup>189</sup> Here several abstract spaces are being spanned:

- <sup>190</sup> –  $a$  spans the three  $SU(2)_L$  gauge fields with generators expanded in Pauli matrices,  $T^\alpha = \frac{1}{2}\sigma^\alpha$
- <sup>191</sup> –  $\alpha$  spans the eight  $SU(3)_C$  gauge fields, with generators expanded in Gell-Mann matrices,  $\tau^\alpha = \frac{1}{2}\lambda^\alpha$
- <sup>192</sup> – L/R represent left and right projections of Dirac fermion fields. The Strong interaction is not chiral, so  $Q = L+R$

- 196 –  $\mu$  and  $\nu$  are four-vector indices
- 197 –  $i, j, k$  are summed over the three generations of SM particles.

198 **2.6 Higgs Mechanism**

199 The SM Lagrangian without the addition of a Higgs field does not allow for  
200 gauge boson and fermion mass terms:  $\frac{1}{2}m_A^2 A_\mu A_\mu$  and  $m(\bar{\psi}\psi)$ , as these terms are  
201 not gauge invariant. By introducing the Higgs field, mass terms for these particles  
202 may be included in a gauge invariant way. This field is a complex doublet with a  
203 potential  $V(\Phi)$ :

$$\Psi = \begin{pmatrix} \Phi^\dagger \\ \Phi^0 \end{pmatrix} \quad (2.24)$$

204  $V(\Phi) = \mu^2 \Phi^\dagger \Phi + \lambda |\Phi^\dagger \Phi|^2 \quad (2.25)$

205 The minima of this field occurs for  $|\Phi| = \sqrt{\frac{\mu^2}{2\lambda}} \equiv \frac{v}{2}$ . This yields degenerate  
206 minima, this symmetry is broken by choosing a specific minima (a.k.a. sponta-  
207 neous symmetry breaking). By convention  $\Phi_{min} = \frac{1}{\sqrt{2}} \begin{pmatrix} 0 \\ v \end{pmatrix}$  is chosen. This means  
208 the ground state of the Higgs field (Higgs vacuum) is non-zero,  $\sqrt{\frac{-\mu^2}{\lambda}}$ . The Higgs  
209 Field may now be expanded around this new ground state:

$$\Phi(x) = \frac{1}{\sqrt{2}} \begin{pmatrix} 0 \\ v + h(x) \end{pmatrix} \quad (2.26)$$

210 This non-zero Higgs vacuum now generates mass terms for the gauge bosons  
211 from the following term in the Lagrangian:

$$|(-\frac{1}{2}g_1B_\mu - \frac{1}{2}g_2\sigma^aW_\mu^a)\Phi|^2 = \frac{1}{2}m_W^2W_\mu^+W^{-\mu} + \frac{1}{2}m_Z^2Z_\mu Z^\mu \quad (2.27)$$

212 where:

$$W_\mu^\pm \equiv \frac{1}{\sqrt{2}}(W_\mu^1 \mp iW_\mu^2) \quad (2.28)$$

$$\begin{aligned} \text{213} \quad Z_\mu &\equiv \frac{1}{\sqrt{g_1^2 + g_2^2}}(g_2W_\mu^2 - g_1B_\mu) \end{aligned} \quad (2.29)$$

$$\begin{aligned} \text{214} \quad m_W &= \frac{vg_2}{\sqrt{2}} \end{aligned} \quad (2.30)$$

$$\begin{aligned} \text{215} \quad m_Z &= \frac{v}{\sqrt{2}}\sqrt{g_1^2 + g_2^2} \end{aligned} \quad (2.31)$$

216 The Higgs field also generates a mass term for the Higgs boson and self-  
217 interactions for the Higgs boson.

## 218 2.7 Electroweak Theory

219  $SU(2)_L$  generates  $W^\pm, W^0$  gauge bosons, which would be massless if  $SU(2)_L$   
220 was a perfect symmetry. These bosons are massive as this symmetry is broken.

221 The mass eigenstates,  $Z$  and  $\gamma$  given by:

$$\begin{pmatrix} Z_\mu \\ A_\mu \end{pmatrix} = \begin{pmatrix} \cos\theta_W & -\sin\theta_W \\ \sin\theta_W & \cos\theta_W \end{pmatrix} \begin{pmatrix} W_\mu^3 \\ B_\mu \end{pmatrix} \quad (2.32)$$

222 Here  $\theta_W$  is the Weinberg angle given by:

$$\cos\theta_W = \frac{g_2}{\sqrt{g_1^2 + g_2^2}} = \frac{m_W}{m_Z} \quad (2.33)$$

## <sup>223</sup> 2.8 Quantum ChromoDynamics

<sup>224</sup> As mentioned earlier the Strong Force, which binds the proton together, is  
<sup>225</sup> mediated by gluons. Quantum Chromodynamics is the QFT which describes the  
<sup>226</sup> interactions of quarks and gluons via  $SU(3)_C$  symmetry. QCD contains features  
<sup>227</sup> not present in Electroweak Interactions due to  $SU(3)_C$  generators not commuting  
<sup>228</sup> (a.k.a.  $SU(3)_C$  is a non-abelian group). For example, in QCD there is color  
<sup>229</sup> confinement and asymptotic freedom due to the structure constants being non-  
<sup>230</sup> zero. Requiring  $SU(3)_C$  local gauge invariance implies:

$$\psi(x) \rightarrow \psi(x)' = \exp[i g_S \alpha(x) \cdot \hat{T}] \psi(x) \quad (2.34)$$

<sup>231</sup> where  $\alpha(x)$  is the local phase function,  $g_S$  is the strong coupling constant, and  
<sup>232</sup>  $\hat{T}$  are the eight generators of  $SU(3)$  (note  $\hat{T}^a = \frac{1}{2}\lambda^a a$ , where  $\lambda^a$  are the Gell-Mann  
<sup>233</sup> matrices). As the Gell-Mann matrices are 3x3, this means  $\psi$  has three degrees of  
<sup>234</sup> freedom under these  $SU(3)$  rotations. So we represent  $\psi$  under  $SU(3)$  rotations  
<sup>235</sup> as:

$$\psi = \begin{pmatrix} \psi_{red} \\ \psi_{green} \\ \psi_{blue} \end{pmatrix} \quad (2.35)$$

<sup>236</sup> Consequently, particle fields transforming under  $SU(3)$  rotations have three  
<sup>237</sup> components which physicists describe as color components (red, green, and blue).  
<sup>238</sup> A particle's corresponding antiparticle has the corresponding anticolor. This color  
<sup>239</sup> is the "charge" of QCD and is conserved under  $SU(3)$  rotations. Combining colors,  
<sup>240</sup> color neutral states (e.g. red and antired, or red, green and blue) may be created.  
<sup>241</sup> For the Free Dirac Lagrangian to remain invariant under  $SU(3)$  transformations,  
<sup>242</sup> we must again postulate a boson field that modifies the derivative. The gluon

243 field tensor is given by ( $\alpha = 1, \dots, 8$ ):

$$G_{\mu\nu}^k = \partial^\mu G_\alpha^\nu - \partial^\nu G_\alpha^\mu - g_S f^{\alpha\beta\gamma} G_\beta^\mu G_\gamma^\nu \quad (2.36)$$

244 Here  $f^{\alpha\beta\gamma}$  are the structure constants of  $SU(3)$ . Combining all this gives the  
245 QCD Lagrangian:

$$\mathcal{L}_{QCD} = \bar{\psi}_q i\gamma^\mu (D_\mu)_{ij} \psi^{qj} - m \bar{\psi}^{qi} \psi_{qi} - \frac{1}{4} G_{\mu\nu}^\alpha G^{\alpha\mu\nu} \quad (2.37)$$

246 Here  $i$  are the color indices, and  $q$  are the quark flavors. It is important to  
247 note that quarks transform under the fundamental representation of  $SU(3)$ , while  
248 gluons transform under the adjoint representation. This means quarks carry a  
249 single color charge (red, green, blue, antired, antigreen, antiblue) and gluons carry  
250 a color and anticolor charge.

251 Figure 2.3 shows the three dominant QCD interactions. Since gluons carry  
252 color charge, they interact with one another. This does not occur in QED, as  
253 photons do not have electric charge and therefore do not interact with each other.  
254 In QED, a bare electron's effective charge is largest closest to the electron and  
255 decreases as a function of distance. This is because the QED vacuum fills with  
256 particle antiparticle pairs spontaneously, which screen the charge of the bare elec-  
257 tron. The larger the distance from the electron, the smaller the effective charge  
258 and therefore the weaker the force. So for a pair of electrons, as the distance  
259 between them increases the repulsive force decreases and they may be observed  
260 separately.

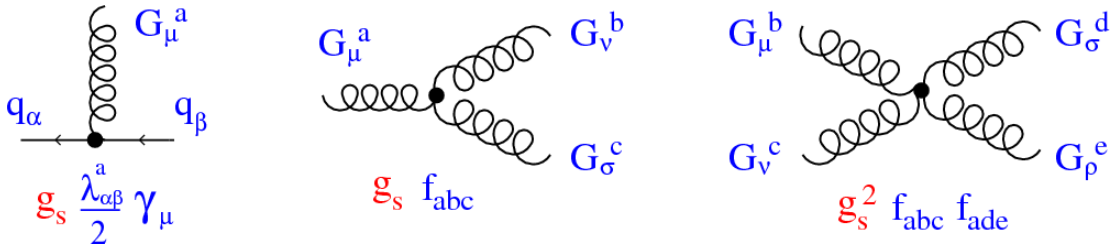


**Figure 2.3:** This figure shows the three dominant QCD interactions. From Ref. [17]

As the distance from a quark increases it's effective color charge increases due to the vacuum polarization in QCD. Color charge grows as the distance from the source increases (a.k.a. color is anti-screened in QCD). In this way, strong interactions become stronger at large distances (low momenta interactions). At small distances (large momenta interactions) strong interactions are significantly weaker and considered nearly free. This effect of referred to as asymptotic freedom. At large distances, a quark's effective charge is large and the strong force is more significant. This force becomes so strong that quarks form colorless bound states instead of remaining free particles. This effect is known as color confinement. This running of all SM fields is shown in Figure 2.4.

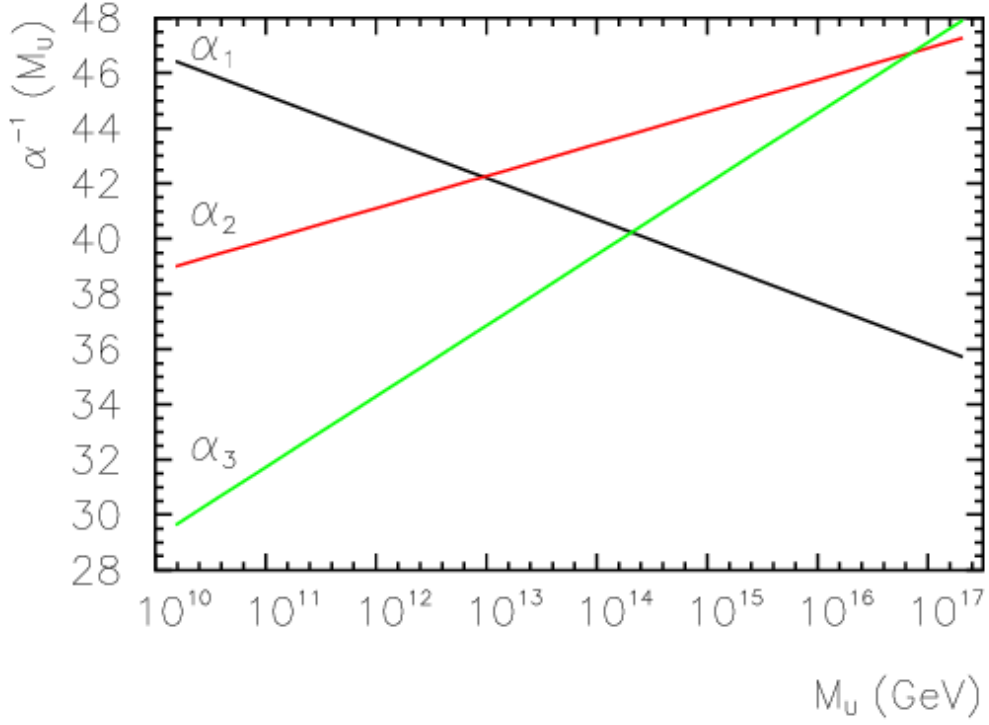


**Figure 2.4:** Strength of the U(1), SU(2), and SU(3) gauge couplings as a function of the energy scale of the interaction ( $Q$ ). From Ref. [11]

Commonly the change in a particle's effective charge under a given force is quantified with  $\beta(r) \equiv -\frac{de(r)}{d\ln r}$ , where  $e(r)$  is the effective charge of a given particle under a force. In QED this function is positive but in QCD this function is negative leading to confinement and asymptotic freedom. Moreover, one can calculate how the coupling ( $\alpha$ ) of a force varies with energies. (More deeply this amounts to incorporating renormalization and vacuum polarization in the boson propagators).

For QCD this is:

$$\alpha_S(x) = \frac{\alpha_S(\mu^2)}{1 + \beta_0 \alpha_S(\mu^2) \ln(Q^2/\mu^2)} \quad (2.38)$$

278

$$\beta_0 = \frac{11N_c - 2n_f}{12\pi} \quad (2.39)$$

279 where  $Q$  is the momentum of the the force is probed at,  $\mu^2$  is the renormalization scale.

281 As stated previously, quarks and gluons have not been observed in isolation.  
 282 Instead they form bound colorless states. Hadronization is the process by which  
 283 quarks and gluons form hadrons. The process of hadronization is still an active  
 284 area of research. One qualitative description is show in Figure [Natasha add  
 285 figure]. In this figure, as two quarks separate the color field between them is  
 286 restricted to a tube with energy density of 1GeV/fm. As they separate further,  
 287 the energy in the color field increases, until there is enough energy to produce  
 288  $q\bar{q}$  pairs, which breaks the color field. This process repeats until quarks and  
 289 antiquarks have low enough energy to form colorless hadrons. The resulting spray  
 290 of hadrons is called a jet.

291 Since quarks and gluons carry different color charges, their respective jets have  
 292 different properties. As quarks carry only a single color charge (vs. gluons which  
 293 have color and anticolor charge), so their jets have less constituent particles. More  
 294 precisely, the Altarelli-Parisi splitting functions [3] contain a factor  $C_A$  for gluon  
 295 radiation off a gluon and  $C_F$  for gluon radiation off a quark ( $C_A/C_F = 9/4$ ). These  
 296 color factors are the prefactor in the Feynman diagrams for these processes [1],  
 297 which leads to gluon jets having more constituents and therefore more tracks than  
 298 quark jets. Gluon jets also tend to have a larger radius with lower momentum  
 299 constituents than quarks. There are many novel techniques to distinguish quarks  
 300 from gluons. For this study the number of charged particles will be focused on.

301 **Chapter 3**

302 **Standard Model Successes and**  
303 **Limitations**

304 The Standard Model has consistently described much of reality to an extreme  
305 degree of accuracy. It has predicted cross sections for strong and electroweak pro-  
306 cesses that span over ten order of magnitude correctly [see Fig. 3.1] and contains  
307 no known logical inconsistencies. Despite the strength and reality of the Stan-  
308 dard Model, it still fails to describe aspects of reality and suffers from aesthetic  
309 issues. To date, dark matter and energy comprise 95% of the universe, but are  
310 not accounted for in the SM. Additionally, neutrinos are known to have mass but  
311 are massless in the SM. There are mechanisms for introducing massive neutrinos  
312 in the SM, but these mechanisms create hierarchy problems.

313 Possibly the most significant aesthetic issue is the hierarchy between the elec-  
314 troweak and Planck scales. The electroweak scale is the scale of electroweak  
315 symmetry breaking. The Planck scale is the scale where the gravitational force  
316 is comparable in strength to the other forces. The Planck scale is where the SM  
317 breaks down, as there is not an experimentally verified theory of quantum gravity,  
318 and at this scale gravity cannot be ignored (like it can at the electro-weak scale).

319 These scales differ by  $\sim 30$  orders of magnitude. Understanding the difference  
320 in these energy scales, may help explain the weakness of gravity at electroweak  
321 scales, and possibly a QFT for gravity. (NB: This hierarchy can also be framed in  
322 terms of the corrections to the Higgs mass, which depend on the UV cutoff scale -  
323 where the SM is suppose to break, which is taken at the Planck scale. This leads  
324 the quantum corrections to the Higgs mass to force the Higgs mass to  $10^{18}$  TeV.)

325 These stark contrasts in scales may indicate that a more fundamental theory  
326 exists. It is hoped that such a theory would explain and motivate some of the ad-  
327 hoc features of the SM. In particular, there currently are no experimentally verified  
328 explanations of why there are three generations of fermions, the values of the 19  
329 SM parameters (6 quark masses, 3 charged lepton masses, 3 gauge couplings,  
330 Higgs parameters  $(\mu^2, \lambda)$ ), the structure of the fermion representations, etc.

## Standard Model Production Cross Section Measurements

Status: July 2018

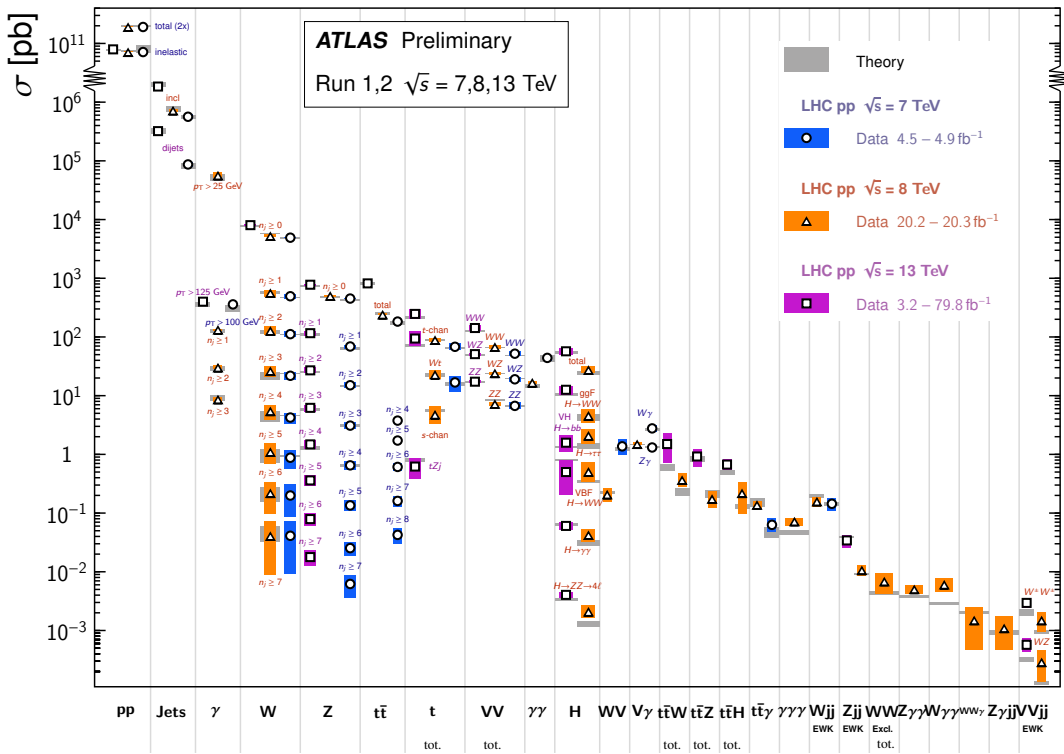


**Figure 3.1:** A comparison of cross section measurements at  $\sqrt{s} = 7,8,13$  TeV from ATLAS compared to theoretical measurements. From Ref. [5]

<sup>331</sup> **Chapter 4**

<sup>332</sup> **New Physics Models with**

<sup>333</sup> **Diboson Resonances**

<sup>334</sup> **4.1 Randall Sundrum Bulk Model**

<sup>335</sup>      The electroweak-planck hierarchy may be explained by the existence of extra  
<sup>336</sup> dimensions, like the 5D Randall Sundrum Bulk Model ([18], [2]). In this model,  
<sup>337</sup> there is one extra warped spatial dimension,  $y$ , with a metric:

$$ds^2 = e^{-2k|y|} \eta_{\mu\nu} dx^\mu dx^\nu + dy^2 \quad (4.1)$$

<sup>338</sup>      where  $e^{-k|y|}$  is the warp factor of the extra dimension, which is compactified on  
<sup>339</sup> a  $S^1/Z_2$  orbifold (a.k.a. a circle where  $y \rightarrow -y$ ). This can be visualized as every  
<sup>340</sup> point in space time having a line extending from it a distance  $L$ , representing  
<sup>341</sup> this fifth dimension. At the end of this line is the Planck brane. This fourth  
<sup>342</sup> spatial dimension separates two 4-D branes: Planck brane and TeV brane. We  
<sup>343</sup> live on the TeV brane, as shown in Figure 4.1. The Higgs field (and to a lesser  
<sup>344</sup> degree the top quark and graviton fields) is localized near the TeV Brane, while

345 the light fermion fields are localized more near the Planck brane. Fundamental  
 346 parameters are set on the Planck brane. The warp factor may be scaled away from  
 347 all dimensionless SM terms by field redefinitions. However, the only dimensionful  
 348 parameter,  $m_H^2 = v^2$  is rescaled by  $\tilde{v} \sim e^{-kL} M_{Pl} \sim 1\text{TeV}$  for  $kL \sim 35$ , explaining  
 349 why gravity is so weak on the TeV brane. Also, by localizing the light fermion  
 350 fields near the Planck brane and top and graviton fields near the TeV brane, the  
 351 light quarks will have smaller masses.

352 The two free parameters of this theory are  $M_{Pl}$  and  $k$ . Based on this RS Bulk  
 353 model, all SM particles should have Kaluza-Klein (KK) excitations. In particular,  
 354 the graviton would have KK excitations that prefer to decay to WW or ZZ, which  
 355 is why this analysis searches for RS Gravitons.

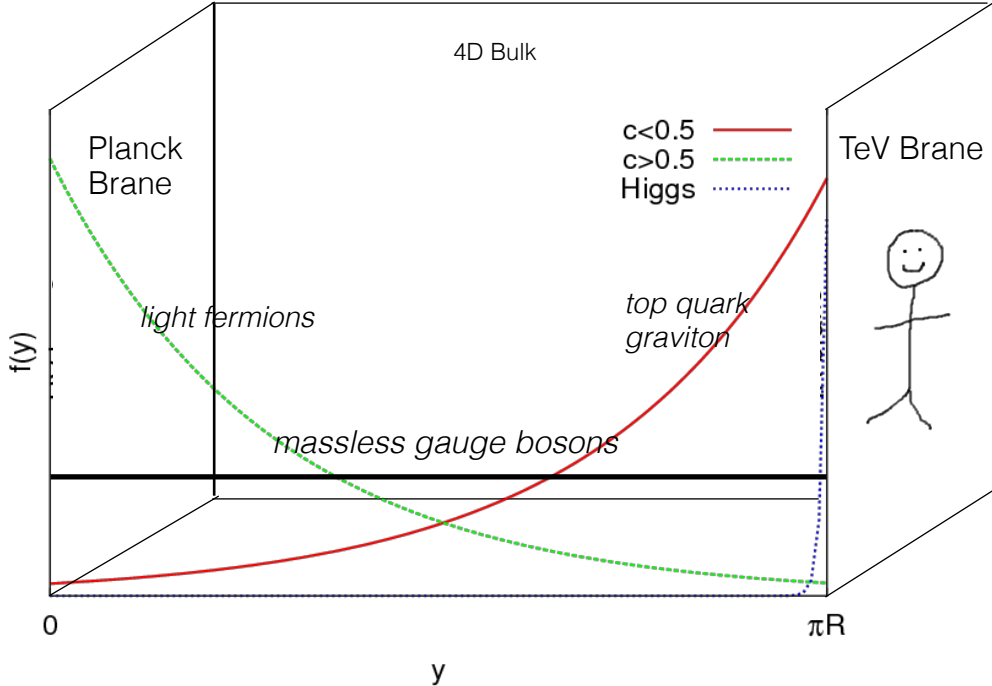


**Figure 4.1:** Cartoon of RS Bulk Model

## <sup>356</sup> 4.2 Extended Scalar Sector

<sup>357</sup> A further striking asymmetry of the SM is the simplicity of the scalar sector in  
<sup>358</sup> comparison to the boson and fermion sectors. To date, the scalar sector has only  
<sup>359</sup> one member, the Higgs boson. Therefore, it is natural to posit an extension to the  
<sup>360</sup> scalar sector. From a theoretical standpoint this could also help generate baryon  
<sup>361</sup> asymmetry through additional sources of CP violation. This analysis searches for  
<sup>362</sup> a simple extension to the scalar sector as proposed in Ref. [20]. The extended  
<sup>363</sup> scalar sector includes a real Higgs singlet ( $S$ ) and complex  $SU(2)_L$  doublet ( $\Phi$ )  
<sup>364</sup> (the SM Higgs), where mass eigenstates are mixtures of the fields.  $S$  has a vev of  
<sup>365</sup>  $v$  and  $\Phi$  has a vev of  $x$ . This then gives a Lagrangian of:

$$\mathcal{L} \supset (D^\mu \Phi)^\dagger D_\mu \Phi + \partial^\mu S \partial_\mu S - m^2 \Phi^\dagger \Phi - \mu^2 S^2 + \lambda_1 (\Phi^\dagger \Phi)^2 + \lambda_2 S^4 + \lambda_3 \Phi^\dagger \Phi S^2 \quad (4.2)$$

<sup>366</sup> The mass eigenstates of the scalar sector are then mixtures of  $S$  and  $\Phi$  and  
<sup>367</sup> the free parameters of the theory are  $m_H$ ,  $\sin \alpha$ , and  $\tan \beta = v/x$ . The fields are  
<sup>368</sup> then given by:

$$\Phi \equiv \begin{pmatrix} 0 \\ \frac{\tilde{h}+v}{\sqrt{2}} \end{pmatrix} \quad (4.3)$$

$$S \equiv \frac{h' + x}{\sqrt{2}} \quad (4.4)$$

<sup>370</sup> Diagonalizing the mass matrix leads to the mass eigenstates  $h$  (discovered  
<sup>371</sup> Higgs boson) and  $H$  (the physical particles):

$$\begin{pmatrix} h \\ H \end{pmatrix} = \begin{pmatrix} \cos \alpha & -\sin \alpha \\ \sin \alpha & \cos \alpha \end{pmatrix} \quad (4.5)$$

<sup>372</sup> This suppressed h and H production and SM H couplings:

$$BR_{H \rightarrow SM} = \sin^2 \alpha \times \frac{\Gamma_{SM, H \rightarrow SM}}{\Gamma_{tot}} \quad (4.6)$$

<sup>373</sup> Moreover, in the case that  $m_H > m_h$ ,  $H \rightarrow hh$  is possible. This further suppresses

<sup>374</sup>  $H \rightarrow VV/ff$ . This search is most sensitive to  $H \rightarrow WW$ .

### <sup>375</sup> 4.3 Simple Standard Model Extensions

<sup>376</sup> The RS Bulk model is motivated by resolving the hierarchy problem. Extending the Scalar sector is a natural space to look for new physics due to the complexity of fermion and boson groups. There are many other interesting and well motivated frameworks, but there is a lack of completely predictive models, due to model flexibility (free parameters). Therefore it is hard for experimentalists to know which theories to search for in data. However, as seen in [16], a "Simplified Model" approach may be taken. In the search for reasonably narrow width particles, as in this search, the search is not sensitive to all the details and free parameters of the theory. Generally such searches are only sensitive to the resonance mass and its interactions. Therefore, a theory's Lagrangian may be reduced to only retain this information (mass parameters and couplings). Experimental results using this framework may then be reinterpreted in a given theory.

<sup>388</sup> In the simplified approach, the new resonance searched for is represented as a real vector field in the adjoint representation of  $SU(2)_L$  with vanishing hypercharge. This results in one neutral and two charged bosons. Defined as:

$$V^\pm = \frac{V_\mu^1 \mp iV_\mu^2}{\sqrt{2}} \quad (4.7)$$

<sup>391</sup>

$$V_\mu^0 = V_\mu^3 \quad (4.8)$$

392 The SM Lagrangian is then augmented with the additional terms:

$$\mathcal{L} \supset -\frac{1}{4}D_{[\mu}V_{\nu]}^a D^{[\mu}V^{\nu]}{}^a + \frac{m_V^2}{2}V_\mu^a V^{a\mu} + ig_V c_H V_\mu^a H^\dagger \tau^a \overset{\leftrightarrow}{D}{}^\mu H + \frac{g^2}{g_V} c_F V_\mu^a J_F^{\mu a} \quad (4.9)$$

393 In order the terms represent: the kinetic,  $V$  mass, Higgs- $V$  interaction, and  
394  $V$ -left-handed fermion interaction terms. Phenomenologically the three physical  
395 particles this predicts are degenerate, where  $V$  couples most strongly to  $VV$ , via  
396 the  $g_V$  coupling factor. The dominant production modes are DY and VBF.

397 Two versions of HVT are considered, Model A and B. Model A is a weakly  
398 coupled model where  $g_V \sim 1$ , like the extended gauge symmetry discussed in Ref  
399 . [16]. Model B is a strongly coupled model, where  $1 < g_V < 4\pi$ . The width  
400 of the resonance grows with  $g_V$  so for this narrow resonance search only  $g_V$  is  
401 chosen to be less than 6 (so  $\Gamma/M < 10\%$ ). More precisely, the coupling of these  
402 resonances to fermions scales as  $g_f = g^2 c_F/g_V$ , where  $g$  is the SM  $SU(2)_L$  gauge  
403 coupling and  $c_F$  is the free parameter (expected to be of order 1 for Model A and  
404 B). This then means that for Model B the coupling to fermions is more suppressed  
405 than for Model A, leading to a smaller DY production rate and BR to fermionic  
406 final states. The coupling of  $V$  to SM bosons scales as  $g_H = g_V c_H$ , where  $c_H$  is  
407 a free parameter on the order of 1 for Model A and B. So for small values of  $g_V$   
408 (i.e. Model A - weakly coupled theories) the BR to gauge bosons is smaller than  
409 for Model B. So weakly coupled vectors have large production cross sections and  
410 decay prominently to leptons or jets, while strongly coupled vectors are produced  
411 less and decay predominantly to gauge bosons.

412 Vectors in Model A and B are generally produced via quark-anti-quark annihi-  
413 lation. The more rare production via vector-boson-fusion is considered by setting  
414  $g_H = 1$  and  $g_F = 0$ . In Model B diboson final states are enhanced as stated  
415 previously due to  $g_H$  and moreover the BR to  $WZ$ ,  $WH$ ,  $WW$ , and  $ZH$  are the

<sup>416</sup> same.

<sup>417</sup> In summary,  $V$  couples most strongly to left-handed fermions and  $VV$  dependent on  $g_V$ .

419

## Part III

420

## Experimental Setup

421 **Chapter 5**

422 **LHC**

423 The Large Hadron Collider (LHC) is the highest-energy particle collider in the  
424 world. It was designed to expand the frontier of high energy particle collisions in  
425 energy and luminosity. This enables LHC experiments to test the Standard Model  
426 and search for new physics at higher energies than tested with previous colliders.  
427 Collisions at higher energies not only produce more massive particles but also  
428 more weakly interacting particles. Fig. 5.1 shows production cross sections for  
429 various processes at hadron colliders. The rate for electroweak physics processes  
430 including  $W$  and  $Z$  scale with the center-of-momentum energy,  $\sqrt{s}$ .

431 The LHC consists of a 26.7 km (17 miles) ring, approximately 100 m un-  
432 derground, outside Geneva, Switzerland. Counter-circulating proton (and occa-  
433 sionally heavy ions) beams collide inside four experiments along the beam line:  
434 ATLAS, CMS, LHCb, ALICE. ATLAS and CMS are general purpose detectors de-  
435 signed to explore the high energy frontier. LHCb is designed to study the physics  
436 of  $b$ -quarks. ALICE specializes in studying heavy ion collisions.

## proton - (anti)proton cross sections

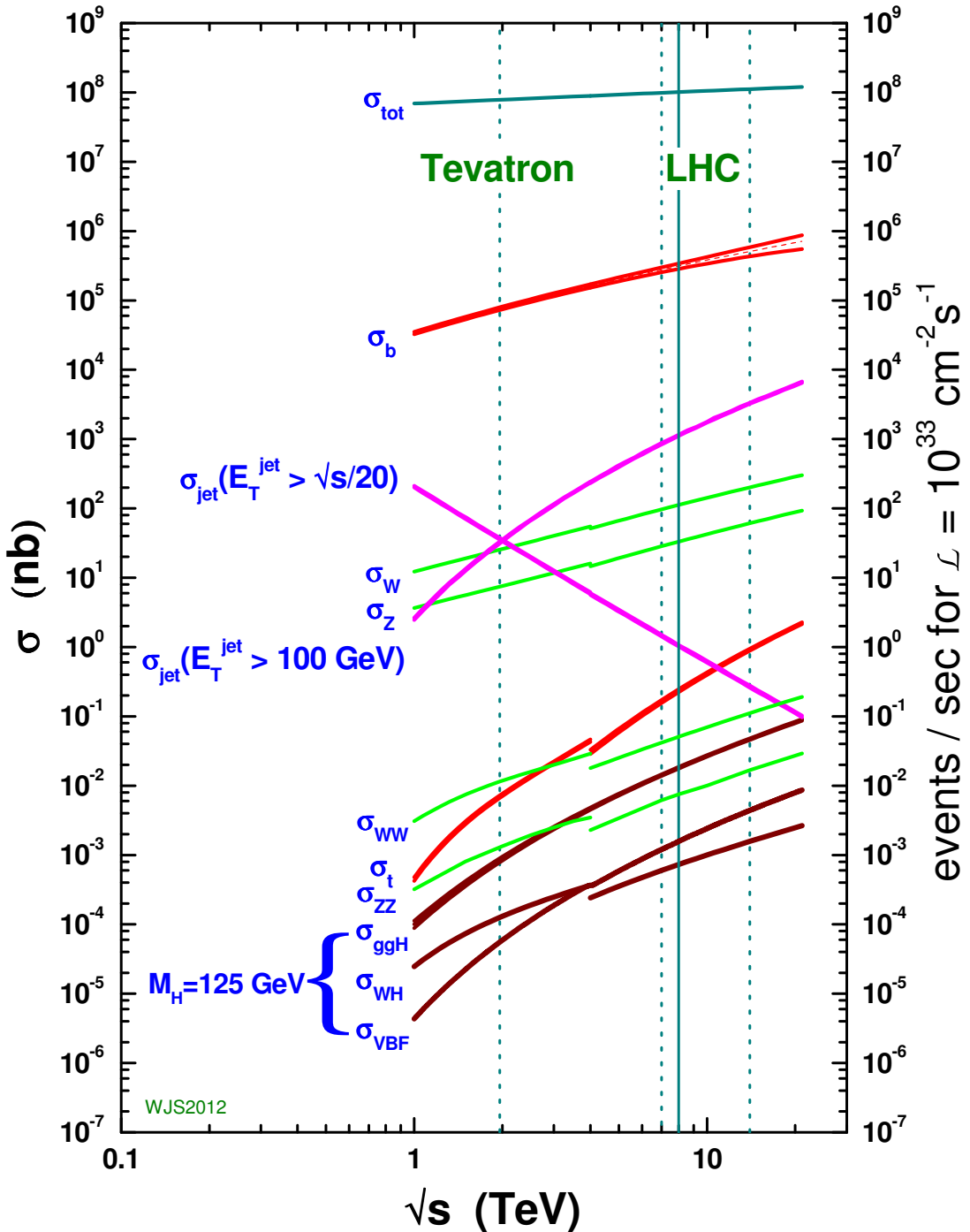


Figure 5.1: Scaling of cross sections with  $\sqrt{s}$ . Natasha: write more here

437        The first proton beams circulated in September, 2008. Nine days later an elec-  
438        trical fault lead to mechanical damage and liquid helium leaks in the collider. This  
439        incident delayed further operation until November 2009, when the LHC became  
440        the world's highest energy particle collider, at 1.18TeV per beam. This first oper-  
441        ational run continued until 2013, reaching 7 and 8 TeV collision energies. During  
442        this run a particle with properties consistent with the Standard Model Higgs bo-  
443        son was discovered. The next run began after a two year shutdown after upgrades  
444        to the LHC and experiments. This run lasted from 2013 to 2018 reaching 13 TeV  
445        collision energies. This analysis uses data from the second operational run.

## 446        5.1 LHC Layout and Design

447        The layout of the LHC is shown in Figure 5.2. The red and blue lines in the  
448        figure represent the counter-circulating proton beams. The LHC is divided into  
449        eight octants. Octant 4 contains the RF cavities that accelerate the protons and  
450        octant 6 contains the beam dump system. Octants 3 and 7 house the collimation  
451        systems for beam cleaning. The beams collide inside the four aforementioned  
452        experiments. Each octant contains a curved and straight section. The LHC  
453        magnets are built with NbTi superconductors cooled with super-fluid Helium to  
454        2K, creating a 8.3T magnetic field to bend the proton beams.

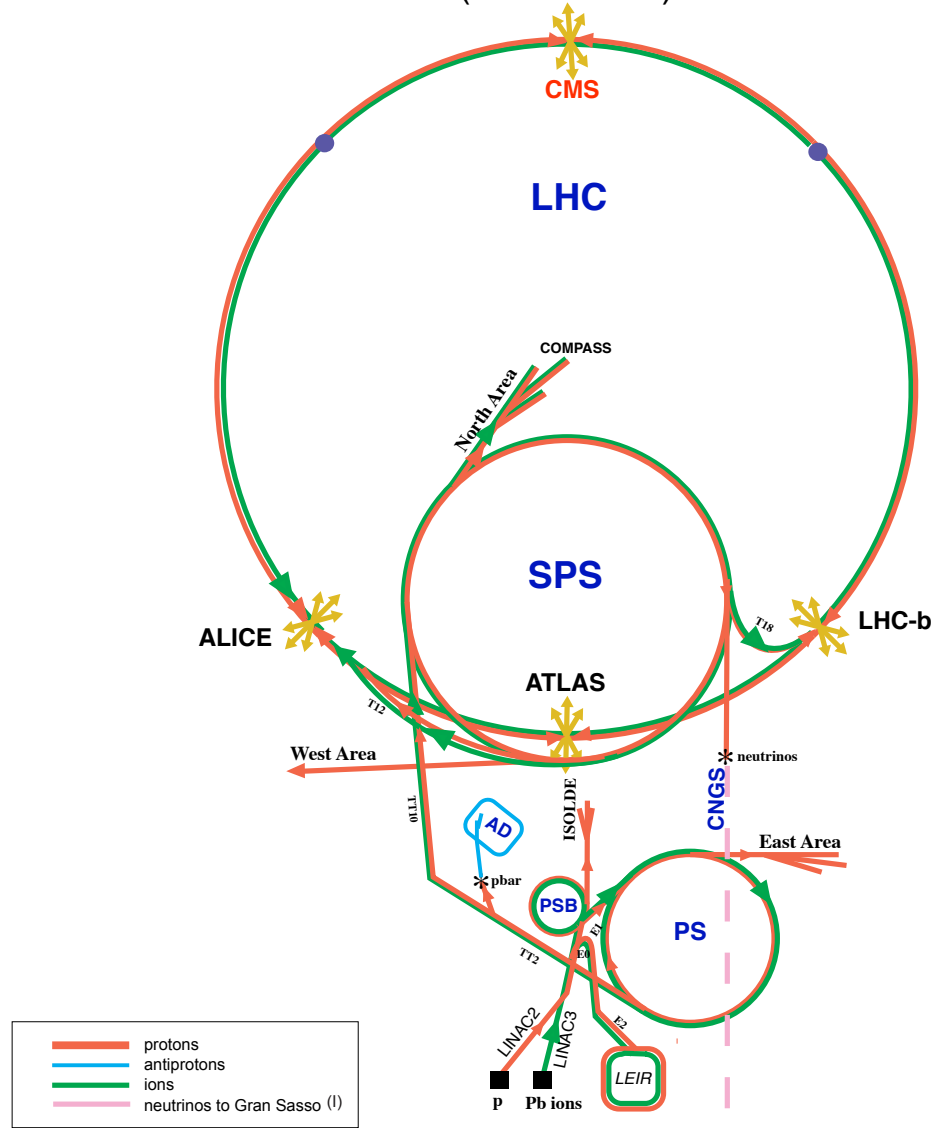


**Figure 5.2:** LHC Layout. Natasha write more

455        Four sequential particle accelerators are used to accelerate protons from rest  
 456        as shown in Figure 5.3. First, Hydrogen gas is ionized to produce protons which  
 457        are then accelerated to 50 MeV using Linac 2, a linear accelerator. The result-  
 458        ing proton beam is then passed to three circular particle accelerators: Proton  
 459        Synchrotron Booster, Proton Synchrotron, and Super Proton Synchrotron (SPS),

460 accelerating protons to 1.4, 25, and 450 GeV, respectively. Once the protons exit  
461 the SPS, they are injected into the LHC at octant 2 and 8. Each proton bunch  
462 contains  $\sim 10^{11}$  protons. The spacing between bunches is 25 ns, which means  
463 each beam contains 3564 bunches. However, some bunches are left empty due  
464 to injection and safety requirements, yielding 2808 bunches per beam. Once the  
465 proton beams are injected they are accelerated to 13 TeV.

## CERN Accelerators (not to scale)



LHC: Large Hadron Collider

SPS: Super Proton Synchrotron

AD: Antiproton Decelerator

ISOLDE: Isotope Separator OnLine DEvice

PSB: Proton Synchrotron Booster

PS: Proton Synchrotron

LINAC: LINear ACcelerator

LEIR: Low Energy Ion Ring

CNGS: Cern Neutrinos to Gran Sasso

Rudolf LEY, PS Division, CERN, 02.09.96  
Revised and adapted by Antonella Del Rosso, ETT Div.,  
in collaboration with B. Desforges, SL Div., and  
D. Manglunki, PS Div. CERN, 23.05.01

**Figure 5.3:** LHC Accelerator. Natasha write more

466 As many new physics models predict cross-sections below the weak scale it was  
467 important to design the LHC to be capable of collecting enough data, by running  
468 in high luminosity conditions. The machine luminosity depends only on beam  
469 parameters:

$$L = \frac{N_p^2 f}{4\epsilon\beta^*} F \quad (5.1)$$

470 where  $N_p$  is the number of protons per bunch,  $f$  is the bunch crossing frequency,  
471  $\epsilon$  is the transverse beam emittance,  $\beta^*$  is the amplitude function at the collision  
472 point, and  $F$  is the geometric luminosity reduction factor due to the beams crossing  
473 at an angle (rather than head-on).

474 **Chapter 6**

475 **The ATLAS Detector**

476 The ATLAS detector measures the position, momentum and energy of parti-  
477 cles produced in the proton collisions by using magnetic fields, silicon detectors,  
478 sampling calorimeters, and gaseous wire detectors. It is located approximately  
479 100 m underground at Point-1 around the LHC beam line and weighs 7000 metric  
480 tons. The detector is 46 m long, 25 m high, 25 m wide as shown in Figure 6.2.  
481 The detector can be divided into three subsystems: the Inner Detector (ID), the  
482 Calorimeters, and the Muon Spectrometer (MS). Figure 6.3 shows an overview of  
483 how different particles interact in the detector.

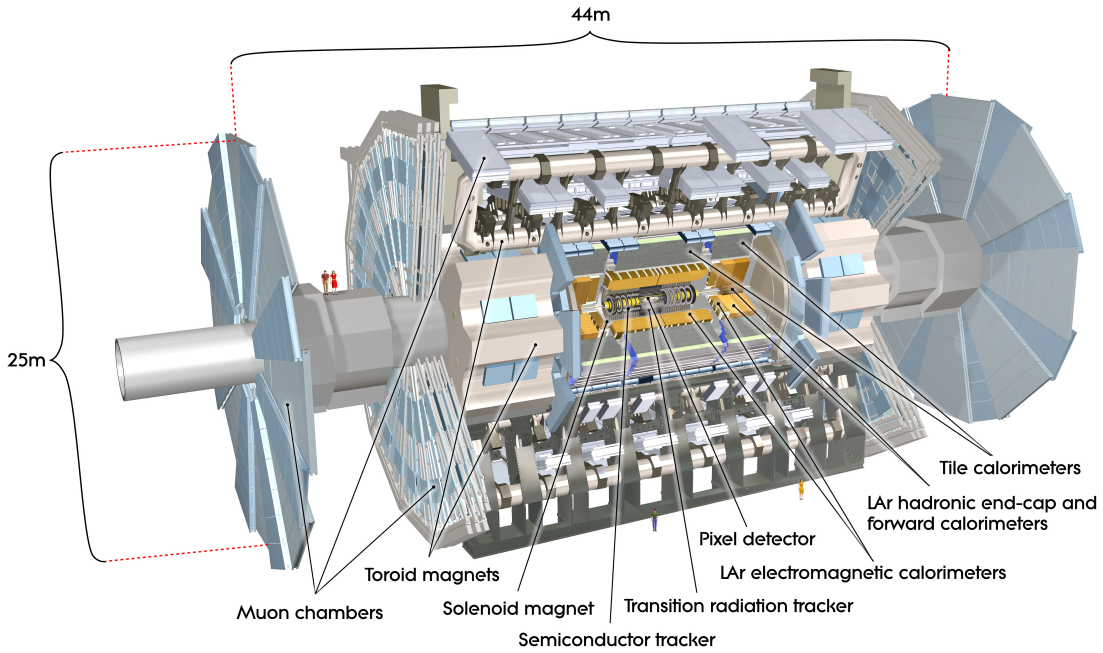


**Figure 6.1:** Big picture layout of ATLAS detector. Natasha: write more

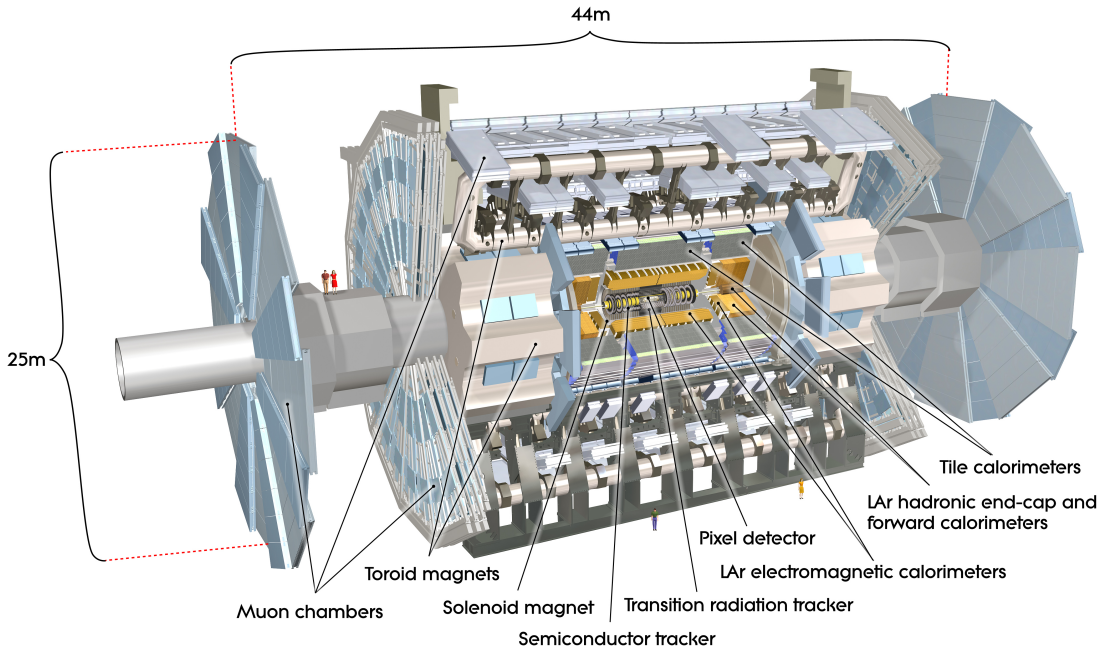


**Figure 6.2:** Big picture layout of ATLAS detector. Natasha: write more

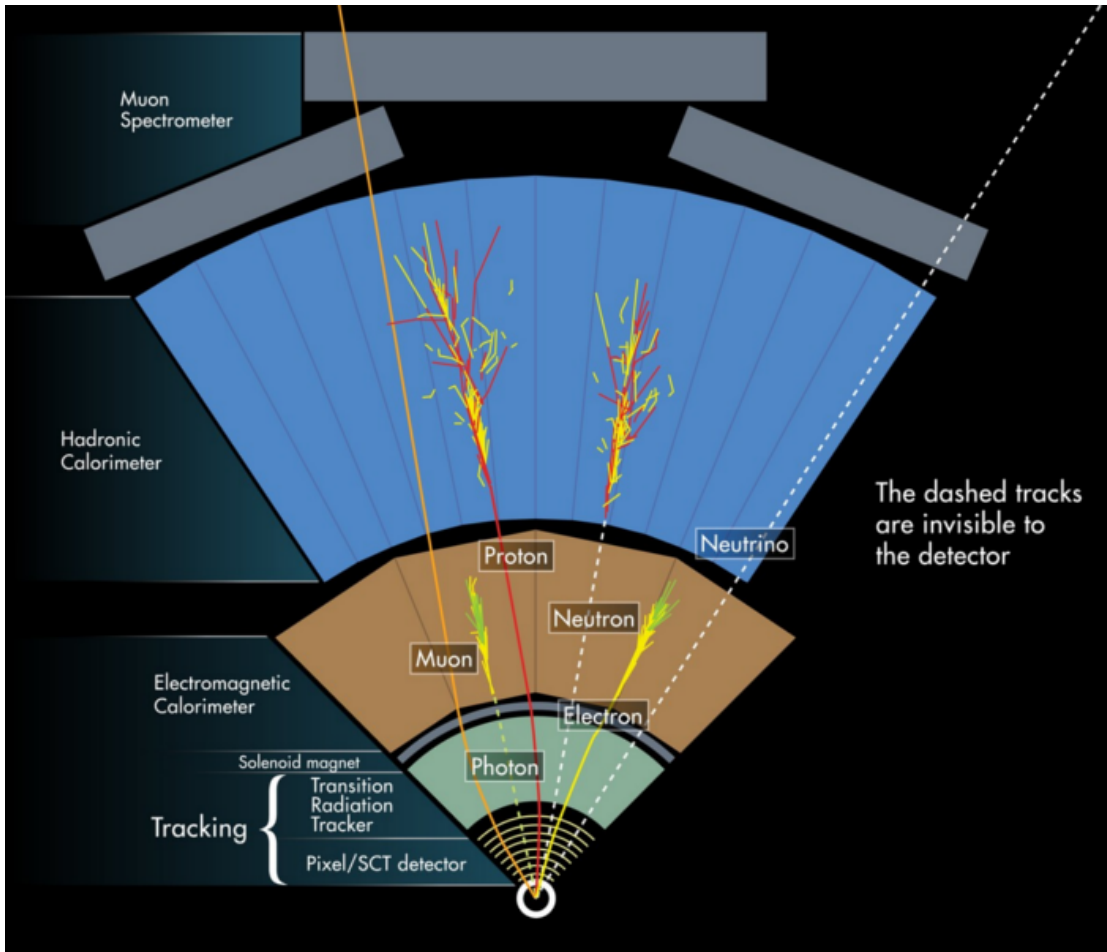


**Figure 6.3:** A simplified schematic of how different particles interact and are detected within ATLAS.

## 484 6.1 Coordinate System

485     The trajectory of particles within ATLAS is measured relative to the nominal  
 486 interaction point. The  $z$ -axis points along the beam line, such that when the  
 487 LHC is viewed from above, the counter-clockwise circulating beam points along  
 488 the positive- $z$  direction. The  $x - y$  plane is transverse to the beam line, with the  
 489 positive  $x$ -axis pointing towards the center of the LHC ring. The positive  $y$ -axis  
 490 points vertically upward. The azimuthal angle,  $\phi$ , is the angular distance about

491 the  $z$ -axis, with  $\phi = 0$  along the  $x$ -axis. The polar angle from the  $z$ -axis is denoted  
492 as  $\theta$ . However, this quantity is not Lorentz invariant, like rapidity,  $y = \frac{1}{2} \ln \frac{E+p_z}{E-p_z}$ ,  
493 where  $E$  is the energy of the particle considered, and  $p_z$ , is it's momentum along  
494 the  $z$ -axis. Pseudo-rapidity is preferred as  $\Delta\eta$  is invariant under boosts along  $z$   
495 and particle production is approximately invariant under  $\eta$ . For massless particles,  
496 rapidity and a related quantity, pseudorapidity, are the identical. The pseudora-  
497 pidity is defined as:  $\eta = -\ln \tan(\frac{\theta}{2})$ . This quantity is preferred as it is purely a  
498 geometric quantity, independent of particle energy. Angular separation between  
499 particles in ATLAS are given by  $\Delta R = \sqrt{\Delta\eta^2 + \Delta\phi^2}$ . The distance from the  
500 beamline is given by  $r = \sqrt{x^2 + y^2}$

## 501 6.2 Inner Detector

502 The Inner Detector (ID) was designed to identify and reconstruct vertices,  
503 distinguish pions from electrons, and measure the momentum of charged particles.  
504 The ID uses three different technologies for particle reconstruction: the Pixel  
505 Detector, Semiconductor Tracker (SCT), and the Transition Radiation Tracker  
506 (TRT), shown in Figure 6.4 and 6.5. The entire ID is immersed in a 2T solenoidal  
507 magnetic field parallel to the  $+z$ -axis, causing charged particles to bend in the  
508 transverse-plane, allowing particle momentum measurements.

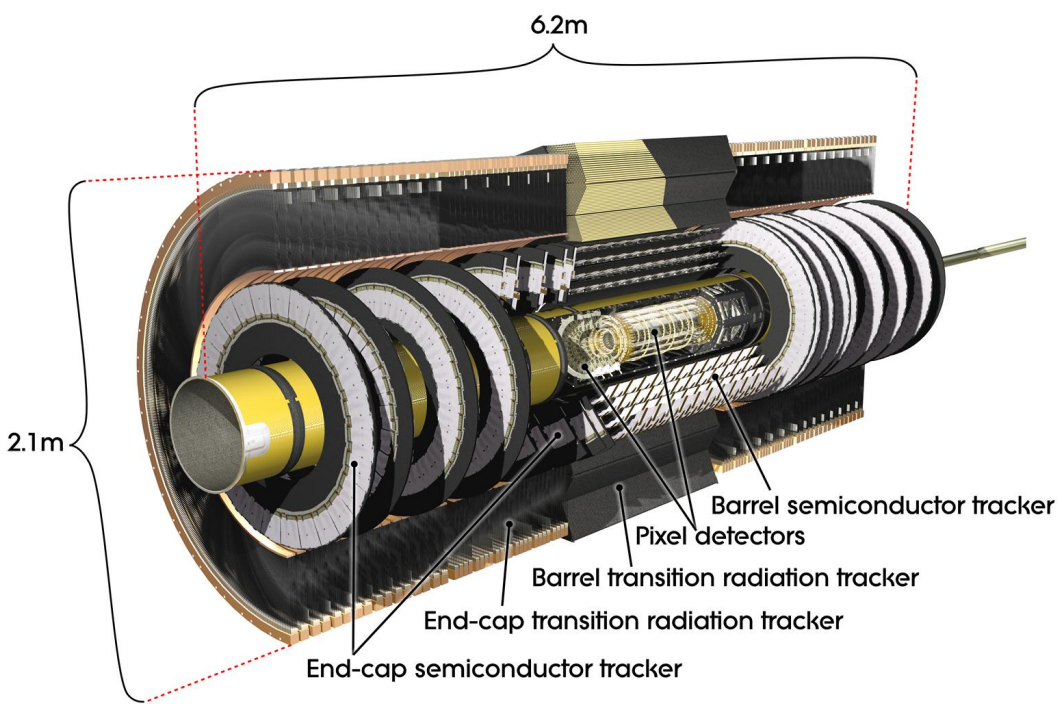


**Figure 6.4:** Layout of ATLAS Inner Detector

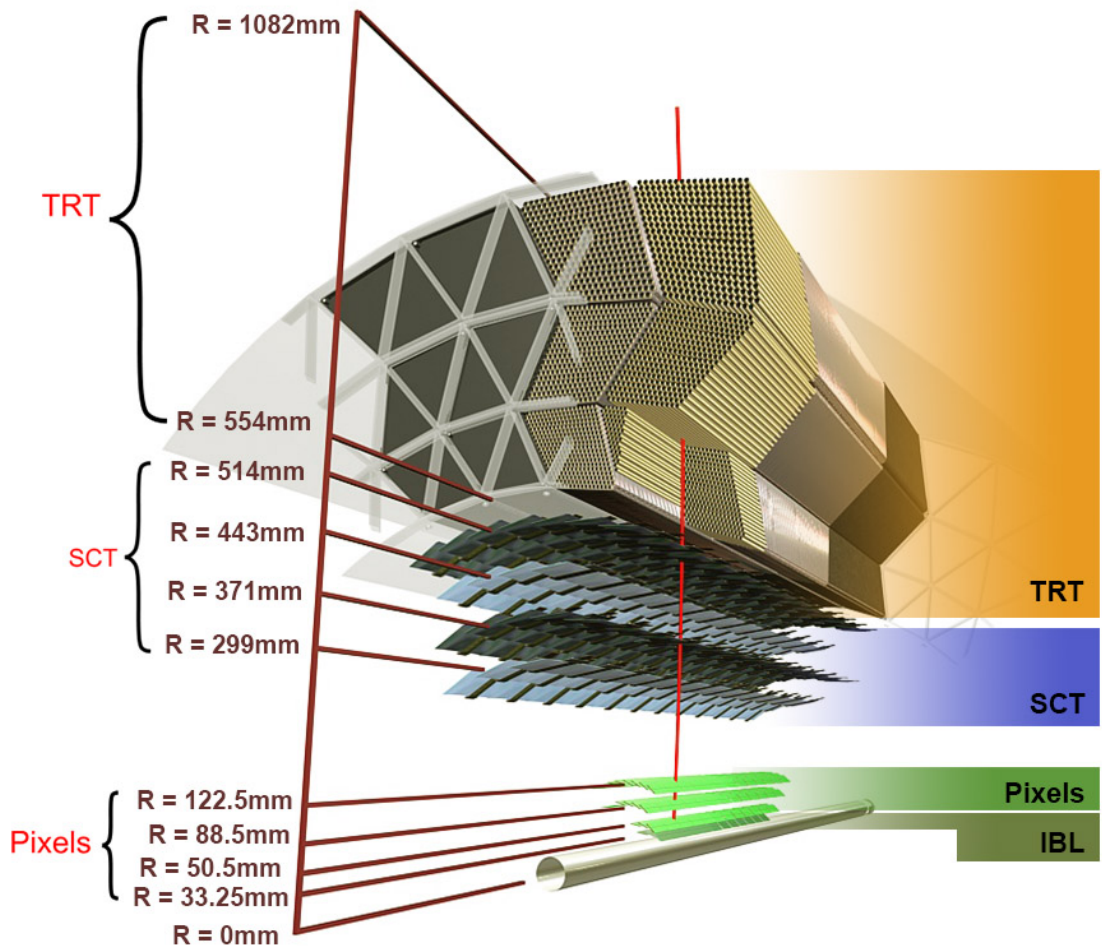


Figure 6.5: Layout of ATLAS ID Barrel System.

509 **6.2.1 Pixel Detector**

510 The pixel detector consists of four barrel layers between  $r = 32.7$  and  $122.5$   
511 mm, extending to  $|z| = 400.5$  mm. The remaining detectors are arranged in bar-  
512 rels and forward and backward rings. The innermost pixel barrel, the Insertable  
513 b-Layer (IBL), only extends to  $|z| = 332$  mm. The pixel detectors closer to the  
514 beam line (larger  $\eta$  values) consists of six parallel cylindrical rings of pixel de-  
515 tectors transverse to the beam line. The entire pixel detector consists of 1744  
516 identical pixel sensors each with 46080 readout channels, totaling about 80 mil-  
517 lion individual pixels. Most of the pixel sensors are  $50 \times 400 \mu\text{m}^2$ . Each pixel has  
518 a position resolution of  $14 \mu\text{m}$  in  $\phi$  and  $115 \mu\text{m}$  in the  $z$  direction.

519 **6.2.2 Semiconductor Tracker**

520 The SCT is located outside the pixel detector and has the same barrel and  
521 endcap geometry as the pixel detector. SCT sensors are  $80 \mu\text{m} \times 12$  cm with  
522 a  $80 \mu\text{m}$  strip pitch. In the barrel the strips are parallel to the  $z$ -axis and are  
523 segmented in  $\phi$ . In the endcaps, the strips extend radially. Sensors are grouped in  
524 modules containing two layers of strips rotated 40 mrad with respect to each other.  
525 This offset allows for the two-dimensional position of a track to be determined by  
526 identifying the crossing point of the strips that registered a hit. SCT modules  
527 measure tracks with an accuracy of  $17 \mu\text{m}$  in  $r - \phi$  and  $580 \mu\text{m}$  in  $z(r)$  in the  
528 barrel (end-cap) region.

529 **6.2.3 Transition Radiation Tracker**

530 The transition radiation tracker (TRT), enveloping the SCT, is a gaseous  
531 straw-tube tracker mainly used for electron/pion track separation. Each straw  
532 is 4 mm in diameter and filled with a Xe- $\text{CO}_2$ - $\text{O}_2$  gas mixture. An anode wire at

533 the center of the straw is held at ground potential, while the walls of the straw  
534 are kept at -1.4kV. When a charged particle passing through the TRT ionizes the  
535 gaseous mixture, the resulting ions form an avalanche on the anode wire with a  
536 gain of  $\sim 10^4$ . The signal from the anode wire is then digitized and discriminated.  
537 Signals passing a low threshold cutoff are used to distinguish noise from tracks.  
538 Signals passing a high threshold cutoff are sensitive to transition radiation (TR).  
539 TR photons are emitted when charged particles pass between materials with dif-  
540 ferent dielectric constants. The probability that a charged particle with energy  $E$   
541 and mass  $m$  passing between two materials emits a TR photon in the keV range  
542 is proportional to  $\gamma = E/m$ . In the TRT straws these often then convert via the  
543 photoelectric effect, causing a large avalanche triggering the high-threshold. Since  
544 electrons have a smaller mass than pions, electron tracks are more likely to trig-  
545 ger the high threshold. This then provides discrimination between electrons and  
546 charged hadrons.

547 The barrel region of the TRT extends from  $r = 563\text{-}1066$  mm and  $|z| < 712$   
548 mm. Barrel Straws are 144 cm long (divided  $\sim \eta \approx 0$ ) and orientated parallel to  
549 the beam direction. End-cap straws extend radially and are 37 cm long. There  
550 are 53,544 straws in the barrel and 160,000 straws in the end-caps. Radiator mats  
551 of polypropylene/polyethylene fibers in the barrel are aligned perpendicular to the  
552 barrel straws (with holes for the straws to pass through). In the end-cap region,  
553 radiator foils are layered between the radial TRT straws.

554 The arrival time of the signal pulse is sensitive to the distance between the  
555 charged particle track and the anode wire and allows for a hit resolution of  $130\mu\text{m}$ .  
556 The TRT extends to  $|\eta| = 2.0$  and provides about 36 hits per track.

## 557 6.3 Calorimeters

558 The ATLAS electromagnetic and hadronic calorimeters (EMC and HCAL,  
559 respectively) absorb and measure the energy of high energy hadrons, photons,  
560 and electrons with  $|\eta| < 4.9$ . Both systems use sampling calorimeters which  
561 consist of alternating layers of dense absorbing and active layers. In the absorbing  
562 layer particles interact and lose energy, creating showers. These showers are then  
563 detected and measured in the active layer. The amount of charge measured in the  
564 active material scales with the energy of the incident particle, and thus provides a  
565 measurement of the particle's energy. An overview of the layout of the calorimeter  
566 system is shown in Figure 6.6.

567 The EMC measures and contains the energy of electromagnetically interacting  
568 particles. It consists of layered accordion-shaped Lead absorber plates and elec-  
569 trodes immersed in liquid Argon with 170k channels.. Using accordion-shaped  
570 electrode and absorbers ensures  $\phi$  symmetry and coverage. The EMC is com-  
571 posed of a barrel part ( $|\eta| < 1.475$ ), two end-caps ( $1.375 < |\eta| < 3.2$ ), and a  
572 presampler ( $|\eta| < 1.8$ ). The presampler, containing only liquid Argon, corrects  
573 for upstream energy losses of electrons and photons. The EMC barrel is segmented  
574 into three layers. The first layer has finest segmentation with readout cells ex-  
575 tending  $\Delta\eta \times \Delta\phi = 0.025/8 \times 0.1$ . This provides a precise shower measurements  
576 used to separate prompt photons from  $\pi^0 \rightarrow \gamma\gamma$  decays. The second layer has  
577 coarser segmentation and is approximately 16 radiation lengths long. A radiation  
578 length is the average distance an electron travels before losing all but  $1/e$  of its  
579 energy to bremsstrahlung. The last layer is the most coarse and measures the tail  
580 of the electromagnetic shower. A schematic of the ECAL is shown in Figure 6.7.

581 The hadronic calorimeter located outside the EMC and is used to contain  
582 and measure the energy of hadronically interacting particles. It consists of a tile

583 calorimeter (TileCal), hadronic end-cap calorimeter (HEC), and liquid Argon for-  
 584 ward calorimeter (FCAL). TileCal is located behind the LAr EMC and uses steel  
 585 absorbers and liquid Argon as the active material. TileCal consists of three barrel  
 586 layers in the central and forward regions, extending up to  $|\eta| < 1.7$ . Photons  
 587 generated from hadronic interactions are collected via wavelength-shifting fibers  
 588 connected to photomultiplier tubes, as shown in Figure 6.8. The HEC lies behind  
 589 the EMC endcap wheels. It uses copper absorbers and liquid Argon as the active  
 590 material and covers  $1.5 < |\eta| < 3.2$ . Finally, the FCAL covers  $3.1 < |\eta| < 4.9$   
 591 and consists of three modules all using liquid Argon as the active material. The  
 592 first module uses copper absorber and was designed for electromagnetic measure-  
 593 ments. The second and third modules consist of tungsten absorber and are used  
 594 to measure the kinematics of hadronically interacting particles. A schematic of  
 595 the HCAL is shown in Figure 6.8.

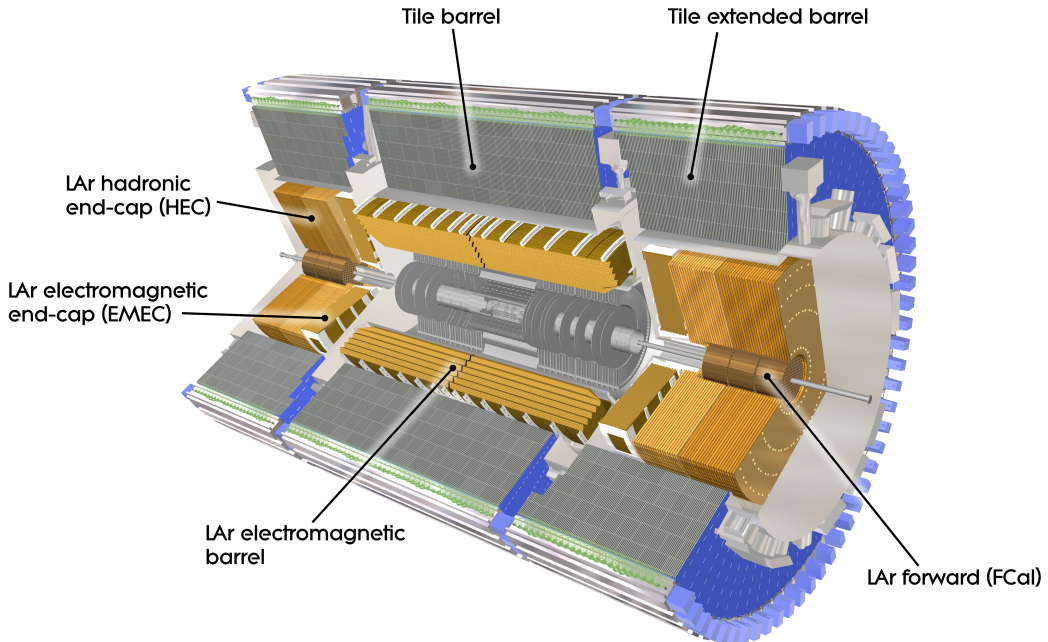


**Figure 6.6:** Overview of ATLAS electromagnetic and hadronic calorimeters.

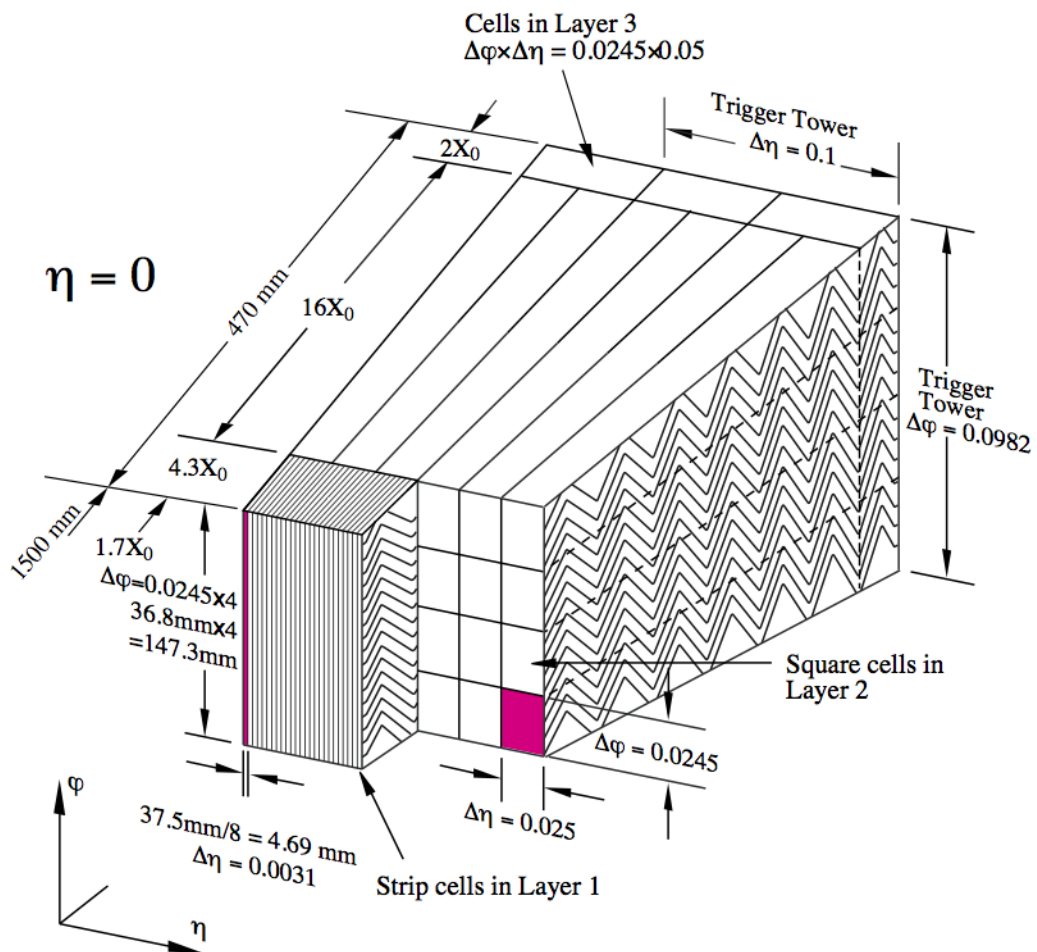


Figure 6.7: Schematic of ECAL.

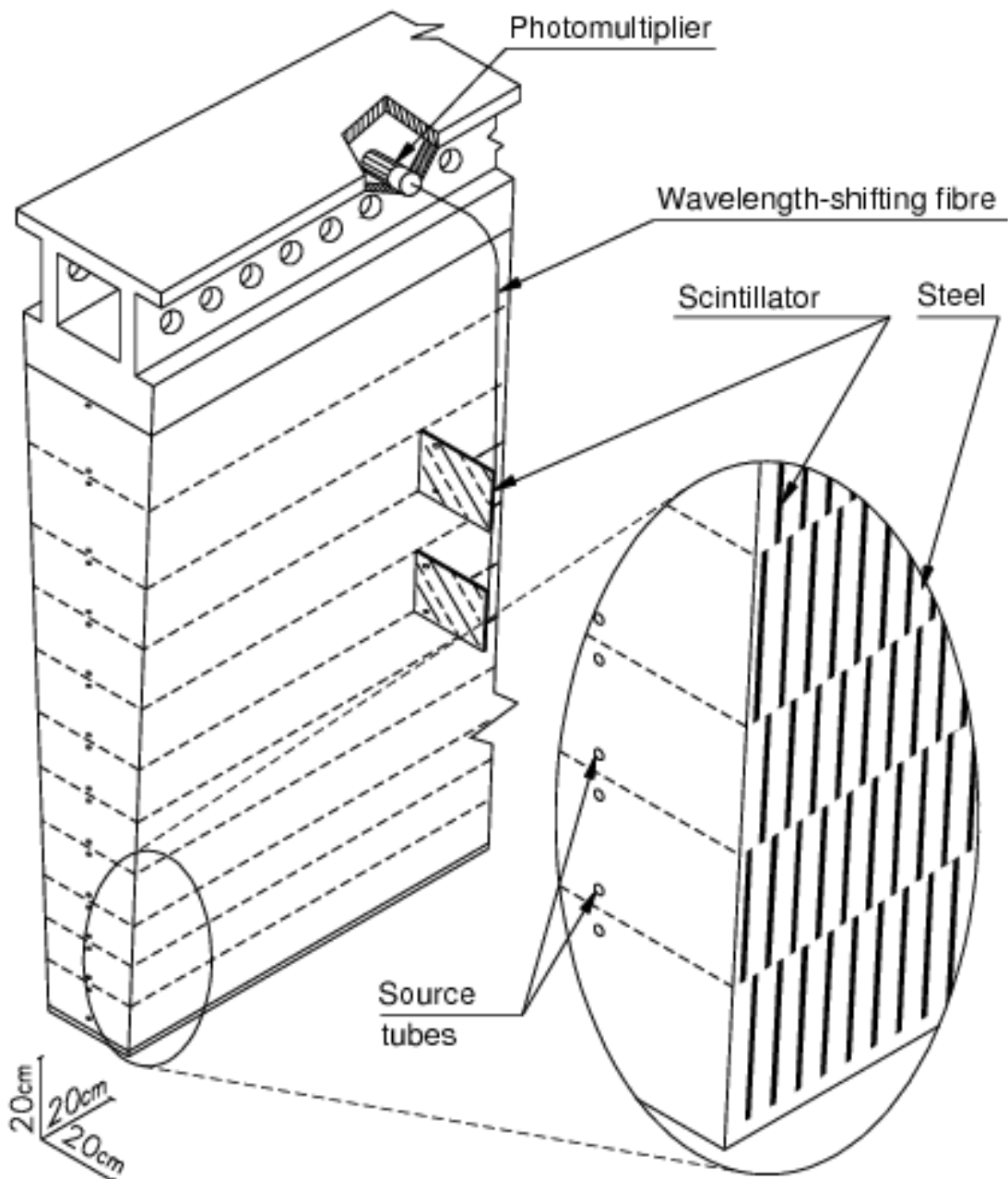


Figure 6.8: Schematic of HCAL.

596        The energy resolution of the calorimeter subsystems are:

$$597 \quad \frac{\sigma_E}{E} = \frac{10\%}{\sqrt{E}} \oplus 0.7\% \text{ EMC}$$

$$598 \quad \frac{\sigma_E}{E} = \frac{50\%}{\sqrt{E}} \oplus 3\% \text{ hadronic barrel}$$

$$599 \quad \frac{\sigma_E}{E} = \frac{100\%}{\sqrt{E}} \oplus 10\% \text{ hadronic end-cap}$$

600 **6.4 Muon Spectrometer**

601        The muon spectrometer (MS) is the outermost detector system in ATLAS.

602        Muons with a  $p_T > 4$  GeV are energetic enough to reach the MS. To measure the  
603        momentum of these muons barrel and end-cap toroid magnets are used covering  
604         $|\eta| < 1.4$  and  $1.6 < |\eta| < 2.7$ . For  $1.4 < |\eta| < 1.6$ , a combination of the barrel  
605        and end-cap toroidal magnetic fields bend muon trajectories. The detector in the  
606        barrel region form three concentric rings at  $R = 5, 7.5, 10$ m and are segmented  
607        in  $\phi$  to accommodate the magnets. The end-cap region consists of three circular  
608        planes perpendicular to  $z$  and located at  $|z| = 7.4, 14, 21.5$ m from the interaction  
609        region. An additional detector at  $|z| = 10.8$ m covers the transition region between  
610        the barrel and end-cap.

611        The MS readout consists of four subsystems: Monitored Drift Tubes (MDT),  
612        Cathode Strip Chambers (CSC), Resistive Plate Chambers (RPC), and Thin Gap  
613        Chambers (TGC). The first two subsystems are used primarily for measuring  
614        muon track parameters, while the RPC and TGC subsystems are used for muon  
615        triggering. A schematic of this system is shown in Figure 6.9.

616        The MDT subsystem consists of precision tracking chambers for  $|\eta| < 2.7$ ,  
617        except for the inner most end-cap layer ( $2.0 < |\eta| < 2.7$ ), where CSCs are used.  
618        The basic unit of MDT chambers are thin walled Aluminum tubes with a diameter  
619        of 3 cm and length of 0.9-6.2 m. These tubes are filled with a mixture of Ar-CO<sub>2</sub>  
620        gas with a 50μm W-Rn wire running down the center of the tube, which is kept at

621 3080 V. Since the maximum drift time of these chambers is  $\sim 700$  ns, they are not  
622 used for triggering. MDT chambers consist of 3-4 layers of tubes mounted on a  
623 rectangular support system, as seen in Figure 6.10, orientated along  $\phi$  to measure  
624 the coordinate in the bending plane of the magnetic field with a resolution of 35  
625  $\mu\text{m}$ .

626 The MDT subsystem can only handle hit rates below  $150\text{Hz}/\text{cm}^2$ . For this  
627 reason, CSCs are used in the innermost end-cap layer where hit rates are larger.  
628 CSCs can handle hit rates up to  $1000\text{Hz}/\text{cm}^2$ . CSC are multiwire proportional  
629 chambers. These chambers are filled with a Ar- $\text{CO}_2$  gas mixture and evenly spaced  
630 wires kept at 1900 V. These wires are orientated in the radial direction but not  
631 read out. Instead on one side of the cathode are copper strips parallel to the wires,  
632 measuring  $\eta$ , while on the other side of the cathode are strips parallel to the wires  
633 measuring  $\phi$ . The width between strips is approximately 1.5 mm providing a  
634 resolution of 60  $\mu\text{m}$  in the bending-plane and 5 mm in the non-bending plane.

635 Since the CSC and MDT systems do not have prompt timing signals, the RPC  
636 and TGC systems are used for triggering. The RPC system is used in the barrel  
637 region ( $|\eta| < 1.05$ ). RPC consist of two parallel resistive plates separated by a 2  
638 mm insulated spacer with 100 mm spacing kept at 9.8 kV, as shown in Figure 6.11.  
639 A gaseous mixture of  $\text{C}_2\text{H}_2\text{F}_4$ ,  $\text{C}_4\text{H}_{10}$ , and  $\text{SF}_6$  fills the space between the two  
640 plates. Metallic strips on the outer faces of the plates are used to read out signals  
641 produced by the gas ionizing. The middle barrel layer consists of two layers of  
642 RPCs on either side of the MDT layer and one layer on the outermost MDT  
643 layer. Each layer contains two orthogonal sets of metallic strips providing  $\eta$  and  
644  $\phi$  measurements. The timing resolution of RPCs is 1.5 ns, and therefore may be  
645 used to identify bunch crossings.

646 Finally, the TGCs are used in the end-cap regions and are primarily used to

647 provide L1 trigger decisions and  $\phi$  measurements. TGCs are multi-wire propor-  
 648 tional chambers consisting of arrays of gold-coated tungsten wires placed between  
 649 two cathode planes. These wires are separated by 1.8 mm and cathodes are 1.4 mm  
 650 from the wires. Orthogonal to the wires, on the opposite side of the cathode plane  
 651 are copper strips held at 2900 V. The chambers are filled with a mixture of  $CO_2$   
 652 and n-pentane gas, the latter acts as a quenching gas to prevent avalanches initi-  
 653 ated by secondary  $\gamma$ -rays from the primary avalanche. Figure 6.12 is a schematic  
 654 of a TGC. The timing resolution of TGCs is less than 25 ns and therefore they  
 655 are used for bunch crossing measurements.

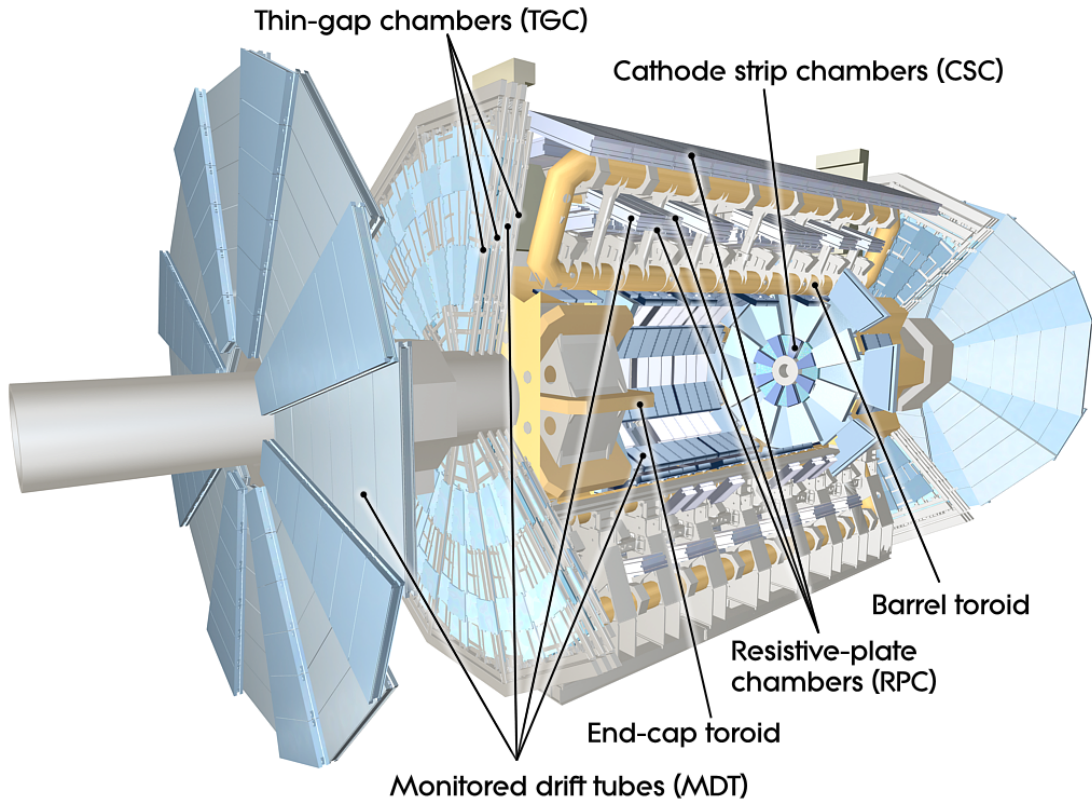


**Figure 6.9:** Schematic of Muon Spectrometer [cite G35]

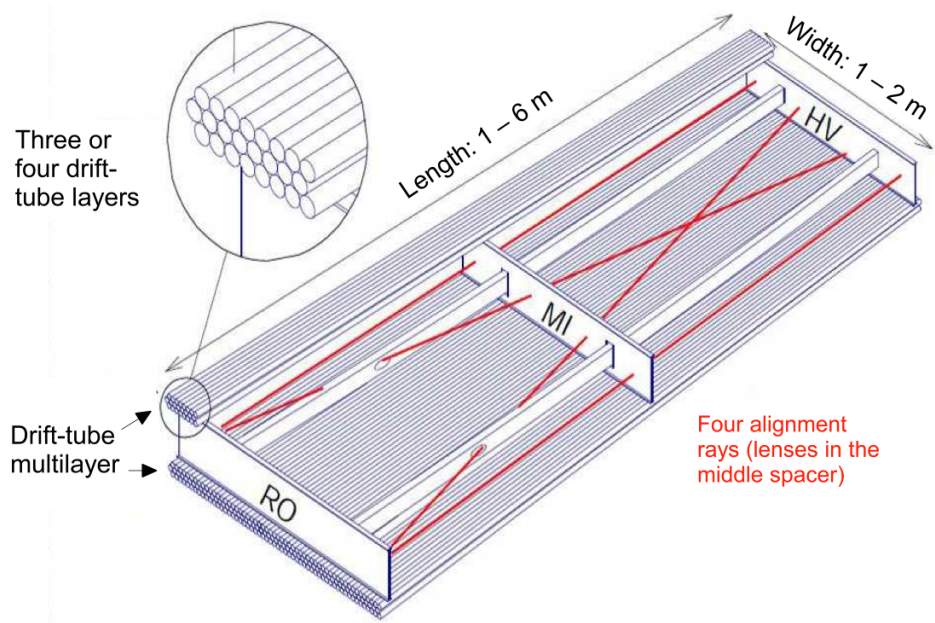


**Figure 6.10:** Schematic of MDT chamber. [cite G35]

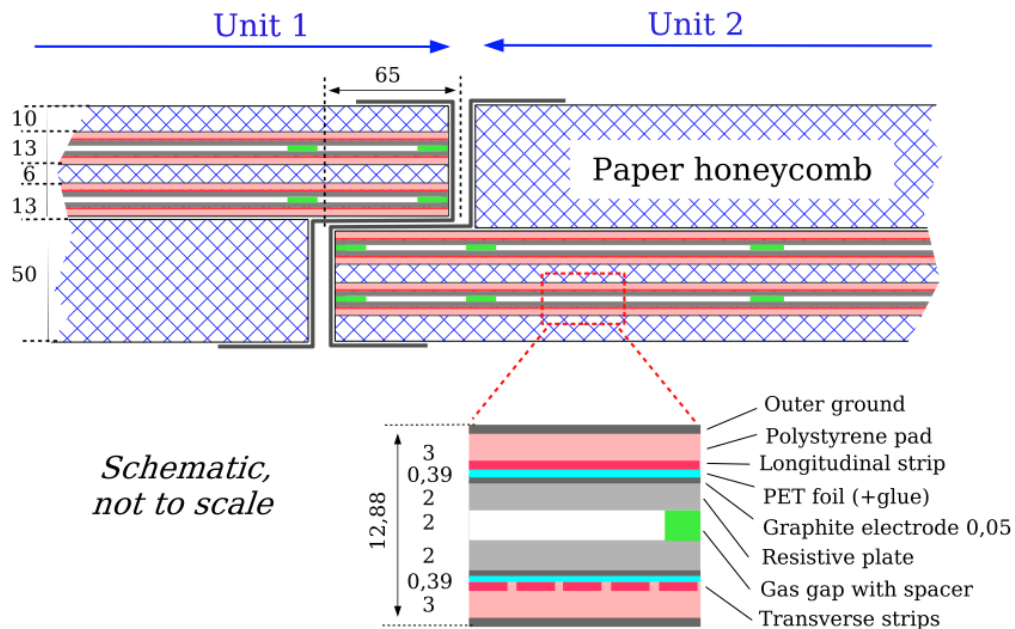


**Figure 6.11:** Schematic of RPC chamber, which is used for triggering in the central region of the detector [cite G35].

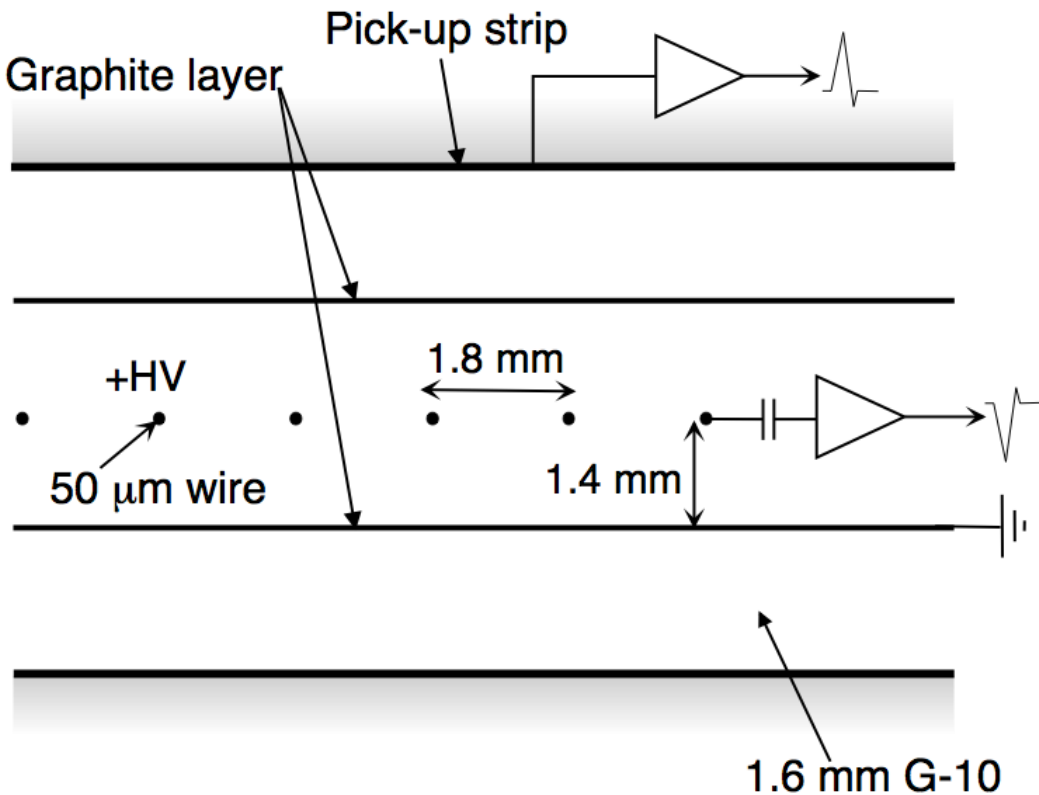


**Figure 6.12:** Schematic of TGC chamber, which is used for triggering in the muon end-cap region. [cite G35]

## 656    6.5 Magnet System

657    A particles with charge,  $q$ , and velocity  $v$ , moving in magnetic field,  $B$ , ex-  
 658    periences a force,  $F = qv \times B$ . This force can cause charged particles to have a  
 659    curved trajectory in magnetic fields, which the ID and MS use to determine the  
 660    particles  $p_T$ . The central solenoid provides the magnetic field for the ID and the  
 661    toroidal magnets provide the magnetic field for the MS.

662    The layout of the magnet system is shown in Figure 6.13. The central solenoid  
 663    consists of a single-layer Al-stabilized NbTi conductor coil wound inside an Al

664 support cylinder. The solenoid is 5.8 m long, 50 cm thick and has an inner radius  
665 of 1.23 m. It is cooled to 4.5 K to reach superconducting temperatures and shares  
666 the liquid argon calorimeter vacuum vessel to minimize material in the detector.  
667 A current of 7.730kA produces a 1.998 T solenoidal magnetic field, pointing in  
668 the  $+z$  direction.

669 The toroidal magnet system consists of a barrel and two end-cap toroidal  
670 magnets used to create a magnetic field outside the calorimeters that is orientated  
671 along  $\phi$ . Each barrel toroid is 25.3 m long with an inner and outer diameter of 9.4  
672 and 20.1 m and weighs 830 tonnes. Endcap toroids are 5 m long with an inner and  
673 outer radius of 1.65 and 10.7 m. Both toroid systems use Al-stabilized Nb/Ti/Cu  
674 conductors. The magnetic field strength in the barrel and endcap regions are 0.5  
675 and 1 T, respectively.

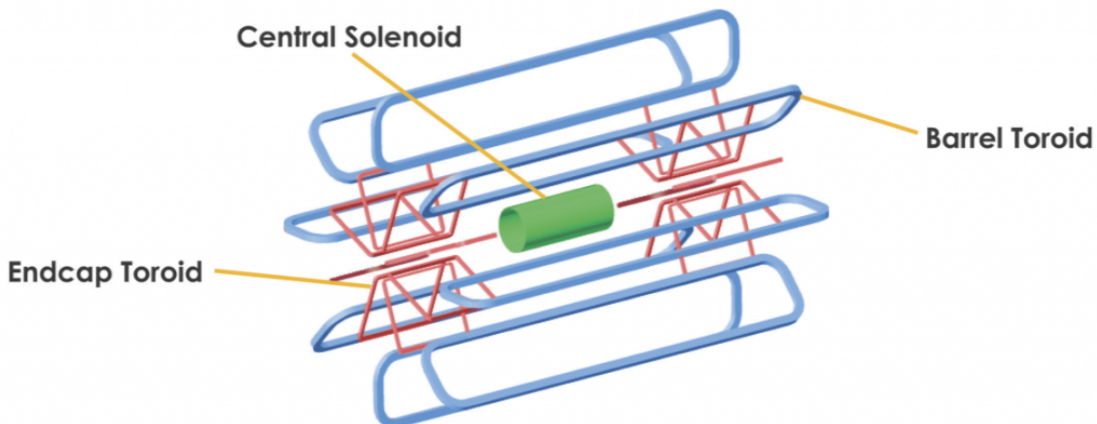


**Figure 6.13:** Layout of ATLAS magnet systems.

## 676 **6.6 Trigger System**

677 Since collisions occur every 25 ns and reading out all detector channels and  
678 storing that information is not currently feasible (would require saving 60 million  
679 megabytes per second), the majority of events are not kept for analysis. ATLAS

680 uses a multi-stage trigger system to select approximately 1,000 of the 1.7 billion  
681 collisions that occur each second (corresponding to a rate of 1 kHz from the 40  
682 MHz proton collision rate). The first stage of the trigger system is the hardware  
683 level (L1) trigger. This trigger reduces the event rate to  $\sim$ 100 kHz by identifying  
684 Regions-of-Interest (ROIs) containing high  $p_T$  leptons, photons, jets, or  $E_T^{miss}$  by  
685 using information from RPCs, TGCs, and calorimeters to make a  $2.5 \mu\text{s}$  decision.  
686 This information is then passed to a high-level trigger (HLT) which further de-  
687 creases event rates to  $\sim$  1 kHz. The HLT uses finer granularity measurements  
688 from the MS and ID to perform simplified offline reconstruction to decide which  
689 events to keep.

## **Part IV**

690

## **Method**

691

692 **Chapter 7**

693 **Dataset and Simulated Samples**

694 **7.1 Dataset**

695 This analysis uses  $pp$  collision data collected from 2015 to 2018 at  $\sqrt{s} = 13$   
696 TeV, corresponding to 139/fb of data as shown in Figure 7.1 and 7.2. From this  
697 dataset, only those events in which the tracker, calorimeters, and muon spectrom-  
698 eter have good data quality are used. For a given event, the solenoid and toroidal  
699 magnets must also be operating at their nominal field strengths. In addition to  
700 this, events must pass further quality checks to reject events where detector sub-  
701 systems may have failed. These selections reject events that containing LAr noise  
702 bursts, saturation in the electromagnetic calorimeter, TileCal errors, and failures  
703 in event recovery due to tracker failures. Events with information missing from  
704 subsystems (usually due to busy detector conditions) are rejected. Events must  
705 also contain a primary vertex with at least two associated tracks, where the pri-  
706 mary vertex is selected as the vertex with the largest  $\sum p_T^2$  over tracks associated  
707 with the vertex and  $p_T > 0.5$  GeV.

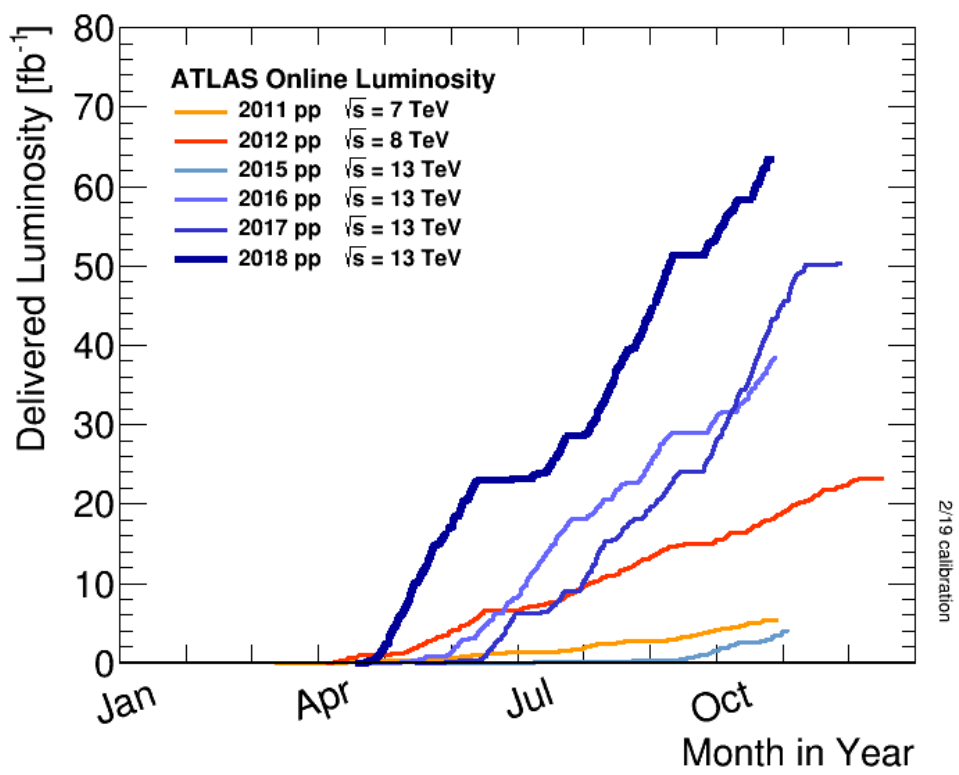


**Figure 7.1:** Integrated luminosity for data collected from ATLAS from 2011 - 2018



**Figure 7.2:** Mean number of interactions per crossing for data collected from ATLAS from 2011 - 2018

708 **7.2 Simulated Samples**

709 Samples are simulated in order to model backgrounds, evaluate signal ac-  
710 ceptance, optimize event selection and estimate systematic and statistical uncer-  
711 tainties. The dominant backgrounds for this analysis are  $W/Z + \text{jets}$ , diboson  
712 ( $WZ/WW$ ),  $t\bar{t}$ , single top and multijet production.

713  $W/Z+\text{jet}$  events are simulated using Sherpa 2.2.1 at NLO [cite [29]] and merged  
714 with the Sherpa parton shower using the ME+PS@NLO prescription [12]. These  
715 events are then normalized to NNLO cross sections. The  $t\bar{t}$  and single-top back-  
716 grounds are generated with Powheg-Box with NNPDF3.0NLO PDF sets in the  
717 matrix element calculation [cite[35]]. For all processes, the parton shower, frag-  
718 mentation, and underlying event are simulated using Pythia 8.320 with the A14  
719 tune set[cite[ATL-PHYS-PUB-2014-02]]. Diboson processes are generated using  
720 Sherpa 2.2.1.

721 Signal samples are simulated using MadGraph 5-2.2.2 [cite 42] and Pythia  
722 8.186 with NNPDF230LO. RS Graviton samples are generated with  $k/M_{PL}=1$ .  
723 HVT Model A (B) samples are simulated with  $g_V = 1(3)$ , as the difference in the  
724 width of the samples is smaller than detector resolution. Model C is generated by  
725 setting  $g_H = 1$  and  $g_f = 0$  to model VBF production of HVT bosons. Signals are  
726 generated for masses between 300 GeV and 5 TeV.

727 **Chapter 8**

728 **Objects**

729 **8.1 Electrons**

730 Electrons are reconstructed from electromagnetic showers in the LAr EM  
731 calorimeter. During reconstruction cells of  $\Delta\eta \times \Delta\phi = 0.025 \times 0.025$  are grouped  
732 into  $3 \times 5$  clusters. These clusters are then scanned for local maxima that seed  
733 electron clusters. These clusters must then be matched to ID track from the PV.  
734 This requirement minimizes non-prompt electron and fake electron backgrounds.  
735 Electrons must pass identification and isolation requirements. Electron identifica-  
736 tion (loose, medium, tight) classification is based on a multivariate discriminant  
737 that identifies electrons using a likelihood based method. For this analysis, events  
738 are required to have one tight electron and no additional loose electrons. Elec-  
739 trons are also required to be isolated. The electrons are considered isolated if the  
740 quotient of the sum of the transverse momentum (of calorimeter energy deposits)  
741 in a cone around the electron of size  $\Delta R = 0.2$  and the transverse momentum  
742 of the electron to be less than  $0.015 * p_T$  or 3.5 GeV, whichever is smaller. This  
743 requirement rejects non-prompt photons and other fake leptons. Electrons in this  
744 analysis are also required to have  $p_T > 30$  GeV and  $|\eta| < 2.47$ . Electrons are also

745 required to have  $p_T > 30$  GeV.

746 Electrons are calibrated to determine data-driven scale factors using  $J/\Psi \rightarrow$   
747  $ee$ ,  $Z \rightarrow ee$ ,  $Z \rightarrow \ell\ell\gamma$  processes. These corrections account for the non-uniform  
748 response of the detector which introduces modeling and reconstruction uncertain-  
749 ties.

## 750 8.2 Muons

751 As muons traverse the entire detector, they are reconstructed from ID and  
752 MS tracks. For this analysis the muon identification and isolation working points  
753 are chosen to minimize the contributions from non-prompt muons. Towards this  
754 end, each selected event must contain exactly one muon that passes the medium  
755 identification working point, and no additional muons (that pass the loose working  
756 point). For the medium working point, two types of reconstructed muons are  
757 used: combined and extrapolated muons (CB and ME, respectively). For CB  
758 muons, ID and MS tracks are reconstructed independently and a combined track  
759 fit is performed by adding or removing MS tracks to improve the fit quality.  
760 ME muons are reconstructed from only MS tracks with hits in at least two layers,  
761 which ensures the track originates from the PV. ME muons extend the acceptance  
762 for muon reconstruction outside the ID from  $2.5 < |\eta| < 2.7$ . The medium  
763 identification working point uses CB and ME tracks. CB tracks must have at  
764 least 3 hits in two MDT layers. ME tracks are required to have at least three  
765 MDT/CSC hits. To further minimize contributions from fake muons, the selected  
766 muons are required to be isolated from other tracks, as muons from  $W, Z$  decays are  
767 often isolated from other particles. To insure the selected muons are isolated, the  
768 scalar sum of the transverse momentum of tracks in a cone of  $\Delta R = 0.3$  compared  
769 to the transverse momentum of the muon must be less than 0.06. Muons are also

770 required to have  $p_T > 30$  GeV.

771 Muons are calibrated using well-studied resonances  $J/\Psi \rightarrow \mu\mu$  (low- $p_T$ ),  $Z \rightarrow$   
772  $\mu\mu$  (high- $p_T$ ). Figure 8.1 shows the combined muon  $p_T$  uncertainty from this  
773 calibration. The total systematic uncertainty is less than 1% for all  $p_T$  ranges  
774 considered in this analysis.

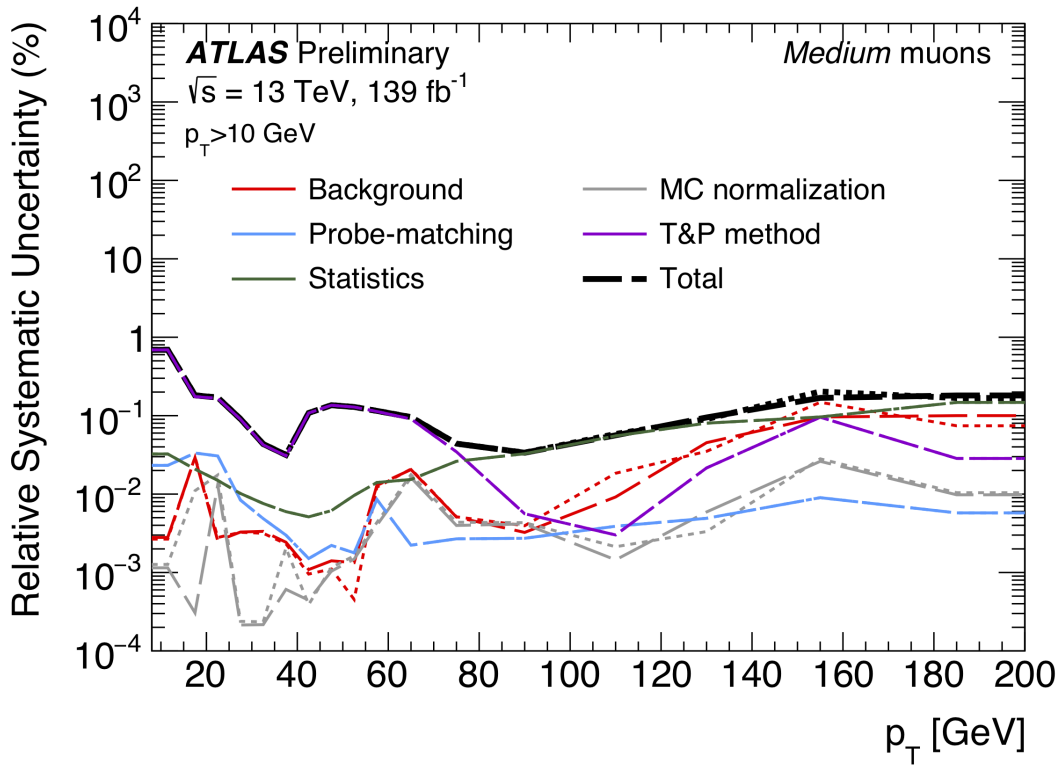


**Figure 8.1:** This figure shows the breakdown of the muon reconstruction efficiency scale factor measured in  $Z \rightarrow \mu\mu$  as a function of  $p_T$  [4].

### 775 8.3 Jets

776 Three types of jets are used in this analysis: variable radius, small-R and  
777 large-R jets. Variable radius jets are used to reconstruct  $Z$  bosons decaying to  
778 two  $b$ -jets in the jet catchment area of large-R jet in the Merged regime. Small-R

779 jets are used to reconstruct the hadronically decaying  $W/Z$  candidates in the  
780 resolved analysis and the forward jets from resonances produced through vector  
781 boson fusion. Large-R jets are used to reconstruct the hadronically decaying boson  
782 in the merged regime.

783 For all of these jet collections, the jet energy is calibrated sequentially as shown  
784 in Figure 8.2. After the jet direction is corrected to point to the PV, the energy  
785 of the jet is corrected. First, the jet energy is corrected to account for pileup  
786 contributions based on the  $p_T$  and area of the jet (these corrections are extracted  
787 from a  $pp \rightarrow jj$  sample). Following this, another pileup correction is applied that  
788 scales with  $\mu$  and  $N_{PV}$ .

789 MC-based corrections are then applied that are meant to transform the jet  
790 energy and  $\eta$  back to truth level. Therefore, these corrections account for the  
791 non-compensating nature of the ATLAS calorimeters and inhomogeneity of the  
792 detector. Following this, the Global Sequential Calibration is applied that re-  
793 duces flavor dependence of jet calibrations and accounts for energy leakage of jets  
794 outside the calorimeters. Finally, in-situ corrections are applied that account for  
795 differences in jet responses between data and simulation ( $\gamma/Z + \text{jet}$  and fake lep-  
796 ton samples are used). These differences can be due to mismodelling of the hard  
797 scatter event, pile-up, jet formation, etc.

798 To further reject fake jets, jets must pass quality requirements based on the  
799 following variables ([cite P42]):

- 800 -  $f_Q^{LAr}$ : fraction of energy of jet's LAr cells with poor signal shape
- 801 -  $f_Q^{HEC}$ : fraction of energy of jet's HEC cells with poor signal shape
- 802 -  $E_{neg}$ : sum of cells with negative energy
- 803 -  $f_{EM}$ : fraction of jet's energy deposited in EM calorimeter

- 804     -  $f_{HEC}$ : fraction of jet's energy deposited in HEC calorimeter
- 805     -  $f_{max}$ : maximum energy fraction in any single calorimeter layer
- 806     -  $f_{ch}$ : ratio of the scalar sum of the  $p_T$  of a jet's charged tracks to the jet's  $p_T$
- 807     Jets selected for the resolved analysis must pass one of the following criteria:
- 808     -  $f_{HEC} > 0.5$  and  $|f_Q^{HEC}| > 0.5$  and  $\langle Q \rangle > 0.8$
- 809     -  $|E_{neg}| > 60$  GeV
- 810     -  $f_{EM} > 0.95$  and  $f_Q^{LAr} > 0.8$  and  $\langle Q \rangle > 0.8$  and  $|\eta| < 2.8$
- 811     -  $f_{max} > 0.99$  and  $|\eta| < 2$
- 812     -  $f_{EM} < 0.05$  and  $f_{ch} < 0.05$  and  $|\eta| < 2$
- 813     -  $f_{EM} < 0.05$  and  $|\eta| > 2$

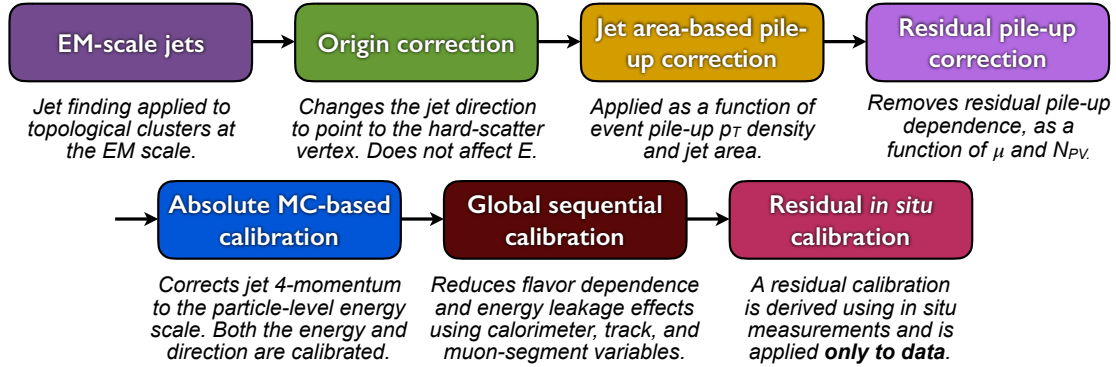


**Figure 8.2:** [7] This diagram shows the calibration stages for EM jets.

814 **8.3.1 Small-R jets**

815 Small-R jets are used to reconstruct the hadronically decaying  $W/Z$  candi-  
816 date when the two resulting jets are well-separated in  $\eta\text{-}\phi$  space. Small-R jets  
817 are also used to identify forward jets from resonances produced through vector  
818 boson fusion. Small-R jets are constructed from topologically connected clusters  
819 of calorimeter cells (topoclusters), seeded from calorimeter cells with energy de-  
820 posits significantly above the noise threshold. These cells are then used as inputs  
821 to the  $anti-k_t$  algorithm [15] with a radius parameter,  $R = 0.4$ .

822 Jets used in this analysis must have  $p_T > 30$  GeV and  $|\eta| < 2.5$ . To further  
823 reduce fake jets the jet-vertex-tagger (JVT) is used to reject pile-up jets [6]. The  
824 JVT uses two track-based variables, corrJVF and  $R_{p_T}$  to calculate the likelihood  
825 that the jet originated from the PV. The corrJVF compares the scalar sum of the  
826  $p_T$  of tracks associated with the jet and PV to the scalar sum of the  $p_T$  of tracks  
827 associated with the jet. This variable also includes a correction that reduces the  
828 dependency of corrJVF with the number of reconstructed vertices in the event.  
829 The other discriminant,  $R_{p_T}$ , is given by the ratio of the scalar sum of the  $p_T$  of  
830 tracks associated with the jet and PV to the  $p_T$  of the jet. Both of these variables  
831 peak around zero for pileup jets, as these jets are unlikely to have tracks associated  
832 with the PV. JVT cuts are applied to all jets with  $p_T > 120$  GeV. Central jets  
833 ( $|\eta| < 2.4$ ) are required to have a  $JVT > 0.59$  and forward jets ( $2.4 < |\eta| < 2.5$ )  
834 are required to have  $JVT > 0.11$ .

835 **8.3.2 Large-R jets**

836 Large-R ( $R = 1.0$ ) jets are used to reconstruct the hadronically decaying  $W/Z$   
837 candidate when the resulting jets are not well-separated in  $\eta\text{-}\phi$  space, and overlap  
838 forming one large-R jet. Track-Calorimeter Clusters (TCCs) are used to reconstruct these

jets [cite ANA 50]. These jets are constructed using a pseudo particle flow method  
 using ID tracks matched to calorimeter clusters. The angular resolution of the  
 calorimeter degrades sharply with jet  $p_T$ , but the jet energy resolution improves.  
 The tracker has excellent angular resolution which improves with  $p_T$ . Therefore,  
 by matching tracks to jets, TCCs have more precise energy and angular resolution  
 than jets constructed from calorimeter information only. These jets are required  
 to have  $p_T > 200$  GeV,  $|\eta| < 2.0$  and  $m_J > 50$  GeV.

TCC jets are trimmed as detailed in [cite ANA 45], which suppresses pileup  
 and soft radiation in the jet, the jet mass is calculated as the four-vector sum  
 of the jet's constituents (assuming massless constituents). The jet mass peaks  
 around the  $W/Z$  boson mass for  $W/Z \rightarrow qq$  jets, and more broadly for quark and  
 gluon induced jets.

These jets are then tagged as  $W$  jet if it passes optimized jet mass and  $D_2$   
 cuts for  $W$  bosons, and a  $Z$  jet if it passes the optimized cuts for the  $Z$  boson.  
 The jet substructure variable  $D_2$  is given by the ratio of energy correlation func-  
 tions. These fuctions are derived from the energies and pair-wise angles of a jet's  
 constituents [cite ANA 46, 47]:

$$D_2^{\beta=1} = E_{CF3} \left( \frac{E_{CF1}}{E_{CF2}} \right)^3 \quad (8.1)$$

Where the energy correlation functions are defined as:

$$E_{CF1} = \sum_i p_{T,i} \quad (8.2)$$

$$E_{CF2} = \sum_{ij} p_{T,i} p_{T,j} \Delta R_{ij} \quad (8.3)$$

$$E_{CF3} = \sum_{ijk} p_{T,i} p_{T,j} p_{T,k} \Delta R_{ij} \Delta R_{jk} \Delta R_{ki} \quad (8.4)$$

859        A two-dimensional optimization of the jet mass and  $D_2$  thresholds was per-  
 860        formed to provide maximum sensitivity for this analysis. This optimization was  
 861        done by maximizing the signal sensitivity (using HVT  $W'$  and  $G_{KK}$  samples)  
 862        against the single quark and gluon jet backgrounds in bins of jet  $p_T$ . Figure 8.3  
 863        shows the optimized thresholds on  $D_2$  and jet mass as a function of jet  $p_T$ . Figure  
 864        8.4 shows the efficiency of the optimized  $W/Z$  taggers as a function of jet  $p_T$ .

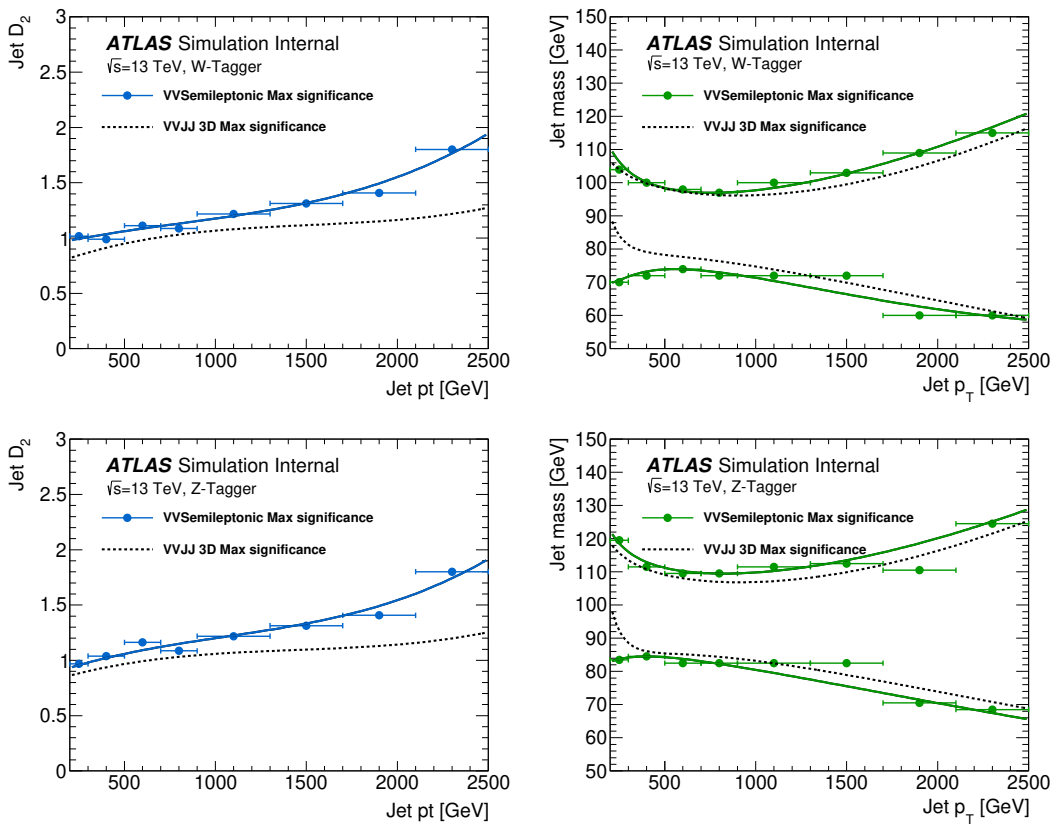


**Figure 8.3:** The upper cut on  $D_2$  (a) and jet mass window cut i.e. the upper and lower boundary of the mass (b) of the  $W$ -tagger as a function of jet  $p_T$ . Corresponding values for  $Z$ -tagger are shown in (c) and (d). The optimal cut values for maximum significance are shown as solid markers and the fitted function as solid lines. Working points from  $VV \rightarrow JJ$ [ATLAS-HDBS-2018-31-002] is also shown as dashed lines as a reference. Natasha reword?

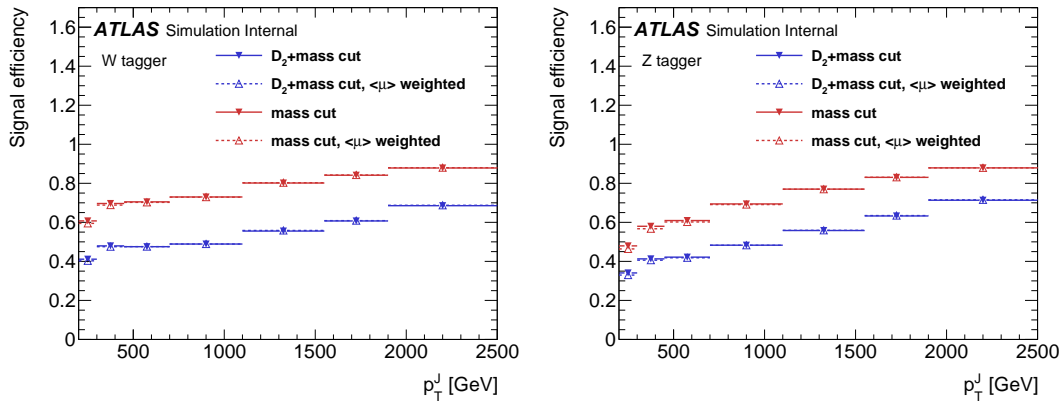


**Figure 8.4:** Natasha write caption

### 865 8.3.3 Variable Radius jets

866 To more accept more boosted  $Z$  bosons decaying to  $b\bar{b}$  that would normally be  
 867 rejected due to topological cuts discussed 9.4 variable radius (VR) track jets are  
 868 used to identify  $b$ -jets within the catchment area of large- $R$  jets [14]. VR jets are  
 869 constructed from ID tracks using the anti- $k_t$  algorithm with a radius parameter  
 870 that depends on the  $p_T$  of the track, shown in Equation 8.5.

$$R_{eff}(p_{T,i}) = \frac{\rho}{p_{T,i}} \quad (8.5)$$

871 For this search  $\rho = 30$  GeV and an upper and lower limit on cone size are set  
 872 to 0.02 and 0.4, respectively, to prevent unphysical asymptotic behavior of  $\rho$ .  
 873 Collinear VR jets are possible, so track jets that are not separated by the the  
 874 smaller jet's cone size are not used. Additionally, VR jets are required to have  
 875  $p_T > 10$  GeV and  $|\eta| < 2.5$ .

876 **8.3.4 Jet Flavor Tagging**

877 To further classify events, the small-R and VR jets originating from a b-quark  
878 are classified using a multivariate  $b$ -tagging algorithm (BDT), MV2c10 [cite G 210  
879 199]. This algorithm uses the impact parameters of the jet's ID tracks, secondary  
880 vertices (if they exist), and reconstructed flight paths of  $b$  and  $c$  hadrons in the  
881 jet to determine if the jet was induced by a  $b$ -quark. For this analysis the 85%  
882 efficient working point of this algorithm is used giving  $c$ ,  $\tau$ , and light-flavor jet  
883 rejection of 3, 8, and 34 respectively in simulated  $t\bar{t}$  samples.

884 **8.4 MET/Neutrinos**

885 As neutrinos are uncharged and colorless they do not leave tracks or jets in the  
886 detector. For this reason, neutrinos are reconstructed calculated the  $E_T^{miss}$ , the  
887 negative vector sum of  $p_T$  all the physics objects and an extra "soft" term. The  
888 "soft" term accounts for energy deposits not associated with any of the objects in  
889 the event. For this analysis the soft term is given by the sum  $p_T$  of all ID tracks  
890 not associated with objects in the event. The selected tracks must be matched to  
891 the primary vertex, which decreases pile-up contamination [cite G 217 218]. The  
892 tight working point is used [Natasha look up what this means].

893 **8.5 Overlap Removal**

894 Reconstructed jets and leptons in this analysis can arise from the same energy  
895 deposits. For instance, a cluster of energy from an electron can also be a valid  
896 calorimeter seed for a jet. To mitigate this confusion of multiple objects originating  
897 from a single jet or lepton overlapping objects are removed via a procedure referred  
898 to a overlap removal. In this procedure the separation of the two objects,  $\Delta(R) =$

899  $\sqrt{(\Delta\eta)^2 + (\Delta\phi)^2}$  determines which object is removed from the event.

900 The overlap selections used in this analysis are:

901 - when an electron shares a track with another electron with the lower  $p_T$   
902       electron is rejected, as it is more likely to be a fake electron

903 - when a muon and electron share a track the muon is rejected if it is a  
904       calo-muon, otherwise the electron is rejected

905 - when  $\Delta R < 0.2$  for an electron and jet, the jet is rejected to maximize signal  
906       acceptance

907 - when  $\Delta R > 0.2$  for an electron and jet, the electron is rejected as likely  
908       originated from decays within the jet

909 - when  $\Delta R < \min(0.4, 0.04 + 10\text{GeV}/p_T^\mu)$  the muon is rejected, again maximiz-  
910       ing signal acceptance, otherwise the jet is rejected

911 - when  $\Delta R < 1.0$  for the a large-R jet and electron, the jet is rejected

912 **Chapter 9**

913 **Event Selection and**

914 **Categorization**

915 **9.1 Pre-selection**

916 Before applying topological cuts to suppress backgrounds and reduce data  
917 size in this search, preselection cuts are applied which include trigger and event  
918 requirements. Events must contain exactly one tight lepton (no additional loose  
919 leptons), the  $p_T^{\ell\nu} > 75$  GeV, and there must be at least two small-R jets or one  
920 large-R jet.

921 **9.2 Trigger**

922 The data were collected using the lowest unprescaled single-lepton or  $E_T^{miss}$   
923 triggers, as summarized in Table 9.1. Since the muon term is not considered in the  
924 trigger  $E_T^{miss}$  calculation, the  $E_T^{miss}$  trigger is fully efficient to events with high- $p_T$   
925 muons. For this reason, the  $E_T^{miss}$  trigger is used for events where  $p_T^\mu > 150$  GeV, to  
926 compensate for the poor efficiency of the single muon trigger above  $p_T^\mu > 150$  GeV.

**Table 9.1:** The list of triggers used in the analysis.

Data-taking period	$e\nu qq$ channel	$\mu\nu qq$ ( $p_T(\mu\nu) < 150$ GeV) channel	$\mu\nu qq$ ( $p_T(\mu\nu) > 150$ GeV) channel
2015	HLT_e24_lhmedium_L1EM20 OR HLT_e60_lhmedium OR HLT_e120_lhloose	HLT_mu20_iloose_L1MU15 OR HLT_mu50	HLT_xe70
2016a (run $< 302919$ ) $(L < 1.0 \times 10^{34} \text{ cm}^{-2} \text{ s}^{-1})$	HLT_e26_lhtight_nod0_ivarloose OR HLT_e60_lhmedium_nod0 OR HLT_e140_lhloose_nod0 HLT_e300_etcut	HLT_mu26_ivarmedium OR HLT_mu50	HLT_xe90_mht_L1XE50
2016b (run $\geq 302919$ ) $(L < 1.7 \times 10^{34} \text{ cm}^{-2} \text{ s}^{-1})$	same as above	same as above	HLT_xe110_mht_L1XE50
2017	same as above	same as above	HLT_xe110_pufit_L1XE55
2018	same as above	same as above	HLT_xe110_pufit_xe70_L1XE50

927 **9.3 non-VBF/VBF RNN**

928 To classify events as originating from non-VBF or VBF production a recursive  
929 neural network (RNN [21]) is used. This approach is more powerful than a cut-  
930 based classification as it improves signal efficiency and analysis sensitivity by  
931 exploiting correlations between variables that the RNN learns. In particular, a  
932 RNN architecture is ideal as it can handle variable numbers of jets in the events.

933 The RNN uses the four-momentum of candidate VBF jets to classify events  
934 as VBF or non-VBF topologies. Sometimes jets are incorrectly reconstructed,  
935 so the number of jets in the event is expected to vary across the input samples.  
936 VBF candidate jets are identified by removing jets from the event that are likely  
937 from  $W/Z \rightarrow qq$ . For the resolved regime this means removing the two leading  
938 small-R jets from the VBF candidate jet list. For the merged regime this means  
939 removing small-R jets separated by less than 1.0 in  $dR$  from the large-R jet. VBF  
940 candidate jets are also required to be within  $|\eta| < 4.5$ . From the list of remaining  
941 VBF candidate jets, the two highest- $p_T$  jets are chosen.

942 The architecture of the RNN is shown in Figure 9.2. The RNN is composed  
943 of Long Short Term Memory Cells (LSTM) that extract meaningful information  
944 and retains<sup>3</sup> it. The logic embedded in the LSTM is shown in Figure ???. LSTMs  
945 are useful for VBF event classification for events with two jets, where using the  
946 kinematic properties of both jets (and their correlations) will lead to more efficient  
947 event classification.

948 In this RNN architecture, the VBF candidates are first passed to a masking  
949 layer which checks the number of jets in the event. If there is only one jet, only one  
950 vertical LSTM layer is used. The output of masking is then passed to a LSTM,  
951 with a tanh activation function. The output of the LSTM is then passed to a  
952 second horizontal LSTM layer (and vertical LSTM layer if there are two jets in

953 the event). Finally the output of the last LSTM cell is passed to a dense layer  
954 and then to a sigmoid activation layer, leading to an overall RNN score.

955 The weights and other parameters of the network are learned by training the  
956 network with VBF and non-VBF signals over 200 epochs with an Adam Optimizer  
957 [13]. To prevent overfitting during training, dropout is applied to RNN weights  
958 and training is truncated if the network parameters are unchanged after ten it-  
959 erations [23]. Figure 9.4 shows the ROC curve for the RNN using k-fold cross  
960 validation [19].

961 Figure 9.3 shows the RNN discriminant for backgrounds, GGF signals, and  
962 VBF signals. The RNN score is  $\sim 0$  for GGF and background processes and  $\sim 1$   
963 for VBF processes. Figure 9.5 shows the limits for various signal processes based  
964 on the RNN cut applied. Requiring the RNN score to be  $> 0.8$  was chosen as  
965 it provided the best significance (and signal efficiency) for this final state and  
966 the  $\nu\nu qq$  and  $\ell\ell qq$  channels, which this channel will be combined with for future  
967 publications.

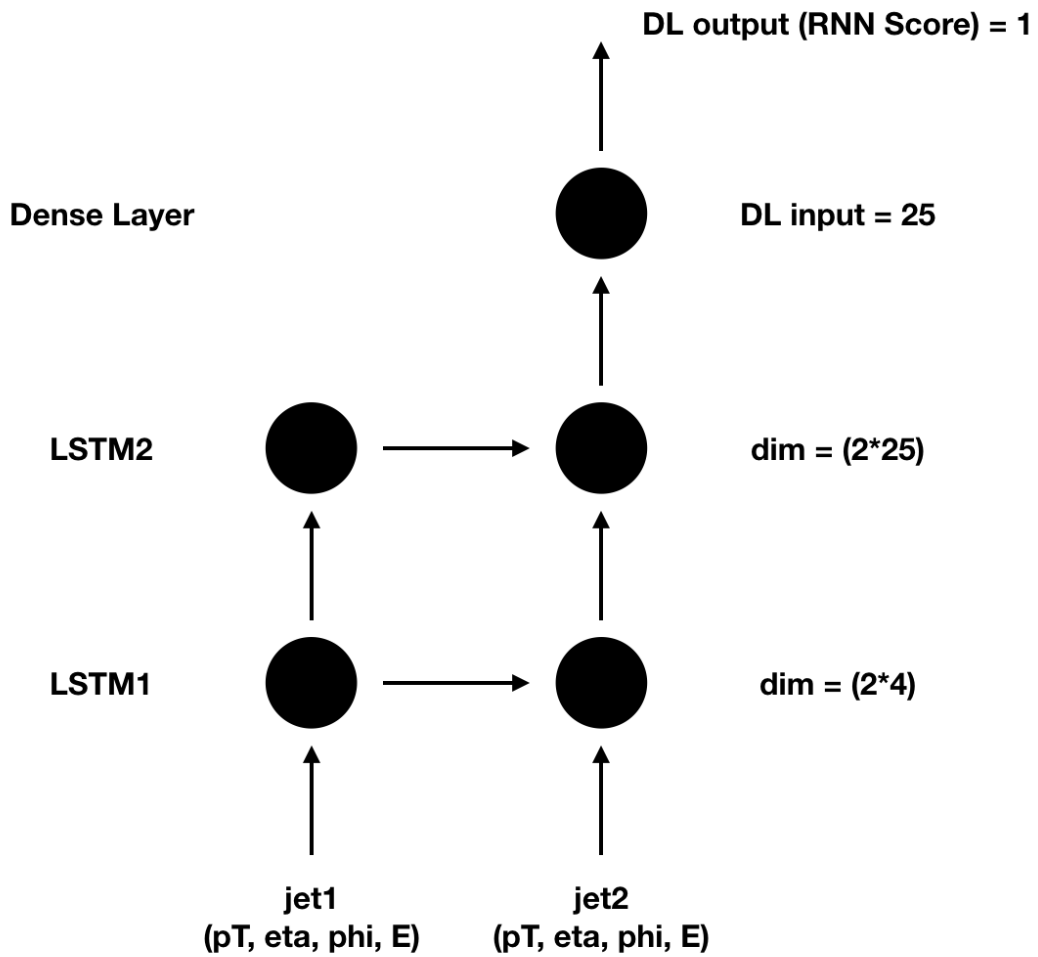


**Figure 9.1:** RNN architecture. Natasha add caption

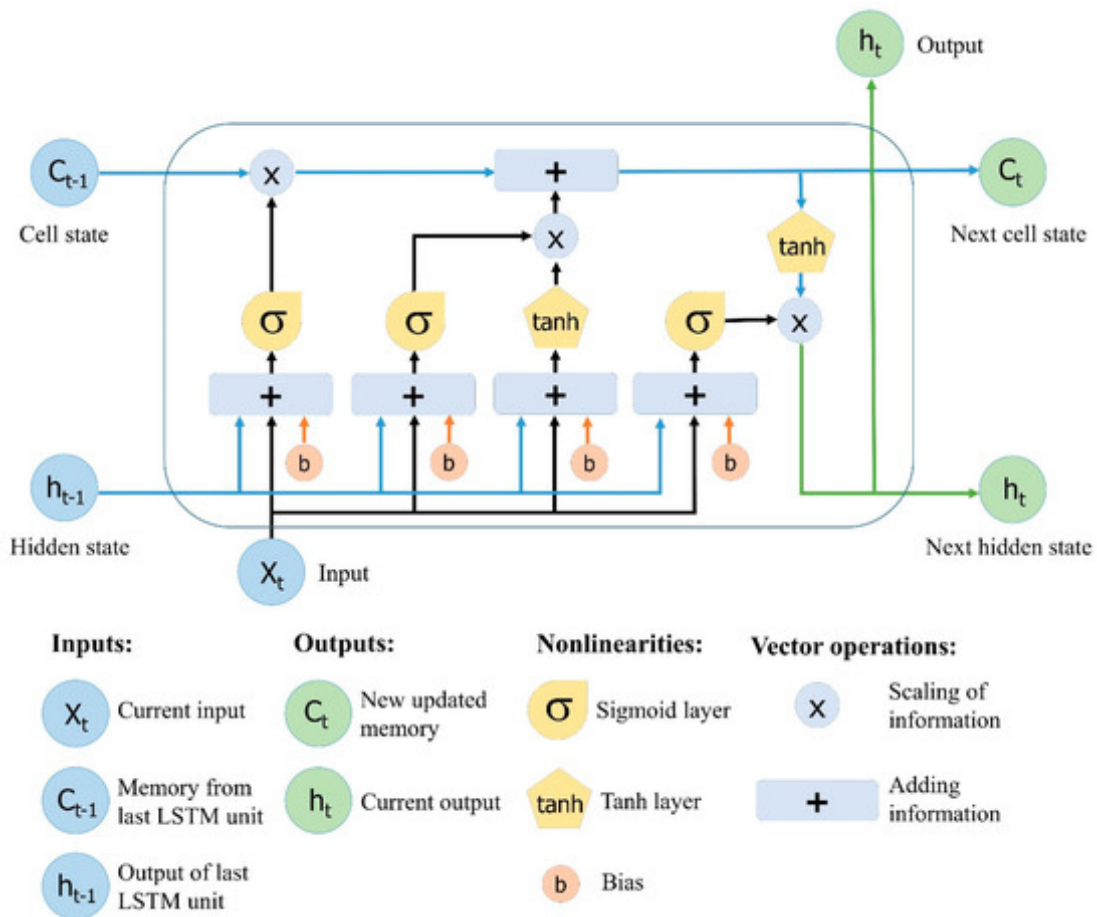


**Figure 9.2:** This figure shows the embedded logic in LSTM cells. This image was taken from [22].

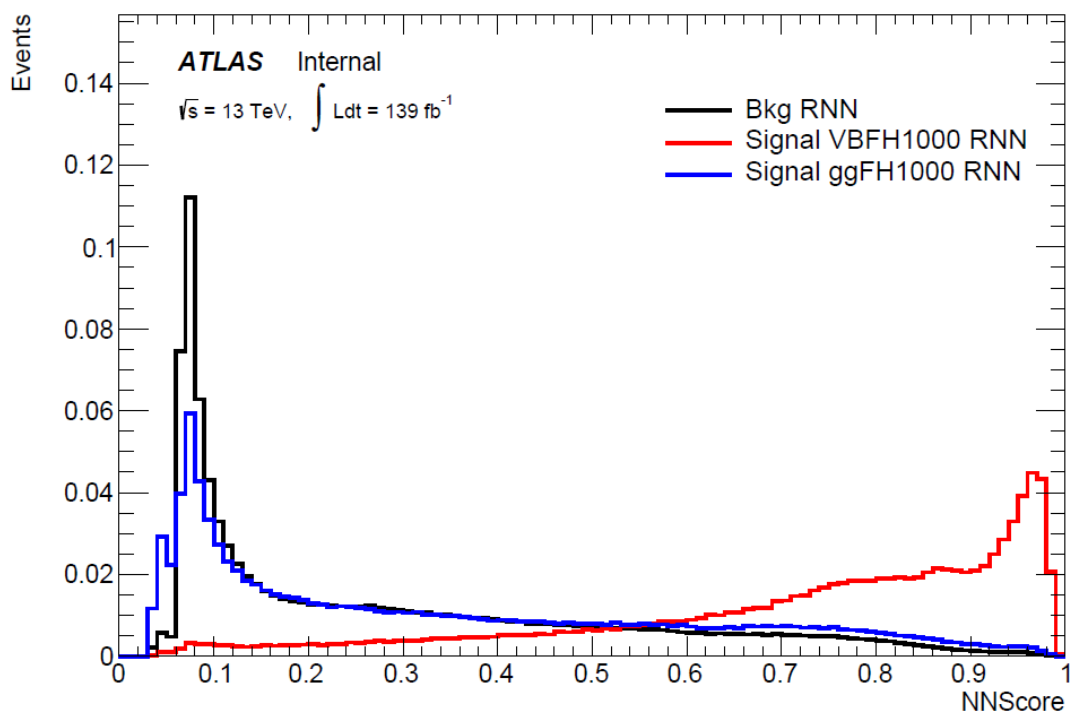


**Figure 9.3:** RNN Score distribution for ggF and VBF signals and backgrounds.

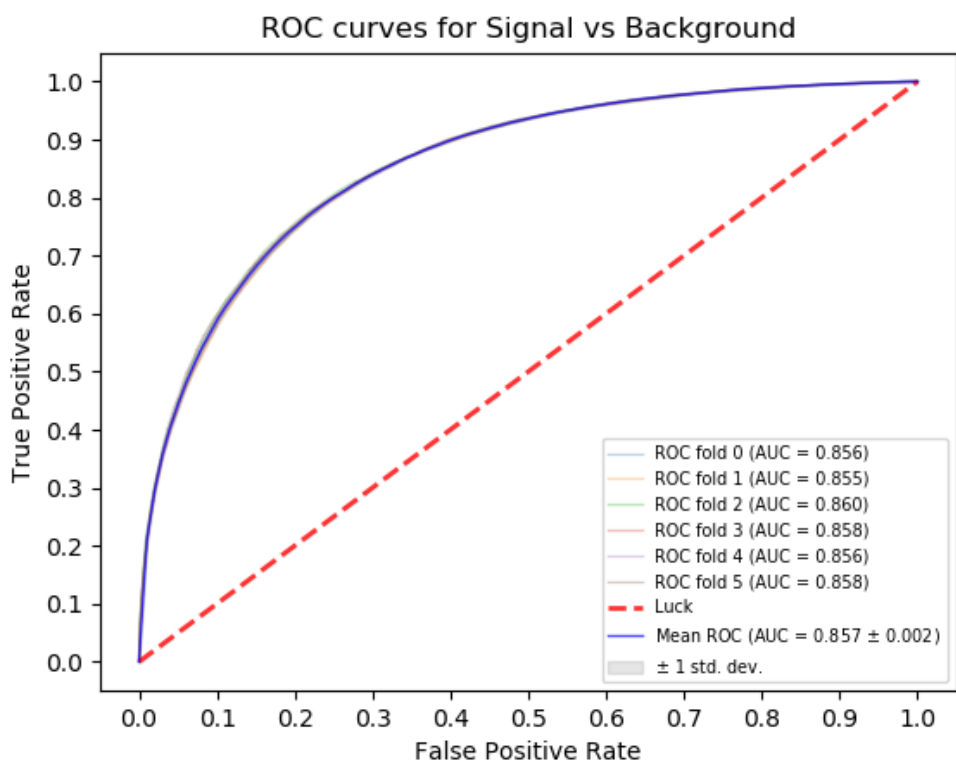


**Figure 9.4:** ROC curve using k-fold validation for RNN.

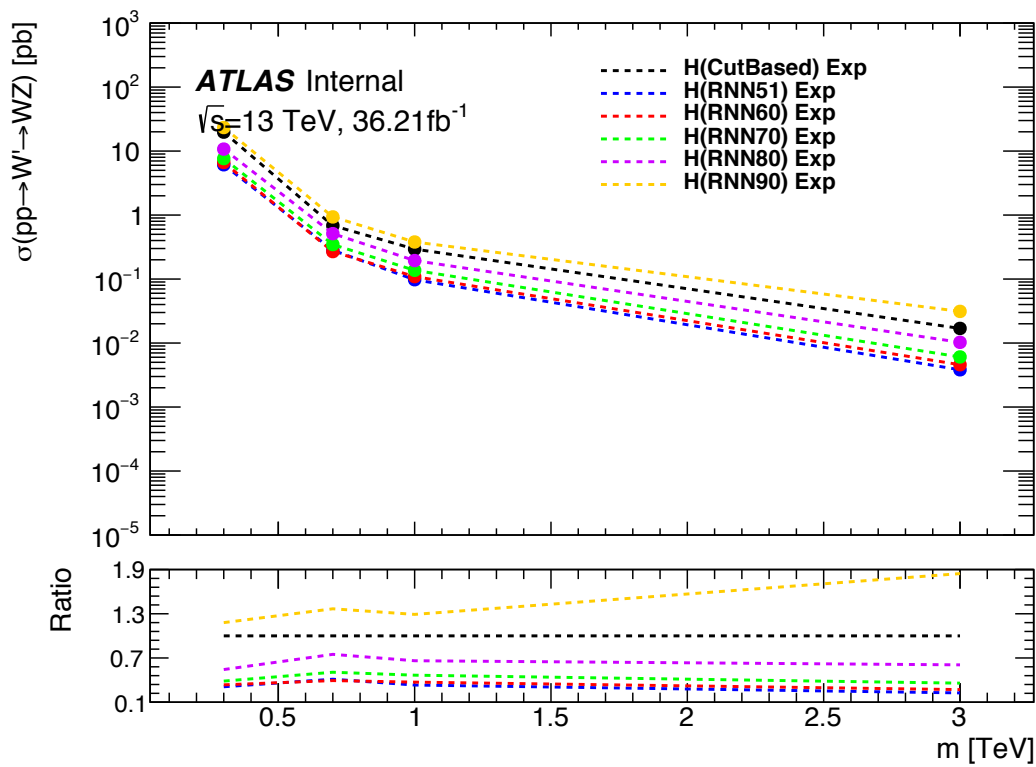


**Figure 9.5:** Comparison of GGF Z' limits for different RNN score selections. The bottom panel shows the ratio of the upper limits set for different RNN cuts to the cut-based analysis. In this panel smaller numbers, indicate that the expected upper limit is smaller than the cut-based analysis, which is desired.

## 968 9.4 Topological Cuts

969 Once an event is classified as VBF or GGF via the RNN, it must pass other  
970 topological cuts that maximize  $S/\sqrt{B}$ . First, to efficiently select events with a  
971  $W \rightarrow \ell\nu$  candidate exactly one tight lepton is required and  $E_T^{miss} > 100(60)$   
972 GeV and  $p_{T,\ell\nu} > 200(75)$  GeV in the merged (resolved) analysis to suppress the  
973 multi-jet background.

974 For the merged analysis, in addition to the  $W \rightarrow \ell\nu$  and  $W/Z \rightarrow J$  selections  
975 above, the  $\min(p_{T,\ell\nu}, p_{T,J})/m_{WV} > 0.35(0.25)$  for the GGF (VBF) category. To  
976 reduce  $t\bar{t}$  contamination events with the signal region and  $W$ +jets control region  
977 events with at least one b jet with  $\Delta R > 1.0$  from the large-R jet are excluded.  
978 High purity signal regions require the  $D_2$  and  $W/Z$  mass window cut to be passed,  
979 whereas the low purity region only requires the  $W/Z$  mass window cut to be  
980 passed. Finally for events to be classified as tagged the large-R jet must contain  
981 exactly two b-tagged jets. Untagged events must have no more than one b-tagged  
982 jet matched to the large-R jet. These selections are shown in Table 9.2. The  
983 distributions for the variables used in merged analysis for top control regions are  
984 shown in Figure 9.7-9.10.

985 Events failing the merged selection are then re-analyzed in the resolved cat-  
986 egory. To enhance resolved signals, the event should contain two high- $p_T$  boson  
987 candidates that are back-to-back in the  $\phi$  as shown by the cuts in Table 18. Again  
988 to suppress the  $t\bar{t}$  background in the WCR and SR events are required to have no  
989 additional b-jets.

990 The  $WV$  system mass,  $m_{WV}$  is reconstructed from the lepton, neutrino, and  
991 hadronically-decaying boson candidate. The momentum of the neutrino along the  
992  $z$ -direction is obtained by constraining the  $W$  boson mass of the lepton neutrino  
993 system to be  $80.3$  GeV/ $c^2$ . For complex solutions to this constraint,  $p_Z$  is taken

994 as either the real component of the solution or the one with the smaller absolute  
995 value of the two real solutions. For the resolved analysis,  $m_{WV}$  is reconstructed  
996 by constraining the  $W(Z)$  dijet system:

$$p_{T,jj}^{corr} = p_{T,jj} \times \frac{m_{W/Z}}{m_{jj}} \quad (9.1)$$

997

$$m_{jj}^{corr} = m_{W/Z} \quad (9.2)$$

998 where  $m_{jj}$  and  $m_{W/Z}$  are the reconstructed invariant mass of the hadronically-  
999 decaying  $W/Z$  boson and the PDG values of the  $W/Z$  boson masses, respectively.  
1000 A summary of the resolved selections is shown in Table 9.3. The distributions for  
1001 the variables used in the resolved analysis in the TCR are shown in Figure 9.11,  
1002 9.12.

1003 The analysis cutflow is shows in Figure 9.6. Events classified as VBF events  
1004 are classified as Merged High purity, low purity or resolved signal region selections  
1005 sequentially. If the event does not pass any of these selections but passes a VBF  
1006 control region selection it is classified as a VBF CR event. If the event fails the  
1007 VBF selection it is then checked if it passes the Merged High purity, Low purity  
1008 or resolved signal region selections (NB: for the WZ decay modes all the regions  
1009 have tagged and untagged categories). If the event fails all the GGF signal region  
1010 selections, it is then kept for GGF control region selections, if it passes those  
1011 selections.

**Table 9.2:** Summary of selection criteria used to define the signal region (SR),  $W+jets$  control region ( $W$  CR) and  $t\bar{t}$  control region ( $t\bar{t}$  CR) for merged 1-lepton channel.

Selection	SR		$W$ CR (WR)		$t\bar{t}$ CR (TR1)	
	HP	LP	HP	LP	HP	LP
$W \rightarrow \ell\nu$	Num of Tight leptons		1			
	Num of Loose leptons		0			
	$E_T^{\text{miss}}$		> 100 GeV			
	$p_T(\ell\nu)$		> 200 GeV			
$W/Z \rightarrow J$	Num of large- $R$ jets		$\geq 1$			
	$D_2$ cut		pass	fail	pass	fail
	$W/Z$ mass window cut		pass	pass	fail	pass
	Numb. of associated VR track jets $b$ -tagged		For $Z \rightarrow J$ : $\leq 1$ ( $= 2$ ) for untagged (tagged) category			
Topology cut	$\min(p_{T,\ell\nu}, p_{T,J}) / m_{WV}$		> 0.35(0.25) for DY/ggF (VBF) category			
Top-quark veto	Num of $b$ -tagged jets outside of large- $R$ jet		0		$\geq 1$	
	Pass VBF selection		no (yes) for DY/ggF (VBF) category			

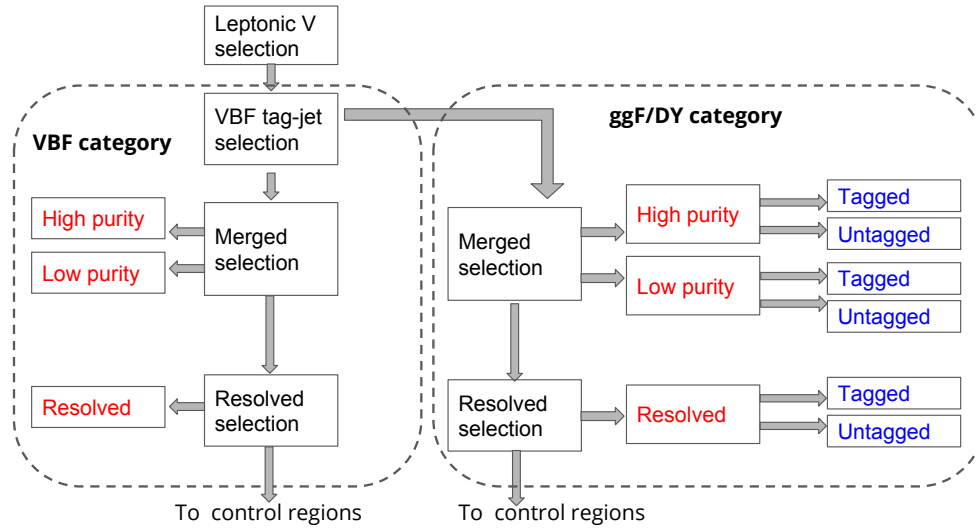


**Figure 9.6:** Event Categorization. Natasha write more.

**Table 9.3:** The list of selection cuts in the resolved analysis for the  $WW$  and  $WZ$  signal regions (SR),  $W$ +jets control region (WR) and  $t\bar{t}$  control region (TR).

cuts		SR	$W$ CR (WR)	$t\bar{t}$ CR (TR1)
$W \rightarrow \ell\nu$	Number of Tight leptons		1	
	Number of Loose leptons		0	
	$E_T^{miss}$		$> 60$ GeV	
	$\$p_T(\ell\nu)$		$> 75$ GeV	
$W/Z \rightarrow jj$	Number of small-R jets		$\geq 2$	
	Leading jet $p_T$		$> 60$ GeV	
	Subleading jet $p_T$		$> 45$ GeV	
	$Z \rightarrow q\bar{q}$	$78 < m_{jj} < 105$ GeV	$50 < m_{jj} < 68$ GeV or	$50 < m_{jj} < 150$ GeV
Topology cuts	$W \rightarrow q\bar{q}$	$68 < m_{jj} < 98$ GeV	$105 < m_{jj} < 150$ GeV	
	Num. of $b$ -tagged jets	For $Z \rightarrow jj$ : $\leq 1$ ( $= 2$ ) for untagged (tagged) category		
	$\Delta\phi(j, \ell)$		$> 1.0$	
	$\Delta\phi(j, E_T^{miss})$		$> 1.0$	
Top veto	$\Delta\phi(j, j)$		$< 1.5$	
	$\Delta\phi(\ell, E_T^{miss})$		$< 1.5$	
min $(p_{T,\ell\nu}, p_{T,jj}) / m_{WV}$		$> 0.35(0.25)$ for DY/ggF (VBF) category		
Top veto	Number of additional $b$ -tagged jets	0		$\geq 1$
	Pass VBF selection	no (yes) for DY/ggF (VBF) category		

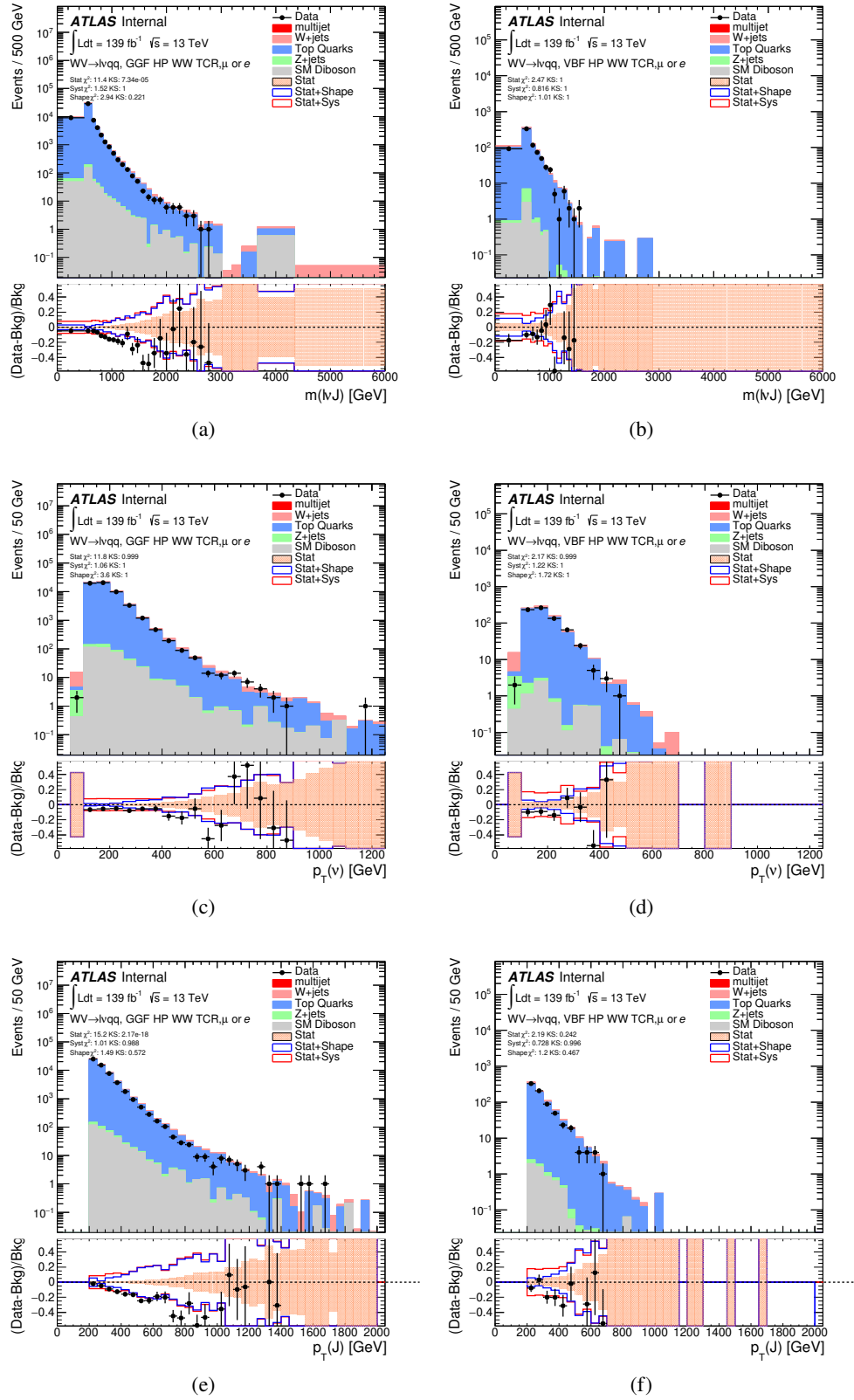


**Figure 9.7:** Data MC comparison for the merged  $WW$  HP TCR. The bottom panel shows the ratio of the difference<sup>89</sup> between data and simulation to simulation. The red bands include the all systematic and statistical uncertainties on the background.

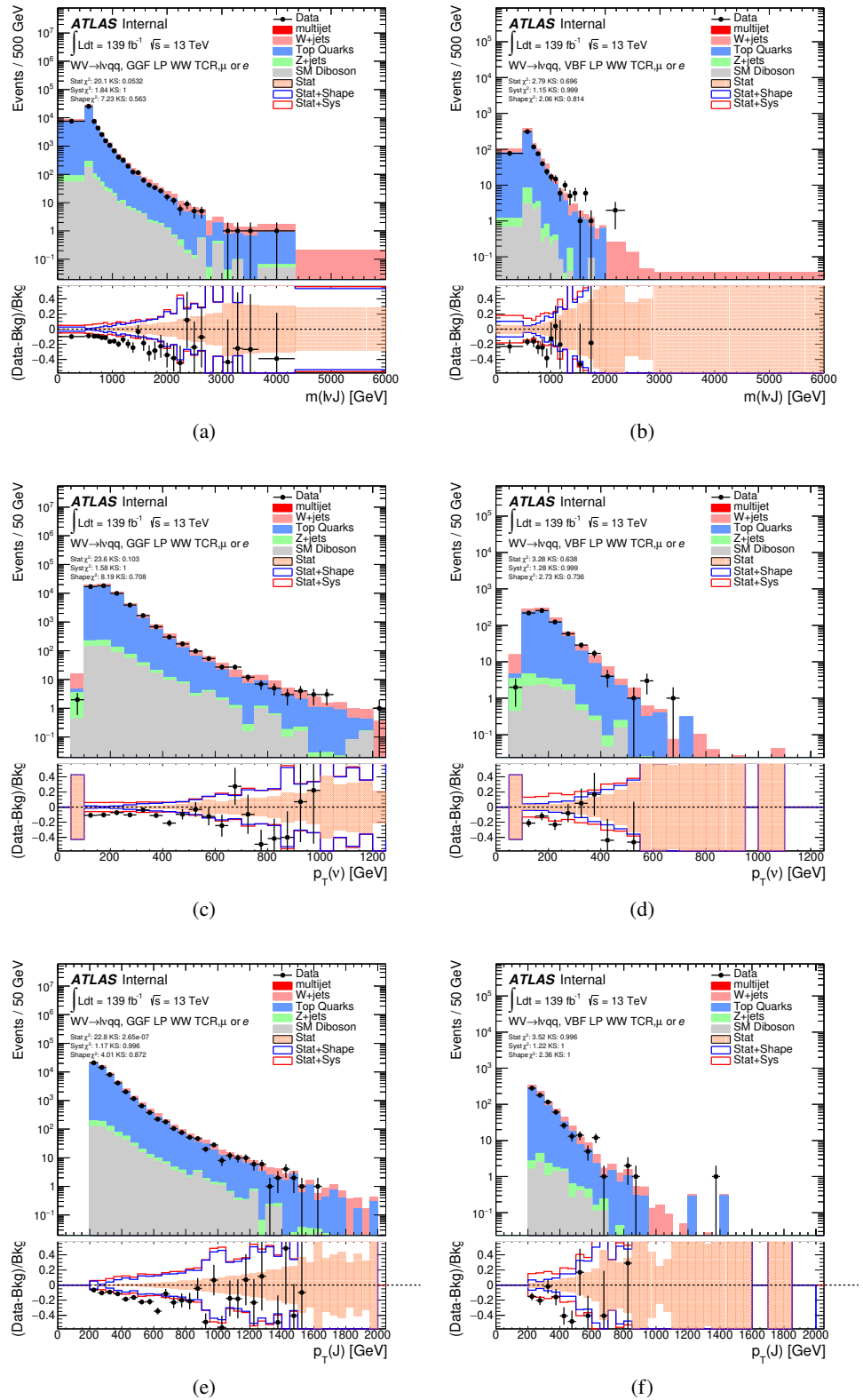


**Figure 9.8:** Data MC comparison for the merged  $WW$  LP TCR. The bottom panel shows the ratio of the difference between data and simulation to simulation. The red bands include the all systematic and statistical uncertainties on the background.

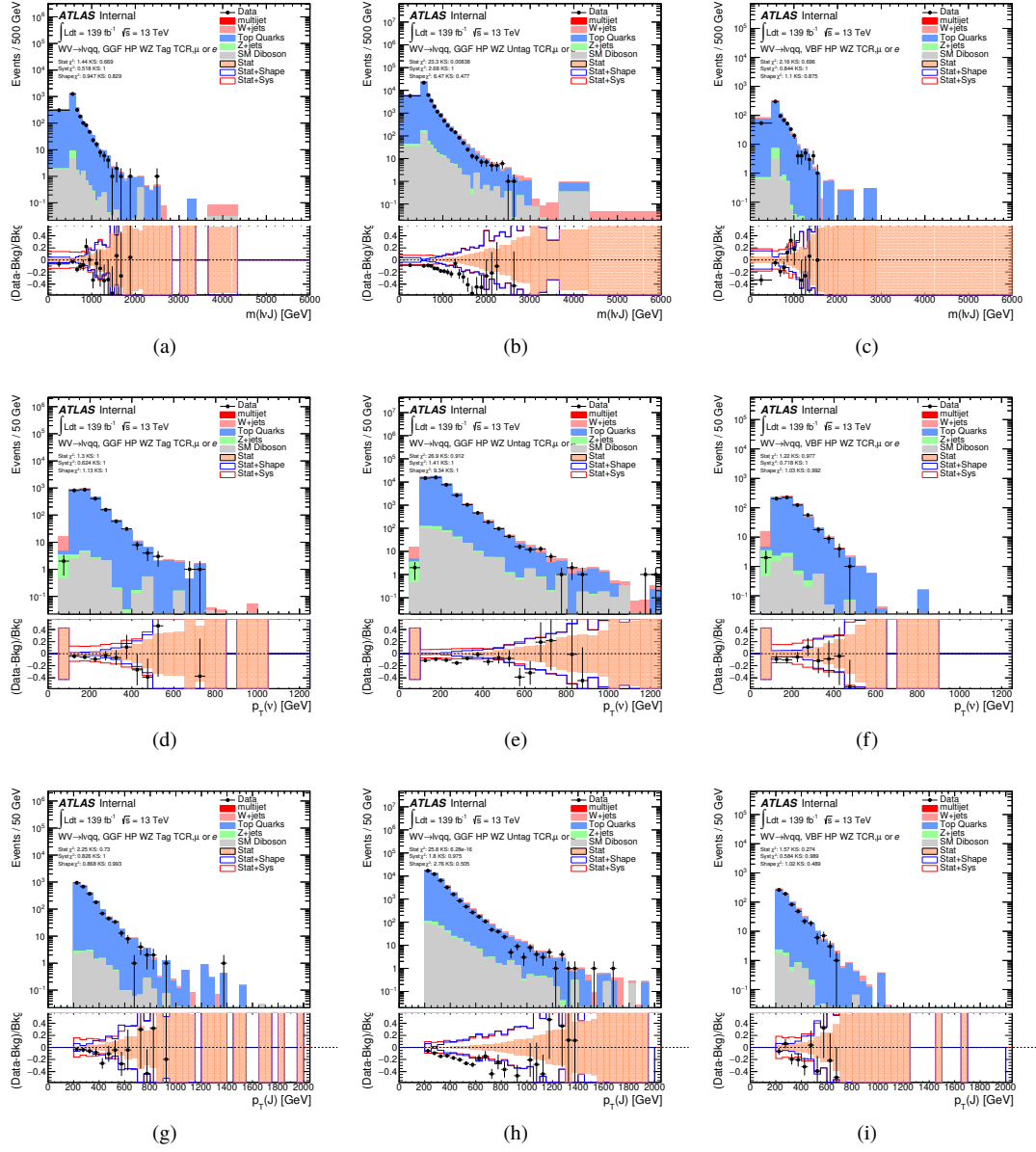


**Figure 9.9:** Data MC comparison for the merged  $WZ$  HP TCR. The bottom panel shows the ratio of the difference between data and simulation to simulation. The red bands include the all systematic and statistical uncertainties on the background.

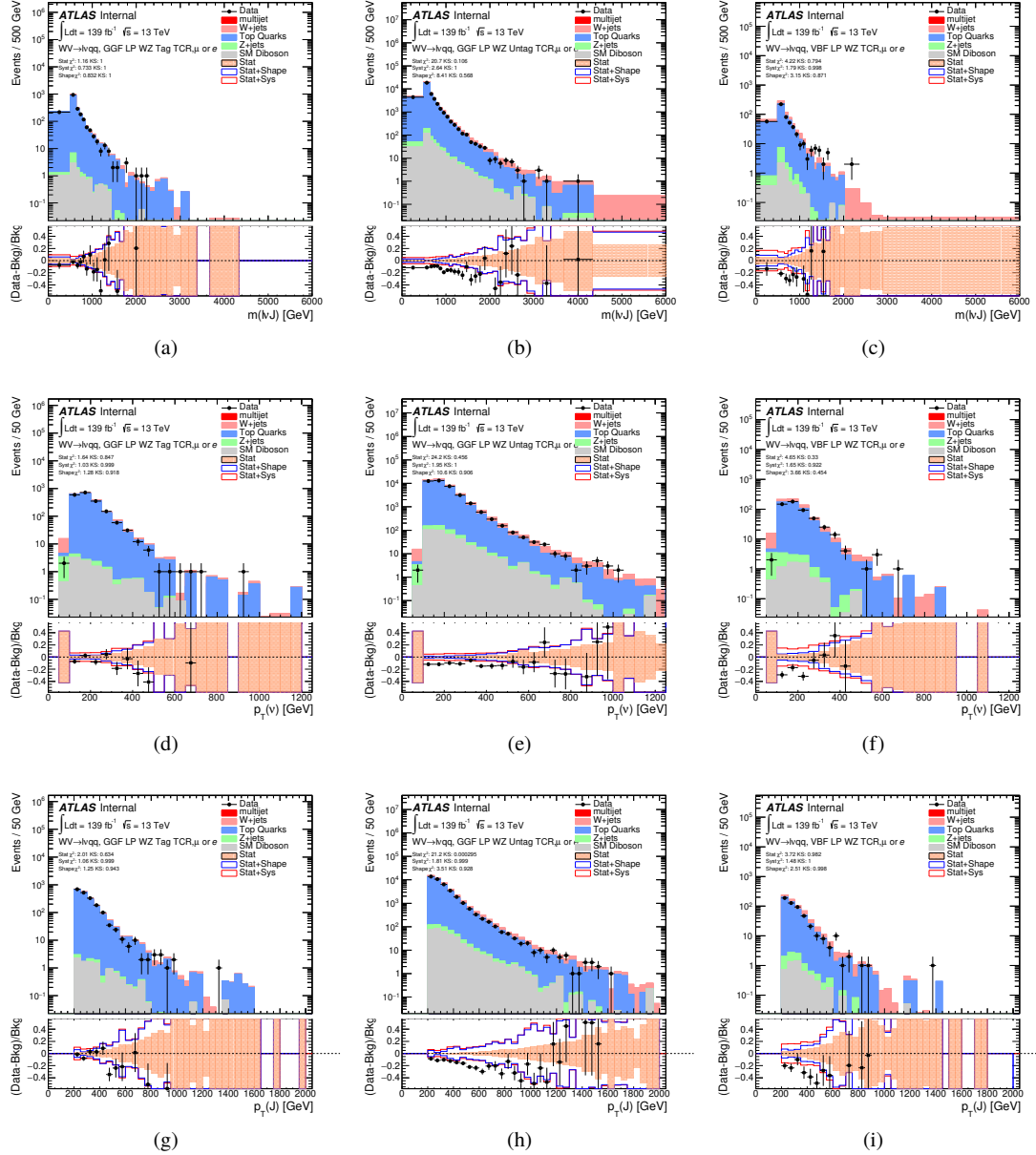


**Figure 9.10:** Data MC comparison for the merged  $WZ$  LP TCR. The bottom panel shows the ratio of the difference between data and simulation to simulation. The red bands include the all systematic and statistical uncertainties on the background.

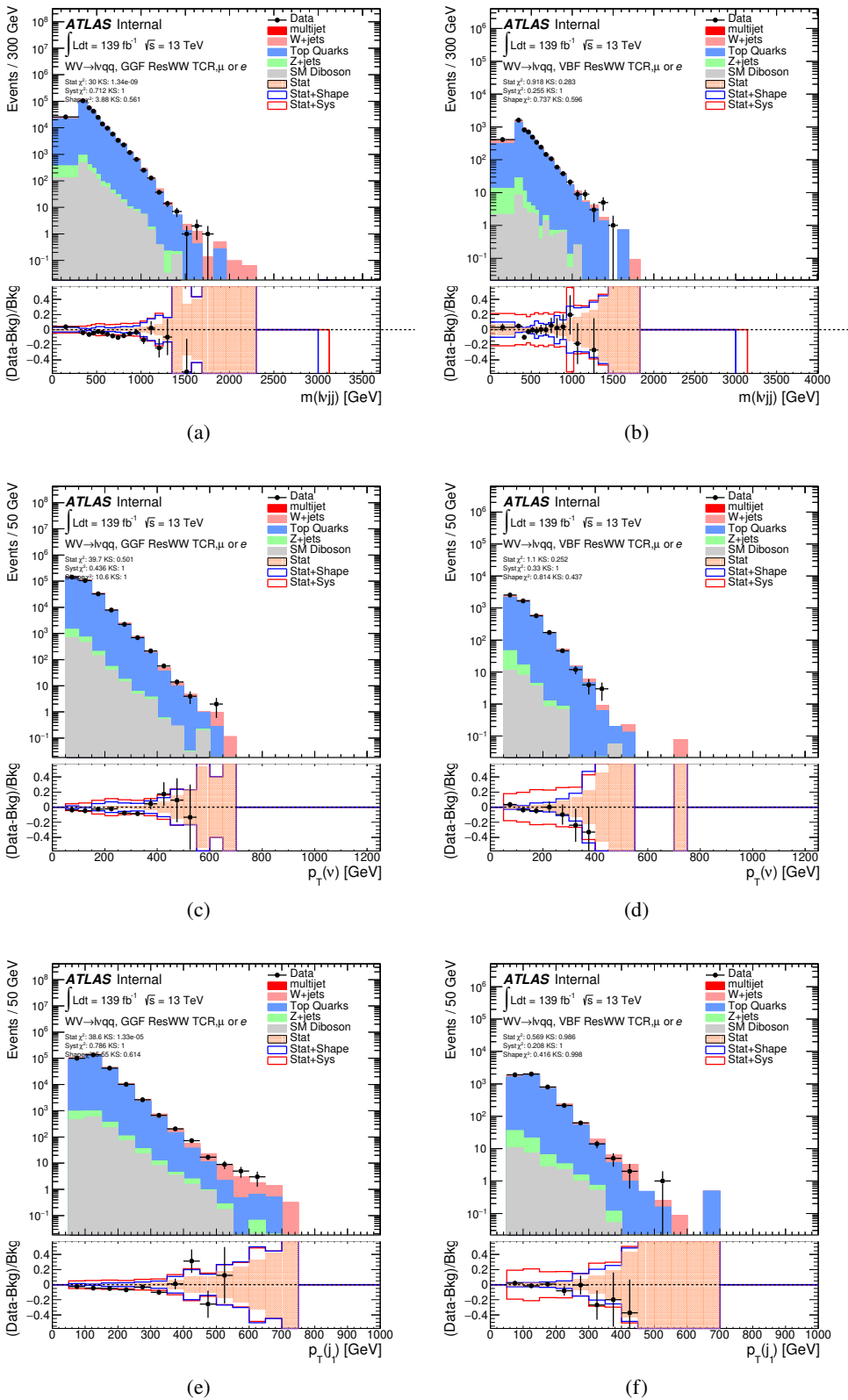


**Figure 9.11:** Data MC comparison for the resolved  $WW$  TCR. The bottom panel shows the ratio of the difference between data and simulation to simulation. The red bands include the all systematic and statistical uncertainties on the background.<sup>93</sup>

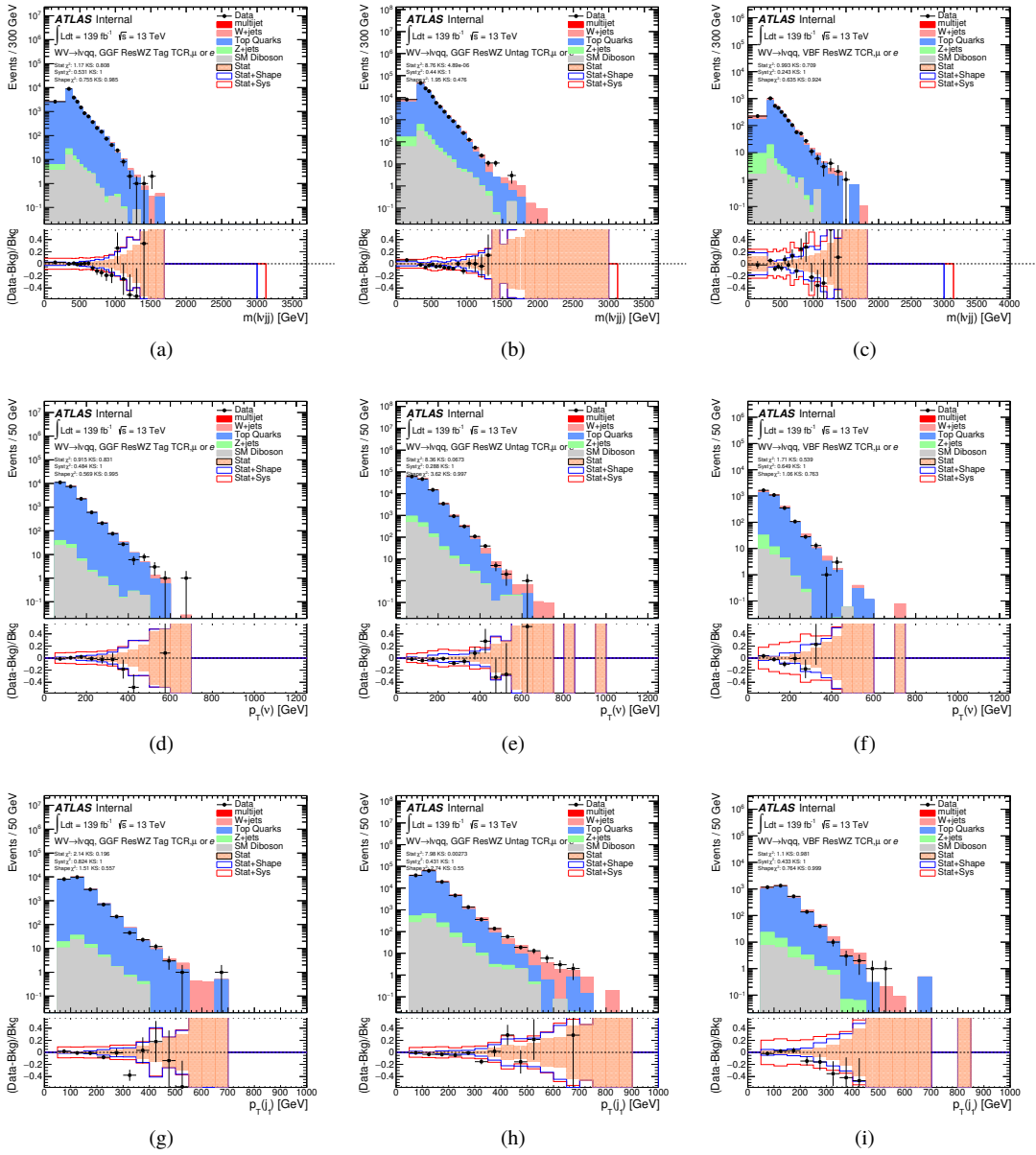


**Figure 9.12:** Data MC comparison for the resolved  $WZ$  TCR. The bottom panel shows the ratio of the difference between data and simulation to simulation. The red bands include the all systematic and statistical uncertainties on the background.

1012    **9.5 Selection Acceptance times efficiency for Sig-**  
 1013    **nal Events**

1014    The acceptance times efficiency for the signal region selection is defined as:

$$A \cdot \epsilon = \frac{N_{\text{events selected}}^{\text{truth}}}{N_{\text{events generated}}^{\text{truth}}} \cdot \frac{N_{\text{events selected}}^{\text{reco}}}{N_{\text{events selected}}^{\text{truth}}} = \frac{N_{\text{events selected}}^{\text{reco}}}{N_{\text{events generated}}^{\text{truth}}} \quad (9.3)$$

1015    The distributions of  $A \cdot \epsilon$  as a function of the resonance mass for the different spin  
 1016    models are shown in Figures 9.14 - ??.

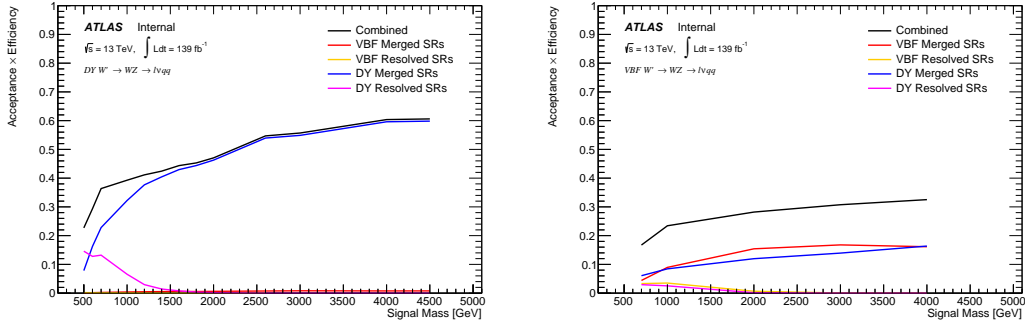


**Figure 9.13:** Selection acceptance times efficiency for the  $W' \rightarrow WZ \rightarrow \ell\nu qq$  events from MC simulations as a function of the  $W'$  mass for (a) Drell-Yan and (b) VBF production, combining the merged HP and LP signal regions of the  $WW \rightarrow \ell\nu J$  selection and the resolved regions of the  $WW \rightarrow \ell\nu jj$  selection.

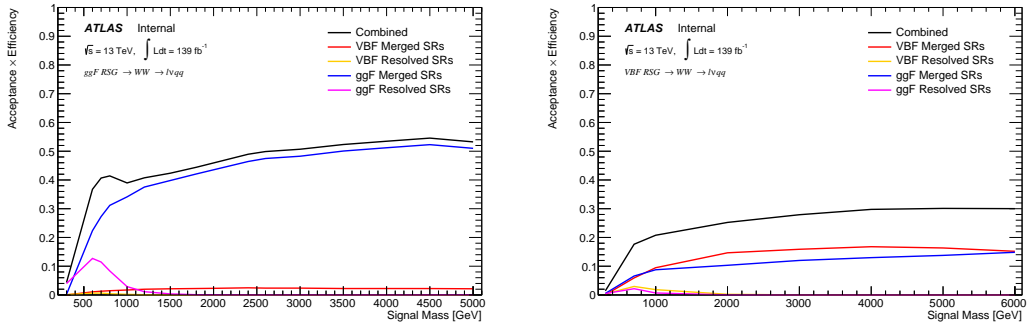


**Figure 9.14:** Selection acceptance times efficiency for the  $G \rightarrow WW \rightarrow \ell\nu qq$  events from MC simulations as a function of the  $G$  mass for (a) Drell-Yan and (b) VBF production, combining the merged HP and LP signal regions of the  $WW \rightarrow \ell\nu J$  selection and the resolved regions of the  $WW \rightarrow \ell\nu jj$  selection.

## 1017 9.6 Background Estimate

### 1018 9.6.1 Control Regions

1019 To more accurately model the two dominant backgrounds in this analysis,  
 1020  $W+jets$  and  $t\bar{t}$ , control regions are constructed for each. These control regions  
 1021 are dominated by these processes and used to extract normalization factors in  
 1022 the final likelihood fit that are then used in the signal region estimates. For the  
 1023  $t\bar{t}$  control region the event must contain at least one such b jet. The WCR is  
 1024 constructed using the  $m_{jj/J}$  mass window sidebands. All other backgrounds are  
 1025 estimated using simulation, except fake lepton backgrounds, which are derived  
 1026 using a data-driven method.

### 1027 9.6.2 Fake Lepton Backgrounds

1028 Backgrounds in this analysis containing real leptons (e.g.  $W/Z+jets$ , diboson,  
 1029  $t\bar{t}$ , single- $t$ ) are well-modeled with simulated samples and constrained with data  
 1030 from CRs. However, the fake lepton background (also referred to as the multijet  
 1031 background) is not well-modeled with simulation. For this reason, the multijet

background is extracted from data. Heavy flavor decay products, jets, and converted photons can be mistakenly reconstructed as electrons. Fake electrons often arise from jet fakes while non-prompt muons usually arise from heavy flavor decay. For this analysis, these fake electrons generally fail the electron ID criteria and fake muons fail the muon isolation requirement. Therefore, to derive the multijet template shape the SR and CR selections and inverted lepton requirements are used as seen in Table 9.4. NB: by inverting the lepton isolation/identification criteria the SRs and CRs are orthogonal.

The template shape of the MJ background is determined by using a multijet validation region (MJVR) that requires the inverted lepton isolation/identification requirement and the two signal jets to satisfy the  $m_{jj}$  requirement used in the  $W+jets$  CRs. The  $E_T^{miss}$  distribution in MJCR is shown in Figure 9.15 for 2017 data. The template is then extracted by subtracting the data in the MJVR from the electroweak background processes. The resulting template and electroweak backgrounds are then fit to data. In this fit, the  $E_T^{miss}$  distribution compared to data to extract electroweak background, multijet electron and muon background normalizations. The fitted scale factors from this MJVR template are then applied in the MJCR template. The electron and muon background normalizations in the MJCR template are parameters in the final simultaneous fit. Technically, there should be a separate template for every CR and SR, but some MJ regions have insufficient statistics to do this. Additionally, the shapes for the MJ templates for VBF and ggF regions are found to be compatible within statistical uncertainty. Therefore, the sample MJ template used for VBF and ggF CR/SRs, but with different pre-MJ-fit scale factors.

This template method was validated using WCR and full Run 2 data. The results of the fit are shown in Table 9.5. The multijet contribution in the muon

channel for  $p_T^W > 150$  GeV is consistent with zero, and therefore neglected in the final fit. Applying the extracted normalization factor to MJVR in WCRs for various kinematic variables such as  $E_T^{miss}$ ,  $W$  transverse mass, lepton  $p_T$ , and the invariant mass as show in Figures 9.16 -9.25. These figures show good agreement between the data and background estimate.

**Table 9.4:** Definitions of “inverted” leptons used in multijet control region

	Criterion	signal lepton	inverted lepton
Electron	ID	TightLH	MediumLH !TightLH
	Calo Isolation	FixedCutHighPtCaloOnlyIso	FixedCutHighPtCaloOnlyIso
Muon	ID	WHSignalMuon	WHSignalMuon
	Track Isolation	FixedCutTightTrackOnlyIso	!FixedCutTightTrackOnlyIso $ptvarcone30/pt < 0.07^*$

\*Only applied to events with  $pTW < 150\text{GeV}$

1063

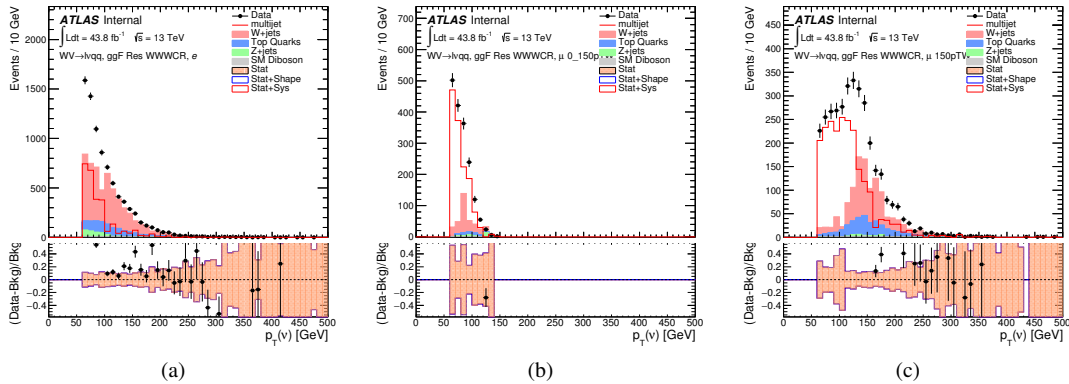


**Figure 9.15:** The  $E_T^{miss}$  distribution in MJCR for 2017 data in the electron channel(left), muon channel with  $W$ -boson  $p_T < 150$  GeV (center) and  $> 150$  GeV (right). Multi-jet templates are calculated as remaining data components after excluding known MC

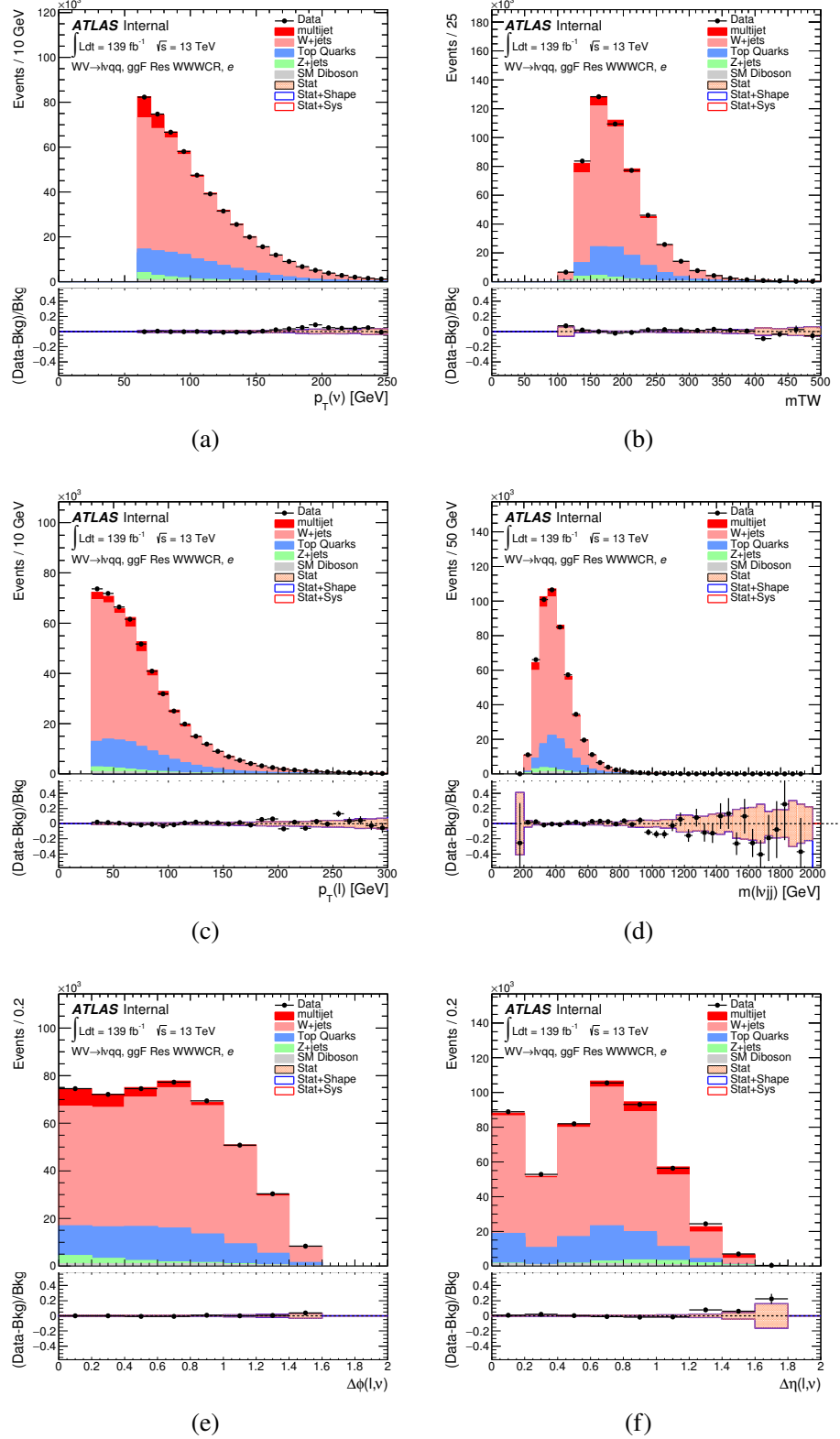


**Figure 9.16:** Postfit Data/MC comparison of distributions of  $E_T^{miss}$ ,  $m_T^W$ , lepton and neutrino  $p_T$ ,  $m_{\ell\nu jj}$ , lepton- $\nu$  angular distance in the  $WW$  electron channel. The MJ template is obtained from the pre-MJ-fit.

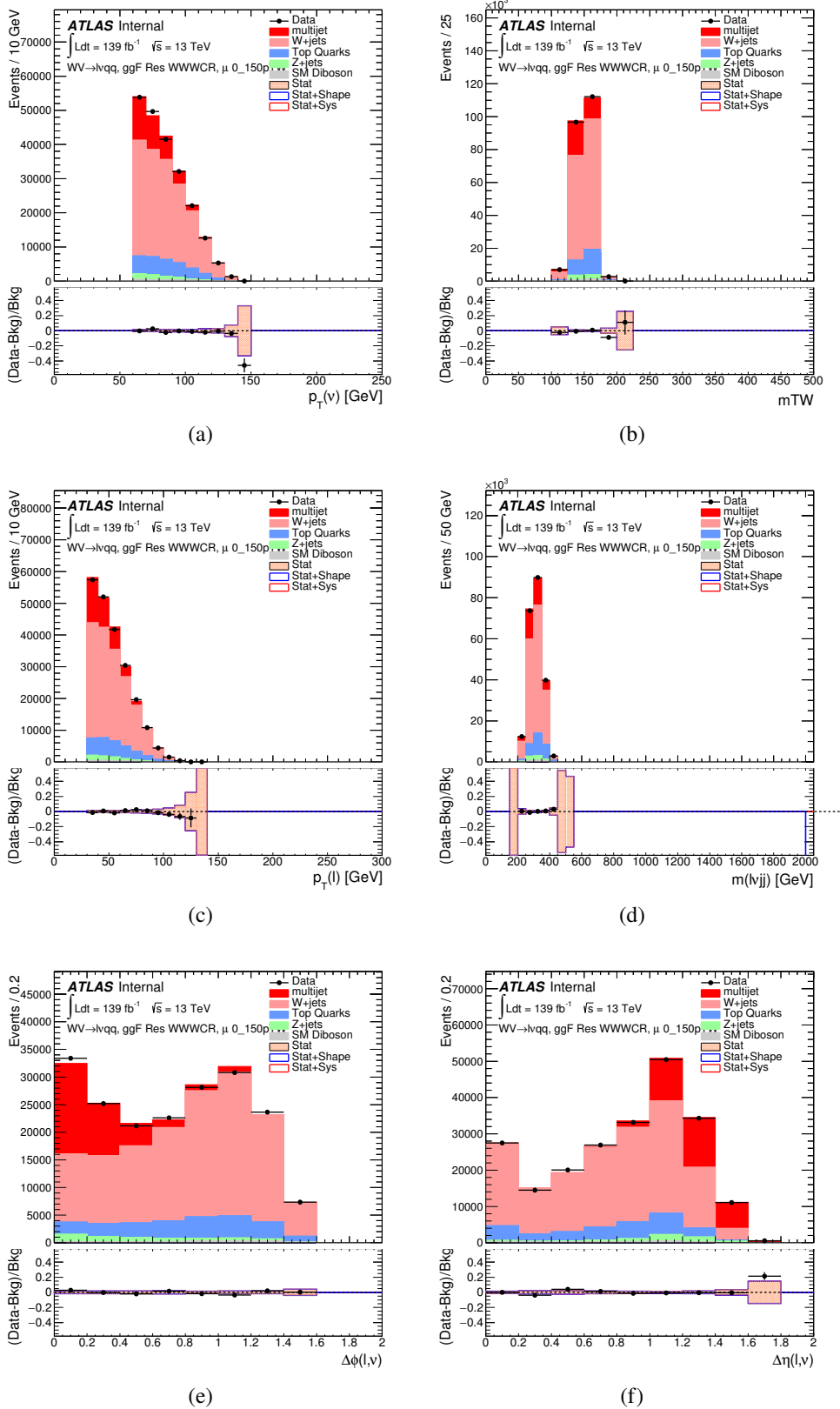


**Figure 9.17:** Postfit Data/MC comparison of distributions of  $E_T^{miss}$ ,  $m_T^W$ , lepton and neutrino  $p_T$ ,  $m_{l\nu jj}$ , lepton- $\nu$  angular distance in the  $WW$  muon channel. The MJ template is obtained from the pre-MJ-fit.

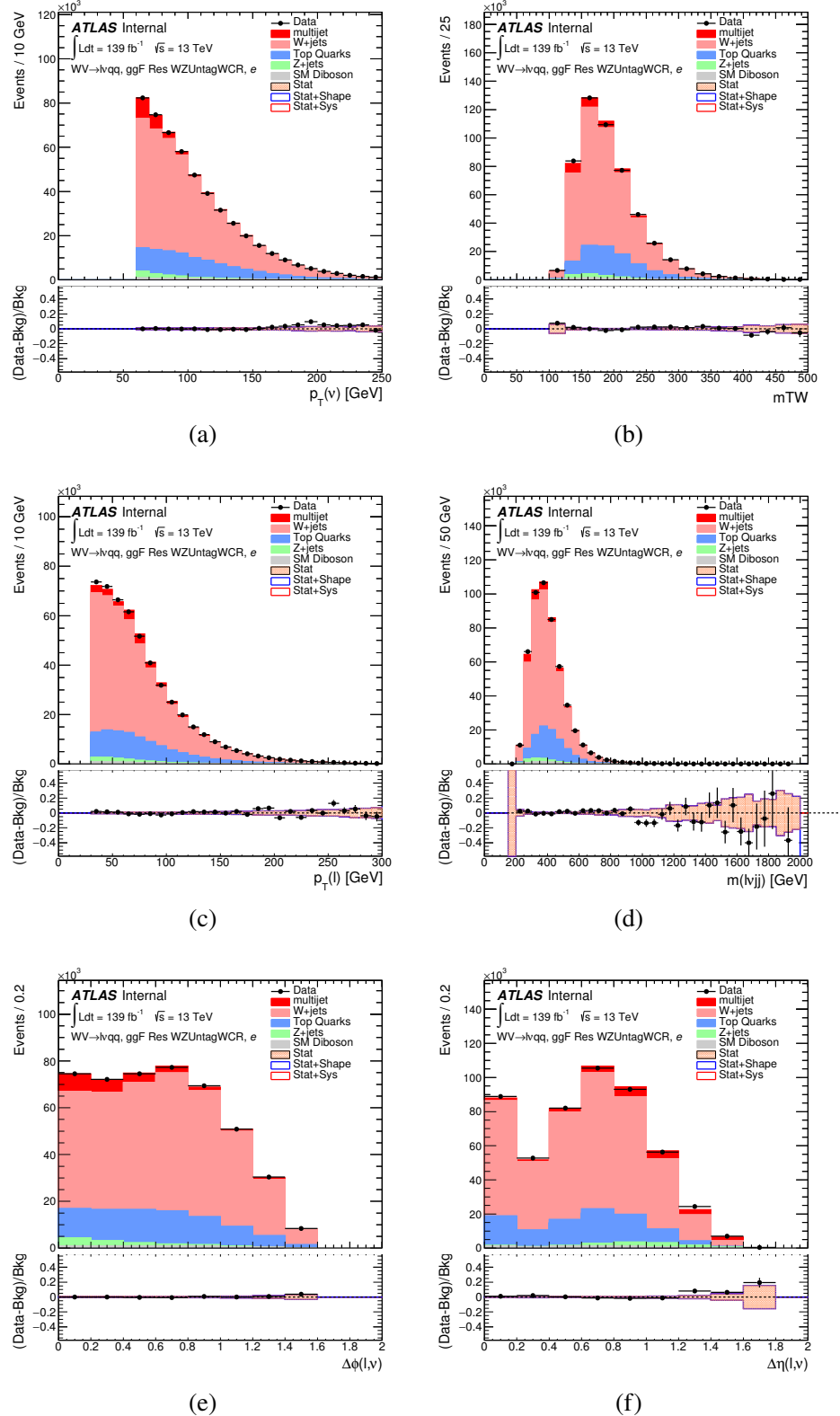


**Figure 9.18:** Postfit Data/MC comparison of distributions of  $E_T^{miss}$ ,  $m_T^W$ , lepton and neutrino  $p_T$ ,  $m_{l\nu jj}$ , lepton- $\nu$  angular distance in the  $WZ$  untag electron channel. The MJ template is obtained from the pre-MJ-fit.

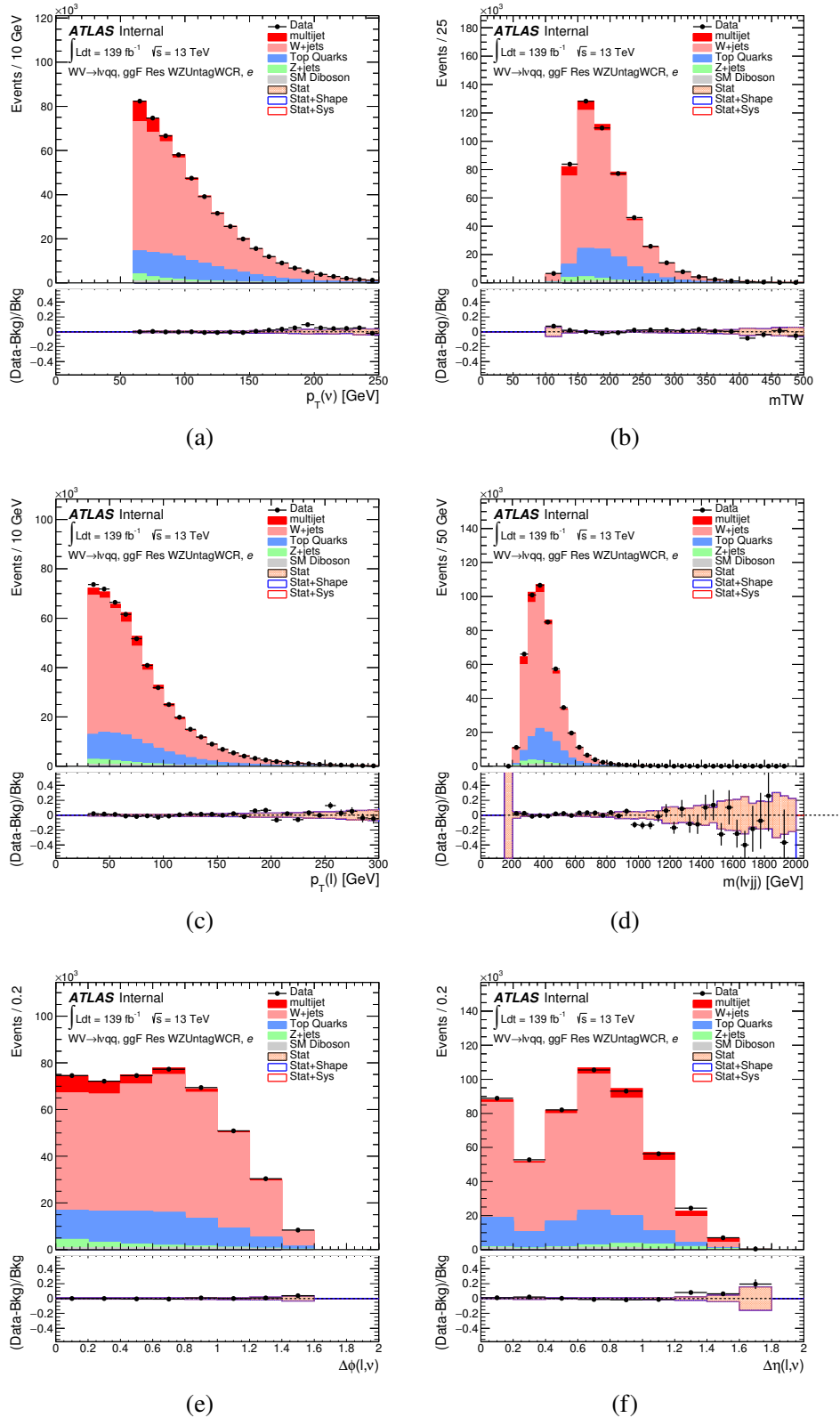


**Figure 9.19:** Postfit Data/MC comparison of distributions of  $E_T^{miss}$ ,  $m_T^W$ , lepton and neutrino  $p_T$ ,  $m_{l\nu jj}$ , lepton- $\nu$  angular distance in the  $WZ$  untag muon channel. The MJ template is obtained from the pre-MJ-fit.

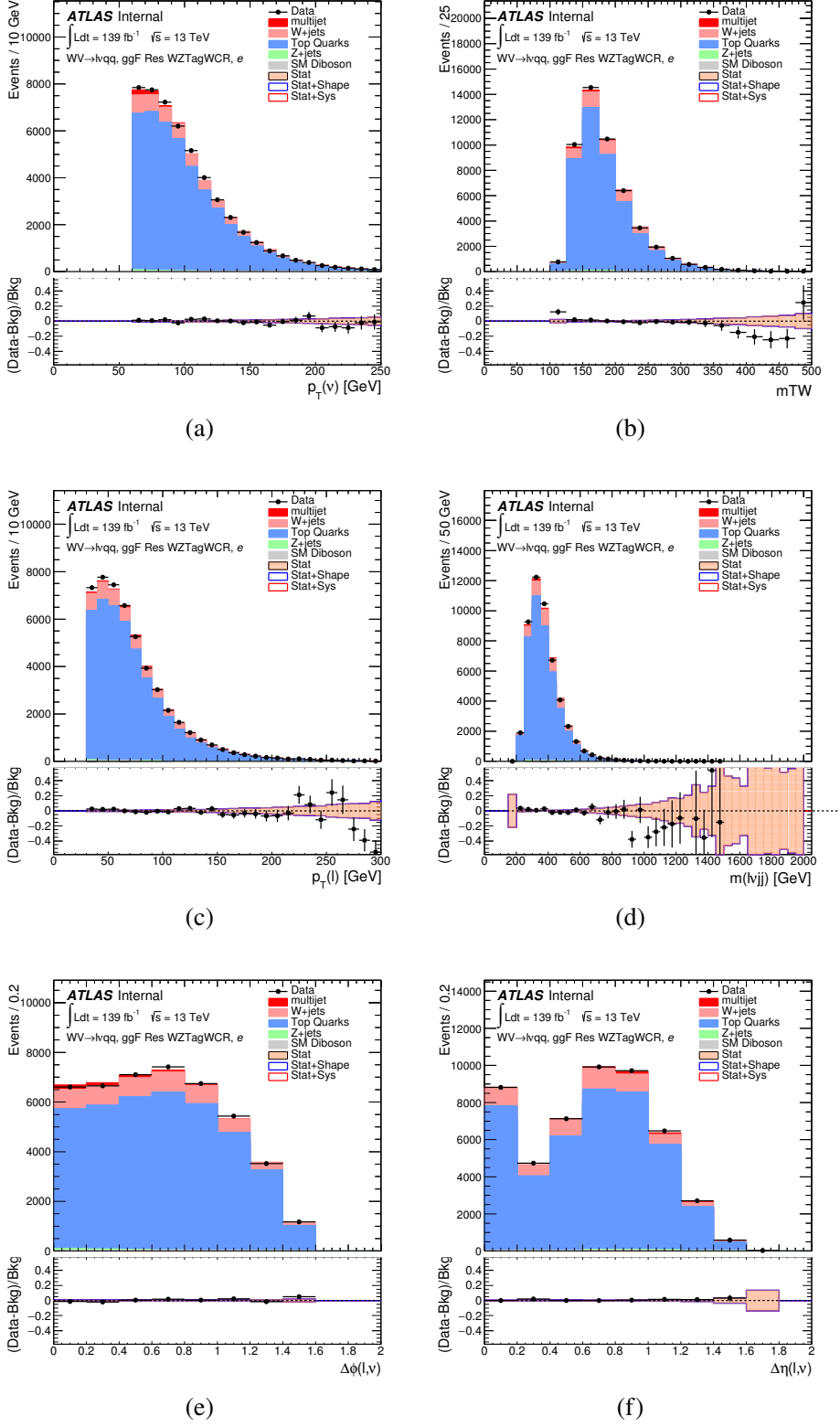


**Figure 9.20:** Postfit Data/MC comparison of distributions of  $E_T^{miss}$ ,  $m_T^W$ , lepton and neutrino  $p_T$ ,  $m_{l\nu jj}$ , lepton- $\nu$  angular distance in the  $WZ$  untag electron channel. The MJ template is obtained from the pre-MJ-fit.

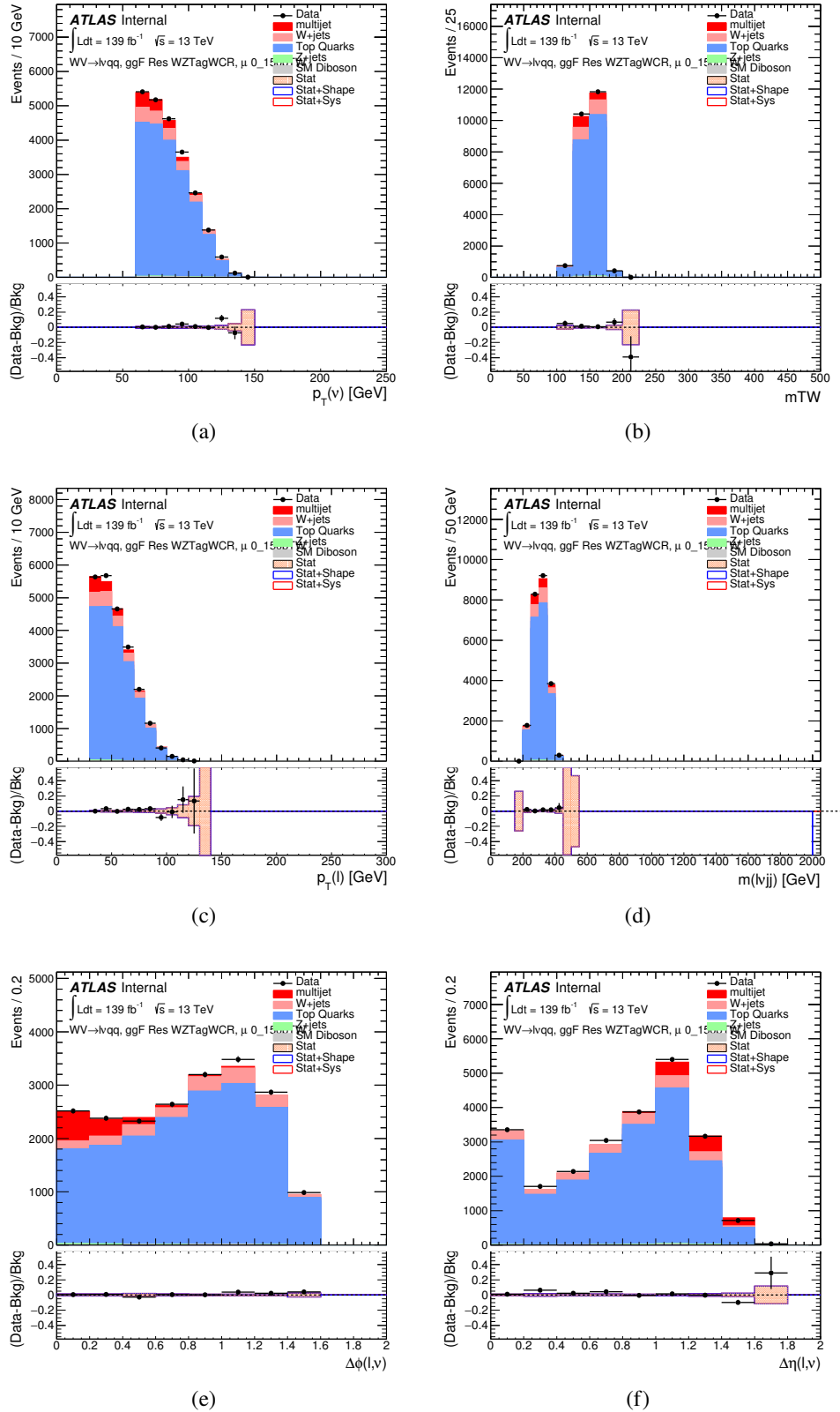


**Figure 9.21:** Postfit Data/MC comparison of distributions of  $E_T^{miss}$ ,  $m_T^W$ , lepton and neutrino  $p_T$ ,  $m_{l\nu jj}$ , lepton- $\nu$  angular distance in the  $WZ$  untag muon channel. The MJ template is obtained from the pre-MJ-fit.

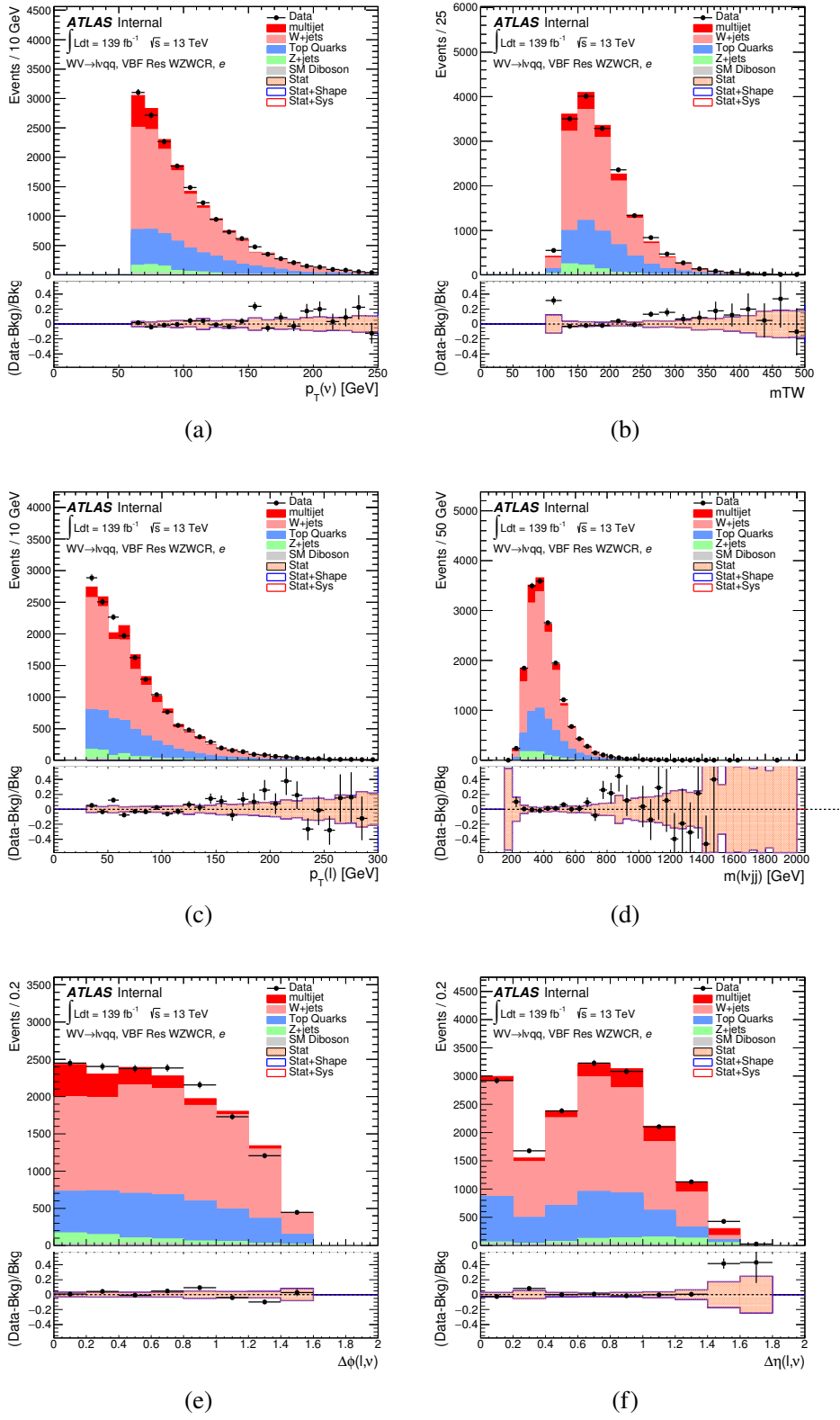


**Figure 9.22:** Postfit Data/MC comparison of distributions of  $E_T^{miss}$ ,  $m_T^W$ , lepton and neutrino  $p_T$ ,  $m_{l\nu jj}$ , lepton- $\nu$  angular distance in the VBF  $WW$  electron channel. The MJ template is obtained from the pre-MJ-fit.

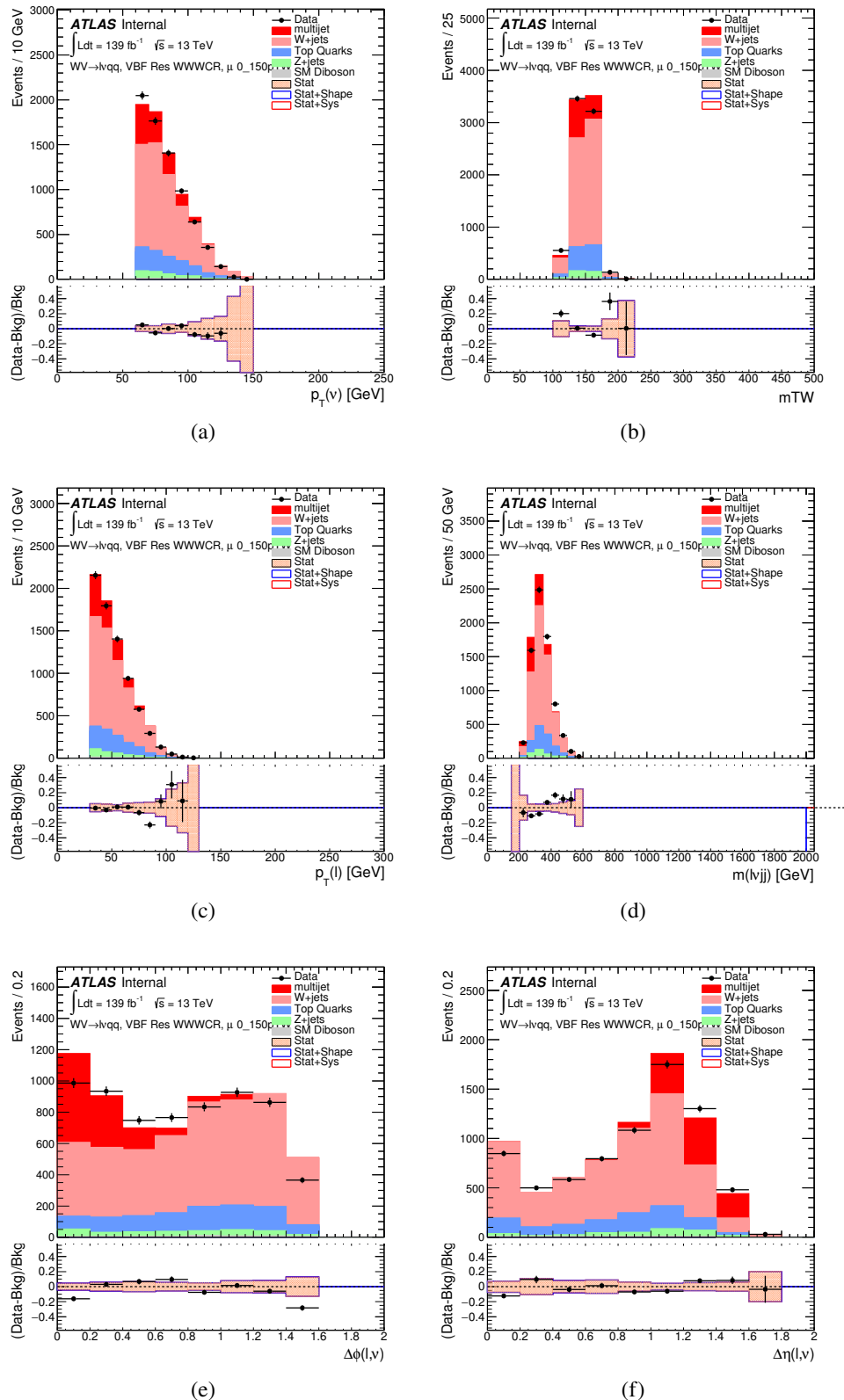


**Figure 9.23:** Postfit Data/MC comparison of distributions of  $E_T^{miss}$ ,  $m_T^W$ , lepton and neutrino  $p_T$ ,  $m_{l\nu jj}$ , lepton- $\nu$  angular distance in the VBF  $WW$  muon channel. The MJ template is obtained from the pre-MJ-fit.

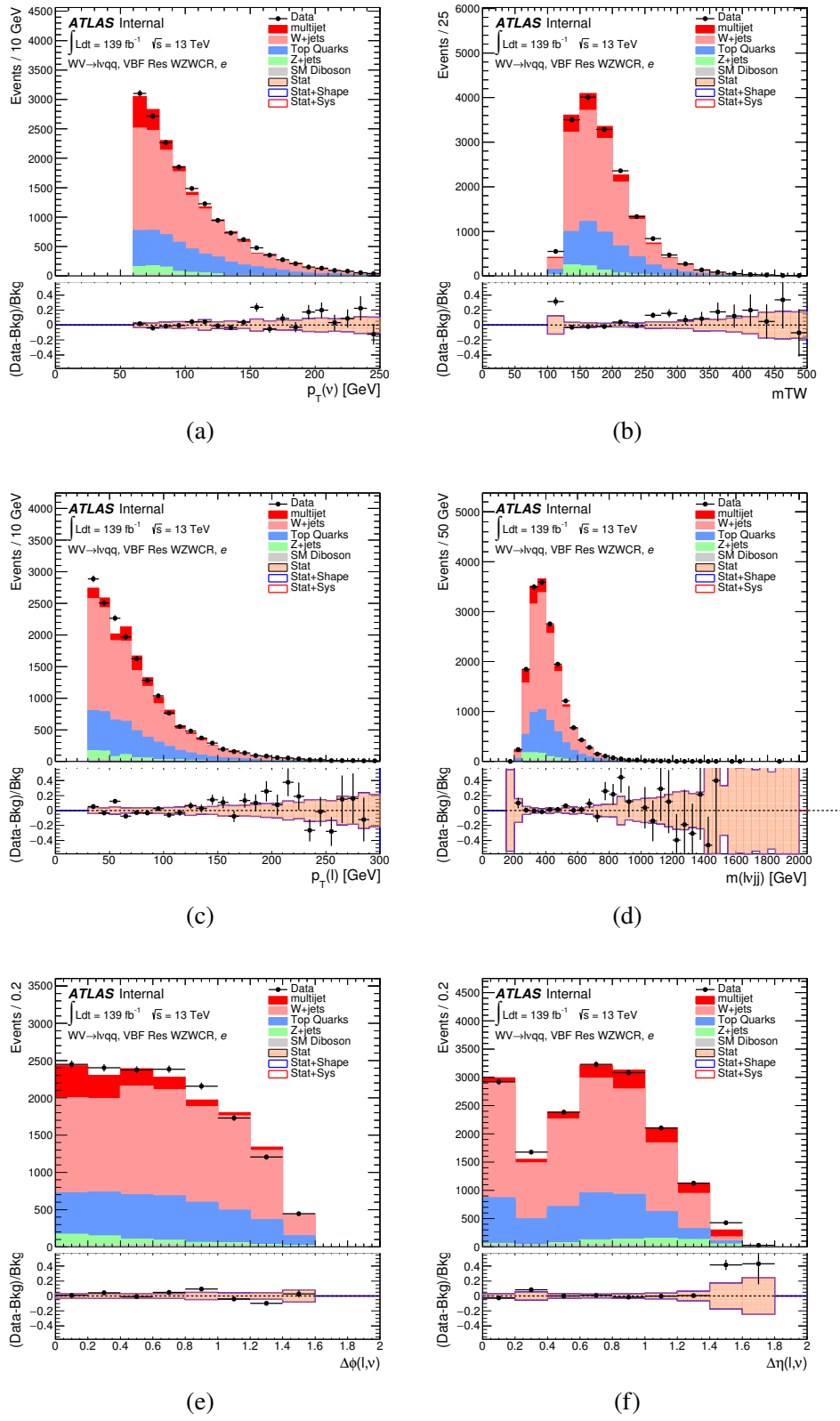


**Figure 9.24:** Postfit Data/MC comparison of distributions of  $E_T^{miss}$ ,  $m_T^W$ , lepton and neutrino  $p_T$ ,  $m_{l\nu jj}$ , lepton- $\nu$  angular distance in the VBF  $WZ$  electron channel. The MJ template is obtained from the pre-MJ-fit.

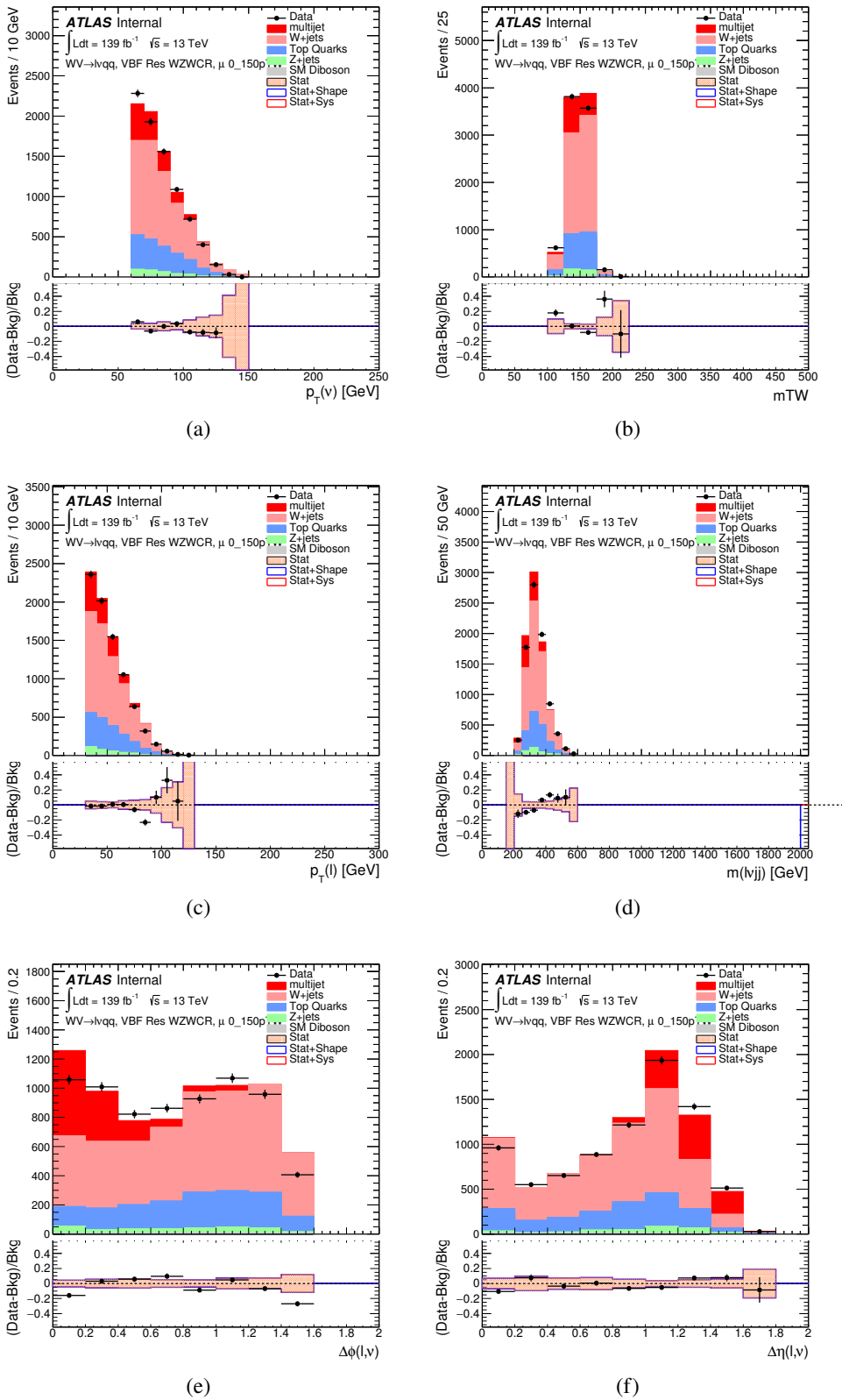


**Figure 9.25:** Postfit Data/MC comparison of distributions of  $E_T^{miss}$ ,  $m_T^W$ , lepton and neutrino  $p_T$ ,  $m_{l\nu jj}$ , lepton- $\nu$  angular distance in the VBF  $WZ$  muon channel. The MJ template is obtained from the pre-MJ-fit.

Full Run 2  
ggF Res WWWCR

Sample	Yield	R.U.	SF
Top&W	$645040 \pm 1971.68$	0.31%	0.998
Z&VV	24075.9		fixed
MJ_el	$24156.3 \pm 1224.62$	5.06%	3.973
MJ_mu	$35528.5 \pm 923.94$	2.60%	9.019

ggF Res WZ01bWCR

Sample	Yield	R.U.	SF
Top&W	$644690 \pm 1981.4$	0.31%	0.997
Z&VV	24075.9		fixed
MJ_el	$24366.5 \pm 1232.69$	5.05%	3.874
MJ_mu	$35528.5 \pm 921.27$	2.58%	8.746

ggF Res WZ2bWCR

Sample	Yield	R.U.	SF
Top&W	$71236.5 \pm 688.74$	0.97%	1.031
Z&VV	518.5		fixed
MJ_el	$595.63 \pm 449.34$	75.44%	0.094
MJ_mu	$1196.9 \pm 222.13$	18.56%	0.294

VBF Res WWWCR

Sample	Yield	R.U.	SF
Top&W	$19032.3 \pm 364.43$	1.91%	0.928
Z&VV	1091.63		fixed
MJ_el	$1425.73 \pm 214.42$	15.03%	0.235
MJ_mu	$1281.36 \pm 157.21$	11.83%	0.314

VBF Res WZWCR

Sample	Yield	R.U.	SF
Top&W	$21341.8 \pm 392.21$	1.84%	0.942
Z&VV	1111.75		fixed
MJ_el	$1413.76 \pm 230.36$	16.29%	0.225
MJ_mu	$1281.36 \pm 157.21$	12.27%	0.314

**Table 9.5:** Fit validation result in WCRs for 2015+16 data. The fit is done in various WCRs, in order to obtain the corresponding scale factors for MJ templates: ggF resolved WCR for the  $WW \rightarrow lvqq$  selection, ggF resolved untagged WCR for the  $WZ \rightarrow lvqq$  selection, ggF resolved tagged WCR for the  $WZ \rightarrow lvqq$  selection, VBF resolved WCR for the  $WW \rightarrow lvqq$  selection, and VBF resolved WCR for the  $WZ \rightarrow lvqq$  selection. Post-fit event yields for electroweak processes and MJ contributions are shown. The SF column shows the corresponding normalization scale factors for electroweak processes from the fit. R.U. stands for relative uncertainty.

1064 **Chapter 10**

1065 **Systematic Uncertainties**

1066 This section describes the sources of systematic uncertainties considered in  
1067 this analysis. These uncertainties are divided into three categories: experimental  
1068 uncertainties, background modeling uncertainties, and theoretical uncertainties on  
1069 signal processes. In the statistical analysis each systematic uncertainty is treated  
1070 as a nuisance parameter estimated on the  $m_{VV}$  distribution.

1071 **10.1 Experimental Systematics**

1072 The uncertainty on the integrated luminosity of the dataset used is 1.7% and  
1073 a systematic in the final fit. This uncertainty was calculated using  $x - y$  beam  
1074 separation scans [ref P55].

1075 An additional source of systematic uncertainty is assigned to the pileup mod-  
1076eling in MC samples. This ensures simulated detector response and particle re-  
1077construction conditions are as similar as possible. The distribution of the average  
1078 number of interactions per bunch crossing applied to simulation is called the  $\mu$  pro-  
1079file. The pileup modeling uncertainty is accounted for by re-weighting simulated  
1080events so the average number of interactions per bunch crossing varies within its

1081 uncertainty due to systematics from vertex reconstruction [ref ATL-COM-SOFT-  
1082 2015-119]. The associated re-weighting factors are propagated through the entire  
1083 analysis chain to construct a systematic uncertainty on  $m_{VV}$ .

1084 The single-lepton and  $E_T^{miss}$  triggers used are not fully efficient, so scale factors  
1085 are applied to simulation to more accurately model the data. These scale factors  
1086 are given by the ratio of the distribution of offline objects before trigger selection  
1087 and after trigger selection. The associated uncertainty on these scale factors are  
1088 used in the final fit.

1089 Uncertainties on small-R jet energy scale and resolution are measured in-situ  
1090 by calculating the response between data and simulation. This analysis uses a  
1091 reduced set of JES and JER uncertainties (totaling 30 and 8 systematics, re-  
1092 spectively). These reduced sets of systematics are calculated using a principal  
1093 component analysis, yield largely uncorrelated independent systematics. These  
1094 uncertainties on JES and JER account for the dependence on  $p_T$ ,  $\eta$ ,  $\mu$ , flavor re-  
1095 sponse and global sequential corrections. Systematic uncertainties associated with  
1096  $b$ -tagging are also considered. These systematics are evaluated as uncertainties on  
1097 the scale factor which account for the difference in  $b$ -tagging efficiencies in data  
1098 and MC, and the flavor dependence (between b, c, and light jets).

1099 The uncertainty on the  $p_T$  scale of the large-R jets is determined by comparing  
1100 the jet's  $p_T^{calo}$  to  $p_T^{track}$  in di-jet simulation and data. In addition to this uncertain-  
1101 ties from tracking, modeling (Pythia vs Herwig), and statistical constraints are  
1102 also calculated. The large-R jet  $p_T$  resolution is given by smearing the jet  $p_T$  with  
1103 a Gaussian with a 2% width.

1104 The  $W/Z$  tagging efficiency SF is estimated by comparing the tagging effi-  
1105 ciency in simulation with that in data for four regions of the  $W/Z$  tagger ( $D_2$  fail,  
1106  $m_J$  fail;  $D_2$  pass,  $m_J$  fail;  $D_2$  fail,  $m_J$  pass;  $D_2$  pass,  $m_J$  pass). (Additionally,

1107 separate scale factors are determined for events with large-R jets from  $W$  bosons  
 1108 and top backgrounds.) A simultaneous template fit is used to fit the signal jets  
 1109 (jets initiated by  $W/Z$  bosons or top quarks) and background jets (all other jets  
 1110 from the simulated backgrounds) to the data in the four regions. using the  $m_J$   
 1111 distributions. The SF for a given region is then given by:

$$SF = \frac{\epsilon_{data} = \frac{N_{fitted-signals}^{region}}{N_{all-regions}^{fitted-signals}}}{\epsilon_{MC} = \frac{N_{signal}^{region}}{N_{signal}^{all-regions}}} \quad (10.1)$$

1112 The effects of experimental and theoretical uncertainties on the efficiency scale  
 1113 factor are determined by taking the ratio of efficiencies in data and simulation.  
 1114 By taking this ratio the uncertainties not arising for jet mass and  $D_2$  cancel.

1115 Lepton identification, reconstruction, isolation systematic uncertainties are de-  
 1116 termined by reconstructing the  $Z$  mass peak with a tag and probe method. The  
 1117 lepton energy and momentum scales are also measured with the  $Z$  mass peak.

1118 As  $E_T^{miss}$  is calculated using all the physics objects in the event, all those objects  
 1119 associated errors result in an uncertainty on  $E_T^{miss}$ . Additionally, the unassociated  
 1120 tracks used to construct  $E_T^{miss}$  contribute to the uncertainty on  $E_T^{miss}$ .

## 1121 10.2 Theory Systematics

1122 Theoretical uncertainties for signal and background processes arise from un-  
 1123 certainties in the parameters used in Monte Carlo simulation. In particular for  
 1124 the  $t\bar{t}$ ,  $W/Z+jets$ , diboson backgrounds and signal samples, the QCD scale, PDF,  
 1125 generator and hadronization uncertainties were evaluated. To assess the QCD  
 1126 scale uncertainty the renormalization and factorization scales were scaled up and  
 1127 down by a factor of two at the event generation stage of sample production. Un-

certainties due to the choice of the parton distribution functions were evaluated by re-weighting samples from the nominal PDF to a set of error PDFs which account for the uncertainty of the fits used to produce the PDF set. In addition to this, samples are re-weighted to different PDF sets to account for the arbitrariness of the PDF choice. The difference between the  $m_{WV}$  distributions using different event generators is assessed by comparing samples generated with different generators. Similarly, the uncertainty in hadronization models is accounted for by comparing samples created using different hadronization models (e.g.  $t\bar{t}$  Powheg is compared to AMC@NLO,  $W + jets$  compares Sherpa and MadGraph+Pythia samples). Figures 10.2 - 10.8 show the impact of these uncertainties on the  $t\bar{t}$  and  $W/Z + jets$  backgrounds. Additionally, contributions to the diboson background for the VBF analysis were found to be small and were accounted for by including a 5(10)% systematic in the diboson normalization in the final fit.

The normalization of the  $t\bar{t}$  and  $W+jets$  processes impact the multijet template shape. The impact of these normalizations was assessed by including a shape systematic on the multijet background from varying the  $t\bar{t}$  and  $W+jets$  normalization factors.

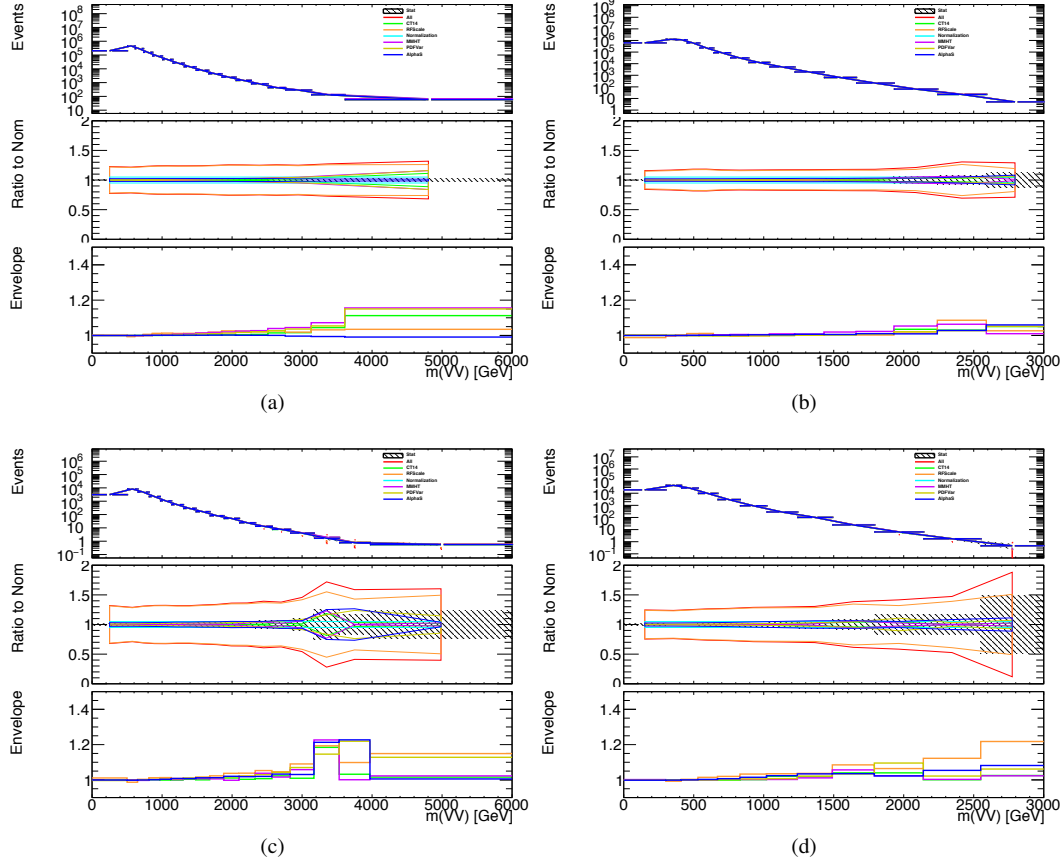


**Figure 10.1:** The  $W/Z + \text{jet}$  systematics for the a) Merged ggF, b) Resolved ggF, c) Merged VBF, and d) Resolved VBF regions. The top subplot shows the nominal and variation distributions/bands, the middle shows the ratio of the two, and the final shows just the shape of the envelope (the final uncertainty).

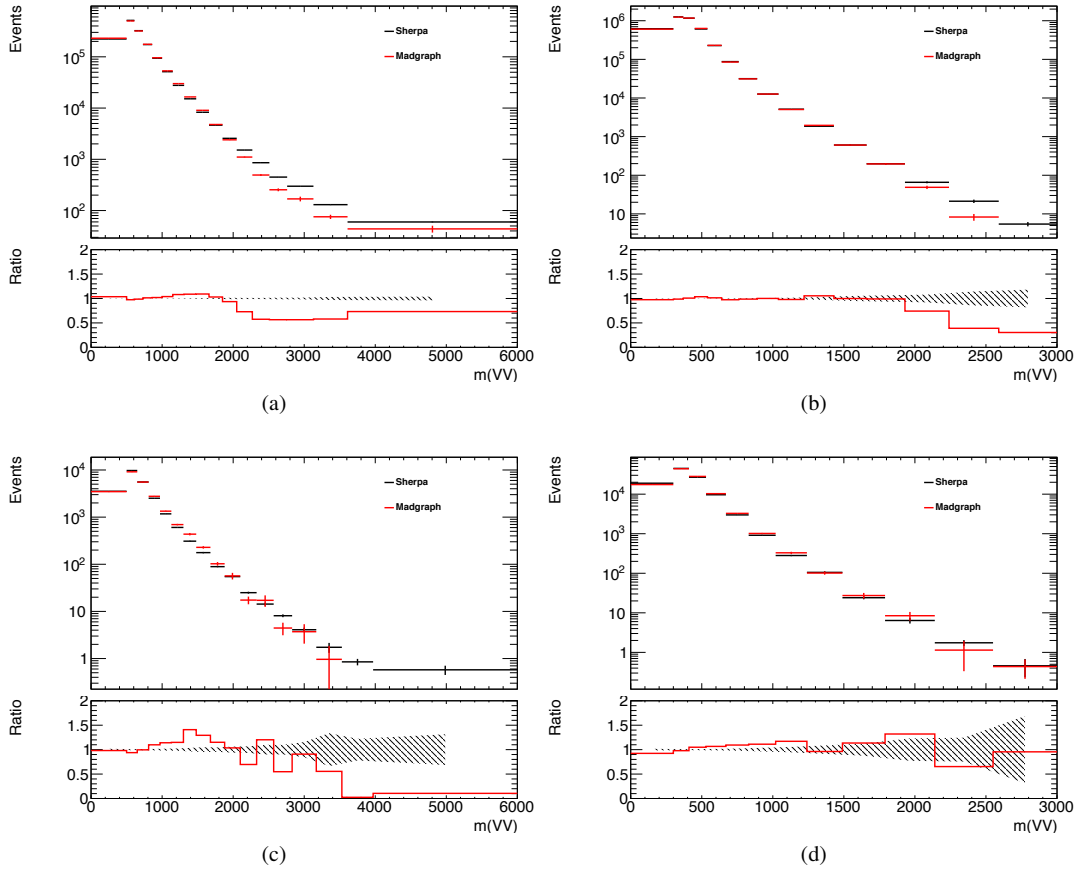


**Figure 10.2:** The two-point generator comparison between Sherpa and MadGraph for the  $W/Z + \text{jet}$  samples in the a) Merged ggF, b) Resolved ggF, c) Merged VBF, and d) Resolved VBF regions. The normalization of the Madgraph sample is set to the Sherpa value to consider only shape effects. The bottom inset shows the ratio of the two.

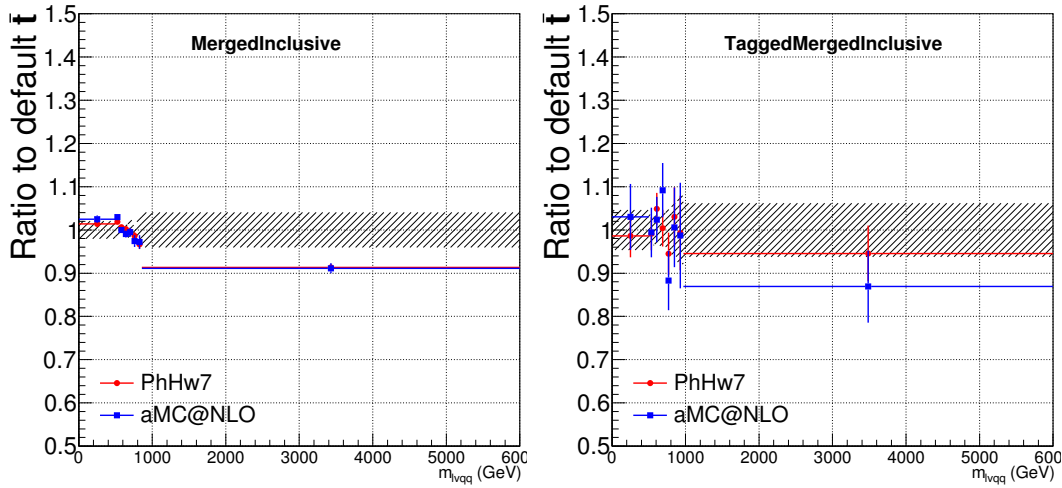


**Figure 10.3:** Ratio between the variations of generator (red) and hadronization (blue) variations for the Merged regime for  $t\bar{t}$  sample.

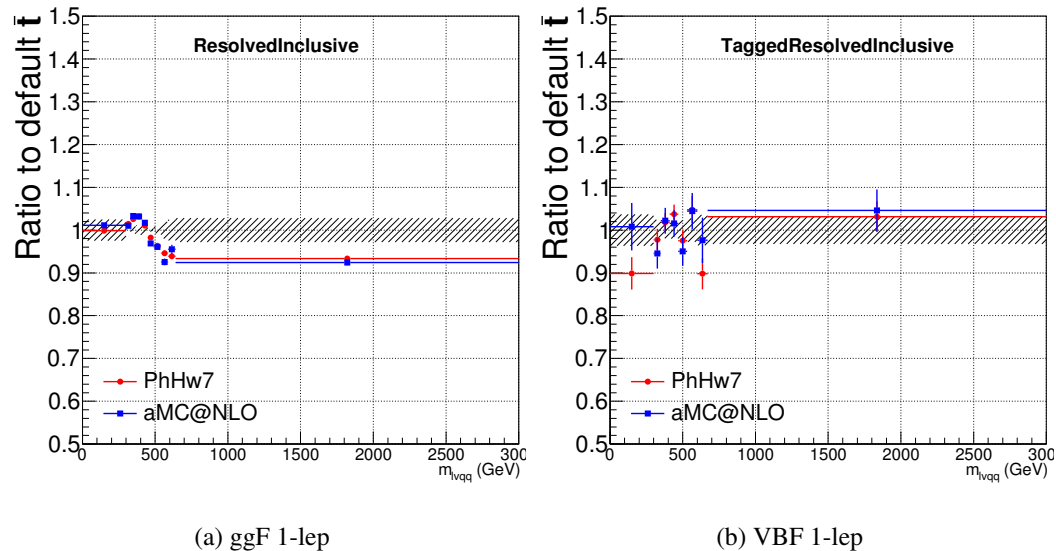


**Figure 10.4:** Ratio between the variations of generator (red) and hadronization (blue) variations for the Resolved regime for  $t\bar{t}$  sample.

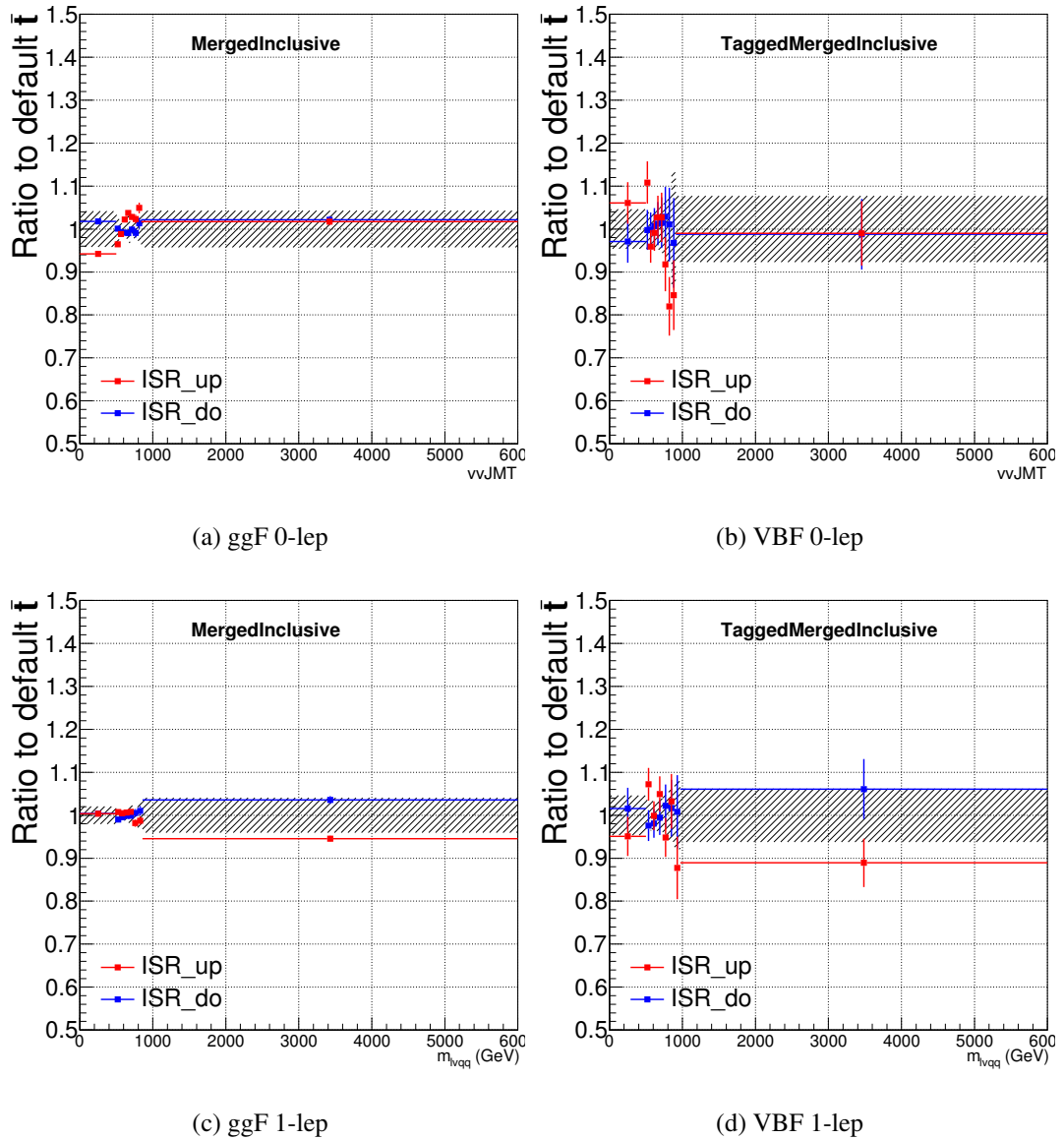


**Figure 10.5:** Ratio between the variations of ISR up (red) and down (blue) variations for the Merged regime for  $t\bar{t}$  sample.

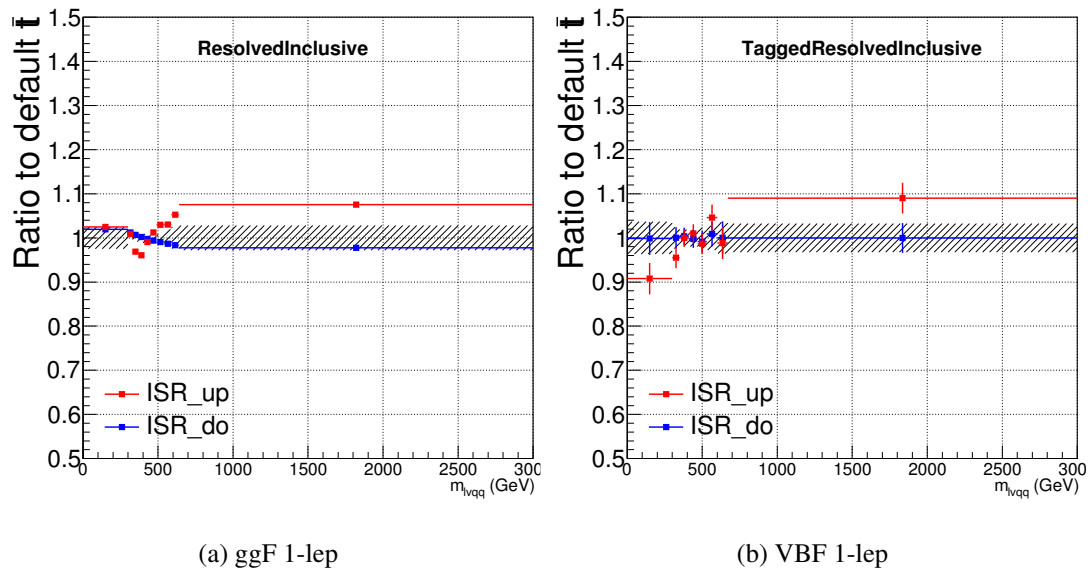


**Figure 10.6:** Ratio between the variations of ISR up (red) and down (blue) variations for the Resolved regime for  $t\bar{t}$  sample.

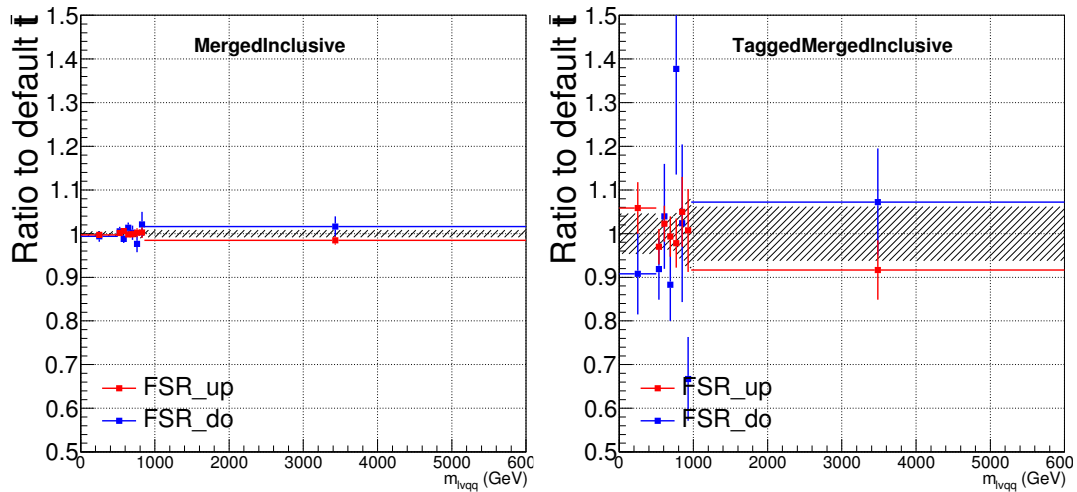


**Figure 10.7:** Ratio between the variations of FSR up (red) and down (blue) variations for the Merged regime for  $t\bar{t}$  sample.

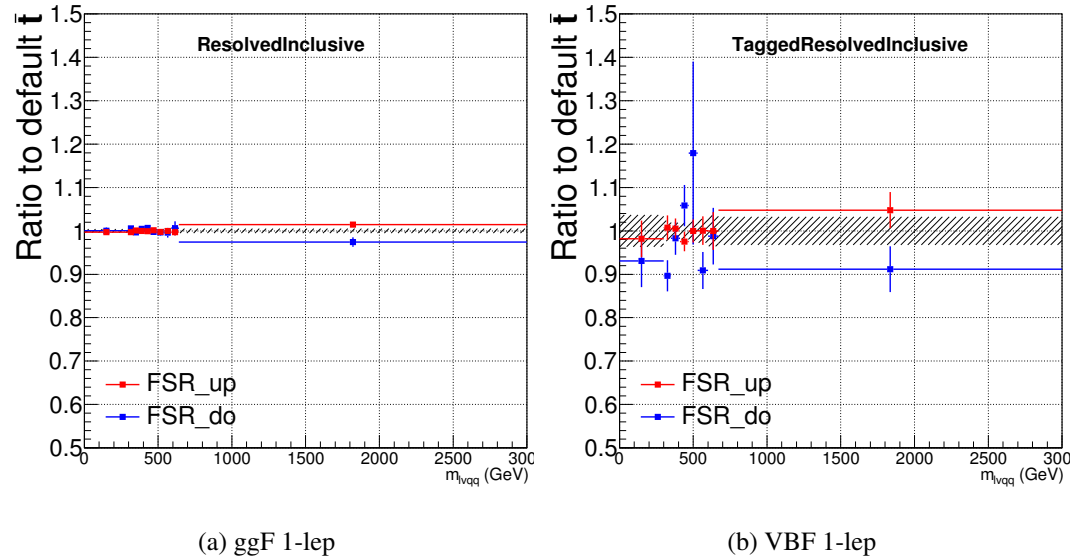


**Figure 10.8:** Ratio between the variations of FSR up (red) and down (blue) variations for the Resolved regime for  $t\bar{t}$  sample.

<sub>1145</sub> **Chapter 11**

<sub>1146</sub> **Statistical Analysis**

<sub>1147</sub> To determine the compatibility of the data collected with the proposed reso-  
<sub>1148</sub> nances a statistical procedure based on a likelihood function is used. A discovery  
<sub>1149</sub> test is used to measure the compatibility of the observed data with the back-  
<sub>1150</sub> ground only hypothesis. If the observed data is sufficiently incompatible with the  
<sub>1151</sub> background only hypothesis, this could indicate a discovery. In the absence of  
<sub>1152</sub> discovery, upper limits on the signal strength parameter,  $\mu$ , are assessed using the  
<sub>1153</sub> CLs method.

<sub>1154</sub> **11.1 Likelihood Function Definition**

<sub>1155</sub> The likelihood function is product of Poisson probabilities for all analysis bins  
<sub>1156</sub> and systematic constraints:

$$\mathcal{L}(\mu, \boldsymbol{\theta}) = \prod_c \prod_i \frac{(\mu s_{ci}(\boldsymbol{\theta}) + b_{ci}(\boldsymbol{\theta}))^{n_{ci}}}{n_{ci}!} e^{-(\mu s_{ci}(\boldsymbol{\theta}) + b_{ci}(\boldsymbol{\theta}))} \prod_k (\theta'_k | \theta_k) \quad (11.1)$$

<sub>1157</sub> Here  $c$  are the analysis channels considered and  $i$  runs over all the  $m_{\ell\nu qq}$  bins

used in the fit. The signal strength parameter,  $\mu$ , multiplies the expected signal yield in each analysis bin,  $s_{ci}$ . The background content for channel  $c$  and bin  $i$  is given by  $b_{ci}$ . The dependence of signal and background predictions on systematic uncertainties is described by the aforementioned set of nuisance parameters  $\boldsymbol{\theta}$ , which are parameterized by Gaussian or log-normal priors denoted here as  $\theta_k$ . Statistical uncertainties of the simulated bin contents are also included as systematic uncertainties. Most systematics are correlated among all the analysis regions and considered to be independent from each other. The validity of this assumption is checked by evaluating the covariance of nuisance parameters.

## 11.2 Fit Configuration

The binning of  $m_{\ell\nu qq}$  in signal regions for likelihood fit is determined by the statistical uncertainty of signal mass width. For each signal mass point, the signal mass resolution is given by the fitted Gaussian width of the  $m_{\ell\nu qq}$ . The fitted signal widths are then fit to a line to give a parameterized signal mass width, as shown in Figures 11.1 and 11.2. Bin widths are set first to this parameterized signal mass resolution. Then if the statistical uncertainty of the data or simulated background is more than 50%, bins are merged until the statistical uncertainty is less than 50%. All control regions contain only a single bin.

For this analysis, each signal model is fit in the Merged and Resolved channels for the relevant signal production mode simultaneously. The  $W + \text{jets}$  and  $t\bar{t}$  normalizations are given by the best fit values in the overall fit and these fitted normalizations are then applied to those backgrounds in the SRs.

Systematics may be affected by low statistics, leading to unsmooth  $m_{VV}$  distributions with unphysically large fluctuations. This can lead to artificial pulls and constraints in the fit. To remove such issues a multi-step smoothing pro-

1183 cedure is applied to all systematic variation distributions in all regions. First,  
1184 distributions are rebinned until the statistical error per bin is at least 5%. Next  
1185 all local extrema are identified. The bins around smallest extrema are iteratively  
1186 merged until only four local extrema remain. Then distributions are rebinned so  
1187 that statistical uncertainties in each bin are  $< 5\%$ .

1188 For some systematics, up and down variations may be in the same direction  
1189 with respect to the nominal distributions. This causes the variations to not cover  
1190 the nominal choice, and the interpretation of the confidence interval is skewed as  
1191 the nominal distribution should be bracketed by the up and down variations. This  
1192 asymmetry may also lead to unconstrained systematics in the fit. To handle such  
1193 asymmetric systematics, if the up and down variation for a given systematic are in  
1194 the same direction for at least three  $m_{VV}$  bins the variation is averaged for those  
1195 bins. The averaging procedure replaces bin-by-bin the up and down variation bins  
1196 by  $b_{\pm}^{new} = b_{nom} \pm \frac{|b_+ - b_-|}{2}$ , where  $b_{nom}$  is the nominal bin content and  $b_{\pm}$  are the  
1197 original up and down variation bin content. The same procedure is also applied to  
1198 any variations where the integral of the difference between the up/down variation  
1199 and the nominal distribution is twice that of the other down/up variation, further  
1200 ensuring variations are symmetric around the nominal distribution.

1201 Finally, systematics that have a negligible effect on the  $m_{VV}$  distribution are  
1202 not considered in the fit. Shape systematics where no bin in the variational dis-  
1203 tribution deviates more than 1% from the nominal distribution (after normalizing  
1204 all histograms to the nominal) are not included in the fit. Also, statistical bin  
1205 uncertainties  $< 1\%$  are ignored.

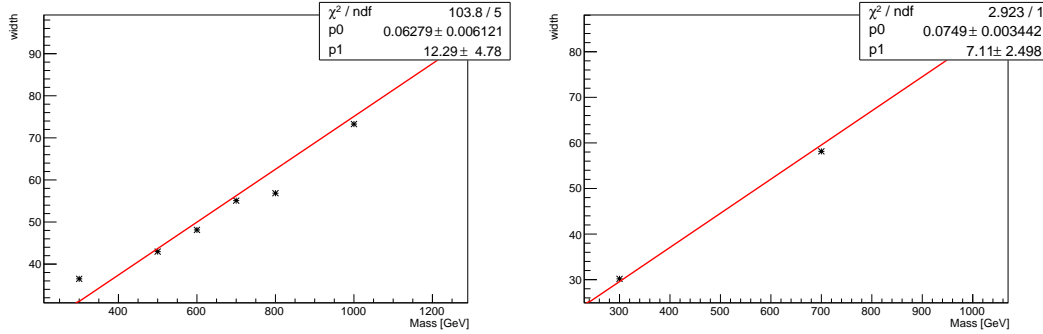


**Figure 11.1:** The HVT signal mass resolution as a function of mass fit with a straight line in the Resolved ggF region (left) and VBF (right) region.

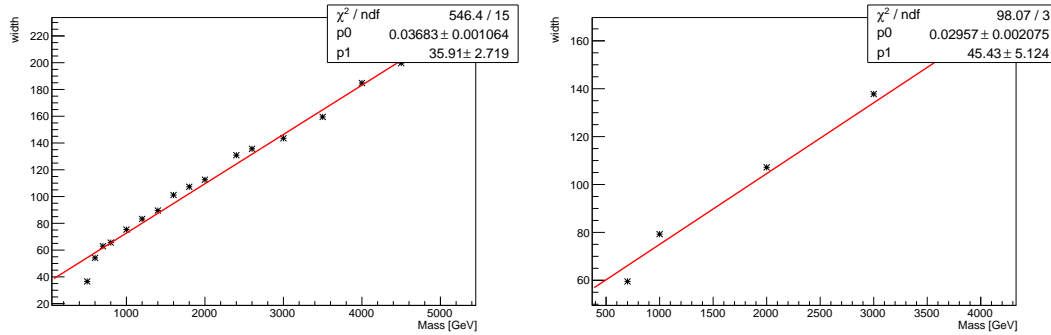


**Figure 11.2:** The HVT signal mass resolution as a function of mass fit with a straight line in the Merged ggF region (left) and VBF (right) region.

### 1206    11.3 Best Fit $\mu$

1207    The best fit signal strength parameter is denoted by  $\hat{\mu}$  and calculated by  
 1208    maximizing the likelihood function with respect to all systematics and  $\mu$ . The  
 1209    corresponding set of systematics that maximize the likelihood are given by  $\hat{\mu}$ .  
 1210    The first term in the likelihood is maximized when the expected number of signal  
 1211    and background events is equal to the number of events in data ( $n_{ci} = \mu s_{ci} +$   
 1212     $b_{ci}$ ). Thus, by maximizing the likelihood, the fit determines values of  $\mu$  and  $\theta$   
 1213    that give the best agreement between expected and measured event yields. The

1214 second term in the likelihood is a penalty term which decreases the likelihood  
1215 when systematics are shifted from their nominal values. This prevents the fit  
1216 from profiling systematics in unphysical ways to maximize the likelihood. The  
1217 uncertainty on  $\mu$  is calculated by varying  $\mu$  up and down until the natural log of  
1218 the likelihood function shifts by one-half.

## 1219 11.4 Discovery Test

1220 To determine if the observed dataset is consistent with tested signal model a  
1221 likelihood ratio is constructed:

$$\lambda(\mu) = \frac{\mathcal{L}(\mu, \hat{\theta}_\mu)}{\mathcal{L}(\hat{\mu}, \hat{\theta})} \quad (11.2)$$

1222 The denominator in this equation is the maximized value of  $\mathcal{L}$  over all system-  
1223 atics and  $\mu$ . The numerator is the maximized likelihood over all systematics for  
1224 a given  $\mu$  value, where the maximized systematics are given by  $\hat{\mu}_\mu$ . To test for  
1225 the existence of signal the observed dataset the null hypothesis ( $H_0$ ) is defined as  
1226 the background only hypothesis and the alternate hypothesis includes signal and  
1227 background ( $H_1$ ). This test quantifies the compatibility of observed data with  
1228  $H_0$  by calculating a p-value representing the probability of observing data as dis-  
1229 crepant or more than the observed data under the  $H_0$ . The test statistic used to  
1230 calculate this p-value is given by ( $r_0$ ):

$$r_0 = \begin{cases} -2 \ln \lambda(0), \hat{\mu} > 0 \\ +2 \ln \lambda(0), \hat{\mu} < 0 \end{cases} \quad (11.3)$$

1231 The expected distribution of the the test statistic under  $H_0$  ( $f(r_0|0)$ ) is used to  
1232 calculate the p-value:

$$p_0 = \int_{r_0, obs}^{\infty} f(r_0 | 0) dr_0 \quad (11.4)$$

1233        Small p-values indicate the observed data is poorly described by  $H_0$ . This  
 1234        equivalent Z-score of a given p-value is usually used to further quantify the agree-  
 1235        ment between the observed data and  $H_0$ . The Z-score is given by the number of  
 1236        standard deviations away from the mean of a Gaussian distribution, the integral  
 1237        of the upper tail of the distribution would equal the p-value. Mathematically:

$$Z = \Phi^{-1}(1 - p_0) \quad (11.5)$$

1238        where  $\Phi$  is the Gaussian cumulative distribution function. The statistical  
 1239        significance of these tests are expressed as the  $Z$ -score. In particle physics,  $3\sigma$  is  
 1240        considered evidence for new phenomena and  $5\sigma$  is the threshold for discovery.

## 1241        11.5 Exclusion Limits

1242        In the absence of discovery, upper limits on the signal strength,  $\mu$  are set using  
 1243        the CLs method [cite P60]. The test statistic for this test,  $q_\mu$ , is constructed as:

$$\tilde{\lambda}_\mu = \begin{cases} \frac{\mathcal{L}(\mu, \hat{\theta}_\mu)}{\mathcal{L}(\hat{\mu}, \hat{\theta})}, \hat{\mu} > 0 \\ \frac{\mathcal{L}(\mu, \hat{\theta}_\mu)}{\mathcal{L}(0, \hat{\theta}_0)}, \hat{\mu} < 0 \end{cases} \quad (11.6)$$

$$\tilde{q}_\mu = \begin{cases} -2 \ln \tilde{\lambda}(\mu), \hat{\mu} < \mu \\ +2 \ln \tilde{\lambda}(\mu), \hat{\mu} > \mu \end{cases} \quad (11.7)$$

1244        As defined, larger values of  $q_\mu$  correspond to increasing incompatibility between  
 1245        the observed data and the background + signal hypothesis. The observed value  
 1246        of the test statistic,  $q_{\mu, obs}$ , is then compared to its expected distribution,  $f$ , to

1247 calculate p-values to assess the likelihood of the background+signal hypothesis.

1248 Using these distributions,  $CL_s$  values are computed as:

$$1249 \quad CL_{s+b} = \int_{q_{\mu,obs}}^{\infty} f(q_{\mu}|\mu) dq_{\mu} \quad (11.8)$$

$$1250 \quad CL_b = \int_{q_0^{obs}}^{\infty} f(q_{\mu}|\mu = 0) dq_{\mu} \quad (11.9)$$

$$1251 \quad CL_s = \frac{CL_{s+b}}{CL_b} \quad (11.10)$$

1251      $CL_{s+b}$  is the p-value for the signal + background hypothesis and  $CL_b$  is the  
1252     p-value for the background only hypothesis. The  $CL_s$  value is interpreted as  
1253     the probability to observe the background + signal hypothesis normalized to the  
1254     probability of background-only hypothesis. Normalizing by  $CL_b$  prevents setting  
1255     artificially strong exclusion limits due to downward fluctuations in data.

1256     For a given signal hypothesis,  $\mu$  values are scanned simultaneously over all  
1257      $m_{WV}$  bins to find the  $\mu$  value that yields  $CL_s=0.05$ , meaning the likelihood of  
1258     finding data more incompatible with the signal+background hypothesis (relative  
1259     to the background only hypothesis) is 5%. The 95% upper limit on the cross  
1260     section is then calculated as the product of the  $\mu$  value found, branching ratio,  
1261     and theory cross section.

## **Part V**

1262

## **Results**

1263

1264 **Chapter 12**

1265 **Statistical Interpretation**

1266 **12.1 Discovery Tests**

1267 To test for the existence of signal in the observed dataset, the discovery tests  
1268 discussed earlier are used to calculate p-values as a function of resonance mass.  
1269 The results of these tests are shown in Figures 12.1 - 12.5. Across the different  
1270 DY signals the largest excesses are  $\sim 2.2\sigma$  at 600 GeV and  $1.8\sigma$  at 2 TeV. The  
1271 largest excesses for VBF signals are  $< 2.5\sigma$  at for 1 TeV resonances. As these  
1272 deviations do not constitute discoveries, upper limits on  $\mu$  are calculated.

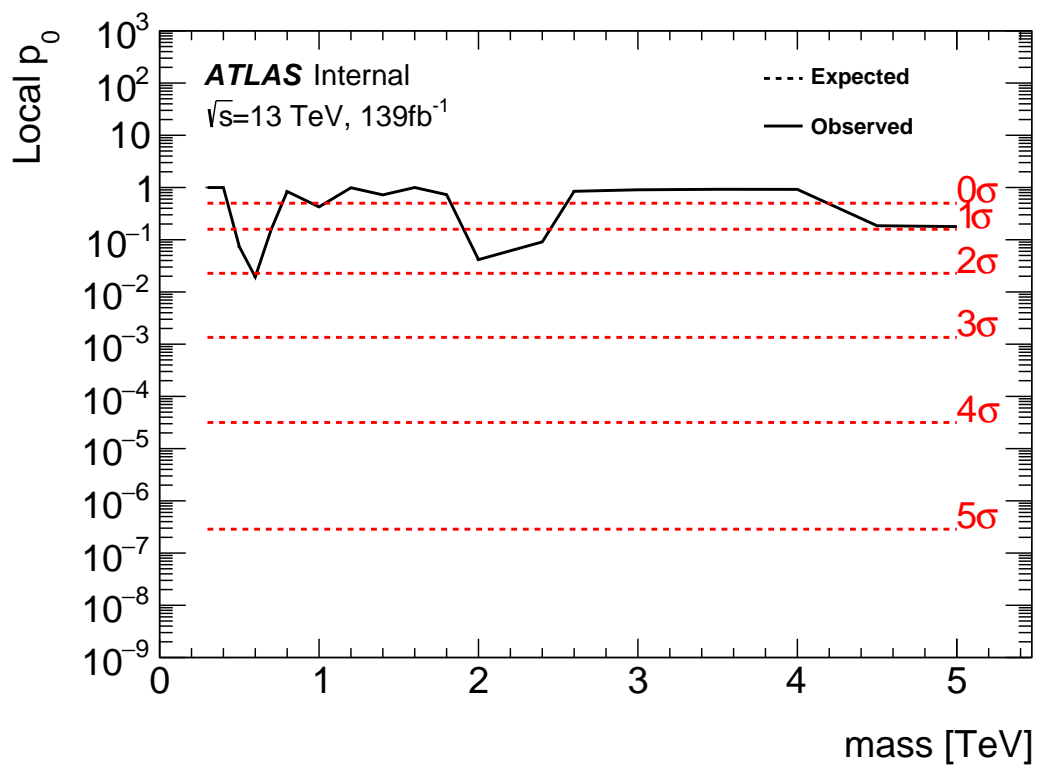


**Figure 12.1:** These plots show the measured  $p_0$  value as a function of resonance mass for HVT Z' DY production.

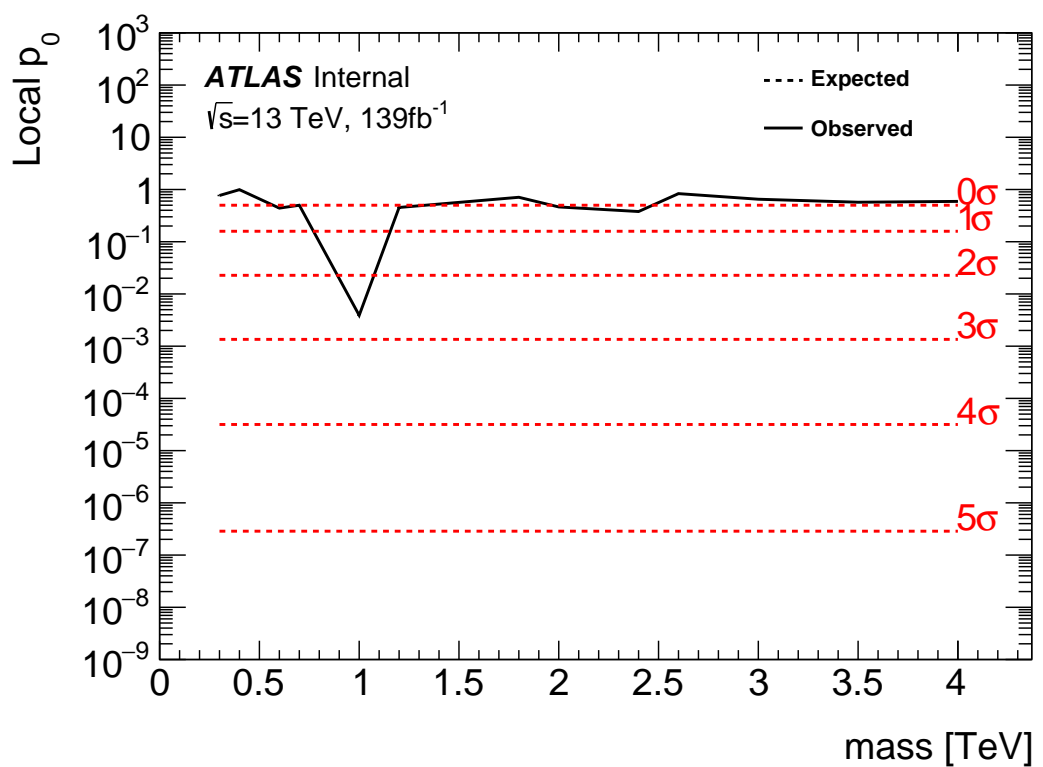


**Figure 12.2:** These plots show the measured  $p_0$  value as a function of resonance mass for HVT Z' VBF production.

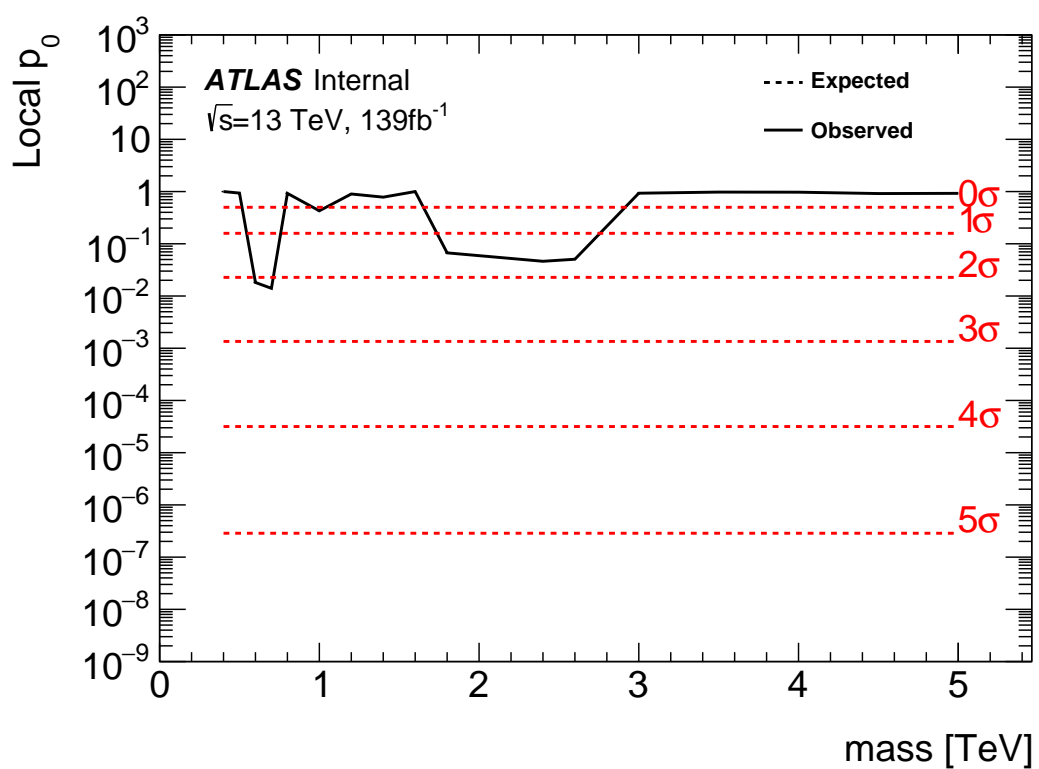


**Figure 12.3:** These plots show the measured  $p_0$  value as a function of resonance mass for HVT W' DY production.

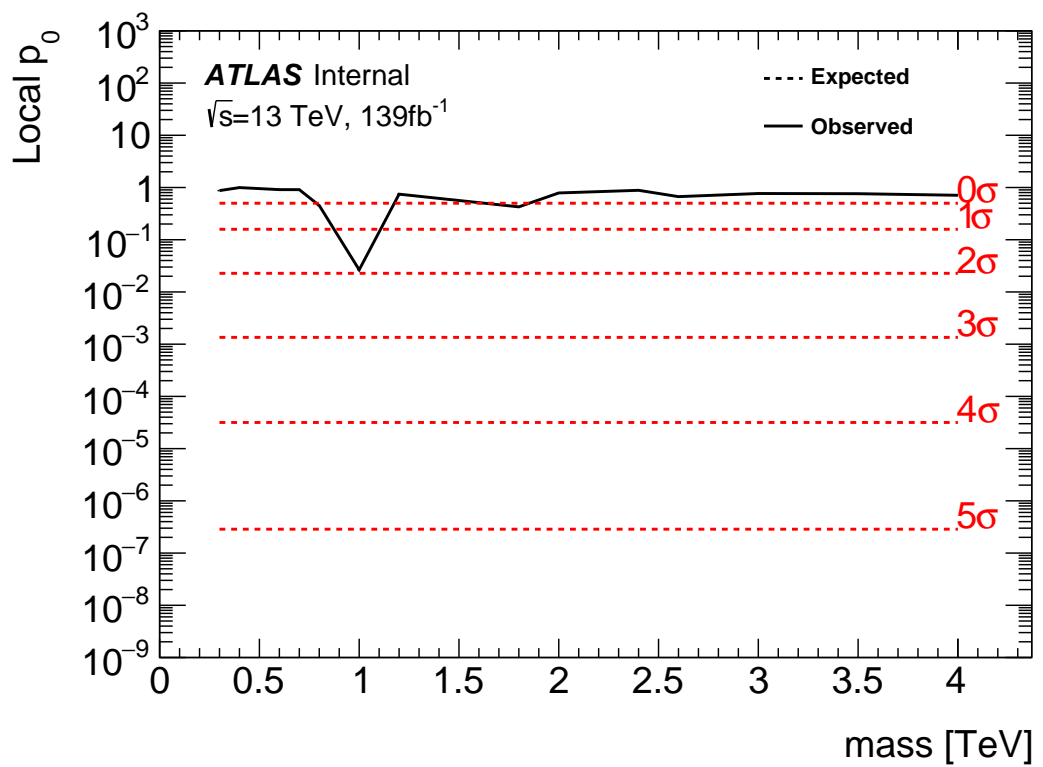


**Figure 12.4:** These plots show the measured  $p_0$  value as a function of resonance mass for HVT W' VBF production.

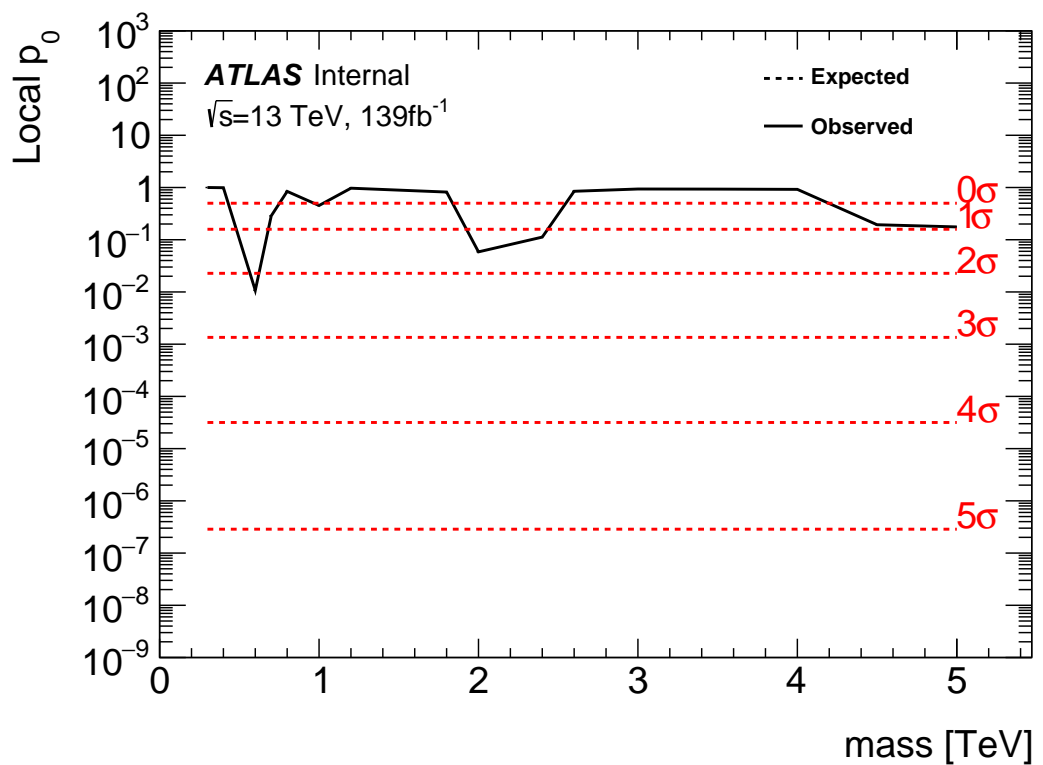


**Figure 12.5:** These plots show the measured  $p_0$  value as a function of resonance mass for the RS Graviton DY production.

## 12.2 Systematic Profiling and Correlations

1273     The ranked systematics and their fitted values are shown for the different analysis regions in Figure 12.6 - 12.8. Note that background normalizations for  $W+jets$  and  $t\bar{t}$  are left free to float in the fit. This means the nominal normalization values are at one and the uncertainties are not plotted in the ranked plots. Overall, systematics are not pulled outside their uncertainties, especially for highly ranked nuisance parameters.

1280     The correlation between systematics are shown in Figures ???. Correlations 1281 between background normalization are expected. The remaining systematic correlations are not very strong or unexpected.

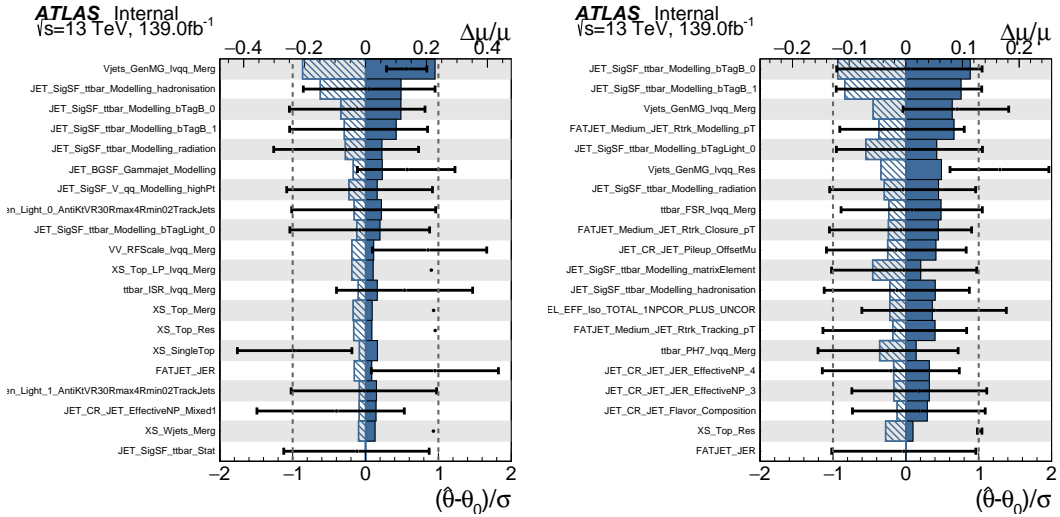


**Figure 12.6:** Ranked systematics and their fitted values for  $WW$  DY (right) and VBF (left) selections.

1282

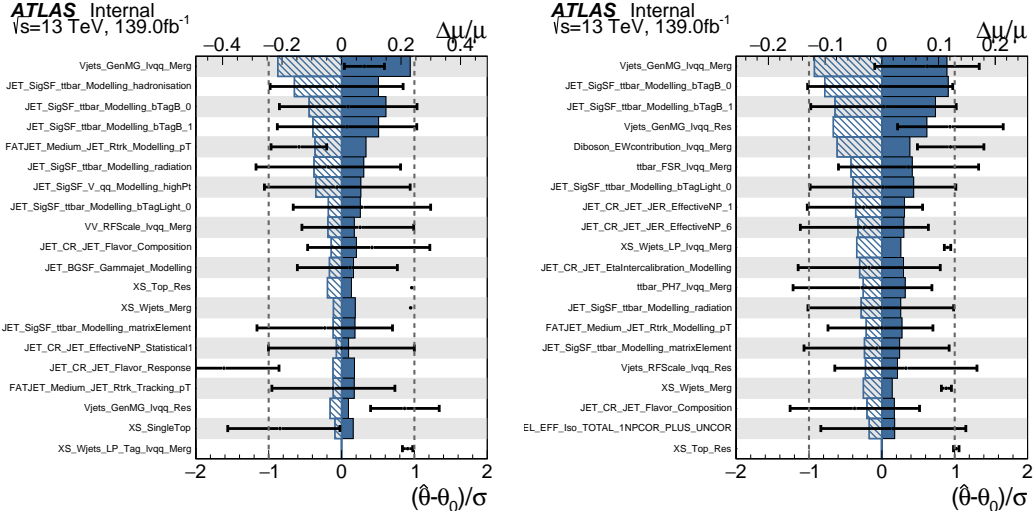


**Figure 12.7:** Ranked systematics and their fitted values for  $WZ$  DY (right) and VBF (left) selections.

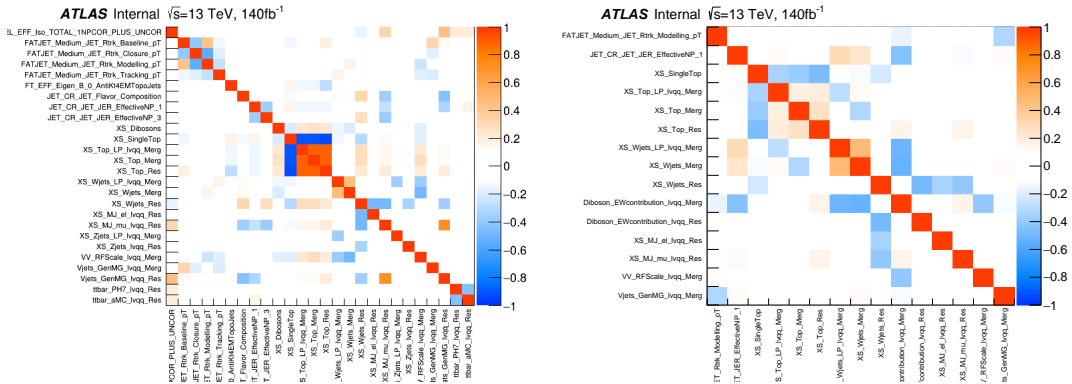


**Figure 12.8:** Correlations between systematics for  $WW$  DY (right) and VBF (left) selections.

## 12.3 Expected and Measured Yields

The yield tables for the four analysis regions are shown in Tables ?? - ?? . The fitted background normalizations are shown in Tables ??-?? . The control region  $m_{\ell\nu qq}$  distributions are shown in Figures 12.9 - 12.12. The signal region  $m_{\ell\nu qq}$  distributions are shown in Figures 12.13 - ?? .

	HP WCR	LP WCR	Resolved WCR
Electron Multi-jet	-	-	$16507.83 \pm 2314.87$
Muon Multi-jet	-	-	$19977.12 \pm 2816.06$
Diboson	$1833.41 \pm 177.78$	$3323.93 \pm 320.92$	$9147.67 \pm 961.63$
Single-top	$2160.62 \pm 402.34$	$3551.09 \pm 660.00$	$20058.36 \pm 3817.26$
$t\bar{t}$	$15518.86 \pm 338.22$	$24069.54 \pm 453.15$	$138866.23 \pm 1989.71$
$W+jets$	$40141.57 \pm 357.79$	$88113.06 \pm 487.87$	$673200.38 \pm 4120.53$
$Z+jets$	$778.83 \pm 78.93$	$1765.54 \pm 179.10$	$16570.50 \pm 1672.71$
Total	$60433.29 \pm 664.92$	$120823.16 \pm 1006.99$	$894328.12 \pm 7247.12$
Data	60264.00	120852.00	895362.00
	HP TCR	LP TCR	Resolved TCR
Electron Multi-jet	-	-	-
Muon Multi-jet	-	-	-
Diboson	$421.11 \pm 37.98$	$550.44 \pm 53.10$	$996.87 \pm 119.63$
Single-top	$4691.44 \pm 846.11$	$3466.26 \pm 631.03$	$16848.71 \pm 3258.26$
$t\bar{t}$	$38945.18 \pm 848.77$	$33836.95 \pm 637.04$	$224226.14 \pm 3212.76$
$W+jets$	$2258.34 \pm 20.13$	$6564.78 \pm 36.35$	$23466.41 \pm 143.63$
$Z+jets$	$66.35 \pm 6.72$	$213.26 \pm 21.63$	$846.66 \pm 85.47$
Total	$46382.43 \pm 1199.25$	$44631.70 \pm 899.23$	$266384.78 \pm 4580.43$
Data	46354.00	44629.00	266443.00
	WW SR	LP SR	Resolved 1-lepton SR
Electron Multi-jet	-	-	$10788.40 \pm 1512.85$
Muon Multi-jet	-	-	$15759.50 \pm 2221.53$
Diboson	$4990.30 \pm 376.50$	$3901.07 \pm 313.22$	$16971.29 \pm 1523.77$
Single-top	$3117.71 \pm 565.07$	$2176.46 \pm 400.52$	$20422.85 \pm 3731.94$
$t\bar{t}$	$13785.77 \pm 302.14$	$11005.12 \pm 207.41$	$126965.25 \pm 1819.66$
$W+jets$	$24718.56 \pm 223.72$	$60080.66 \pm 333.12$	$444133.56 \pm 2719.02$
$Z+jets$	$478.18 \pm 48.46$	$1226.69 \pm 124.44$	$11686.32 \pm 1179.69$
Total	$47090.52 \pm 777.65$	$78389.98 \pm 654.22$	$646727.19 \pm 5963.98$
Data	47330.00	78380.00	645610.00

**Table 12.1:** Expected and Measured for DY  $WW$   $W+jets$ ,  $t\bar{t}$  control regions and signal regions.

	HP Untagged WCR	LP Untagged WCR	Resolved Untagged WCR
Electron Multi-jet	-	-	$15080.03 \pm 2277.99$
Muon Multi-jet	-	-	$27347.10 \pm 2950.07$
Diboson	$1508.48 \pm 154.20$	$2758.24 \pm 284.50$	$9038.55 \pm 728.69$
Single-top	$1756.59 \pm 306.69$	$2913.18 \pm 515.93$	$20511.74 \pm 3523.47$
$t\bar{t}$	$13134.00 \pm 238.30$	$21815.37 \pm 334.98$	$140157.77 \pm 2636.96$
$W+jets$	$40654.84 \pm 333.65$	$87657.76 \pm 501.96$	$665909.12 \pm 4420.62$
$Z+jets$	$768.72 \pm 77.97$	$1759.87 \pm 178.96$	$16512.46 \pm 1673.23$
Total	$57822.63 \pm 540.40$	$116904.42 \pm 862.16$	$894556.75 \pm 7492.20$
Data	57699.00	117306.00	895362.00
	HP Tagged WCR	LP Tagged WCR	Resolved Tagged WCR
Electron Multi-jet	-	-	$384.58 \pm 57.11$
Muon Multi-jet	-	-	$602.93 \pm 190.12$
Diboson	$30.22 \pm 4.69$	$48.95 \pm 7.16$	$264.64 \pm 28.24$
Single-top	$308.44 \pm 56.19$	$371.59 \pm 69.43$	$5752.39 \pm 1029.97$
$t\bar{t}$	$1683.82 \pm 48.73$	$2041.48 \pm 70.00$	$58431.49 \pm 614.30$
$W+jets$	$583.55 \pm 75.37$	$1109.45 \pm 85.78$	$11891.68 \pm 903.01$
$Z+jets$	$13.19 \pm 1.34$	$23.06 \pm 2.34$	$324.74 \pm 32.85$
Total	$2619.22 \pm 106.00$	$3594.53 \pm 130.90$	$77652.45 \pm 1514.89$
Data	2565.00	3546.00	77973.00
	HP Untagged TCR	LP Untagged TCR	Resolved Untagged TCR
Electron Multi-jet	-	-	-
Muon Multi-jet	-	-	-
Diboson	$289.45 \pm 28.45$	$346.78 \pm 35.85$	$650.85 \pm 65.56$
Single-top	$3107.99 \pm 538.03$	$2250.64 \pm 385.41$	$9606.87 \pm 1698.22$
$t\bar{t}$	$30992.40 \pm 562.33$	$26954.21 \pm 413.89$	$91893.59 \pm 1728.91$
$W+jets$	$2236.29 \pm 18.35$	$4874.03 \pm 27.91$	$16122.97 \pm 107.03$
$Z+jets$	$71.54 \pm 7.26$	$155.50 \pm 15.81$	$577.71 \pm 58.54$
Total	$36697.66 \pm 779.03$	$34581.16 \pm 567.59$	$118851.98 \pm 2427.40$
Data	36677.00	34573.00	118928.00
	HP Tagged TCR	LP Tagged TCR	Resolved Tagged TCR
Electron Multi-jet	-	-	-
Muon Multi-jet	-	-	-
Diboson	$9.72 \pm 1.13$	$8.75 \pm 1.16$	$34.06 \pm 4.98$
Single-top	$105.87 \pm 20.65$	$119.66 \pm 22.68$	$656.89 \pm 132.96$
$t\bar{t}$	$1904.75 \pm 50.61$	$1483.86 \pm 47.05$	$17965.33 \pm 188.87$
$W+jets$	$32.36 \pm 4.28$	$85.74 \pm 6.96$	$489.01 \pm 37.13$
$Z+jets$	$1.27 \pm 0.13$	$1.93 \pm 0.20$	$19.14 \pm 1.94$
Total	$2053.98 \pm 54.84$	$1699.93 \pm 52.70$	$19164.43 \pm 234.01$
Data	2047.00	1708.00	19143.00

**Table 12.2:** Expected and Measured for DY  $WZ$   $W+jets$ ,  $t\bar{t}$  tag and untag control regions.

	HP Untagged SR	LP Untagged SR	Resolved Untagged SR
Electron Multi-jet	-	-	$7782.17 \pm 1175.56$
Muon Multi-jet	-	-	$17004.81 \pm 1834.40$
Diboson	$3041.17 \pm 273.77$	$2266.35 \pm 212.79$	$14724.12 \pm 1224.31$
Single-top	$2123.28 \pm 373.83$	$1379.35 \pm 240.92$	$18336.88 \pm 3082.47$
$t\bar{t}$	$11678.86 \pm 213.63$	$8906.34 \pm 136.88$	$112669.24 \pm 2122.46$
$W+jets$	$22741.32 \pm 191.47$	$41726.76 \pm 240.56$	$342934.00 \pm 2280.21$
$Z+jets$	$442.03 \pm 44.84$	$849.79 \pm 86.42$	$9271.83 \pm 939.52$
Total	$40026.65 \pm 546.81$	$55128.59 \pm 432.90$	$522723.03 \pm 5131.71$
Data	40193.00	54735.00	521813.00
	HP Tagged SR	LP Tagged SR	Resolved Tagged SR
Electron Multi-jet	-	-	$199.22 \pm 29.58$
Muon Multi-jet	-	-	$393.43 \pm 124.06$
Diboson	$102.58 \pm 11.59$	$65.44 \pm 8.05$	$624.07 \pm 58.10$
Single-top	$178.21 \pm 33.62$	$155.53 \pm 28.95$	$3470.39 \pm 617.48$
$t\bar{t}$	$1017.93 \pm 31.95$	$706.76 \pm 26.20$	$38189.30 \pm 401.91$
$W+jets$	$325.58 \pm 41.62$	$575.36 \pm 43.29$	$6161.96 \pm 467.71$
$Z+jets$	$7.81 \pm 0.80$	$11.62 \pm 1.19$	$183.36 \pm 18.55$
Total	$1632.11 \pm 63.39$	$1514.70 \pm 58.86$	$49221.74 \pm 884.06$
Data	1699.00	1559.00	48919.00

**Table 12.3:** Expected and Measured for DY  $WZ$   $W+jets$ ,  $t\bar{t}$  tag and untag signal regions.

	HP WCR	LP WCR	Resolved WCR
Electron Multi-jet	-	-	$898.48 \pm 137.82$
Muon Multi-jet	-	-	$601.46 \pm 182.74$
Diboson	$107.45 \pm 45.20$	$166.87 \pm 68.11$	$292.10 \pm 235.29$
Single-top	$78.19 \pm 18.22$	$132.71 \pm 31.93$	$879.82 \pm 216.89$
$t\bar{t}$	$400.71 \pm 28.35$	$569.70 \pm 48.88$	$5067.51 \pm 155.69$
$W+jets$	$864.49 \pm 63.44$	$1940.80 \pm 89.41$	$18563.70 \pm 408.99$
$Z+jets$	$19.51 \pm 2.00$	$46.63 \pm 4.77$	$795.20 \pm 80.89$
Total	$1470.35 \pm 84.89$	$2856.71 \pm 126.74$	$27098.28 \pm 594.01$
Data	1495.00	2898.00	27120.00
	HP TCR	LP TCR	Resolved TCR
Electron Multi-jet	-	-	-
Muon Multi-jet	-	-	-
Diboson	$14.95 \pm 6.61$	$27.57 \pm 14.12$	$24.33 \pm 20.32$
Single-top	$68.31 \pm 16.17$	$58.93 \pm 13.56$	$278.60 \pm 73.04$
$t\bar{t}$	$496.60 \pm 31.72$	$401.23 \pm 32.13$	$3834.49 \pm 104.60$
$W+jets$	$50.68 \pm 4.19$	$144.02 \pm 7.86$	$450.01 \pm 11.87$
$Z+jets$	$1.32 \pm 0.14$	$5.35 \pm 0.55$	$29.96 \pm 3.07$
Total	$631.87 \pm 36.45$	$637.10 \pm 38.44$	$4617.39 \pm 129.77$
Data	636.00	634.00	4615.00
	HP SR	LP SR	Resolved SR
Electron Multi-jet	-	-	$596.34 \pm 91.52$
Muon Multi-jet	-	-	$481.01 \pm 144.48$
Diboson	$148.84 \pm 48.64$	$181.42 \pm 67.30$	$395.52 \pm 318.06$
Single-top	$79.49 \pm 19.80$	$56.82 \pm 14.89$	$782.07 \pm 190.79$
$t\bar{t}$	$338.42 \pm 24.14$	$236.80 \pm 20.88$	$4261.70 \pm 138.98$
$W+jets$	$501.13 \pm 39.36$	$1347.76 \pm 64.50$	$11445.73 \pm 291.49$
$Z+jets$	$9.25 \pm 0.95$	$28.77 \pm 2.95$	$567.66 \pm 57.94$
Total	$1077.13 \pm 69.93$	$1851.57 \pm 96.73$	$18530.03 \pm 523.88$
Data	1096.00	1846.00	18530.00

**Table 12.4:** Expected and Measured for VBF  $WW$   $W+jets$ ,  $t\bar{t}$  control regions and signal regions.

	HP WCR	LP WCR	Resolved WCR
Electron Multi-jet	-	-	$870.00 \pm 132.75$
Muon Multi-jet	-	-	$618.45 \pm 196.90$
Diboson	$92.92 \pm 41.77$	$145.90 \pm 64.26$	$228.62 \pm 114.62$
Single-top	$71.13 \pm 16.29$	$118.82 \pm 27.98$	$1209.87 \pm 281.64$
$t\bar{t}$	$427.80 \pm 29.72$	$509.19 \pm 46.57$	$6860.87 \pm 254.83$
$W+jets$	$871.68 \pm 64.22$	$2020.67 \pm 93.54$	$19088.50 \pm 442.10$
$Z+jets$	$19.58 \pm 2.01$	$47.39 \pm 4.85$	$800.19 \pm 82.02$
Total	$1483.11 \pm 83.79$	$2841.97 \pm 125.92$	$29676.50 \pm 644.96$
Data	1495.00	2898.00	29755.00
	HP TCR	LP TCR	Resolved TCR
Electron Multi-jet	-	-	-
Muon Multi-jet	-	-	-
Diboson	$10.12 \pm 4.51$	$12.73 \pm 6.55$	$14.23 \pm 7.49$
Single-top	$51.57 \pm 12.31$	$35.07 \pm 8.17$	$169.21 \pm 44.54$
$t\bar{t}$	$470.06 \pm 28.97$	$298.99 \pm 25.28$	$2414.75 \pm 75.42$
$W+jets$	$49.64 \pm 4.17$	$109.69 \pm 6.16$	$378.22 \pm 12.05$
$Z+jets$	$1.28 \pm 0.13$	$4.81 \pm 0.50$	$17.62 \pm 1.83$
Total	$582.67 \pm 32.07$	$461.30 \pm 28.05$	$2994.03 \pm 88.75$
Data	584.00	459.00	3001.00
	HP SR	LP SR	Resolved SR
Electron Multi-jet	-	-	$444.65 \pm 67.99$
Muon Multi-jet	-	-	$397.29 \pm 125.59$
Diboson	$109.66 \pm 44.13$	$112.28 \pm 46.45$	$265.75 \pm 139.43$
Single-top	$63.16 \pm 15.20$	$48.02 \pm 11.56$	$872.16 \pm 205.00$
$t\bar{t}$	$348.95 \pm 24.34$	$190.68 \pm 17.75$	$5134.25 \pm 193.57$
$W+jets$	$467.21 \pm 37.12$	$973.73 \pm 47.91$	$10226.83 \pm 254.67$
$Z+jets$	$8.15 \pm 0.84$	$23.62 \pm 2.43$	$558.48 \pm 57.25$
Total	$997.13 \pm 64.42$	$1348.33 \pm 70.06$	$17899.41 \pm 432.98$
Data	1018.00	1313.00	17826.00

**Table 12.5:** Expected and Measured for VBF  $WZ$   $W+jets$ ,  $t\bar{t}$  control regions and signal regions.

Background	Fitted Normalization
XS_Top_LP_lvqq_Merg_binned	$0.905^{+0.0166}_{-0.0166}$
XS_Top_Merg	$0.936^{+0.0199}_{-0.0199}$
XS_Top_Res	$0.957^{+0.0134}_{-0.0134}$
XS_Wjets_LP_lvqq_Merg_binned	$0.884^{+0.00489}_{-0.00489}$
XS_Wjets_Merg	$0.931^{+0.00831}_{-0.00831}$
XS_Wjets_Res	$1.03^{+0.00628}_{-0.00628}$

**Table 12.6:** Fitted background normalizations for  $t\bar{t}$  and  $W+jets$  backgrounds for the DY  $WW$  analysis region.

Background	Fitted Normalization
XS_Top_LP_Tag_lvqq_Merg_binned	$0.973^{+0.0333}_{-0.0333}$
XS_Top_LP_lvqq_Merg_binned	$0.894^{+0.0135}_{-0.0135}$
XS_Top_Merg	$0.893^{+0.016}_{-0.016}$
XS_Top_Res	$0.965^{+0.0179}_{-0.0179}$
XS_Top_Tag_lvqq_Merg_binned	$0.954^{+0.0276}_{-0.0276}$
XS_Top_Tag_lvqq_Res_binned	$0.999^{+0.0105}_{-0.0105}$
XS_Wjets_LP_Tag_lvqq_Merg_binned	$0.912^{+0.0703}_{-0.0703}$
XS_Wjets_LP_lvqq_Merg_binned	$0.876^{+0.00502}_{-0.00502}$
XS_Wjets_Merg	$0.948^{+0.00779}_{-0.00779}$
XS_Wjets_Res	$1.01^{+0.00673}_{-0.00673}$
XS_Wjets_Tag_lvqq_Merg_binned	$0.906^{+0.117}_{-0.117}$
XS_Wjets_Tag_lvqq_Res_binned	$1.2^{+0.0904}_{-0.0904}$

**Table 12.7:** Fitted background normalizations for  $t\bar{t}$  and  $W+jets$  backgrounds for the DY  $WZ$  analysis region.

Background	Fitted Normalization
XS_Top_LP_lvqq_Merg_binned	$0.79^{+0.0673}_{-0.0673}$
XS_Top_Merg	$0.888^{+0.061}_{-0.061}$
XS_Top_Res	$1.01^{+0.0311}_{-0.0311}$
XS_Wjets_LP_lvqq_Merg_binned	$0.88^{+0.0423}_{-0.0423}$
XS_Wjets_Merg	$0.881^{+0.0677}_{-0.0677}$
XS_Wjets_Res	$0.932^{+0.0202}_{-0.0202}$

**Table 12.8:** Fitted background normalizations for  $t\bar{t}$  and  $W+jets$  backgrounds for the VBF  $WW$  analysis region.

Background	Fitted Normalization
XS_Top_LP_lvqq_Merg_binned	$0.708^{+0.064}_{-0.064}$
XS_Top_Merg	$0.958^{+0.0644}_{-0.0644}$
XS_Top_Res	$1.02^{+0.038}_{-0.038}$
XS_Wjets_LP_lvqq_Merg_binned	$0.9^{+0.0438}_{-0.0438}$
XS_Wjets_Merg	$0.883^{+0.0685}_{-0.0685}$
XS_Wjets_Res	$0.945^{+0.0219}_{-0.0219}$

**Table 12.9:** Fitted background normalizations for  $t\bar{t}$  and  $W+jets$  backgrounds for the VBF  $WZ$  analysis region.

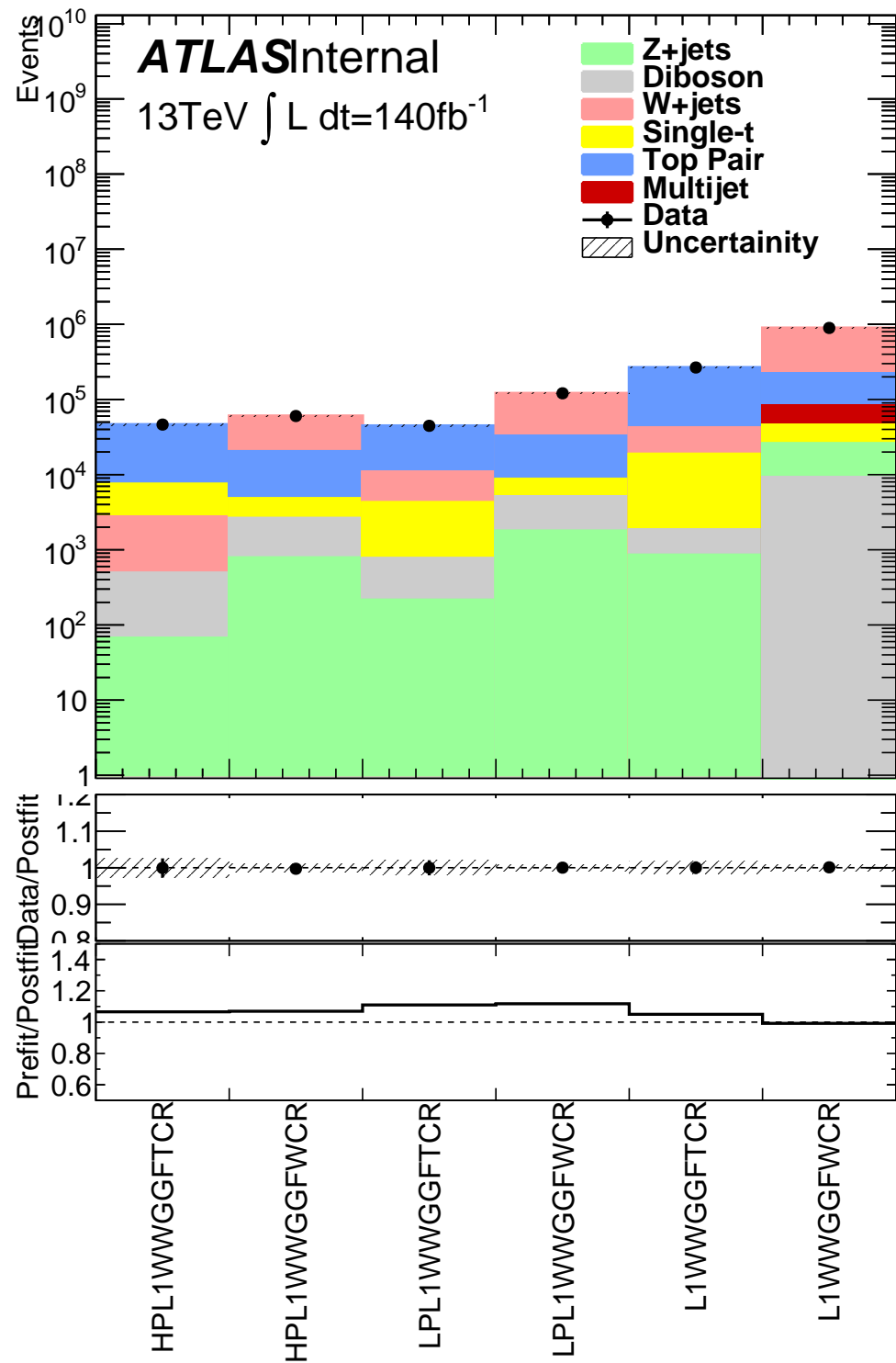


**Figure 12.9:** This figure shows the distribution of  $m_{\ell\nu qq}$  in the DY WW control regions.

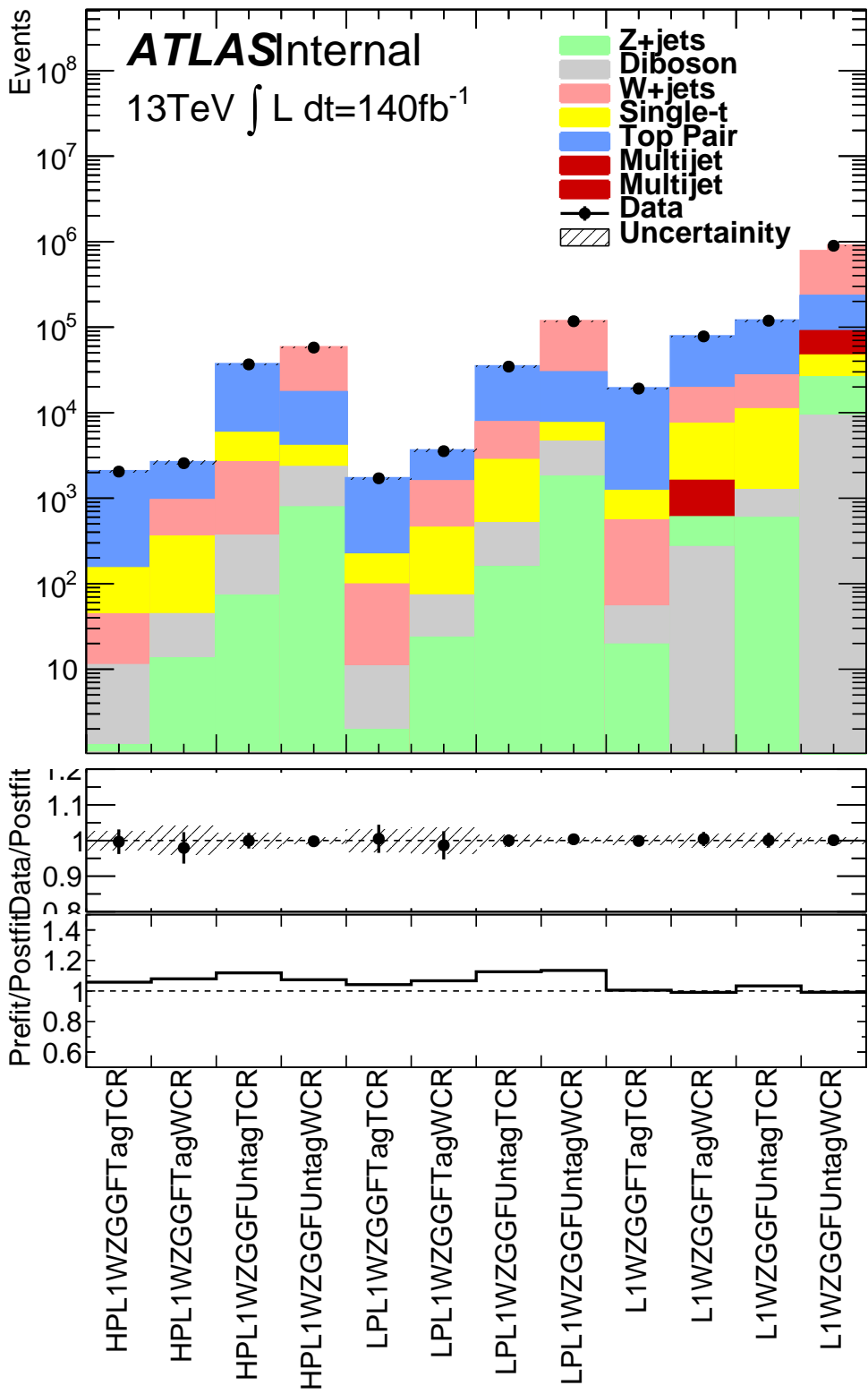


**Figure 12.10:** This figure shows the distribution of  $m_{\ell\nu qq}$  in the DY  $WZ$  control regions.

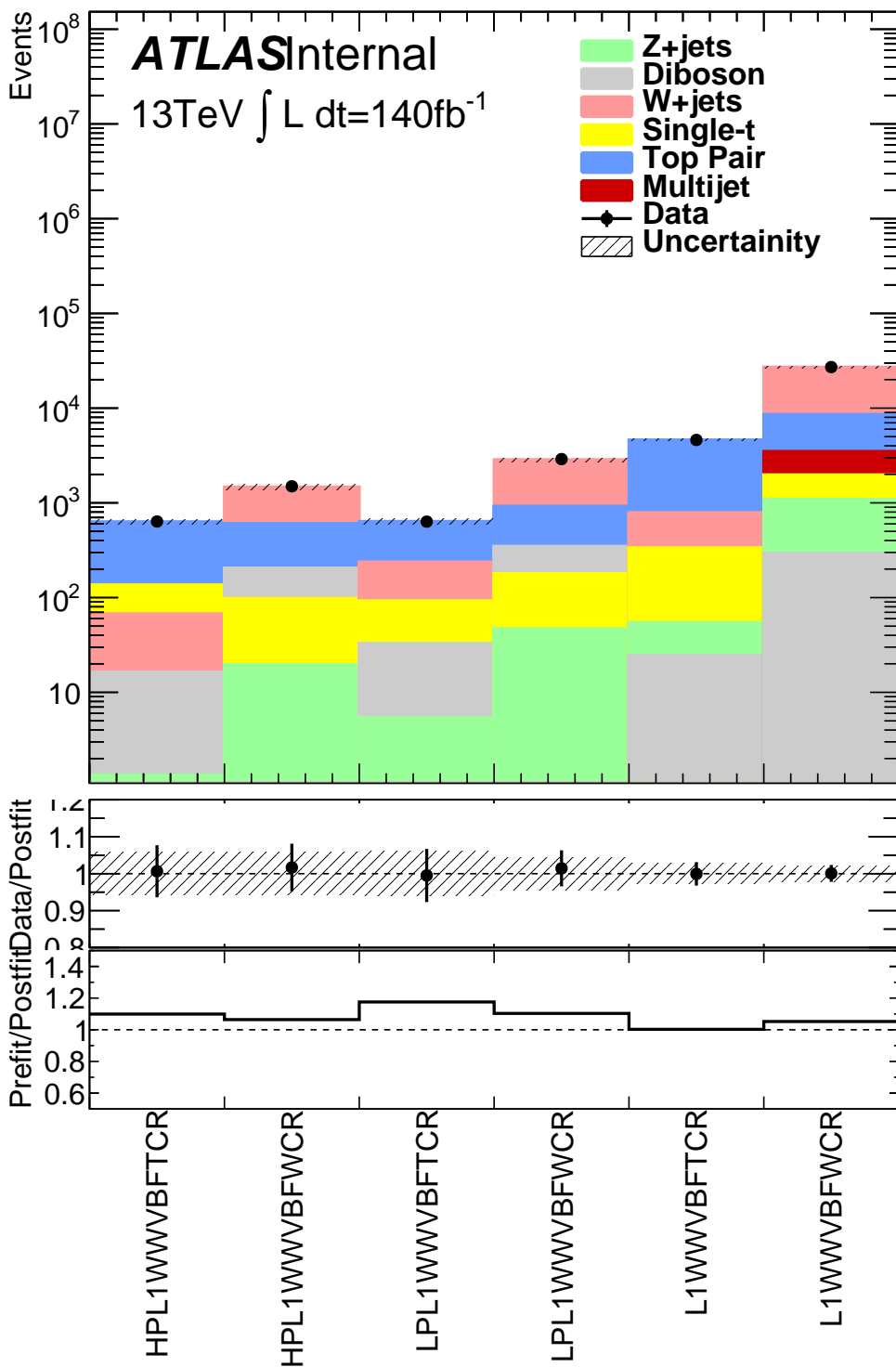


**Figure 12.11:** This figure shows the distribution of  $m_{\ell\nu qq}$  in the VBF  $WW$  control regions.

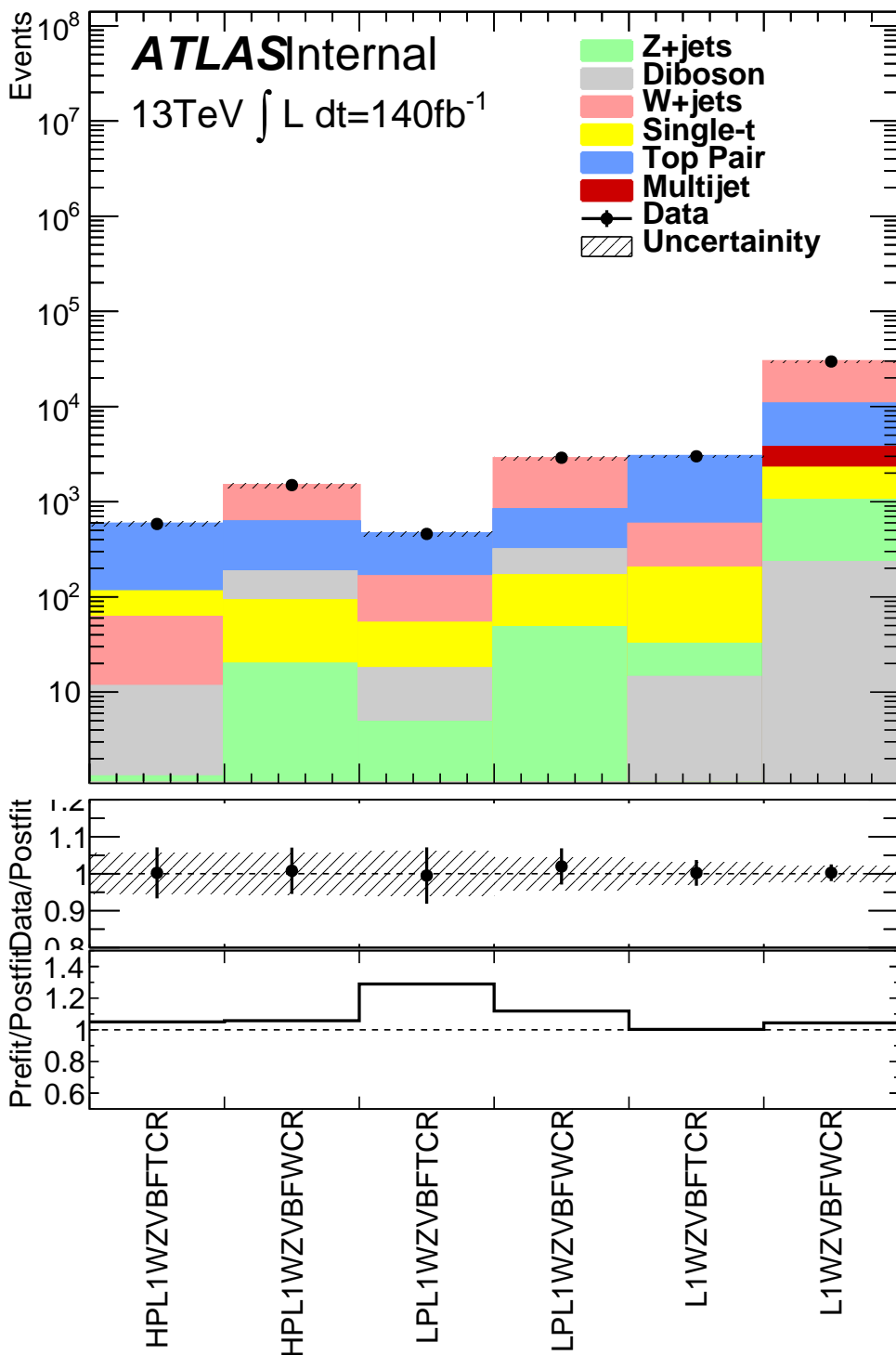


**Figure 12.12:** This figure shows the distribution of  $m_{\ell\nu qq}$  in the VBF  $WZ$  control regions.

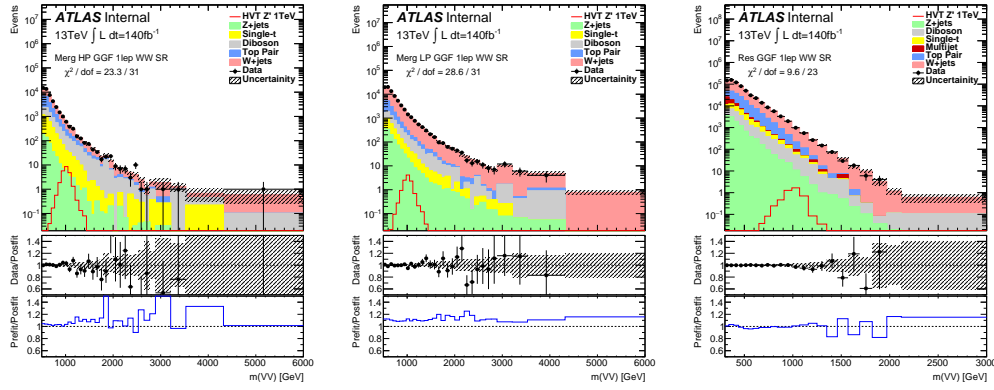


**Figure 12.13:** This figure shows the distribution of  $m_{\ell\nu qq}$  in the GGF  $WW$  signal regions.

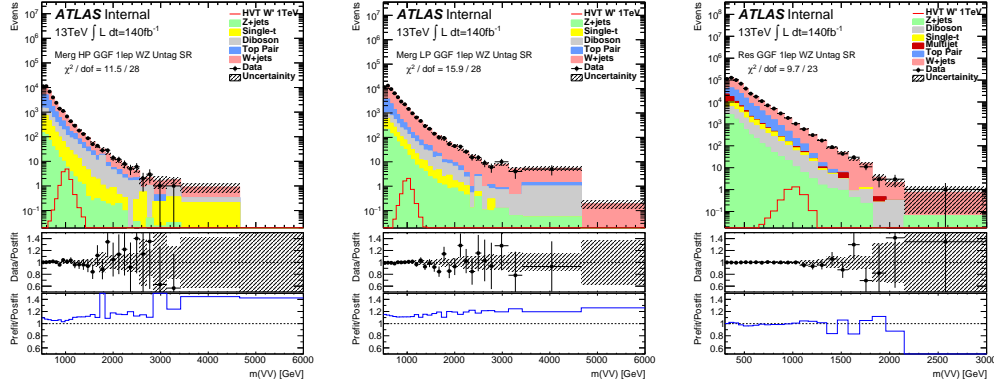


**Figure 12.14:** This figure shows the distribution of  $m_{\ell\nu qq}$  in the GGF  $WZ$  Untag signal regions.

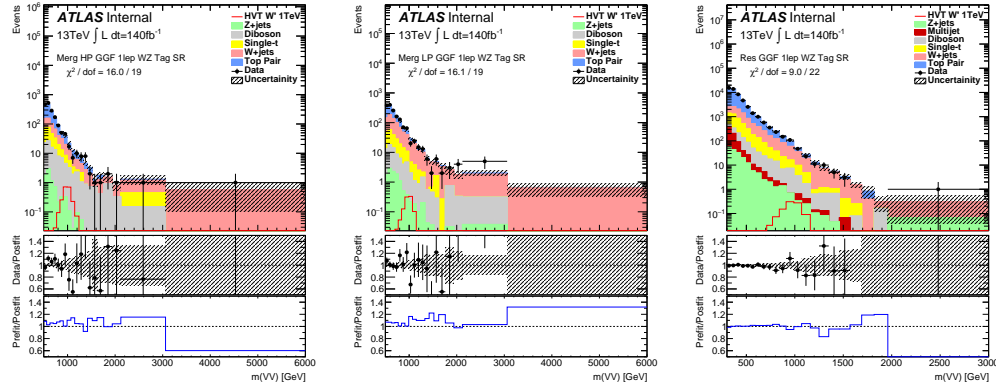


**Figure 12.15:** This figure shows the distribution of  $m_{\ell\nu qq}$  in the GGF  $WZ$  Tag signal regions.

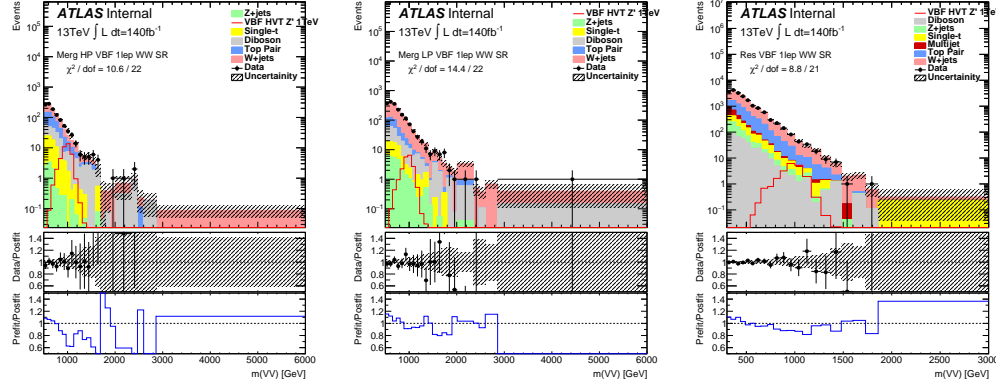


**Figure 12.16:** This figure shows the distribution of  $m_{\ell\nu qq}$  in the VBF  $WZ$  Tag signal regions.

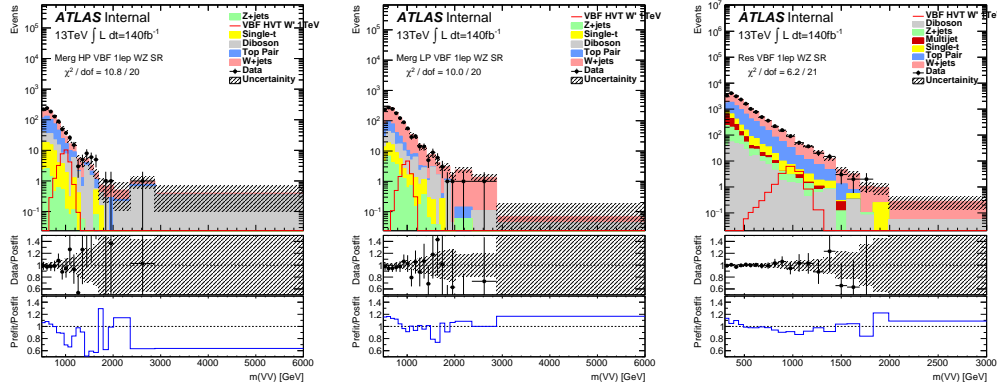


**Figure 12.17:** This figure shows the distribution of  $m_{\ell\nu qq}$  in the VBF  $WZ$  Tag signal regions.

## 12.4 Limits

Using the exclusion limits tests discussed previously, exclusion limits are set on  $\mu$  and consequently cross-sections for different signal models. Exclusion limits for the models considered are shown in Figure 12.18 - 12.20. These limits exclude HVT Model A  $W' < 3.4 \text{ TeV}$  and  $Z' < 3.3 \text{ TeV}$  and Model B  $W' < 3.7 \text{ TeV}$  and  $Z' < 3.7 \text{ TeV}$ . Randall Sundrum Gravitons are excluded for masses below  $1.6 \text{ TeV}$ .

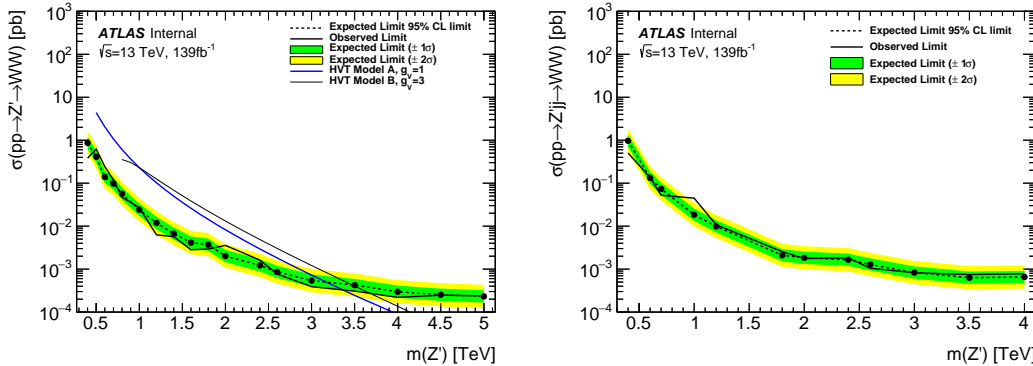


**Figure 12.18:** This figure shows theory, expected and observed limits for HVT  $W'$  DY (left) and VBF (right) production.

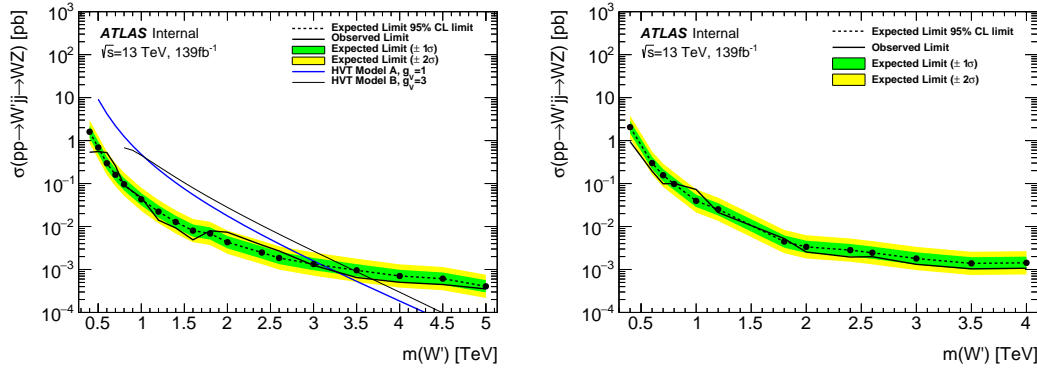


**Figure 12.19:** This figure shows theory, expected and observed limits for HVT  $Z'$  DY (left) and VBF (right) production.

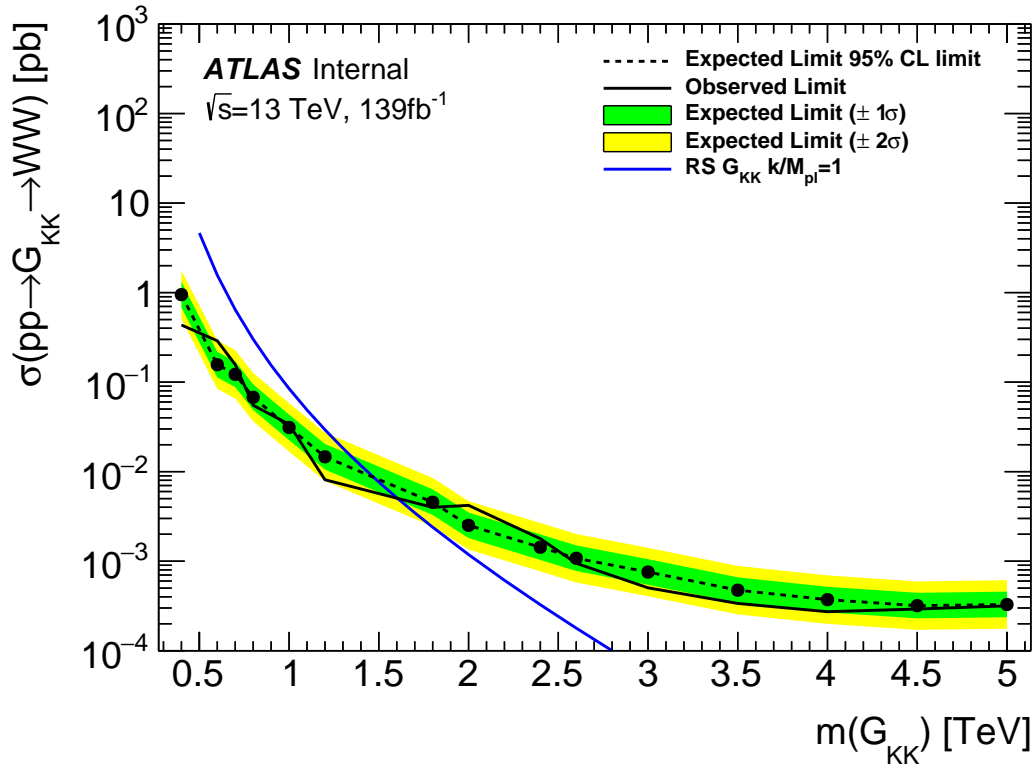


**Figure 12.20:** This figure shows theory, expected and observed limits for RS Gravitons via DY production.

## **Part VI**

1294

## **Quark and Gluon Tagging**

1295

<sub>1296</sub> **Chapter 13**

<sub>1297</sub> **Prospects**

<sub>1298</sub> For the resolved analysis, signal jets are quark enriched and background jets are  
<sub>1299</sub> gluon dominated. By classifying jets in the event as quark or gluon initiated, less  
<sub>1300</sub> background would contaminate the signal region. Figure 13.1 shows the PDGID  
<sub>1301</sub> for the truth parton matched to the jet (meaning the highest energy parton in  
<sub>1302</sub> the jet catchment area) in events passing the resolved signal region selections.  
<sub>1303</sub> PDGID = -1 corresponds to pileup jets,  $0 < \text{PDGID} < 6$  correspond to quarks  
<sub>1304</sub> and  $\text{PDGID} = 21$  corresponds to gluons. From this Figure, it is evident that a  
<sub>1305</sub> notable fraction of the background that contaminates the signal region contains  
<sub>1306</sub> gluon jets, especially for the sub-leading jet.

<sub>1307</sub> As gluons jets have more constituents and therefore more tracks ( $n_{trk}$ ), the  
<sub>1308</sub> background jets have more tracks than the signal jets. This is shown in Fig-  
<sub>1309</sub> ure 13.2. Therefore, by cutting on the number of tracks in a jet, quark and gluon  
<sub>1310</sub> jets may be distinguished (i.e. jets with less than a given number of tracks are  
<sub>1311</sub> classified as a quark, otherwise the jet is classified as a gluon.) Moreover, as the  
<sub>1312</sub> momentum of the jet increases the number of tracks also increases logarithmically  
<sub>1313</sub> [Cite nachman thesis Natasha]. Therefore by applying a cut on the number of  
<sub>1314</sub> tracks that scales with the  $\ln(p_T)$  is more powerful than a threshold cut on the

1315 number of tracks. Figure 13.3-Figure 13.6 show normalized heat maps of  $\ln(p_T)$   
1316 vs the number of reconstructed tracks for the background and a 300 GeV Z' signal.  
1317 In these plots it is evident that the number of tracks in the background jets grows  
1318 more quickly with  $\ln(p_T)$  than for the signal jets. This is expected given that the  
1319 signal is quark dominated and the background is gluon dominated.

1320 In Figure 13.8 is the ROC Curve for quark gluon tagging with cut on the  
1321 number of tracks in a jet that depends on  $\ln(p_T)$ . The sum of the backgrounds in  
1322 the signal region were used for this curve. Here the quark tagging efficiency is the  
1323 ratio of quarks tagged as quarks to the total number of quarks in the signal region.  
1324 The gluon rejection is calculated as the reciprocal of the gluon tagging efficiency.  
1325 Choosing a 90% efficient working point with a rejection of 1.4 corresponds to a  
1326 slope of 4 and intercept of -5. Tagging both jets in this analysis would yield an  
1327 efficiency of  $90\%^{n_{jets}}$ . Focusing on the background in Figure 13.9, this cut helps  
1328 minimize gluon contamination in the signal region. Also, from these heat maps it  
1329 is obvious that the number of tracks in gluon jets grows more quickly than those  
1330 in quark jets.

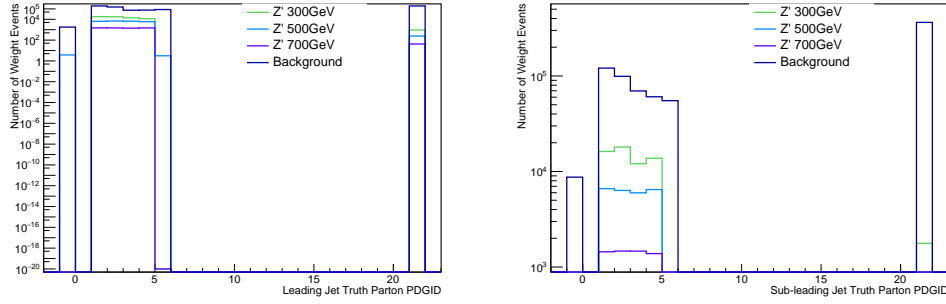


**Figure 13.1:** PDGID of the truth-level parton matched to the small-R jets passing the Resolved GGF WW Signal Region selections for the (a) Leading (b) Sub-Leading jets . These distributions are shown for 300, 500, and 700GeV Z' signals and the background.

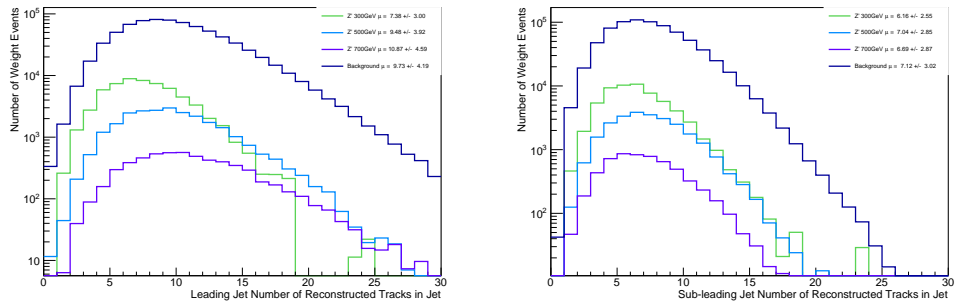


**Figure 13.2:** The number of tracks in small-R jets in events passing the Resolved GGF WW Signal Region selections for the (a) Leading (b) Sub-Leading jets. These distributions are shown for 300, 500, and 700GeV Z' signals and the background.

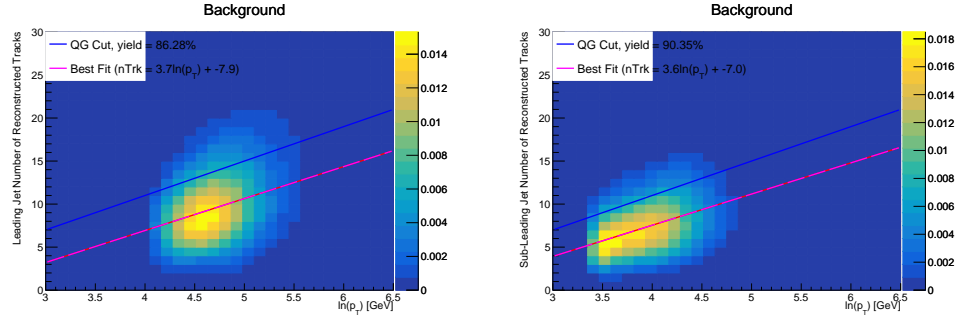


**Figure 13.3:** The number of tracks in background small-R jets in events passing the Resolved GGF WW Signal region selection vs.  $\ln(p_T)$  for (a)Leading (b) Sub-Leading jets. The best fit line for the distribution is also shown, as well as the percentage of jets that pass a cut of number of tracks  $< 4 \times \ln(p_T) - 5$ . Note the number of total entries in these plots has been normalized to one.

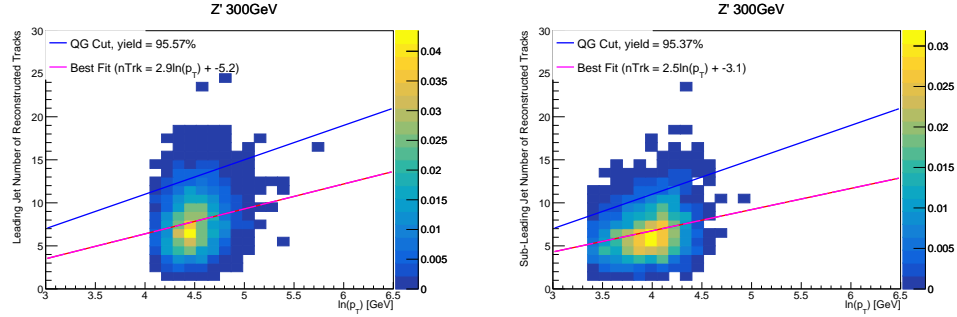


**Figure 13.4:** The number of tracks in small-R jets in 300GeV  $Z'$  events passing the Resolved GGF WW Signal region selection vs.  $\ln(p_T)$  for (a)Leading (b) Sub-Leading jets. The best fit line for the distribution is also shown, as well as the percentage of jets that pass a cut of number of tracks  $< 4 \times \ln(p_T) - 5$ . Note the number of total entries in these plots has been normalized to one.

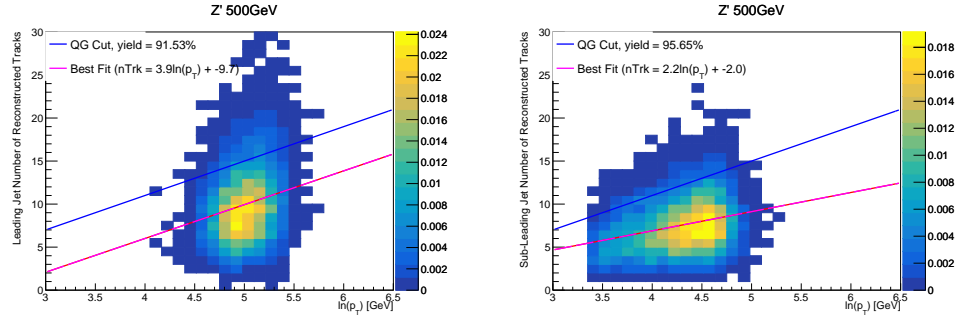


**Figure 13.5:** The number of tracks in small-R jets in 500GeV  $Z'$  events passing the Resolved GGF WW Signal region selection vs.  $\ln(p_T)$  for (a)Leading (b) Sub-Leading jets. The best fit line for the distribution is also shown, as well as the percentage of jets that pass a cut of number of tracks  $< 4 \times \ln(p_T) - 5$ . Note the number of total entries in these plots has been normalized to one.

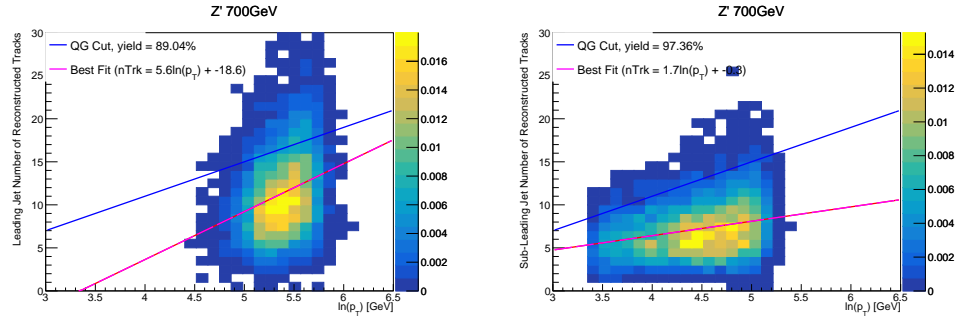


**Figure 13.6:** The number of tracks in small-R jets in 700GeV  $Z'$  events passing the Resolved GGF WW Signal region selection vs.  $\ln(p_T)$  for (a)Leading (b) Sub-Leading jets. The best fit line for the distribution is also shown, as well as the percentage of jets that pass a cut of number of tracks  $< 4 \times \ln(p_T) - 5$ . Note the number of total entries in these plots has been normalized to one.

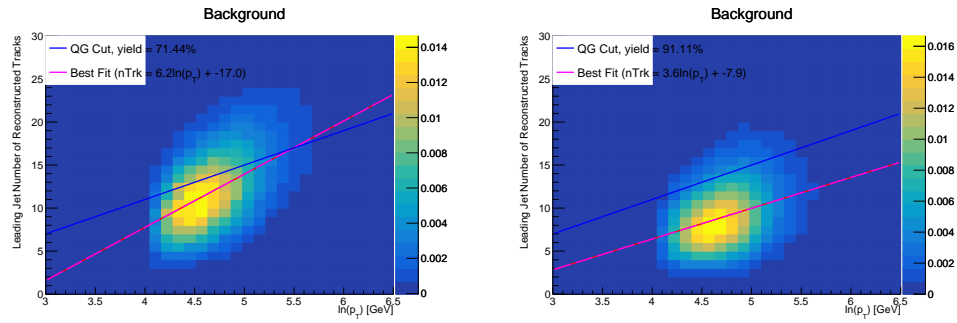


**Figure 13.7:** The number of tracks in leading small-R jets in background events passing the Resolved GGF WW Signal region selection vs.  $\ln(p_T)$  for (a)Gluons (b) Quarks jets. The best fit line for the distribution is also shown, as well as the percentage of jets that pass a cut of number of tracks  $< 4 \times \ln(p_T) - 5$ .Note the number of total entries in these plots has been normalized to one.

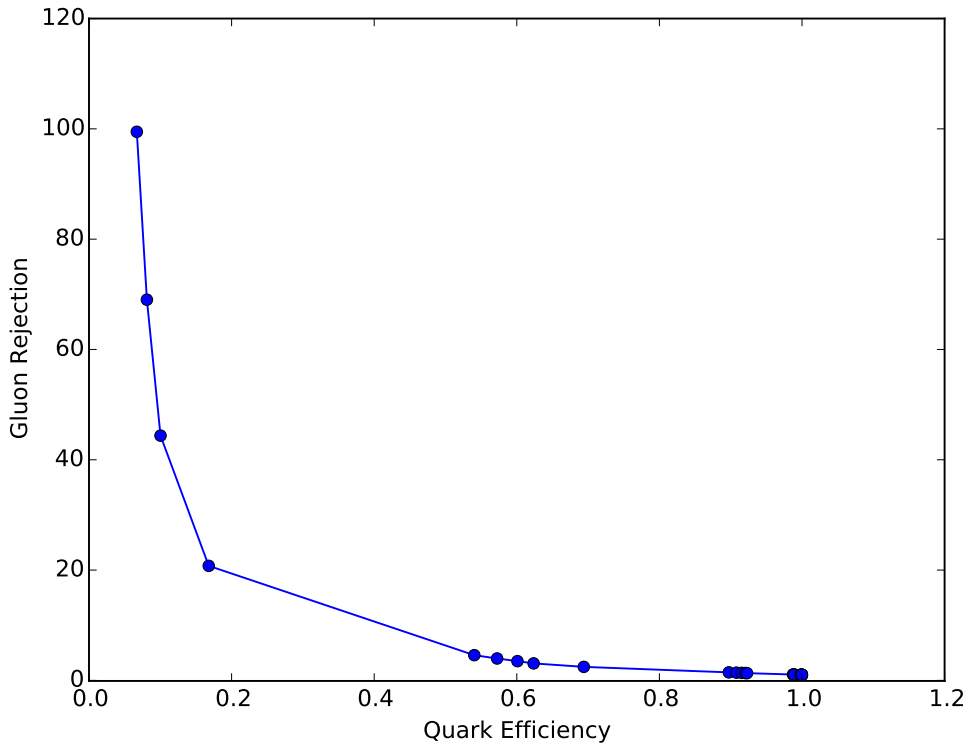


**Figure 13.8:** ROC Curve for Quark and Gluon Tagging with a cut on the number of tracks that depends on the  $\ln(p_T)$ .

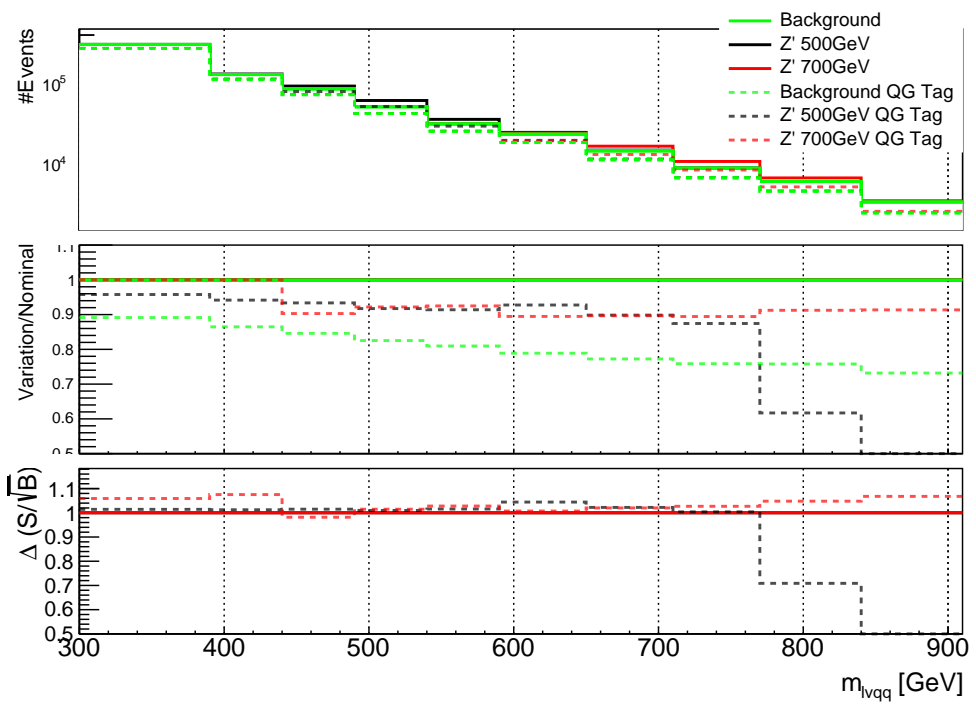


**Figure 13.9:** The top panel shows the distribution of  $m_{lvqq}$  with and without quark gluon tagging. The middle panel shows the ratio of the signals and backgrounds with and without quark gluon tagging. The bottom panel shows the change in  $S/\sqrt{B}$  with quark gluon tagging.

<sub>1331</sub> **Chapter 14**

<sub>1332</sub>  **$n_{trk}$  Calibration**

<sub>1333</sub> As tagger based on nTrk cuts on the number of tracks in jets, a quantity that  
<sub>1334</sub> is not known with infinite precision, means that relevant systematic uncertainties  
<sub>1335</sub> must be evaluated. The sources of uncertainty in  $n_{trk}$  may be split into modeling  
<sub>1336</sub> and experimental uncertainties.

<sub>1337</sub> Modeling uncertainties are obtained by assessing PDF and ME uncertainties  
<sub>1338</sub> on the number of charged particles in particle-level jets in dijet events. The  
<sub>1339</sub> number of charged particles as a function of jet  $p_T$  is calculated using an Iterative  
<sub>1340</sub> Bayesian (IB) technique [cite paper].

<sub>1341</sub> This measurement ([8]) uses the ATLAS 2012 pp collision dataset, correspond-  
<sub>1342</sub> ing to  $20.3/\text{fb}$  at center-of-mass energy  $\sqrt{s} = 8\text{TeV}$ . The number of charged con-  
<sub>1343</sub> stituents depends on fragmentation modeling and matrix elements, which do not  
<sub>1344</sub> depend on  $s$ . For this reason, it is safe to use these uncertainties for  $\text{sqrt}(s)=13\text{TeV}$ .  
<sub>1345</sub> Monte Carlo (MC) samples are used to determine the response matrix. The MC  
<sub>1346</sub> sample is a dijet sample generated with Pythia 8.175 using CT10 PDF and AU2  
<sub>1347</sub> tune. The anti- $k_T$  algorithm is used to cluster jets with a radius parameter  $R$   
<sub>1348</sub>  $= 0.4$ . Jets are required to have  $|\eta| < 2.1$ . Tracks in jets are required to have  
<sub>1349</sub>  $p_T > 500\text{MeV}$ ,  $|\eta| < 2.5$ , track-fit  $\chi^2 < 3.0$  and originate from the primary ver-

tex. Matching tracks to jets is accomplished using ghost-association [cite]. In this technique, jets are re-clustered with the track collection augmented with "ghost" versions of tracks. These "ghosts" tracks have the same direction as their parent track, but infinitesimal track  $p_T$ . This insures meta-jet properties (e.g.  $\eta$ ,  $p_T$ , etc) are unchanged. A track is matched to a jet if it's ghost version remains in the jet after re-clustering. Further details of the data, object, and event selection may be found in [cite 35].

To select dijet topologies events are required to have at least two jets with  $p_T > 50GeV$  that are relatively well-balanced ( $p_T^{lead}/p_T^{sub-lead} < 1.5$ ).

In the IB technique, the prior distribution and number of iterations are the inputs [cite Bayesian paper]. The IB response matrix connects number of charged particles to the number of tracks in jets determined using the simulated samples. This response matrix is used to unfold data to extract the  $n_c$ . Before applying the response matrix a fake factor is applied. This accounts for jets that pass detector level selections, but not particle level selections. Following this, the IB method iteratively applies the response matrix using the nominal Pythia 8.175 sample as a prior. The number of IB iterations is chosen to minimize unfolding bias and statistical fluctuations. For this measurement four iterations was found to be optimal by minimizing the unfolding bias from pseudodata simulated with Herwig++ with a prior from Pythia 8 AU2. Finally, the inefficiency factor is applied to account for events passing particle level selection but not detector level, yielding the unfolded nCharged distribution.

This process is prone to three main sources of bias: response matrix, correction factor, and unfolding procedure uncertainties. The response matrix is sensitive to experimental uncertainties impacting jet track reconstruction and calorimeter jet  $p_T$ . Correction factors are also sensitive to experimental uncertainties (e.g. JES)

1376 as such uncertainties modify detector level acceptance. Sensitivity to particle  
 1377 level acceptance is calculated by comparing Pythia and Herwig. Finally, the bias  
 1378 from the IB prior choice is determined by reweighting the particle-level spectrum,  
 1379 so the simulated detector level spectrum more closely matches the uncorrected  
 1380 data. Unfolding this modified detector-level simulation and comparing it to the re-  
 1381 weighted particle-level spectrum indicates bias from the prior distribution choice.  
 1382

A summary of all the systematic uncertainties associated with this unfolding  
 1383 may be found in [ref paper]. Total uncertainties are < 7% for the number of  
 1384 charged particles in jets. The unfolded distribution of the nCharged in jets from  
 1385 data are further analyzed to extract the quark and gluon nCharged distributions.  
 1386 In dijet events, the jet with a larger  $\eta$  is more energetic and therefore more likely  
 1387 to be a quark. This is due to the quarks in protons generally having a larger  
 1388 fraction of the total momentum of the proton constituents. The more central jet  
 1389 is more likely to be a gluon-initiated jet. This correlation between jet  $\eta$  and flavor  
 1390 may then be used to extract nCharged in  $p_T$  bins using:

$$\langle n_c^f \rangle = f_q^f \langle n_c^q \rangle + f_g^f \langle n_c^g \rangle \quad (14.1)$$

1391

$$\langle n_c^c \rangle = f_q^c \langle n_c^q \rangle + f_g^c \langle n_c^g \rangle \quad (14.2)$$

1392 In this equation the f and c subscripts denote the more forward and central  
 1393 jets, respectively. The q and g subscripts denote quark and gluon. The fraction  
 1394 of more forward jets that are say gluons is denoted by  $f_g^f$ . The other relevant jet  
 1395 fractions are denoted with the same naming scheme. Finally,  $\langle n_c \rangle$  is the average  
 1396 number of charged particles in a jet in a given  $p_T$  bin. To show that Eq. (??) may  
 1397 be used to extract quark and gluon  $n_c$  distributions the extracted distributions  
 1398 are compared to  $n_c$  distributions determined using the jet flavor in simulation.  
 1399 Figure [add figure natasha] shows that the extracted and true distributions differ

1400 by < 1% over the  $p_T$  range probed for this study. Moreover, this implies that  $n_c$   
1401 depends only on the flavor of the initiating parton and jet  $p_T$ .

1402 These extracted distributions are prone to PDF and ME biases. The bias from  
1403 the choice of the CT10 PDF for the Pythia sample is accounted for by comparing  
1404 quark/gluon fractions for the nominal CT10 sample with its eigenvector variations.  
1405 Comparing the quark/gluon fractions from Pythia 8 and Herwig++ quantify the  
1406 uncertainty from the ME calculation. These uncertainties are added in quadra-  
1407 ture with the unfolding uncertainty to give the total modelling uncertainty on  
1408 the extracted  $n_c$  distribution. This is shown in Figure 15.2.

1409 To apply these uncertainties in  $n_c$  distributions in data, per-jet event weights  
1410 are associated with each uncertainty according to:

$$w_i(n_c) = \frac{P(n_c | n_c > \pm \sigma_{n_c}^i)}{P(n_c | n_c >)} \quad (14.3)$$

1411 In Eq. (??), i denotes the uncertainty considered, P is the Poisson probability,  
1412 and  $\sigma_{n_c}^i$  represents the average impact of the uncertainty on  $n_c$ .

1413 The previous uncertainties described accounted for modeling uncertainty as-  
1414 sociated with the number of charged particles in a jet. However,  $n_c$  is not a  
1415 measurable quantity. Instead the number of tracks in a jet is measured, which is  
1416 a proxy for  $n_c$ . Therefore the uncertainties associated with the measurement of  
1417 nTracks must also be considered ([10]). These uncertainties were calculated using  
1418 a Pythia 8 dijet sample with NNPDF 23 and Run 2 data. Track reconstruction  
1419 efficiency and fake rates are the dominant sources of nTrack uncertainties.

1420 The track reconstruction efficiency is affected by the uncertainty of the de-  
1421 scription of the ID material in simulation and the modeling of charged-particle  
1422 interactions with this material. These uncertainties are accounted for by varying  
1423 the ID material by 5-25% (dependent on the region of the detector considered).

1424 The difference in the tracking efficiency between the nominal and varied simula-  
1425 tion give the uncertainty on the track reconstruction efficiency. Another important  
1426 source of track reconstruction inefficiency arises in the core of jets. The high den-  
1427 sity of tracks in the jet cores can cause ID clusters to merge. The fraction of lost  
1428 tracks due to merging is given by the fraction of tracks that have a charge of two  
1429 minimum ionizing particles. This quantity is compared between data and simu-  
1430 lation resulting in an uncertainty of 0.4% on tracks with  $\Delta R < 0.1$ . Combining  
1431 these effects gives a total uncertainty as a function of  $p_T$  and  $\eta$  that is generally  
1432  $< 2\%$  [references figure 44 from [10]].

1433       Fake tracks are the other dominant source of nTrk uncertainty. Fake tracks  
1434 are tracks that cannot be associated to a single particle. Often these tracks are a  
1435 result of random combinations of hits from charged particles that overlap in space.  
1436 In dense environments, such as the core of jets or high-pileup environments, fake  
1437 tracks are more likely. Fake tracks are estimated with a 'control region method'  
1438 which is briefly summarized here [[9]]. By applying a series of track selections  
1439 to enrich the fraction of fake tracks (e.g.  $|d_0| > 0.1$ , track  $\chi^2 > 1.4$ , etc) in  
1440 simulation, templates for fake track parameters are calculated. These templates  
1441 are then fit to data to determine the fraction of fake tracks. On average the fake  
1442 rate is found to be 30% (independent of  $p_T$  and  $\eta$ ).

1443       To assess the impact of these two detector level uncertainties, tracks are ran-  
1444 domly dropped according to the rates described above. Reconstruction and fake  
1445 uncertainties both lower the number of tracks, hence these uncertainties are one-  
1446 sided. By dropping tracks in this way a varied nTrk distribution is calculated for  
1447 both uncertainties. The associated per-jet event weights are then calculated in  
1448 the same way as the modeling weights as:

$$w_i(n_c) = \frac{P(n_{trk} | < n_{trk} > \pm \sigma_{n_{trk}}^i)}{P(n_{trk} | < n_{trk} >)} \quad (14.4)$$

1449        Adding the modeling and detector level uncertainties in quadrature gives the  
 1450        overall nTrack uncertainty. The effects of the individual uncertainties on the nTrk  
 1451        distributions can be seen in Fig 15.4. Fig 15.3 shows the  $m_{lvqq}$  and nTrk distri-  
 1452        butions for the W and Top control regions before likelihood fitting. In these plots  
 1453        the nTrk uncertainties improve agreement between data and MC. The remaining  
 1454        differences are likely covered by likelihood fitting and improving the analysis itself.

1455 **Chapter 15**

1456 **Application**

1457 Using the 90% WP of the  $n_{trk}$  tagger improves  $S/\sqrt{B}$  is  $\sim 3\%$  as shown in  
1458 Figure 13.9. Although,  $n_{trk}$  is the single most powerful discriminating variable  
1459 for quark and gluon jets, the addition of other jet variables would improve the  
1460 classification efficiency. Figure 15.1 shows the possible improvement of 10%  
1461 in jet classification using the truth label of the jets to classify jets. This type of  
1462 improvement is possible by using variables such as jet width, and energy correlata-  
1463 tors. Figure [add BDT figure/use 1612.01551.pdf] shows for a 90% quark tagging  
1464 efficiency for a 100 GeV jet, a BDT improve the gluon rejection by 0.4. Once this  
1465 tagger is calibrated it would improve the analysis sensitivity of this channel.

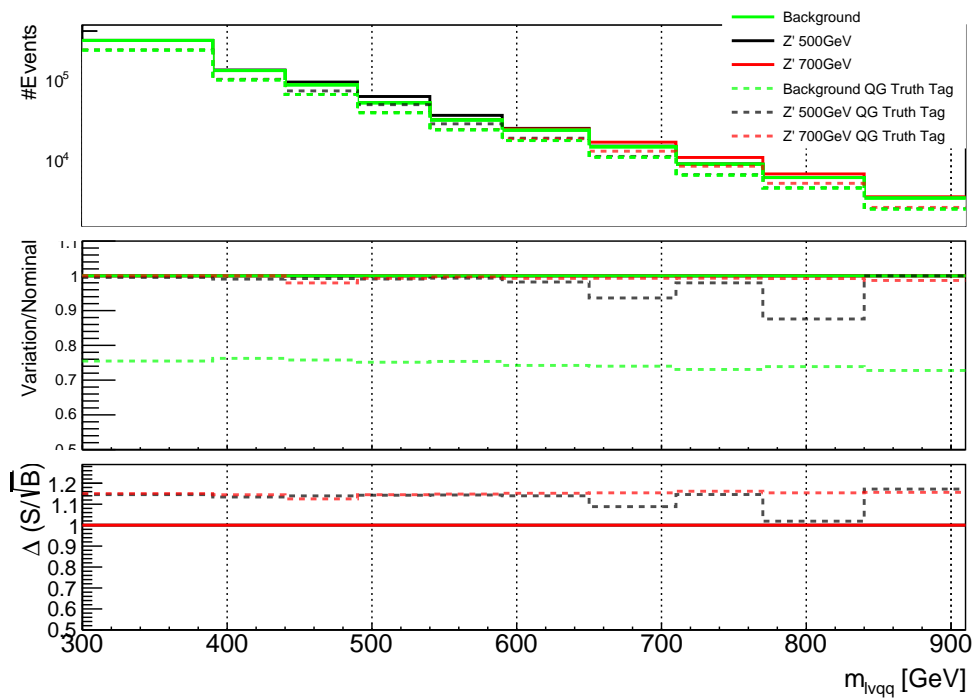


**Figure 15.1:** The top panel shows the distribution of  $m_{lvqq}$  with and without requiring jets to be true quarks. The middle panel shows the ratio of the signals and backgrounds with and without requiring jets to be true quarks. The bottom panel shows the change in  $S/\sqrt{B}$  when requiring jets to be true quarks..

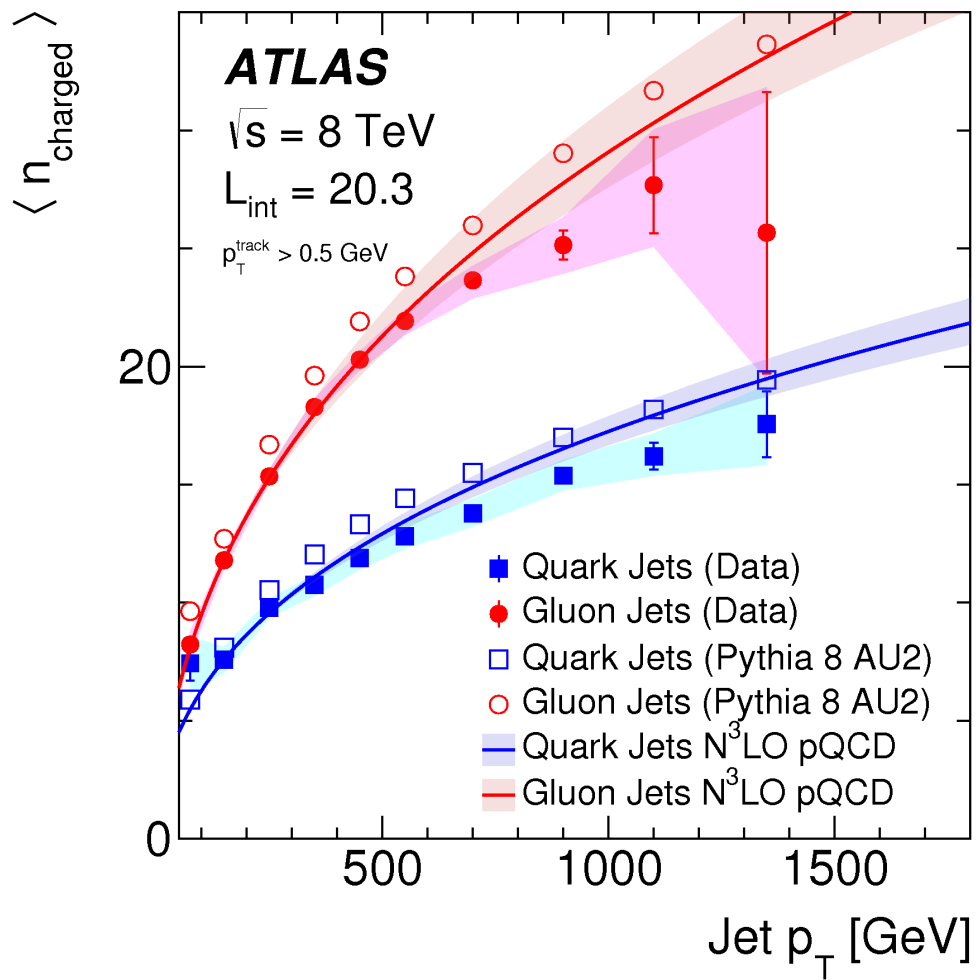


**Figure 15.2:** Unfolded and extracted  $n_C$  qg dstbs..

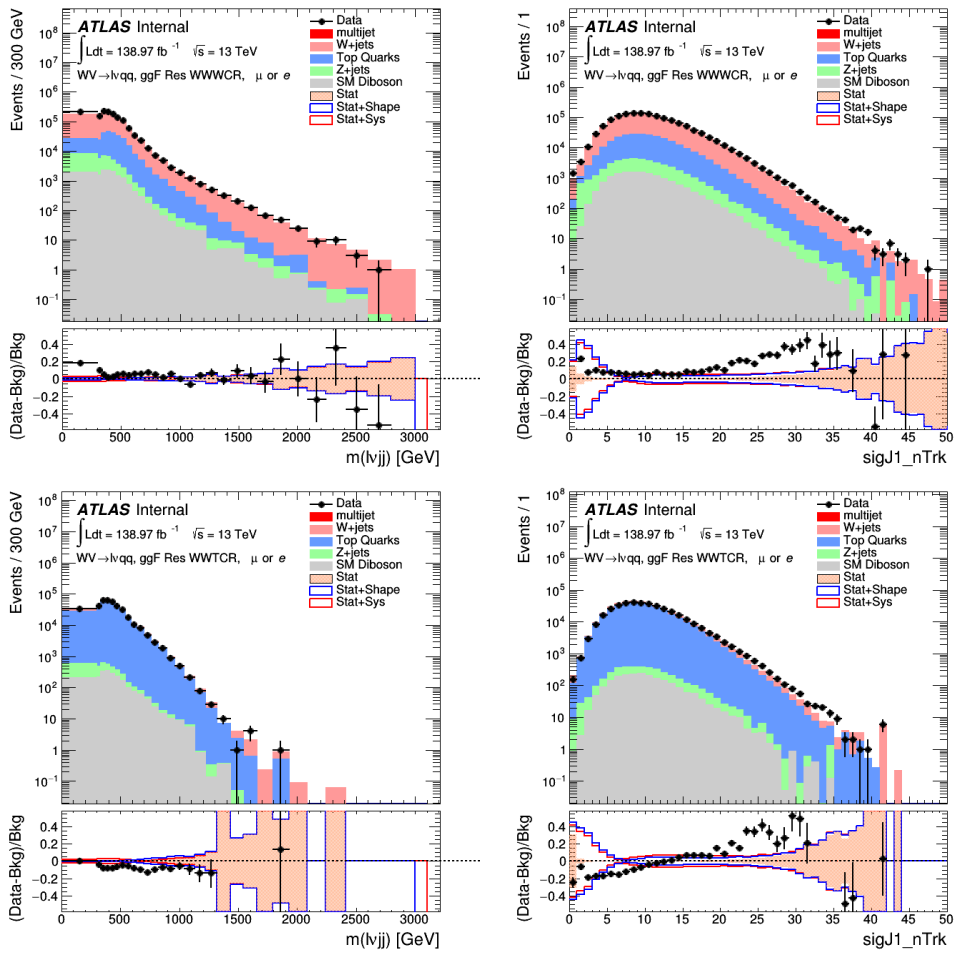


**Figure 15.3:** PDGID of the truth-level parton matched to the small-R jets passing the Resolved GGF WW Signal Region selections for the (a) Leading (b) Sub-Leading jets . These distributions are shown for 300, 500, and 700GeV  $Z'$  signals and the background.

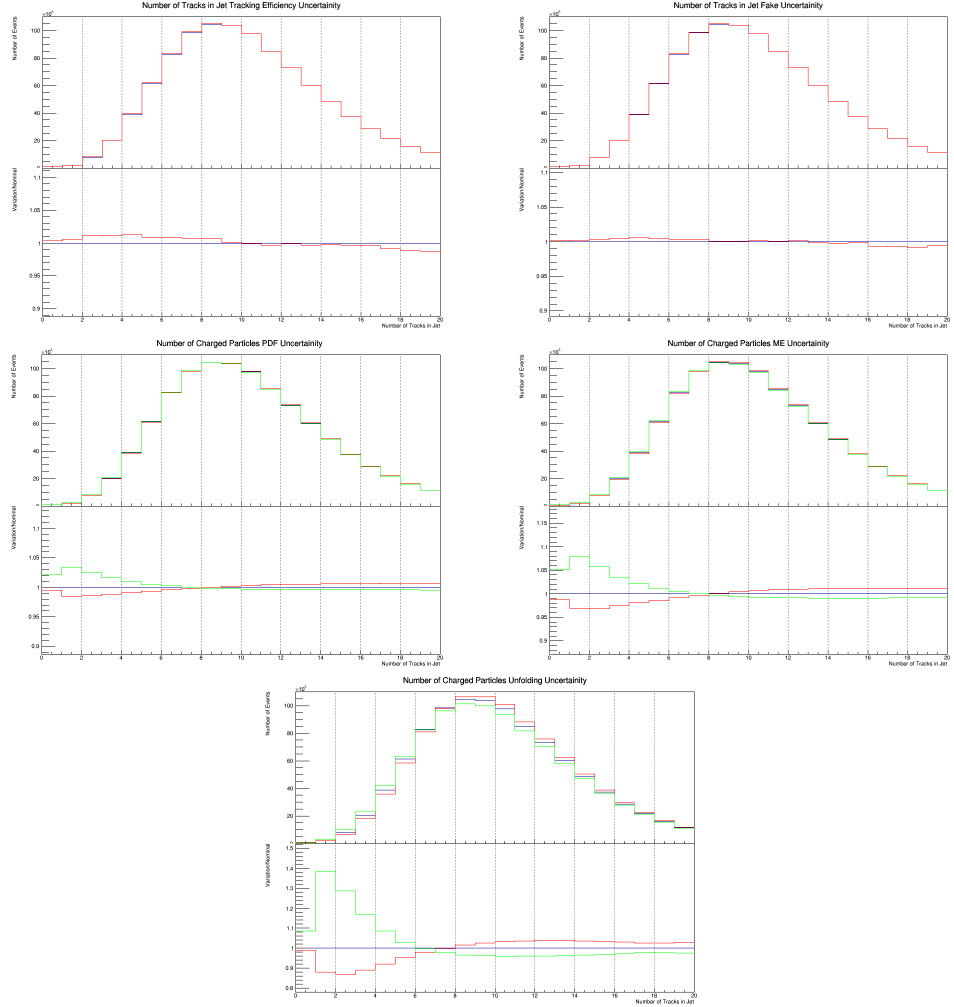


**Figure 15.4:** These figures show the impact of the uncertainties on the number of tracks in the leading jet in the sum of the background sample in the Resolved GGF WW SR (a) tracking efficiency (b) fake (c) PDF (d) ME (e) unfolding uncertainties.

## **Part VII**

1466

## **Conclusion**

1467

1468 **Chapter 16**

1469 **Conclusions**

1470 A search for  $WW$  and  $WZ$  diboson resonance production in  $\ell\nu qq$  final states  
1471 was performed using  $139\text{fb}^{-1}$  of  $pp$  collision data collected at a center-of-mass  
1472 energy of  $\sqrt{s} = 13\text{TeV}$  by that ATLAS detector at the LHC between 2015 and  
1473 2018. No excess of events above the background-only expectation was observed.  
1474 The largest local excess is approximately  $2.7\sigma$ , which is not significant. Limits  
1475 on the production cross section are obtained for the HVT  $W'$  and  $Z'$  and RS  
1476 Gravitons. Signal masses below 3.4 (3.7) TeV are excluded for HVT  $W'$  Model  
1477 A(B). Signal masses below 3.3 (3.7) TeV are excluded for HVT  $Z'$  Model A(B).  
1478 Randall Sundrum Gravitons are excluded for masses below 1.6 TeV. Going forward,  
1479 improving the classification of jets in events would improve analysis sensitivity.  
1480 To distinguish quark from gluon jets a jet tagger based on the number of tracks in  
1481 jets is studied in the context of this search. Finally, the calibration of the number  
1482 of tracks in jets is discussed.

# Bibliography

- [1] Lecture notes particle physics ii.
- [2] Kaustubh Agashe, Hooman Davoudiasl, Gilad Perez, and Amarjit Soni. Warped Gravitons at the LHC and Beyond. *Phys. Rev.*, D76:036006, 2007.
- [3] G. Altarelli and G. Parisi. Asymptotic freedom in parton language. *Nuclear Physics B*, 126(2):298 – 318, 1977.
- [4] ATLAS Collaboration. Atlas muon reconstruction performance in lhc run 2.
- [5] ATLAS Collaboration. Summary plots from the atlas standard model physics group.
- [6] ATLAS Collaboration. Tagging and suppression of pileup jets with the atlas detector.
- [7] ATLAS Collaboration. Jet energy scale measurements and their systematic uncertainties in proton–proton collisions at  $\sqrt{s} = 13$  tev with the atlas detector. arXiv: 1703.09665 [hep-ex].
- [8] ATLAS Collaboration. Measurement of the charged-particle multiplicity inside jets from  $s=\sqrt{8}$  tev pp collisions with the atlas detector. arXiv:1602.00988 [hep-ex].
- [9] ATLAS Collaboration. Performance of the atlas track reconstruction algorithms in dense environments in lhc run 2. arXiv:1704.07983 [hep-ex].
- [10] ATLAS Collaboration. Properties of jet fragmentation using charged particles measured with the atlas detector in pp collisions at  $\sqrt{s} = 13$  tev. arXiv:1906.09254 [hep-ex].
- [11] Alex Dias and V. Pleitez. Grand unification and proton stability near the peccei-quinn scale. *Physical Review D*, 70, 07 2004.
- [12] Stefan Höche, Frank Krauss, Marek Schönherr, and Frank Siegert. Qcd matrix elements + parton showers. the nlo case. *Journal of High Energy Physics*, 2013(4), Apr 2013.

- 1510 [13] Diederik P. Kingma and Jimmy Ba. Adam: A method for stochastic opti-  
1511 mization, 2014.
- 1512 [14] David Krohn, Jesse Thaler, and Lian-Tao Wang. Jets with variable  $r$ . *Journal*  
1513 *of High Energy Physics*, 2009(06):059–059, Jun 2009.
- 1514 [15] Gregory Soyez Matteo Cacciari, Gavin P. Salam. The anti- $k_T$  jet clustering  
1515 algorithm. arXiv:0802.1189 [hep-ph].
- 1516 [16] Duccio Pappadopulo, Andrea Thamm, Riccardo Torre, and Andrea Wulzer.  
1517 Heavy vector triplets: bridging theory and data. *Journal of High Energy*  
1518 *Physics*, 2014(9), Sep 2014.
- 1519 [17] Antonio Pich. The Standard Model of Electroweak Interactions. In *Proceed-  
1520 ings, High-energy Physics. Proceedings, 18th European School (ESHEP 2010):  
1521 Raseborg, Finland, June 20 - July 3, 2010*, pages 1–50, 2012. [,1(2012)].
- 1522 [18] Lisa Randall and Raman Sundrum. A Large mass hierarchy from a small  
1523 extra dimension. *Phys. Rev. Lett.*, 83:3370–3373, 1999.
- 1524 [19] Sebastian Raschka. Model evaluation, model selection, and algorithm selec-  
1525 tion in machine learning, 2018.
- 1526 [20] Tania Robens and Tim Stefaniak. Lhc benchmark scenarios for the real higgs  
1527 singlet extension of the standard model. *The European Physical Journal C*,  
1528 76(5), May 2016.
- 1529 [21] Alex Sherstinsky. Fundamentals of recurrent neural network (RNN) and long  
1530 short-term memory (LSTM) network. *CoRR*, abs/1808.03314, 2018.
- 1531 [22] Muhammed Ali Sit and Ibrahim Demir. Decentralized flood forecasting using  
1532 deep neural networks. Jun 2019.
- 1533 [23] Wojciech Zaremba, Ilya Sutskever, and Oriol Vinyals. Recurrent neural net-  
1534 work regularization, 2014.